The modelling, design and optimisation of a hypervelocity pulsed-power projectile launcher for extreme state research

Mila Fitzgerald

Keble College
University of Oxford

Thesis for the degree of
Doctorate of Philosophy, DPhil

2024

Abstract

Projectile launch techniques, such as gas guns and electromagnetic (**EM**) flyer plates, are capable of creating planar, high-pressure shocks across substantial material volumes, resulting in precise equation of state (EoS) measurements. However, achieving a quasi-equilibrated shock on impact requires the flyer to maintain constant velocity and near-constant density across its thickness, often limiting the maximum achievable velocity and pressure [1]. The electric gun, a pulsed-power driven projectile launcher, was originally invented in the 1970s as a tool for making TPa EoS measurements in metals [2]. However, the technique faces challenges in accelerating flyers thick enough to generate shock pulses with sufficient duration to make precise EoS measurements [3, 4]. Accelerating a thick flyer (> 0.5 mm) to hypervelocity can induce violent state change and disintegration [5]. Despite its limitations, the electric gun's mechanism offers unique advantages over the EM flyer plate, having higher efficiency and avoiding ohmic heating of the flyer [1]. This thesis aims to exploit advances in magneto-hydrodynamic (MHD) modelling techniques and access to M3, a 2.5 MJ pulsed-power device, to understand the state change mechanisms occurring in thick flyers accelerated by the electric gun. This understanding is then used to guide the design of an electric gun load for M3 that mitigates these mechanisms. First, a 0D model of the electric gun was created to expediate the investigation of the effects of the current profile and load geometry on the pressure states in the flyer. This 0D model was then leveraged to inform an experimental study of the effect of the current rise-time on the acceleration of flyers up to 2 mm (twice as thick as had been achieved prior to this thesis) to hypervelocity, revealing two predominant state change mechanisms in the flyer; the build-up of thermal pressures resulting in violent spallation on launch and plasma breakthrough late in flight. Employing these experimental results as a benchmark, the modelling of the electric gun was explored in two-dimensions using the MHD code, B2. For completeness, a material strength algorithm was incorporated in B2, though its effect on the simulated electric gun load performance was found to be secondary to the power loss in the load. Finally, the tools and understanding developed in the preceding chapters were combined to assess the performance of an electric gun load for making EoS measurements on a fixed rise-time device, driving a 20 GPa shock in a PMMA target for 1000 ns over a 10×10 mm area. Overall, this thesis reveals the electric gun to be a complex but versatile projectile launcher, with many promising avenues for advancement remaining.

The modelling, design and optimisation of a hypervelocity pulsed-power projectile launcher for extreme state research

Mila Fitzgerald
Keble College
University of Oxford

Thesis for the degree of
Doctorate of Philosophy, DPhil

2024

Acknowledgements

Whenever I read someone else's thesis, I always read the acknowledgements. This is perhaps because I know how enormously grateful I am for all the people in my life who have contributed to this DPhil, and am curious (nosy) to get a glimpse into another student's experience. My own experience has been greatly shaped by my industrial sponsor, First Light Fusion, who I also worked for as a scientist two days a week. This results in there being double the amount of people I must acknowledge, as opposed to just the Dynamic Behaviour of Materials lab group.

I met my supervisor, Daniel Eakins, when I was a third-year engineering student composed of 25% imposter syndrome, 25% anxiety, and 50% caffiene. Unfortunately, this means he remembers what my writing ability was like when I was 21, as he takes great pleasure in reminding me. Fortunately, this also means I met him at a rather pivotal moment. It was with Dan's encouragement that I considered undertaking a DPhil, a route I'd never have thought of for myself - in fact, at the time, I was strongly inclined to get out of science altogether. Sometimes, you need someone else to believe in you before you can learn to do it for yourself. Thank you, Dan, for teaching me how to hold my own.

Thank you to my industrial supervisor, James Pecover; your endless patience and calm demeanour has been the anchor I needed to complete this DPhil. While it is in a manager's job description to manage, it is rare to find one truly cares in the way that you do, James. You celebrated my successes and guided me through my failures with equal kindness, and you have taught me so much. From you, I have gained a blueprint of how to be a fantastic scientist, which I hope I will one day be able to emulate.

To everyone who ever helped me load the electric gun into M3, fiddle with VISAR, or play the xylophone in the control room: Emilio, Josh, Rosie, Hugo, Luis, Cristian, Adam, Paul, Mo, Simon, Jay, Garry, Pete, Ian E, Ian C, Oli, Lewis, Rafik.

To everyone who helped keep me sane. Thank you to Hannah, for being my rock. To Rosie, for always reminding me *we can do this.* To Kin, allow it, thank you for always being sound. To Adam, for taking me rambling in the fields to talk through anything and everything. To Martin and Nic, for coffee and laughter. To Luca, for your sage advice and presence as a talisman in the M3 control room. To Nick, for new music and believing in me from the start. And last but by no means least, to *both* David Chapmans, who are coincidentally two of the most brilliant and kind scientists I know.

Finally, of course, thank you to Ed and my family, for picking me up when I fall flat on my face.

Contents

List of Figures **vii**

List of Abbreviations **xvi**

1 Introduction **1**

2 Literature Review **8**

- 2.1 Background physics 9
  - 2.1.1 Jump conditions 10
  - 2.1.2 Projectile driven impact 11
  - 2.1.3 Making equation of state measurements 14
- 2.2 Projectile-driven extreme state research 15
- 2.3 Development of the electric gun 19
  - 2.3.1 Empirical improvement of the electric gun 20
  - 2.3.2 Modelling the electric gun 21
  - 2.3.3 Launching thick flyers 22
  - 2.3.4 Summary of development until 1993 24
- 2.4 The modern electric gun 25
  - 2.4.1 Developments in experimental and modelling techniques 25
  - 2.4.2 Accelerating thick flyers 26
  - 2.4.3 Summary 27
- 2.5 Electromagnetic flyer plates 28
  - 2.5.1 EM flyer plate or electric gun with a thick foil 28
  - 2.5.2 Pulsed-power devices 29
  - 2.5.3 EM flyer plates on the Z machine 32
  - 2.5.4 Simplified modelling of EM flyer plates 34
  - 2.5.5 Summary 35
- 2.6 Conclusions 35

3 Research goals **37**

- 3.1 Research goal 1: Develop simplified modelling tools 38
- 3.2 Research goal 2: Explore the capability of the electric gun 39
- 3.3 Research goal 3: Investigate the impact of material strength effects on electric gun loads simulated in a hydrocode in two-dimensions 41

3.4 Research goal 4: Understanding the electric gun load as a tool for the study of dynamic material properties . . . 42

4 Creating a simplified model of the electric gun 44

4.1 Introduction . . . 44
4.2 A 0-D Electric Gun Model for the Optimization of Flyer Acceleration to Hypervelocities 45
4.2.1 Abstract . . . 45
4.2.2 Introduction . . . 46
4.2.3 0D Model: Algorithm and physics . . . 48
4.2.4 0D Model:Verification testing against MHD hydrocode . . . 58
4.2.5 Conclusion . . . 66
4.2.6 Appendix: 0D model material constants . . . 67
4.3 Summary . . . 67

5 Exploring the capability of the electric gun 71

5.1 Introduction . . . 71
5.2 The effect of current rise time on the acceleration thick flyers to hypervelocities using an electric gun . . . 74
5.2.1 Abstract . . . 74
5.2.2 Introduction . . . 75
5.2.3 Numerical Modelling: The effect of rise time on flyer state . . . 77
5.2.4 Experimental Testing: parametric study of flyer thickness on a 1.2 MJ electric gun 84
5.2.5 Conclusions . . . 92
5.3 Redesigning the electric gun: launching thick flyers to hypervelocity with high efficiency 94
5.3.1 Abstract . . . 94
5.3.2 Introduction . . . 94
5.3.3 Background: Flyer destruction mechanisms . . . 96
5.3.4 Method: 0D electric gun model . . . 97
5.3.5 Design: Launching thick flyers on M3 . . . 99
5.3.6 Experimental setup . . . 100
5.3.7 Results . . . 101
5.3.8 Discussion: Electric gun efficiencies . . . 103
5.3.9 Conclusions . . . 104
5.4 Summary . . . 105

6 Simulation of the electric gun in an Eulerian hydrocode 108

6.1 Introduction . . . 108
6.2 Review of previous chapters . . . 110
6.3 Strength model . . . 112
6.4 Practical methods for the implementation of material strength into an Eulerian hydrocode 113
6.4.1 Abstract . . . 113
6.4.2 Introduction . . . 114

6.4.3 Mathematical model of material strength . . . 116
6.4.4 Method: Taylor anvil-on-rod test-case . . . 119
6.4.5 Computational implementation of material strength . . . 122
6.4.6 Cross-code comparison results . . . 137
6.4.7 Discussion . . . 140
6.4.8 Conclusions . . . 143
6.5 Modelling the electric gun with material strength . . . 145
6.5.1 Introduction . . . 145
6.5.2 Background . . . 146
6.5.3 Material models and set-up . . . 155
6.5.4 Results . . . 157
6.5.5 Discussion . . . 169
6.5.6 Conclusions . . . 172
6.6 Summary . . . 174

7 Design and testing of an electric gun for equation of state research 177
7.1 Introduction . . . 178
7.2 The design, modeling and testing of an electric gun load for the study of dynamic materials properties . . . 181
7.2.1 Abstract . . . 181
7.2.2 Introduction . . . 182
7.2.3 Background . . . 185
7.2.4 Modelling and design . . . 188
7.2.5 Experimental validation . . . 197
7.2.6 Conclusions . . . 204
7.3 Summary . . . 206

8 Conclusions and Future Work 210
8.1 Summary of the thesis . . . 210
8.2 Future work . . . 212
8.2.1 X-ray radiography of the electric gun flyer . . . 213
8.2.2 Power loss models . . . 213
8.2.3 Electric gun physics at higher energies . . . 214
8.2.4 The effect of shaping the electric gun current profile . . . 215
8.2.5 Electric gun loads with alternate materials . . . 216

9 Appendix 217
9.1 Fabrication procedures . . . 217
9.1.1 Exploding Foil Layer . . . 217
9.1.2 Flyer fit in barrel recess . . . 217
9.1.3 Adaptations to the barrel and mirror mount . . . 219
9.2 Experimental procedures . . . 220
9.2.1 Vacuum levels and rate of rise . . . 220
9.2.2 Assembly of the electric gun load . . . 220

References **221**

List of Figures

1.1 Diagrams illustrating the electric gun acceleration mechanism: the initial configuration of the foil, flyer, cathode and connection (1.1a); the foil experiences Joule heating, rapidly changing state from solid to plasma, accelerating the dielectric flyer (1.1b); continued discharge of the current causes further acceleration of the foil by Lorentz forces (1.1c). 5

2.1 Illustration of a shock moving through a medium, including the downstream and upstream states. 11
2.2 Diagrams illustrating the process of projectile impact from the point of view of an observer: ($t < 0$) projectile of material 1 moves towards a target of material 2; ($t = 0$) the projectile and target position at the time moment of impact; ($t > 0$) position after impact during pressure wave propagation. 12
2.3 Plot created by Marshall *et al.* [9]: *New quartz Hugoniot data using a diamond standard (black circles) and an aluminum standard (gray circles). Also shown are data acquired at the Sandia Z machine (blue squares) [39, 42, 43], FPMD calculations from Desjarlais, Knudson, and Cochrane (magenta asterisks) [39], Sjostrom and Crockett (dotted green) [28], and tabular EOS models. The fit to the Z-data and FPMD calculations presented by Desjarlais et al. [39] was extrapolated beyond its upper bound, 30 Mbar, represented by the dashed blue curve.* 16
2.4 A simplified diagrams of the original electric gun set-up designed by Weingart *et al.* [21]. 18
2.5 Timeline detailing the advancement of the electric gun, from its invention to the modern day. 19
2.6 Illustration of the operating mechanism in an electromagnetic flyer plate: (t_0) the current is discharged directly through the metal flyer; (t_1) the current moves through the metal barrel walls and through flyer is it accelerates. 28
2.7 *M3* lumped circuit diagram. 30
2.8 An RLC circuit diagram of M3, a 2.5 MJ CDU located at First Light Fusion [68]; relatively simple pulsed-power devices like M3 can be apprximated by RLC circuits. While more precise simulations of long transmission lines can be achieved using PSpice solvers [69], these solvers were not explored in this thesis. 31

4.1 The 0D model allows the user to input detailed parameters regarding the foil, flyer and capacitor bank. These include the foil and flyer material and dimensions, and the capacitor bank parameters necessary for calculating the system current at each timestep. 49

4.2 This flowchart demonstrates the model algorithm characterised as four stages *II A.* calculation of the current in the RLC circuit, *II B.* calculation of the foil state, *II C.* update positions and pressure gradient and *II D.* calculation of the pressure in the flyer. The flowchart also illustrates the dependencies of the calculated values on those upstream; clearly if the pressure in the flyer is to be calculated accurately, the foil state and projectile dynamics must be also. 50

4.3 The positions of the four locations used determine the pressure at the foil-flyer interface, alongside the velocities used to approximate the foil-flyer dynamics. An example of a realistic plot of pressure in the foil and flyer is included. The model assumes the foil and flyer form a continuous interface, the pressure at the front of the flyer is zero and the pressure gradient between z_{Pmax} and z_f is linear. 53

4.4 The four positions tracked by the model, alongside an example of their temporal evolution for the launch of a 0.1 mm thick foil and 1.0 mm thick flyer. The 0D model approximates the complex dynamic movement of the foil, flyer and position of maximum pressure in the foil by simplifying the system to four positions along the z-axis, allowing the model to calculate a more accurate interface pressure P_{zi} using Eq. 5.4 without need for 1D simulation. 56

4.5 The position of the magnetic field through the foil starts at the rear of the foil when the current is first discharged (t_1). Ohmic heating and high magnetic field strengths cause the foil to melt, thus the current density accumulates in the lower resistivity region ahead of the 'melt line' (t_2). Finally, as the foil and flyer move away from the insulation, low resistivity foil plasma fills the expanding volume, and the current path returns to the rear of the foil. The high current density heats the adjacent foil material and increases its resistivity in this region, thus the magnetic field moves back to the foil rear and begin the process again (t_3). 57

4.6 Simplified diagram showing the electric gun load set-up on M3. The close up shows the flyer atop the foil over the pier, with the barrel hidden from view. The current passes from the pier on the bottom electrode through the foil to the top electrode. 59

4.7 Plots showing the results from the 0D model and the 1D simulation in $\mathbb{B}$. Despite the differences in the magnetic field strength, the foil temperature and interface velocity predicted by the model are similar to those calculated by $\mathbb{B}$. 61

4.8 Comparison of the positions of the rear position (z_r), the interface position (z_i) and the position of maximum pressure (z_{Pmax}) in the 0D model and $\mathbb{B}$ over time. At each time step, the position of the foil is plotted, with the 1D foil material in $\mathbb{B}$ coloured by pressure to highlight the maximum pressure and rear position. z_{Pmax} reaches the interface at 0.35 μs and falls back to the rear surface at 0.6 μs in both the model and the $\mathbb{B}$ simulation, however the second excursion arrives at the interface 0.2 μs later in the 0D model (marked by the orange arrow in the 0D model and the blue arrow in $\mathbb{B}$). 62

4.9 Comparison between the maximum flyer pressure in the 0D model and $\mathbb{B}$. The pressures predicted by the model matches $\mathbb{B}$ more closely at earlier times in flight, though remain within a factor of 1.5 of the pressures in $\mathbb{B}$. 63

4.10 Heatmap of maximum flyer pressure on launch across a range of foil and flyer thicknesses, with varying surface area. 64

4.11 Contour plots comparing the maximum flyer pressure on launch for varying foil and flyer thicknesses for different foil surface areas in 1D MHD 𝔹 simulations **(dotted line)** and the 0D model **(solid line)**. The contours across all foil surface areas show the model underestimates the pressure in thicker flyers, with the error increasing to a factor of around 2.5 in the loads with surface area of 30×30 mm and thick foils. 65

5.1 **(a)** Simplified diagram showing the electric gun load set-up, with pier foil width (w) and length (l) labelled. The close up shows the flyer atop the foil over the pier, with the barrel hidden from view. The current passes from the pier on the bottom electrode through the foil to the top electrode. **(b)** The 0D model allows the user to input detailed parameters regarding the foil, flyer and capacitor bank. These include the foil and flyer material and dimensions, and the capacitor bank parameters necessary for calculating the system current at each timestep. 78

5.2 The positions of the four locations used determine the pressure at the foil-flyer interface, alongside the velocities used to approximate the foil-flyer dynamics. The model assumes the foil and flyer form a continuous interface, with pressure at the front of the flyer set to zero and the pressure a linear gradient between z_{Pmax} and z_f. 79

5.3 Comparison between maximum flyer pressure **(a)** and flyer velocity **(b)** calculated by the 0D model and 1D MHD simulations in 𝔹 for a 1.5 mm thick flyer used on M3. . . 82

5.4 Plots tracking the temporal evolution of foil-flyer position, maximum pressure **(a)** and pressure normalised by foil current in the flyer **(b)** calculated by the 0D model throughout launch and flight. M3 has a higher energy and longer current rise time than CEPAGE, therefore the foil and flyer travel further and remain at higher pressures. . . 82

5.5 **(a)** Qualitative illustration of the mechanism for the higher pressures in thicker flyers later in flight. As the position of the front of the flyer is further away from maximum pressure in *ii* relative to the position of the foil-flyer interface, the maximum pressure in the flyer is greater. **(b)** Plot showing the temporal evolution of the maximum flyer pressure in flyers of different thicknesses launched by M3 over a flight distance of 9 mm. The initial spike in pressure increases with flyer thickness as the launch time occurs later. The pressure remains higher in thick flyers later due to the orientation of the pressure gradient between the pressure maximum in the foil and the flyer front, illustrated in Fig. 5.5a. 85

5.6 **(a)** Diagnostics fielded during the experiment include (1) 1D VISAR streak measuring projectile velocity, (2) 2D VISAR fringes mapping flyer surface damage evolution during flight, (3) 1D laser streak capturing shock velocity profile in the target block and (4) high speed imaging of the PMMA target block showing the shock front in 2D. **(b)** Image of barrel with plasma shielding, target block and mirror mount. 86

5.7 The velocity of the shock in the transparent PMMA target block is calculated by differentiating the progression of the shock front position in time. First, the position of the shock front is identified: as the shock front moves through the target its high pressure state turns the PMMA opaque, gradually blocking the laser light as it moves. The boundary between the laser light and opaque (black) region for each timestep is identified automatically by evaluating the pixel value, and the positions are extracted. A polynomial fit is then applied to the shock positions which, when differentiated, gives a less noisy shock velocity profile. 88

5.8 Images taken using the high speed camera focused on the target block showing an example of the shock front generated on impact using the 1 mm thick flyer (red boxes around fiducial marks relate set up to high speed camera images). The small tilt in the shock front, consistent across all shots performed, could be associated with slight asymmetries in the magnetic field strength across the bottom electrode pier [68]. . . . 88

5.9 **(a)** Plots of the temporal evolution shock in block velocity profiles for the 0.25 mm thick flyer and the 0.5 mm flyer launched over 20 mm. The low initial velocity of the shock in the block in both cases is an indication that a high velocity but low density shock front arrived in the target ahead of the flyer, which on secondary impact caused the later velocity increase. This indicates that foil plasma was able to escape in front of the flyer, suggesting that the flyer experienced a loss of intergrity during flight. **(b)** Images of plasma breaking through the 0.25 mm thick flyer from the 2D VISAR fringes used to map the flyer surface. Its view was oriented down the barrel and the dark shadow of the fiducial marker in the target block can be used for reference. The plasma can be seen to first appear at 0.87 μs near the centre of the flyer, indicating the plasma forced its way through the flyer instead of escaping around the edges. 89

5.10 **(a)** Plot showing the maximum pressure of the flyers over time launched by M3 calculated by the 0D, for the different flyer thicknesses and barrel lengths shot experimentally on M3. The time the 0.25 mm thick flyer and 0.5 mm thick flyer shot to a flight distance of 20 mm experienced plasma breakthrough occurred when the 0D model predicted they were at similar pressures. This suggests that the foil plasma was able to force its way through the flyer when the maximum pressure in the flyer material dropped below a certain threshold. **(b)** The measured 1D VISAR velocity profiles in the early stages of launch and flight for the 0.5 mm and 1.0 mm thick flyers. The 0D model has no equation of state in the flyer, so is unable to model the release of the front surface of the flyer into vacuum. However, the simulated velocity is close to the measured profile in both cases, and is likely more indicative of the velocity of densified bulk of the flyer. The impact velocities of the flyers were not captured in this work. However, these results alongside the similar flyer impact times (Table. 5.5) indicate that the impact velocities calculated by the 0D can be used instead. 90

5.11 A flyer plate configuration used at First Light Fusion (left) [68] and a standard electric gun configuration (right). In an electric gun, the current passes through a thin metal foil which drives a dielectric flyer, instead of directly through a thicker metal foil in a plate flyer. 96

5.12 Simplified diagram showing the electric gun load set-up. The 0D model allows the user to input detailed parameters regarding the foil, flyer, and capacitor bank. These include the foil and flyer material and dimensions, and the capacitor bank parameters necessary for calculating the system current at each timestep 98

5.13 The positions of the four points used to determine the pressure at the foil-flyer interface, alongside the velocities used to approximate the foil-flyer dynamics. The model assumes the foil and flyer form a continuous interface, with pressure at the front of the flyer set to zero and a linear pressure gradient between z_{Pmax} and z_f. 99

5.14 Plot showing the current (a) and maximum flyer pressure state (b) calculated by the 0D model for the CEPAGE and M3 load specified in Table 7.1. The magnitude of the pressure peaks in the M3 load closely matches those experienced by the flyer shot on CEPAGE. 100

5.15 1D laser streak capturing shock velocity profile in the target block and (4) high-speed imaging of the PMMA target block showing the shock front in 2D. 101

5.16 Illustrations of the PMMA target block and images of shock fronts taken by high-speed imaging. 103

6.1 Depiction of Taylor anvil-on-rod test, including terminology used throughout this work. 120

6.2 Simulation set-up of the Taylor anvil-on-rod test in B2 and AUTODYN. In some of the test-cases, the plate is simulated as impacting a rigid anvil instead, however, the results analysed in the cross-code comparison are in this plate-on-plate configuration. 122

6.3 The original and staggered Eulerian mesh with the cell-centred and face-centred locations marked. 123

6.4 Illustration of two averaging and differencing schemes ordered in such a way to result in a cell-centred force and work value. The left requires fewer steps, however the stresses are located at the cell faces, which is challenging for advection in orthogonal direction and gradient calculation for the off-diagonal components of the stress tensor. 124

6.5 The method for calculating the shear strain rate $\dot{\varepsilon_{yx}}$ alongside the final location of the nine components of the stress tensor. 125

6.6 An illustration of the process for calculating v_{xy}. The left image represents Equation 6.26a and the right presents Equation 6.26b. 128

6.7 The mechanism depicting the generation of high shear forces at the rod-vacuum interface and the consequences of this effect on a simulation of the Taylor anvil-on-rod test. . . 129

6.8 Illustration showing the representation of a solid shape in an Eulerian grid. In the uncorrected JC model, cell a will have the same yield as a fully occupied cell. 130

6.9 A frame in B2 from a simulation without a density-factor corrected yield. The frames highlight high-velocity low-density material at the rear of the rod, which result in excessively high simulation runtimes. 131

6.10 A comparison of simulations frames at 20 µs with differing f. 132

6.11 Depiction of the interface grid in two-dimensions in a domain with Material 1 and Material 2. The interface grid is set to 1 at the x face of cell (i, j, k) if $(i-1, j, k)$ if both have the same material number and $Y > 0$. 133

6.12 Comparison between simulations without and with the ***IG***. Non-physical blurring at the rod-vacuum interface visible in Figure 6.12a are shown to have been eliminated in Figure 6.12a. 134

6.13 Eulerian simulation of Taylor rod in AUTODYN. The frame shows serrated edge forms at the rod-vacuum interface. 134

6.14 Diagram of the 1D system used to investigate shear forces. 135

6.15 Results from the 1D solver showing plots with and without the shear wave artificial viscosity modification. The simulation without artificial viscosity in B2 begins to develop complex structures, which are not present in the AUTODYN simulation. 136

6.16 Progression of the B2 simulation of the rod without the shear wave artificial viscosity modification. 137

6.17 Plot of the rod profile for a 200 m/s impact in B2, B2 without shear wave artificial viscosity and AUTODYN. 137

6.18 Cross-code comparison showing plots of rod length, flared-end radius and the error between B2 and AUTODYN throughout the simulation of a 100 m/s Taylor anvil-on-rod test. The rod length in the simulations match closely, however, the error in the prediction of the flared-end radius rises to over 20% at late times. 138

6.19 Cross-code comparison of Taylor anvil-on-rod test simulations profiles at 100 m/s. B2 closely replicates the profile until 40 µs, after which time it overpredicted the flared-end radius. 139

6.20 Cross-code comparison showing plots of rod length, flared-end radius and the error between B2 and AUTODYN throughout the simulation of a 200 m/s Taylor anvil-on-rod test. The error between the axial length and flared-end radius in the codes remained below 1.5 % and 5 %. 140

6.21 Cross-code comparison of Taylor anvil-on-rod test simulations profiles at 200 m/s. B2 shows good qualitative agreements with AUTODYN, although the flared-end does not rebound as much. 141

6.22 Cross-code comparison showing plots of rod length, flared-end radius and the error between B2 and AUTODYN throughout the simulation of a 350 m/s Taylor anvil-on-rod test. The error between the codes at this velocity was the lowest out of the cases considered, where the axial length and flared-end radius maximum error was 0.5% and 6% respectively. 142

6.23 Cross-code comparison of Taylor anvil-on-rod test simulations profiles at 350 m/s. The material strength model is clearly still important when predicting the flared-end radius, despite the high velocity of the impact. 143

6.24 Diagram of the electric gun load designed for M3 in detail. 147

6.25 Detailed diagrams of the pier in the electric gun load designed for M3. 148

6.26 Images of the cathode and insulation layers in the electric gun load, which are difficult to model accurately. 149

6.27 The diagram of the electric gun load (left) with regards to the two-dimensional simulation frame of the pier (right). The pressure achieved in the M3 vacuum chamber is of the order 1×10^{-6} Pa 152

6.28 The two-dimensional electric gun load simulation domain, coloured by density, with the static region and ghost cells which define the current path illustrated and labelled. . . 152

6.29 Plots of the experimentally measured velocity profiles [96] compared to 2D MHD predictions with an unattentuated current (i.e. $C_L = 1.0$) 158

6.30 Plots comparing the experimentally measured velocity profiles (in black) [96] with 2D MHD predicitons for different load current factors. It is challenging to choose the most appropriate load current factor, as the VISAR velocimetry lost signal around halfway through flight in both cases. The application of a blanket current scaling factor is likely not representative of the real-world current loss in the load. The development of a pulsed-power load model is a promising avenue for future work to address the discrepancies between the experimental and simulated loads. 159

6.31 Comparison between the flyer velocity profile in 2D MHD simulations of the electric gun load with and without a material strength model. The material strength model has little impact on flyer velocity. 160

6.32 Temporal plots of the mean and maximum pressure in the foil and flyer in 2D MHD simulations with and without a material strength model. The pressure in the foil and flyer is slightly lower in simulations with material strength, though, the maximum difference between them is under 4%. 161

6.33 Temporal plots of the mean and maximum density and temperature flyer in 2D MHD simulations with and without a material strength model. The density in flyer is slightly lower in simulations and the mean temperature is higher in the thicker flyers with the material strength model switched on. However, the percentage difference between the values is small. 162

6.34 Temporal plots of the mean and maximum foil density in 2D MHD simulations with and without a material strength model. The difference in each case is negligible. . . . 163

6.35 Diagrams illustrating the formation of the RT instabilities at the foil-flyer interface. . 163

6.36 Plots showing the evolution of the foil-flyer interface in time as it progresses up the barrel in 2D MHD simulations with material strength on and off. The amplitude of the instabilities is notably larger in simulations with material strength on. 164

6.37 A comparison of the formation of RT instabilities at the foil-flyer over time in loads with 0.25-mm-thick flyers, including plots of their FFT signal. The amplitude of the RT perturbations is larger than the flyer thickness. The perturbations have greater range in frequencies and higher amplitude with strength on. 164

6.38 A comparison of the formation of RT instabilities at the foil-flyer over time in loads with 0.5-mm-thick flyers, including plots of their FFT signal. 167

6.39 A comparison of the formation of RT instabilities at the foil-flyer over time in loads with 1.0-mm-thick flyers, including plots of their FFT signal. The perturbations have greater range in frequencies and higher amplitude with strength on, though the mechanism for this effect is unclear. 167

6.40 A comparison of the formation of RT instabilities at the foil-flyer over time in loads with 1.5-mm-thick flyers, including plots of their FFT signal. The perturbations have greater range in frequencies and higher amplitude with strength on, though the mechanism for this effect is unclear. 168

7.1 Diagrams illustrating the electric gun acceleration mechanism: the initial configuration of the foil, flyer, cathode and connection (7.1a); the foil experiences Joule heating, rapidly changing state from solid to plasma, accelerating the dielectric flyer (7.1b); continued discharge of the current causes further acceleration of the foil by Lorentz forces (7.1c). 183

7.2 Diagrams of the flyer at three characteristic times during acceleration in an electric gun launch, alongside a typical trace of the maximum pressure in the flyer during this period. (*i*) When the current is first discharged, the foil rapidly heats and changes state from solid to a vapor, causing the pressure in the flyer to spike. (*ii*) When the flyer launches and moves up the barrel, the foil becomes free to expand and its pressure initially drops, before increasing again as the discharged current continues to increase. (*iii*) The flyer exits the barrel and the acceleration of the foil plasma abates as it expands into the free space above the barrel, resulting in a rapid drop in the pressure in the flyer. 186

7.3 Illustrations of flyer impact in an electric gun load driven by a fixed rise-time machine. If impact occurs before the current becomes negligible (t =impact), the foil plasma will continue to drive the flyer (t >impact), causing the shock front velocity to vary. 187

7.4 An illustration of the key geometric parameters which can be varied to control the states and dynamics of the flyer. 190

7.5 A matrix of traces of the positions of the foil rear, foil-flyer interface, flyer front, and melt-line predicted by the 0D model, for a range of foil and flyer thicknesses. These traces were used determine a combination of foil and flyer thickness which would avoid the melt-line reaching the foil-flyer interface, thus limiting the maximum pressure in the flyer. 191

7.6 Illustrations of the simulation set-up (coloured by density), including the region kept static (zero velocity) to fix the point of current injection. 192

7.7 Plots contrasting the simulated flyer pressure, temperature, and density states in an electric gun flyer driven by an 0.5-mm-thick and a 0.1-mm-thick foil. The 0.5-mm-thick foil shields the flyer from extreme fluctuations in pressure, resulting in it remaining near solid density late in flight. 193

7.8 B2 simulation domain density profiles for 4 characteristic times during flyer launch. The foil vaporises at late times, exhibiting a significant drop in density by 2.0 µs. 194

7.9 B2 simulation domain (coloured by density) instabilities at the foil-flyer interface late in flight. Increasing the foil thickness reduced the growth rate of the RT instabilities compared to electric gun simulations with thinner foils. 195

7.10 Illustrations of the experimental set-up in the xz (*i*) and yz (*ii*) plane, including the plasma shroud designed to protect the diagnostic line of sight, plasma shielding to suppress foil plasma emitted at the join between the foil and anode, and variable block positions. The velocity of the flyer is measured using 1D VISAR trained on its surface and the velocity of the shock in the PMMA block is captured by a high-speed camera. 198

7.11 Diagrams demonstrating the layout of the side-on images of the block captured by the high-speed camera including: a diagram of the PMMA target block and flyer with the shock direction labelled (*i*); a diagram of the block from the perspective of the high-speed camera (*ii*); and an example of a high-speed camera frame (*iii*). 198

7.12 Plot of the measured experimental velocity over time and the velocity predicted by the 2D MHD hydrocode simulations for an 8 mm stand-off. The simulated impact velocity is used in analysis going forward as the VISAR signal was lost at around 1.5 µs. This could be an indication of the flyer surface melting. 199

7.13 A diagram showing the ratio of the flyer-to-block width at 8 mm stand-off (a) and 2D images of the shock front taken using high-speed imaging (b). The shock front appears planar and continuous throughout the block. 200

7.14 A diagram showing the ratio of the flyer-to-block width at 50 mm stand-off (a) and 2D images of the shock front taken using high-speed imaging (b). The block was deliberately oversized to capture the shock profile at the edge of the flyer. Figure 7.14b shows slow, asymmetric precursor shocks arrive at the edges of the block before the flyer. The flyer shock front appears to be planar and continuous across the block thickness. 201

7.15 A diagram showing the ratio of the flyer-to-block width at 50 mm stand-off (a) and 2D images of the shock front taken using high-speed imaging (b). The block was deliberately oversized to capture the shock profile at the edge of the flyer. Figure 7.15b shows slow, asymmetric precursor shocks arrive at the edges of the block before the flyer. The flyer shock front appears to be planar and continuous across the block thickness. 201

7.16 Plots showing the measured shock front position over time at stand-off distances of 8 mm, 50 mm, and 100 mm. Plots on the left show the position-time data in black, with the GP model mean ± 2 standard deviations in blue. The plots on the right show the GP model predicted mean ± 2 standard deviations in orange. Note, the uncertainty in the velocity profiles is highest at the beginning and end of the measurement window. . 203

7.17 Plots of the shock velocities measured at different stand-off distances side-by-side. The shock velocity at 100 mm is lower than at 50 mm or 8 mm, however, the velocity of ~6 km/s is constant for a duration of 1.0 µs. 204

9.1 Foil-Kapton fabrication workflow. First, a circular layer of Kapton with diameter 150 mm is cut out (a). Then the position of the foil and glue is marked up (b). Using a microbrush, degassed epoxy resin is applied to the Kapton (c). The previously cut foil is carefully laid atop the glue (d). The foil and Kapton is turned over, and the trapped air bubbles are pushed out (e). The foil is inspected for damage and rejected if surface damage exists on either side (f). 218

9.2 The 26.2 x 26.2 mm flyer fits into the 1.6 mm recess, such that the flyer torn out into the barrel is 23 x 23 mm. This recess holds the flyer in place whilst loading and suppress plasma breakthrough. 218

9.3 Comparison between the a poorly fitted flyer (shot 0198) and a flyer with an improved fit (shot 0199). The 1D VISAR from the poorly fitting flyer shows bright light dominating the frames from the first timing dot, thought to be light from plasma escaping in front of the flyer. In contrast, loses VISAR loses the reflective surface at a similar time, but no plasma breakthrough occurs. 219

9.4 Comparison between the barrel and mirror mount designs, before and after improvements made by the author. The original barrel and mirror mount were designed in the past at First Light Fusion. 220

List of Abbreviations

ALE	Arbitrary Lagranagian Eulerian
CEPAGE	Conduite d'Eléments Projetés' Adaptable par Générateur Electrique: *Pulsed-power device at First Light fusion.*
CDU	Capacitor discharge unit.
DMP	Dynamic materials properties.
EM	Electromagnetic.
EoS	Equation of State.
EFI	Exploding foil initiator.
FEOS	Frankfurt Equation of State.
FFT	Fast fourier transformation.
FLF	First Light Fusion: *DPhil industrial sponsor.*
FPI	Fabry–Pérot interferometer.
GP	Gaussian Process.
ICF	Inertial Confinement Fusion.
IG	Interface grid.
JC	Johnson-Cook.
LLNL	Lawrence Livermore National Laboratory.
LTGS	Light triggered gas switch.
M3	Machine 3: *Pulsed-power device at First Light fusion.*
MHD	Magneto-hydrodynamics
MRL	Material Research Laboratories
NIF	National Ignition Facility
PDV	Photon Doppler velocimetry.
PMMA	Poly-[methyl methacrylate].
PEEK	Polyether ether ketone
PTW	Preston-Tonk-Wallace.
QEOS	Quotidian Equation of State.

LEOS	Livermore Equation of State.
RTI	Rayleigh-Taylor Instability.
VISAR	Velocity interferometer system for any reflector.
Z	Z machine: *Pulsed-power device at Sandia National Laboratories.*

Chapter 1

Introduction

When mapping the topology of an unknown mountain, observation of its peaks from afar may give us a broad notion of its structure; however a more accurate map of its features necessitates direct access to its slopes and a means of recording them. In the same way, our understanding of materials at ultra-high pressures and temperatures is inexorably linked to our ability to access these conditions, with the tools necessary for their measurement close at hand. The exploration of these extreme states is motivated by their presence in many of the most consequential topics faced by scientists today, such as nuclear fusion, aerospace applications, and planetary sciences. Consequently, great effort has been afforded to the development of techniques for generating these conditions in a controlled setting, giving rise to several methods for subjecting materials to extreme pressures and temperatures through the generation of shock waves.

Shock waves are defined as violent pressure waves that propagate faster than the speed of sound in the medium through which they are passing, generating highly compressed regions of material downstream of the shock front. A single shock will compress the material to a thermodynamic state along the material's Hugoniot, the locus of all possible shocked material states. Shock waves are a particularly effective tool for measuring quantities like the equation of state of a material, as their properties can be derived by solving the Rankine-Hugoniot jump conditions. Furthermore, the quantities that must be acquired to solve for the thermodynamic states, such as the shock and particle velocities in the target material, can be measured using velocimetry techniques with high temporal resolution. Consequently, if the shock pulse length is of sufficient duration to generate quasi-equilibrated states in the target material, the resulting equation of state values will have high precision.

The methods of generating shock waves can be broadly separated into two categories: direct and indirect drive. Direct drive can be achieved using a variety of techniques, such as laser-driven compression [6] and exploding liner or wire arrays [7]. Indirect drive can refer to the use of lasers to heat an x-ray enclosure called a hohlraum to drive spherical pellets and planar targets [8, 9], or to an impact generated by a projectile launcher. While the former can achieve incredibly high pressures and temperatures, these regions are short-lived and act over a small volume. Although projectile launchers cannot induce pressures of the same magnitude as laser-driven systems, they can introduce a shock over a large material volume for a greater duration. These operational characteristics can simplify the collection of data from the target and improve the accuracy of the measurements, making the projectile launcher a powerful tool for extreme state research.

A researcher may choose a type of projectile launcher based on the desired magnitude and pulse-length of the pressure wave and the volume of material over which this pressure must be applied. The resources available to the facility must also be considered, including costs, turnaround time, and diagnostic capability. Some examples of projectile launchers include the gas gun, laser-driven flyer, and electromagnetic flyer plate. The gas gun is a widely-used projectile launcher, which comes in a range of configurations (from single [10] to three-stage [11]) and is well understood, making both their operation and simulation relatively simple. However, the speed of sound in the operating gas limits the projectile's maximum velocity. Consequently, to achieve flyer velocities over 10 km/s, alternative launch techniques, such as laser-driven flyers [12, 13] and electromagnetic projectile launchers are employed. Table 1.1 details the comparison of a few popular projectile launchers in relation to one another.

Table 1.1: Examples of projectile launchers and their characteristics. The choice of technique is dependant on the material state conditions desired and resources available.

Projectile launcher	Max pressure	Max flyer velocity	Pulse length
Gas gun	GPa	< 10.0 kms^{-1}	µs
Laser driven flyer [12]	GPa	> 10.0 kms^{-1}	ns
EM plate flyer	TPa	> 50.0 kms^{-1}	µs

The measurement of sufficient data to reveal new information about a target places requirements of varying stringency on the flyer state and thickness. For instance, if the flyer is being used to investigate the ballistic impact of spacecraft shielding, the flyer is typically required to move at velocities above 10 km/s [14], but need not be thick, nor at a specific density state [15]. On the other hand, equation of state investigations require the acceleration of a flyer that can support the propagation of a quasi-equilibrated shock state with a long enough duration to make a precise measurement. While this necessary duration length can vary depending on the type of measurement, typically it is considered to be greater than hundreds of nanoseconds. To achieve this, the flyer must be thick, as the pulse length of the shock is proportional to the flyer thickness. One approach to ensuring the flyer's state remains near-constant is to prevent excessive state change during acceleration. Non-uniform melting and vaporisation can create a varying density profile across the flyer thickness, resulting in a fluctuating shock profile on impact. Electromagnetic projectile launch is currently the only technique able to launch thick, solid flyers to velocities over 10 km/s.

Electromagnetic projectile launchers utilise the rapid discharge of current from a pulsed-power device to accelerate a projectile, either using electromagnetic forces, as in electromagnetic (**EM**) flyer plates [16], or the thermal acceleration of an exploding foil, as in exploding foil initiators (**EFI**s) [17]. The EM flyer plate is capable of launching millimetre-thick metal flyers with a wide range of surface areas (like a gas gun) to velocities over 10 km/s (like a laser-driven flyer). It currently offers access to the highest pressure states for equation of state measurements of any projectile launch technique, with its theoretical flyer mass and velocity limited only by the stored energy of the machine powering it. However, in practice, the maximum flyer velocity is constrained by the load efficiency and the requirement to keep a region of the flyer at near-constant density.

Preventing significant state change in the EM flyer plate can be challenging, as the current passes directly through the flyer and accelerates it extremely rapidly. Researchers using the Z machine [18], the highest energy pulsed-power device in the world, have found two primary heating effects capable of melting or vaporising the flyers prior to impact. Firstly, if the flyer was too thin, its leading surface would melt before impact due to ohmic heating. On the other hand, if it was too thick, the flyer would change state due to high-pressure shock waves developed during acceleration. By combining these requirements, they derived a maximum magnetic field strength that could be applied to the flyer, introducing a maximum achievable flyer velocity for equation of state experiments on the Z machine of around 60-70 km/s (depending on the current rise-time) [1].

The efficiency of an electromagnetic projectile launcher can be defined as the proportion of stored electrical energy in the pulsed-power device that is converted into kinetic energy of the flyer. The EM flyer plate is predominantly accelerated by Lorentz forces, which are generated by strong magnetic fields surrounding the current path and, to a lesser degree, ablation at the rear of the flyer caused by thermal expansion [19]. A great deal of the energy delivered to the load is expended in processes other than accelerating the flyer, such as increasing the temperature of all the components through which the current passes. Additionally, a considerable portion of the current can be lost along parasitic pathways due to arcing and breakdown throughout the load. Consequently, the maximum efficiency of the EM flyer plate is typically around a few percent [20].

While the limited efficiency of the EM flyer plate does not prevent pulsed-power devices like the Z machine from accelerating projectiles to hypervelocity (defined as velocities of over 4 km/s in flyers with a mass of grams), on smaller machines, it becomes a greater concern. For instance, 'shot Z757', performed on Z by Hall *et al.* [19], demonstrated an efficiency of around 1.1%, based on the reported capacitor bank energy of 11.6 MJ and the kinetic energy of the 10×10×0.725 mm aluminium flyer, which had a peak velocity of 13 km/s. In order to launch a smaller 5×5×1.0 mm aluminium flyer to 10 km/s using an acceleration technique with an efficiency of 1.1 %, a capacitor bank with a stored energy of over 300 kJ is required. This is more energy than many pulsed-power devices can safely store, resulting in the development of alternative techniques with higher efficiencies to investigate hypervelocity impact. One such technique, the electric gun, has reported efficiencies of up to 25% [5].

The electric gun can be thought of as a hybrid between the EFI and the EM flyer plate. The projectile is driven by both a thermal explosion, as in an EFI, and the magnetic acceleration of the flyer plate. The process (depicted in Figure 1.1) begins with the discharge of a current from a rapid rise-time capacitor bank across a thin metallic foil, resulting in the deposition of a large amount of energy in the foil through ohmic heating. This energy deposition drives a change in the foil state from solid to 'exploding' plasma. This exploding foil plasma acts as a driver gas, accelerating an adjacent thin and insulating plate known as the flyer. The flyer is laid atop the foil in a stiff assembly, such that the foil plasma 'punches out' a section of the flyer material, typically accelerating it for a few millimeters until it impacts a target. The plasma pressure component of the acceleration is known as the thermal pressure. When large currents are discharged to vaporise the foil, considerable magnetic forces exist in the system that also act to accelerate the foil plasma. The electric gun's high efficiencies are a consequence of its ability to convert energy from both the thermal explosion and the magnetic fields inherent in the system into kinetic energy in the flyer. The magnetic contribution to the acceleration allows far higher flyer velocities and impact pressures than can be achieved using an EFI. Meanwhile, the addition of Joule heating in the plasma to the work done accelerating the flyer gives the electric gun an energetic advantage over the EM plate flyer.

Additionally, the insulating flyer does not directly carry current, shielding it from the effects of ohmic heating and pressure applied by the strong magnetic fields in the system. This removes the

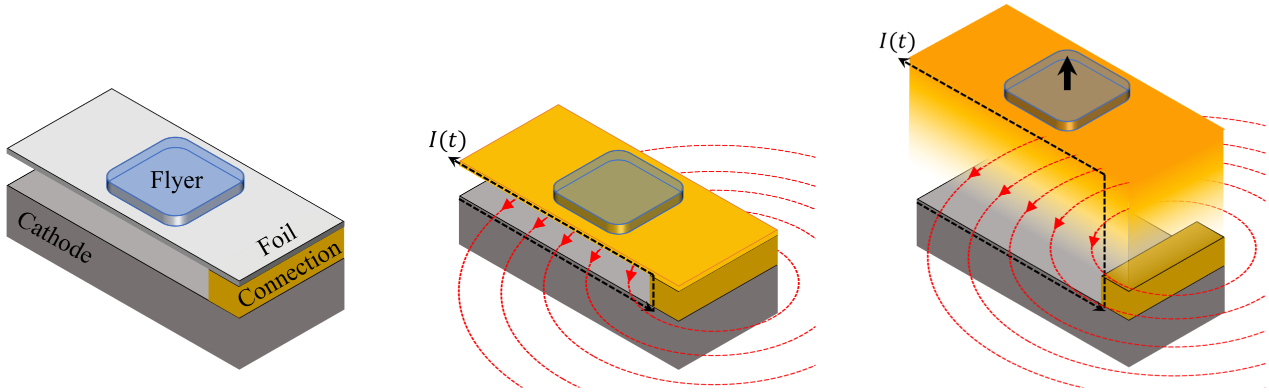

(a) (b) (c)

Figure 1.1: Diagrams illustrating the electric gun acceleration mechanism: the initial configuration of the foil, flyer, cathode and connection (1.1a); the foil experiences Joule heating, rapidly changing state from solid to plasma, accelerating the dielectric flyer (1.1b); continued discharge of the current causes further acceleration of the foil by Lorentz forces (1.1c).

restrictions on the maximum magnetic field strength applicable to the electromagnetic flyer plate [1] and allows the electric gun flyer to be accelerated across significantly greater stand-off distances (the distance between the launch site and the target). The ability to strike a target placed a distance away from the launch site is advantageous for a number of reasons. Firstly, it facilitates the recovery of the target after impact. Secondly, it can protect the diagnostic line of sight at the target from obstructive debris created during launch. Lastly, it can ensure the flyer impacts the target at constant velocity (ballistic impact), as it is physically distanced from accelerating forces.

While the electric gun has some advantages, its application has been hindered by challenges, resulting in its limited use up to this point. The majority of research performed on the electric gun took place at Lawrence Livermore National Laboratory (**LLNL**) between the 1970s and the early 1990s [2, 21–25]. In the modern era, the gun is primarily employed for the hypervelocity ballistic testing of spacecraft shielding. The electric gun is suited to this application due to its ability to launch a flyer from a large stand-off distance (up to 30 cm) without a sabot, with variable surface area and impact velocity [14, 15, 26]. Across both eras of research repeated stumbling blocks in the electric gun's development include:

1. **Challenges in modelling its operating mechanism.** The electric gun's acceleration process involves a complex combination of physics that are challenging to model, including rapid material expansion and compression, phase change from solid to plasma, magnetohydrodynamics and material strength behaviour.

2. **Challenges in experimentally diagnosing its behaviour.** The design of an electric gun is assessed experimentally by measuring the flyer's kinetic energy and state. This data is often challenging to collect, as a poorly optimised electric gun can cause the flyer to disassemble. In addition, a significant amount of plasma is created on vaporising the foil, blocking the optical line of sight both within the barrel and around the target.

3. **Loss of integrity during acceleration of flyers above 0.5 mm thick to hypervelocity.** The pulse length on impact produced by a flyer is proportional to its thickness. Many measurements made in extreme state research require a certain pressure amplitude for a minimum time, which the electric gun is unable to fulfil. Due to the listed issues regarding modelling and experimentally testing the electric gun, the mechanism for the disassembly of thick flyers is still not understood.

4. **Uncertainties in the flyer state.** Projectile impact techniques such as gas guns and EM plate flyers improve the the measurement of material properties, like the equation of state, by accelerating flyers with near-constant density. Previous research has suggested that acceleration of thick flyers using the electric gun can induce varying density profiles across the flyer thickness. As before, an understanding of how processes during operation affect flyer state cannot be obtained due to difficulty modelling the system and collecting diagnostic data regarding the flyer.

These challenges can be divided into two categories. Issues 1 and 2 refer to problems with the methodology surrounding designing and optimising the electric gun. The latter two represent limitations in the current understanding of the electric gun which, if left unresolved, reduce its potential applications.

In this thesis, advancements in simulation and experimental techniques are leveraged to begin to generate solutions to issues 1 and 2. Designing the electric gun load using experimental testing and iteration is both time and resource intensive, made worse in this case by the challenges in collecting diagnostic data during operation. Instead, by developing both numerical models capable of capturing the electric gun's operation and diagnostic acquisition techniques to validate these models, accurate design tools were created to address issues 3 and 4. The primary objective of the work undertaken in this DPhil was to understand the behaviour of the electric gun and its performance in novel load configurations. If the mechanisms for the extreme state change in thick flyers could be successfully mitigated, the gun's high efficiency and insulating flyer could allow existing platforms to unlock an unexplored thermodynamic space. To achieve this, the electric gun must:

- Be able to be modelled and designed using accessible simulation tools.

- Be explored numerically and experimentally to understand the dominant state change mechanisms in the flyer.
- Be a system wherein the physics required to model the load operation is well understood.
- Generate states in targets that can be used to investigate material properties.

These requirements will each be the subject of a different section which, when combined in the order listed, will build the body and narrative of this integrated thesis. The history of the electric gun and further details of its operation are discussed in the next chapter.

Chapter 2

Literature Review

As scientists, the accuracy of our research into phenomena occurring across our universe relies on the quality and breadth of the data we can collect. In some fields, the information necessary to reveal new insights can be collected *in-situ*, with the appropriate equipment. However, often the event a researcher may wish to investigate cannot be directly measured, such as the behaviour of materials under extreme pressure at the core of a planet. She may be able to make educated guesses based on the information that can be collected from afar: for instance, the planet's magnetic field gives insight into the motion and make-up of its core. However, this approach of observation from a distance carries complications. Systems rarely, if ever, occur in a vacuum, thus, it can be challenging to isolate the effects of the specific mechanism the researcher is interested in. Consequently, scientists often employ another method to access phenomena of interest; they create the conditions they are researching themselves. In this way, they can not only access the states they are researching on demand, but they can do so under controlled conditions with diagnostics of their choosing at the ready.

The advancement of the understanding of materials at extreme pressures is inextricably linked to the development of the devices used to generate these pressures in a laboratory setting. In 1905, Percy Williams Bridgman created the first piece of apparatus capable of generating pressures of over 10 GPa in samples packed into a gasket. His device resulted in an explosion of new findings, including studies of the compressibility, electric and thermal conductivity, tensile strength and viscosity of over 100 different compounds [27–30]. As the range of pressures achievable improved through the invention of new techniques, so to did the comprehension that materials under extreme pressure acted in ways that contrasted dramatically with their behaviour at standard temperature pressure conditions. For instance, under high pressures the suppression of the superconducting critical temperature can be observed [31].

With the emergence in the 20th century of research domains such as nuclear fission, nuclear fusion and aerospace, the study of material behaviour at extreme states developed from the investigation of fundamental physics to its effect in practical applications. As the motivation to reach increasingly high pressures has surged, among the novel techniques pioneered, some of the highest pressures achievable in a controlled setting are generated using projectile impact. On impact with a target, the flyer, a thin plate typically with a width ranging from millimetres to centimetres, drives a planar shock wave into the material over its surface area with a pulse length related to the flyer thickness. Depending on the technique, this pulse length can vary from nanoseconds to microseconds. The short duration of the pressure states generated by projectile impact has in turn created new challenges: developing diagnostic techniques precise enough to collect data in the window available. Consequently, great effort is given to not only increasing the velocity at which the projectile can be fired, but also its surface area, thickness and planarity on arrival. It was these efforts which led researchers in the 1970s at Lawrence Livermore National Laboratory (**LLNL**) to begin the development of a new technique for projectile acceleration to hypervelocities, termed the electric gun [2].

2.1 Background physics

To effectively review the research into the electric gun, one must first understand the physics which govern projectile launch techniques. The equation of state (**EoS**) is a fundamental relationship that describes the thermodynamic properties of a material under varying conditions of pressure, temperature, and density. Hugoniot experiments are a key method for probing the EoS in the high-pressure regime, particularly under shock compression. These experiments measure the material's response as it transitions from an initial state to a shocked state, providing data along the Hugoniot curve, which represents all possible states accessible through a single shock. In contrast, isentropic compression experiments explore the material's behavior under quasi-static loading conditions, tracing paths that conserve entropy rather than inducing abrupt increases. Isentropic compression is particularly useful for accessing intermediate states that are not achievable with shocks alone. Together, Hugoniot and isentropic experiments provide complementary data that constrain the EoS across a wide range of conditions, enabling more accurate modelling of material behavior. In this section, the fundamental principles behind the behaviour of strong shockwaves, projectile impact and EoS measurements are discussed.

2.1.1 Jump conditions

The Rankine-Hugoniot conditions provide an advantageous method for deriving a material's EoS through measurements of shockwaves. These relations enable the isolation of new information about a target material. To derive these conditions, the nature of a shock wave is considered. A shock wave is characterised as a violent disturbance that cannot be treated using the linear relations derived for smaller amplitude acoustic waves. Because the shock wave, by definition, moves faster than the speed of sound, it forms a 'front', across which the disturbance is so dramatic that the thermodynamic properties and velocity of the material become discontinuous. To relate these values to one another, consider the system visualised in Figure 2.1, where the shock moves from left to right with velocity U_s (thus the shock frame moves in the opposite direction). Although discontinuous, shocks must still obey the conservation of mass, momentum and energy. For instance, if a material is compressed from density ρ_1 to ρ_2, **conservation of mass** requires,

$$\rho_2(U_s - u) = \rho_1 U_s, \tag{2.1}$$

where u is the velocity of the medium. If this material is accelerated, it acquires the momentum $\rho_1 U_s u t$, which is equal to the impulse due to the pressure forces. The **conservation of momentum** requires,

$$\rho_1 U_s u = P_2 - P_1, \tag{2.2}$$

where P_2 and P_2 are the pressures upstream and downstream respectively. Finally, the **law of energy conservation** states the total increase in the kinetic energy and thermal energy in the material must be equal to the work done by the external forces of $P_1 u t$, therefore,

$$\rho_1 U_s \left(\varepsilon_2 - \varepsilon_1 + \frac{u^2}{2} \right) = P_1 u, \tag{2.3}$$

where ε_1 and ε_2 are specific internal energies that may be calculated from these equations or in some other manner.

The frame of reference may be selected to simplify the analysis of the system. In this case, the observer moves with the shock front. Considering the equations 2.1-2.3, the system has three unknowns (U_s, ρ_2 and P_2) which must be found. U_s is the velocity of the shock front, thus the velocity at which the material moves into the front (where the observer is sat) is moving at $-U_s$, so $u_1 = -U_s$. Similarly, the velocity of the front with respect the the material moving behind it must be $U_s - u$. As a result, $u_2 = -(U_s - u)$ must be the velocity flowing out of the discontinuity. When these values

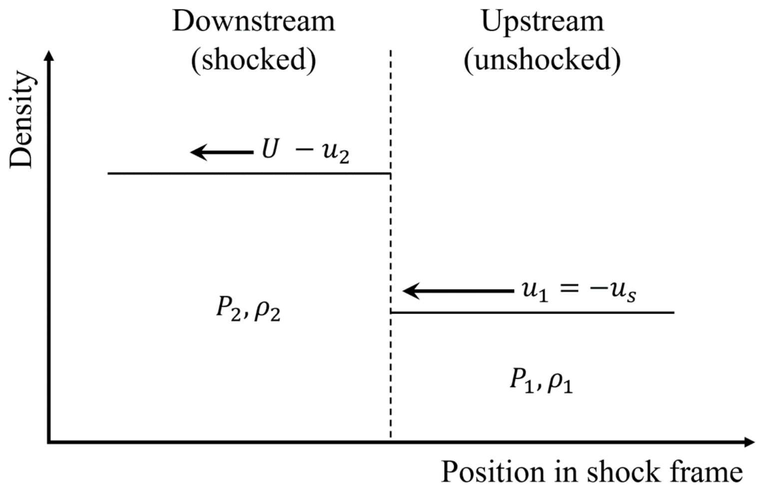

Figure 2.1: Illustration of a shock moving through a medium, including the downstream and upstream states.

are substituted into equations 2.1-2.3, the **Rankine-Hugoniot equations** in one-dimension are derived, where the conservation of mass, momentum and energy become,

$$\rho_2 u_2 = \rho_1 u_1 \tag{2.4a}$$

$$\rho_2 u_2^2 + P_2 = \rho_1 u_1^2 + P_1 \tag{2.4b}$$

$$\varepsilon_2 + \frac{u_2^2}{2} + \frac{P_2}{\rho_2} = \varepsilon_1 + \frac{u_1^2}{2} + \frac{P_1}{\rho_1}. \tag{2.4c}$$

These equations allow us to describe the relationship between the states on either side of a shock wave. With the additional knowledge of the shock velocity and the particle velocity of the fluid (u_p where $u_p = u_1 - u_2$), it is possible to derive the density and pressure of the material using,

$$\rho_2 u_2 = \rho_1 u_1 \tag{2.5a}$$

$$P_2 - P_1 = \rho_1 u_1 (u_1 - u_2) = \rho_1 u_1 u_p, \tag{2.5b}$$

respectively. However, determining u_p can be challenging; the next section addresses how these measurements can be made using flyer impact instead.

2.1.2 Projectile driven impact

When discussing projectile driven impact, the simplest scenario involves a planar, normal, parallel impact between a projectile and a target. This situation refers to the impact between two flat surfaces (planar), in which all points establish contact at the same time (parallel), and where the direction of

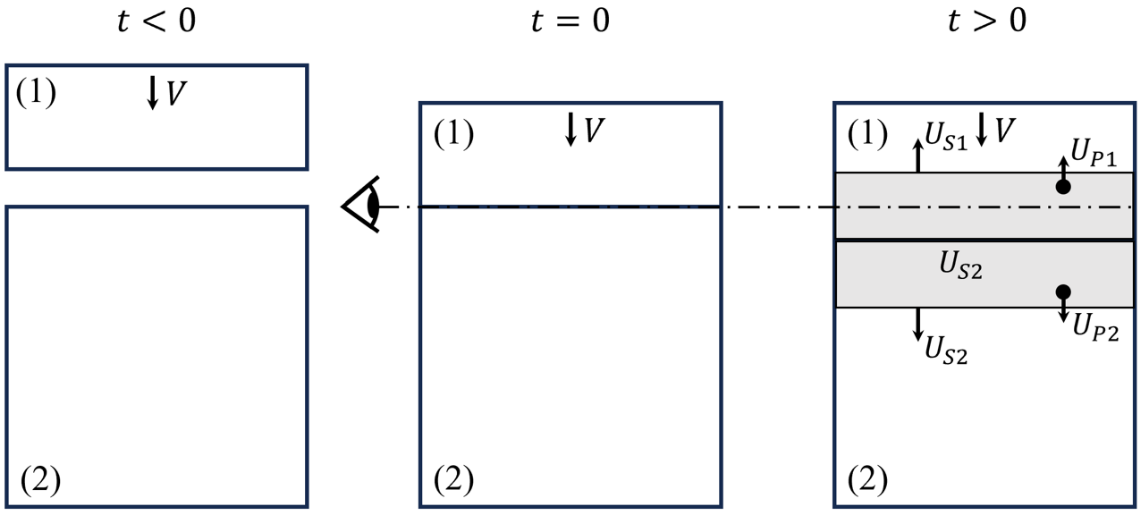

Figure 2.2: Diagrams illustrating the process of projectile impact from the point of view of an observer: ($t < 0$) projectile of material 1 moves towards a target of material 2; ($t = 0$) the projectile and target position at the time moment of impact; ($t > 0$) position after impact during pressure wave propagation.

motion of the projectile is perpendicular to its surface (normal). These conditions are important as they create a system that allows us to use our understanding of the target and projectile before and after impact to determine new information about the target in a straightforward manner. The following scenario is depicted in Figure 2.2. Prior to impact, the projectile travels with velocity V towards the target, which is typically at rest. Following impact, two compressive shock waves are generated travelling in opposite directions: one returns through the projectile with velocity U_{S1} and the other progresses through the target with velocity U_{S2}. The region of the projectile that has not yet interacted with the shock continues to move at velocity V, while the uncompressed region of the target remains at rest. The pressure in the projectile and the target can be calculated by assuming the material is continuous across the impact surface. This assumption results in two conditions which govern the material in the shaded region in Figure 2.2: both regions must have the same velocity and pressure (P) at their boundary, thus,

$$P_1 = P_2. \tag{2.6}$$

In this derivation, the particle velocities u_{p1} and u_{p2} are related to each other with regards to a fixed point of reference, illustrated in Figure 2.2 by an eye observing the system. Before impact ($t < 0$) every particle in the projectile has velocity V. On impact, the particles in the compressed region change speed due to the shock passing back through the projectile, thus their resultant velocity is

$V - u_{p1}$. If the target is initially at rest, the particle velocity in the compressed region will be u_{p2}. Recalling the continuity condition across the surface, it can therefore be stated,

$$V - u_{p1} = u_{p2}. \tag{2.7}$$

The conservation of momentum equation is used to calculate the pressure in the compressed region, where,

$$P_1 = \rho_{01} U_{S1} u_{p1} \tag{2.8a}$$

$$P_2 = \rho_{02} U_{S2} u_{p2}. \tag{2.8b}$$

Beyond this point, an EoS may be used to derive the relationship between the shock speed and the particle speed. A common EoS used in these scenarios is the shock Hugoniot linear relation, which states,

$$U_{s1} = C_1 + S_1 u_{p1} \tag{2.9a}$$

$$U_{s2} = C_2 + S_2 u_{p2}, \tag{2.9b}$$

where C and S are empirically derived material specific values. The constant C is typically close to the speed of sound in the uncompressed material. It should be noted that the shock Hugoniot linear relation is a simplified model that is not suitable for all materials. For instance, materials obeying a phase transition require a higher order relation (secondary). Substituting equation 2.9 into results in,

$$P_1 = \rho_{01}(C_1 + S_1 u_{p1}) u_{p1} \tag{2.10a}$$

$$P_2 = \rho_{02}(C_2 + S_2 u_{p2}) u_{p2}. \tag{2.10b}$$

By substituting equations 2.10 and 2.7 into 2.6, an equation with a single unknown (u_{p2}) may be derived, such that,

$$\rho_{01}(C_1 + S_1(V - u_{p2}))(V - u_{p2}) = \rho_{02}(C_2 + S_2 u_{p2}) u_{p2}. \tag{2.11}$$

Taking the roots of this system yields,

$$u_{p2} = \frac{-(\rho_{02}C_2 + \rho_{01}C_1 + 2\rho_{01}S_1 V) \pm (\Lambda)}{2(\rho_{02}S_2 - \rho_{01}S_2)}, \tag{2.12}$$

where $\Lambda = (\rho_{02}C_2 + \rho_{01}C_1 + 2\rho_{01}S_1V)^2 + 4(\rho_{01})(\rho_{02}S_2 - \rho_{01}S_1)$.

If the projectile and target are made of the same material, equation 2.12 becomes first order, as $(\rho_{02}S_2 - \rho_{01}S_1 = 0)$. With a little work, we find in this case $u_p = \frac{1}{2}V$, meaning the particle velocity in the compressed region is equal to half the impact velocity. This results in the instinctive conclusion that if a projectile impacts a target made of the same material, it will transfer half its momentum to the target material.

Projectile-driven impact is a powerful method for obtaining new information about a target material. When combined with the Rankine-Hugoniot relations, the density and pressure of the target material can be derived using the projectile's velocity and density upon impact, as well as the shock speed in the target. This approach can be simpler and more accurate than relying on measuring the particle velocity directly. The diagnostics and techniques used to measure these variables are discussed in the next section.

2.1.3 Making equation of state measurements

In the previous section, it was observed that the determination of flyer velocity and density upon impact, in conjunction with the shock velocity, enables the derivation of material EoS parameters through the Rankine-Hugoniot relations. Projectile launchers such as gas guns afford precise knowledge of flyer density and velocity on impact due to minimal state alteration during acceleration, resulting in accurate measurements. In scenarios where the flyer states are less certain, direct measurement of material particle velocity alongside shock velocity facilitates direct calculation of the EoS values. Shock waves, by definition, move at high velocities, thus the extreme states they generate are short-lived. Consequently, velocimetry techniques with high temporal resolution are necessary to measure the shock speed, particle speed or flyer velocity.

Velocimetry techniques play a crucial role in measuring the velocity of dynamic events such as explosions, impacts, and shocks. Two commonly used techniques are Velocity Interferometer System for Any Reflector (VISAR) [32] and Photonic Doppler Velocimetry (PDV) [33]. VISAR relies on interferometry principles, where a laser beam is split into reference and object beams, with the object beam reflected off a moving surface. The two beams recombine, and their interference pattern is analyzed to determine the velocity of the moving surface. VISAR is highly accurate and capable of measuring velocities ranging from a few meters per second to several kilometers per second. On the other hand, PDV utilizes the Doppler effect, where light is scattered off a moving surface, and the resulting Doppler shift is used to calculate velocity. PDV offers high spatial resolution and can measure velocities in the range of millimeters per second to several kilometers per second. Both techniques are employed to determine the shock velocities within target materials, either by directly measuring shock fronts in transparent materials like diamond [34] and quartz [35], or by deducing the speeds from shock breakout times at material interfaces in opaque samples [9].

EoS measurements obtained through projectile impact exhibit relatively high precision due to the high volume and extended duration of the conditions achieved upon impact, especially when contrasted with alternative techniques like laser-driven hohlraums [36]. This contrast between the pressure ranges and the precision error of the two techniques is illustrated in the plot of Hugoniot measurements for quartz created by Marshall *et al.*, depicted in Figure 2.3 [9]. The plot displays measurements conducted at the National Ignition Facility (**NIF**), which, despite attaining higher pressures, feature considerably wider error bars compared to those obtained using an electromagnetic flyer plate on the Z machine. This disparity arises because electromagnetic flyer impact generates a longer continuous pressure pulse over a larger volume of material than can be achieved using a hohlraum. Consequently, velocity measurements can be extracted over a increased area and duration, increasing the precision of the measurement and resulting in Hugoniot measurements with minimised error bars.

The plot developed by Marshall et al. emphasises the importance of conducting high-precision EoS measurements. Notably, the measurements obtained from shots conducted at NIF exhibit error bars that encompass three distinct EoS models (LEOS, Sjostrom-Crockett, and Desjarlais). Consequently, the uncertainty in measurements of density at pressures in excess of 20 MBar preclude discrimination between the models. Accurate models validated through precise measurements are essential for making realistic predictions regarding material behaviors under extreme conditions, a necessity in fields such as inertial confinement fusion. For instance, the differences between the models discussed by Marshall *et al.* are not insignificant: at a density of 8 g/cm^3, LEOS [37] and Sjostrom-Crockett predict a pressure of approximately 30 Mbar [38], whereas the value is closer to 40 Mbar using Desjarlais [39]. In inertial confinement fusion experiments, which involve diverse materials like high-density carbon fuel capsules and gold hohlraums [40], discrepancies in material models at each stage of the process can lead to significant disparities between the anticipated and actual fusion yield [41].

2.2 Projectile-driven extreme state research

By the 1970s, a proliferation of projectile launch techniques had emerged, including gas guns, railguns and slappers [44–46]. Researchers at the time faced the same fundamental constraint on their maximum velocity experienced today: maximising the conversion of stored energy into kinetic energy in the

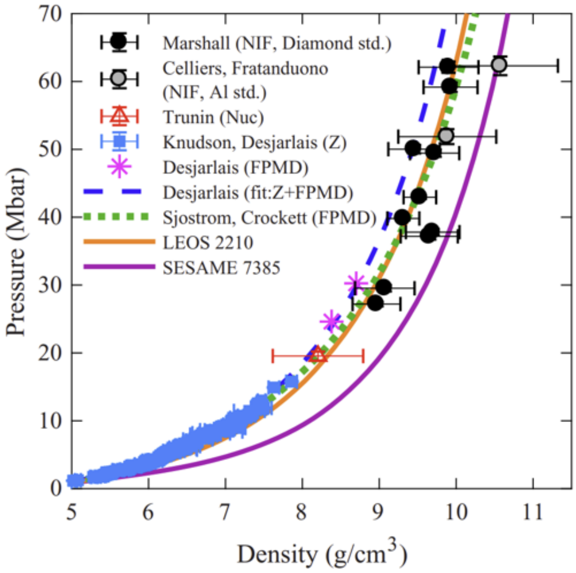

Figure 2.3: Plot created by Marshall *et al.* [9]: *New quartz Hugoniot data using a diamond standard (black circles) and an aluminum standard (gray circles). Also shown are data acquired at the Sandia Z machine (blue squares) [39, 42, 43], FPMD calculations from Desjarlais, Knudson, and Cochrane (magenta asterisks) [39], Sjostrom and Crockett (dotted green) [28], and tabular EOS models. The fit to the Z-data and FPMD calculations presented by Desjarlais et al. [39] was extrapolated beyond its upper bound, 30 Mbar, represented by the dashed blue curve.*

flyer while maintaining its integrity. Ultimately, the maximum velocity of a flyer varies with the acceleration mechanism and flyer geometry, the latter being chosen based on required area and duration of the pressure pulse. At LLNL, Weingart *et al.* were interested in exploring pressures of TPa in metals for EoS measurements. Recalling the equations put forward in Section 2.2, the pressure in a target generated by impact using a flyer is dependent on the velocity and shock impedance of the flyer. Consequently, it was necessary for Weingart *et al.* to impact the sample at hypervelocity (preferably over 10 km/s) and generating a pulse length long enough to extract meaningful diagnostic data from the target. In the following section, the projectile launchers available to Weingart *et al.* at the time, which included gas guns, rail guns, and slappers (the notable laser-driven flyer had not yet been invented), are evaluated in the context of this goal.

Gas guns

Gas guns utilise compressed gases, typically helium or nitrogen, to accelerate projectiles to high velocities, enabling the controlled study of impact phenomena. Gas guns offer versatility in terms of projectile size, velocity, and energy, making them suitable for a wide range of research applications.

Though still one of the most widely used projectile acceleration techniques, gas guns are fundamentally limited in their projectile velocity by the speed of sound in the gas driving it. While using lighter driving gases and multi-stage systems can increase the flyer velocity, their upper limit remains at ~9 km/s. Additionally, projectiles driven to around this limit have been found to sustain considerable damage [47]. Consequently, whilst gas guns are ideal for accelerating high mass (g - kg), thick flyers capable to driving a long shock pulse in a target, their capped velocity limits the magnitude of the pressures they can drive. In summary, whilst the gas gun provided the accuracy required for EoS measurements, it could not generate the pressures of interest to Weingart *et al.*.

Rail guns

The rail gun, much like the gas gun, is able to launch high mass projectiles. Also like the gas gun, the rail gun has a limited maximum velocity which constrains the target pressures achievable on impact. The projectile is accelerated using strong electromagnetic forces generated by discharging a current through the gun's 'rails'. The magnetic field strength is proportional to the current density (J) in the metal rails. However, high current density at the point of contact between the rail and the projectile causes rapidly expanding metal plasma to form in this region. The expansion of this plasma can be sufficiently violent so as to cause irreversible damage to the rail component. As a result, the upper speed limit of the rail gun is around ~5 km/s, fixed due to the melting temperature of their rails [45, 48]. Advancement of the launch technique has largely been abandoned, as the melt temperature of a material is a fundamental property, which researchers are unable to significantly influence at present. As before with the gas gun, the rail gun could not accelerate projectiles to the velocities needed to generate terapascals of pressure without compromising both the projectile and rails.

Slappers and the first electric gun

The slapper, also known as an Exploding Foil Initiator (**EFI**), uses the discharge of current from a fast rise-time capacitor bank to ohmically heat a metal foil. The foil changes state from solid to plasma so rapidly it is described as 'bursting'. The explosive volume change is used to drive a thin dielectric film up a barrel and into a target. Slappers, a recent invention in the 1970s made by Keller and Penning, had thus far only launched flyers to around 2 km/s [46, 49, 50]. However, these velocities had been achieved using a relatively low-energy capacitor bank to drive the acceleration. Weingart *et al.* predicted that by using their new 100 kV, fast rise-time capacitor bank, they could utilise metallic foils

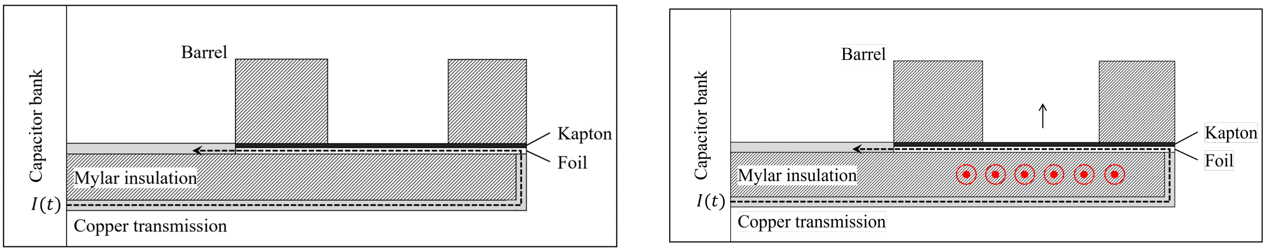

(a) Illustration of the current path $I(t)$ through the foil. When the current is discharged, the foil explodes, punching out the thin Kapton sheet above it, driving it up the barrel and into a target.

(b) An illustration of the magnetic field generated due to the current path shown in figure 2.4a. The magnetic pressure in the foil during flight contributes significantly to the acceleration of the flyer.

Figure 2.4: A simplified diagrams of the original electric gun set-up designed by Weingart *et al.* [21].

to accelerate dielectric flyers to the velocities necessary to generate TPa shocks in a target material [21]. Their set-up, the first 'electric gun', is illustrated in Figure 2.4a.

The electrical Gurney model, created by Stanton and Tucker, is an analog of Gurney theory, a model originally developed to predict velocities of fragments accelerated by high-explosive charges [51]. The electrical Gurney model predicts the final flyer velocities based on a characteristic energy (E_G), the mass of the foil per unit area (C), and the mass of the flyer per unit area (M). Stanton and Tucker assumed this characteristic energy was related to the current density in the foil (J_B) [52], reworking the Gurney equation into the form,

$$V_f = \sqrt{KJ_B^b}\left(\frac{M}{C} + \frac{1}{3}^{-0.5}\right) \tag{2.13a}$$

$$V_f = V_G\left(\frac{M}{C} + \frac{1}{3}^{-0.5}\right), \tag{2.13b}$$

where K and b are empirically determined constants and V_G is a characteristic velocity referred to as the Gurney velocity [21]. By leveraging the fast rise-time of their new capacitor bank, Weingart *et al.* anticipated the factor four increase in current density in the foil would result in a considerably higher flyer velocity. However, the experimental testing of their set-up revealed an unexpected result; the velocity of their thin flyers was far higher than the electrical Gurney model had predicted. This indicated an additional, undetermined, acceleration mechanism must have been active in the electric gun, which Weingart *et al.* set about investigating.

Typically, a chemical explosive will drive a flyer to its maximum velocity by the time its products have expanded to twice their initial volume [53]. Weingart *et al.* found the electric gun flyers

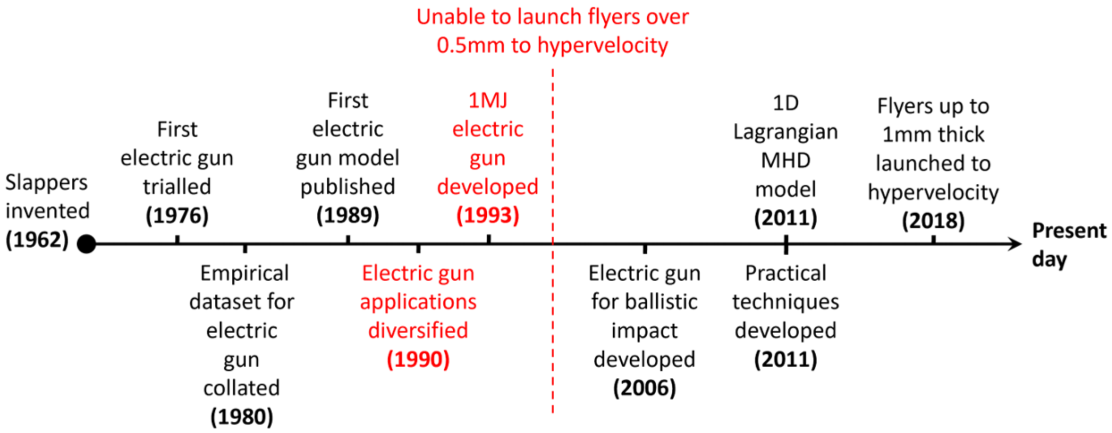

Figure 2.5: Timeline detailing the advancement of the electric gun, from its invention to the modern day.

continued to accelerate even after the foil had expanded by over 100 times. While a small portion of this acceleration was attributed to additional thermal expansion during the continued current deposition after the foil had exploded, it was posited that the majority was instead due to significant magnetic forces in the direction of flight. Figure 2.4b illustrates the direction of the magnetic field lines, determined by the current path through the copper transmission, will result in an additional Lorentz force up the barrel. Weingart *et al.* acknowledged a thorough mathematical description of the plate motion would require a magnetohydrodynamic (**MHD**) calculation coupled to a calculation of the electrical energy deposited in the foil material as it expands. However, this was beyond the modelling capabilities at the time, hence, they were limited to attempting to qualitatively account for the observed flyer velocities by separating the magnetic and hydrodynamic effects [22, 24]. As a result, over the next decade, researchers were limited to developing the electric gun experimentally; a laborious task reviewed in greater detail in the next section.

2.3 Development of the electric gun

The development of the electric gun, following its invention in 1976, occurred primarily in two distinct periods: from the 1970s to the early 1990s, and in the late 2000s, at national laboratories in the United States and China respectively. A timeline detailing significant events during these periods is presented in Figure 2.5. This literature review intends to both give context to the current state of the electric gun and reveal the novel opportunities for advancement of the technique. To best achieve this goal, the topic of the development of the electric gun is explored in a chronological order. Consequently, this section details the advancement of the electric gun at LLNL, until the 1990s.

2.3.1 Empirical improvement of the electric gun

Initially, researchers were unable to model the electric gun due to its complex, MHD, drive mechanism. Consequently, they instead focused on collecting experimental data to derive empirical trends, which could then be used to optimise the gun's performance. A crucial piece of data used to derive these empirical trends was the flyer velocity profile. For instance, the flyer velocity profile allowed them to calculate the empirical constants used in the Gurney equation (equation 2.13). Through extensive experimental parameter studies, researchers at LLNL were able to build a comprehensive library of empirical constants for a range of different foil and flyer surface areas, waveforms and barrel lengths. This information assisted in both the interpretation of experimental results and the design of loads in new parameter spaces in the absence of numerical simulations. Additionally, the flyer velocity profile could be used to calculate the flyer's kinetic energy, which, when compared to the pulsed-power device's discharge energy, gave an estimate of the load efficiency. Using this load efficiency as an optimisation objective, it was revealed that stored electrical energy in the capacitor bank could be converted more efficiently into kinetic energy in thin flyers by designing the load to achieve foil burst near the time of the current peak [22].

The first electric guns employed Fabry-Perot interferometry (**FPI**), which continuously captured the flyer velocity throughout its flight [21]. FPI operates by detecting the Doppler shift of light caused by positional changes in the interferometric pattern behind the Fabry-Perot interferometer. This shift indicates the velocity of the flyer surface reflecting the light. However, the electric gun can accelerate a flyer to hypervelocity in microseconds, necessitating high time resolution techniques to capture the profile in detail. Consequently, VISAR (introduced in Section 2.1.3) was implemented to capture the flyer velocity profile at higher temporal resolutions. Unlike other systems, VISAR is configured to measure changes in light intensity due to sinusoidal interference variation with the velocity of the surface, not its displacement. As a result, VISAR does not need to be differentiated with time, retaining better resolution than FPI. The high temporal resolution of the VISAR diagnostic allowed researchers to observe short timescale events in the flyer velocity profile, such as the thermal and magnetic contributions to acceleration at different times in flight. Without explicit modelling of the interplay between the thermal and magnetic pressures in the foil, VISAR was the only available window into this complex behaviour. For example, Chau *et al.* revealed that Lorentz forces could move thicker foils before burst, resulting in the vaporized foil having a larger initial volume and thereby decreasing the initial thermal pressure [22].

However, using experiments to investigate the electric gun was a resource-intensive task. The measurement of the flyer velocity using VISAR relied on maintaining a reflection from the flyer surface (or a small aluminium spot placed on the flyer). In practice, maintaining this reflection was challenging, as researchers encountered many unanticipated phenomena which compromised the flyer surface. This included the development of hydrodynamic jetting in the flyer material at the juncture of the barrel and the flyer [54], which would obscure the diagnostic line of sight to the flyer surface and decrease the flyer planarity. Additionally, Osher *et al.* found that in shots at atmospheric pressure, the return beam reflected from the flyer could be obscured by additional light from the formation of an air-shock ahead of the flyer at late times [24]. It was also common for the bright foil plasma driving the flyer to escape around the flyer edges during flight, once again interrupting the return beam of the laser. Osher *et al.* also noted the formation of a dimmer light source on the flyer surface during high-energy shots (18 km/s flyer velocity and up) in vacuum. Though they attributed this to electrical arcing across the flyer surface to the presence of strong electric fields, this light could also have been emitted from the aluminium spot on the flyer [24]. Absence of modelling made many of these effects difficult to interpret, requiring extensive further study to isolate and diagnose these effects. As a result, progress made in improving the gun was slow.

2.3.2 Modelling the electric gun

Initially, researchers at LLNL had relied on simple empirical equations [55] to attempt to model the behaviour of the electric gun. Experimental validation revealed equations, such as the Gurney model, were only appropriate at predicting the behaviour of electric gun loads with a final flyer velocity of less than 10 km/s. This suggested the magnetic forces contributed far more significantly in higher velocity loads. To assess the ratio of thermal to magnetic acceleration, Osher *et al.* directly measured the temperature of the foil and calculated the expected flyer velocity based on this value, explicitly proving the foil's thermal expansion could not account for the higher flyer velocities [25]. This motivated Osher *et al.* to utilise advancements in modelling to create their own MHD code to investigate this behaviour further.

The zero-dimensional (**0D**) MHD numerical code, created by Osher *et al.* for the electric gun, can be divided into two sections. First, an RLC circuit model, which used the fixed capacitor-bank parameters, foil geometry, and foil material properties, was incorporated to predict the current waveform applied to the load. The model also accounted for the dynamic load resistance, calculated using the temperature dependent Lee-More resistivity model [56]. This current was then employed to calculate the pressure and temperature state in the foil using the ideal gas equation of state. Knowledge of the current also permitted the determination of the forces based on the Lorentz forces and thermal pressure in the foil, resulting in the explicit calculation of the flyer velocity through the conservation of momentum in the system. Notably, the flyer itself was considered by simply adding its mass to the momentum equations. This is equivalent to modelling the flyer as incompressible and also precluded the calculation of its thermodynamic state.

Investigations using the 0D model revealed that during the rapid heating of the foil before burst, the thermal pressure in the foil rose to tens of GPa [57]. Upon exploding, the thermal expansion of the foil contributed to the flyer's initial acceleration. However, as the foil and flyer moved up the barrel, the volume behind the foil increased, causing the thermal pressure from the foil to decrease with its density. This mechanism provided, for the first time, an explanation for the observation that magnetic acceleration occurred only in flyers accelerated above 10 km/s. To reach these higher velocities, the foil width (W) had to be narrow, increasing the current density and causing the foil to burst before the current peak. Consequently, the total Lorentz force ($J \times B$), which is proportional to the current, peaked later in flight, when the thermal acceleration had largely subsided. Thus, the observation that the magnetic pressure was only present in systems with flyers velocities above 10 km/s was not because it did not exist in lower velocity systems. In these scenarios, the current peak instead aligned with the foil burst, thus the Lorentz forces were insignificant during flight. These findings underscore a broader lesson: interpreting experimental results from complex systems without the context provided by modelling can lead to the misunderstanding of measured data, and inaccurate conclusions.

2.3.3 Launching thick flyers

Accurately modelling the real-world behaviour of the electric gun is challenging, as it involves multiple complex phenomena which occur simultaneously, including the vaporisation of the foil, the compression of the solid flyer and MHD effects. Improvements in modelling MHD, EoS, and resistivity in metals allowed Osher *et al.* to be able to explicitly calculate the interplay between thermal and magnetic acceleration in the exploding foil [25]. Whilst this was a significant step forward in the understanding of the electric gun, accelerating flyers thicker than ~0.5 mm to hypervelocity remained an obstacle. Researchers found thick flyers displayed signs of dramatic state change and, in some cases, complete disintegration. The electric gun was invented as a tool for EoS research, however, the short shock pulse length generated in a target by thin flyers made it challenging to extract a sufficient quantity of diagnostic data to make an accurate EoS measurement. In 1989, Gathers *et al.* reviewed the

LLNL electric gun facility as a tool to make Hugoniot measurements, finding the thin nature of the flyers (0.254 mm thick) limited the precision of the Hugoniot measurement [3]. Ultimately, they conclude that the technique is suitable for making 'quick approximate Hugoniot measurements', but required the ability to launcher thicker flyers if its accuracy was to be improved. Despite this conclusion, there is limited published research in this time period describing any attempts to launch thicker flyers; across the literature available before the 1990s, the thickest flyer reported to have been successfully accelerated was 0.3 mm [2, 21–24, 54, 57, 58].

The first documented study regarding the acceleration of thick flyers was reported by Osher *et al.*, when describing the different potential applications of their electric gun [5]. This study reports accelerating both standard dielectric flyers and composite metal and dielectric flyers of up to 1 mm and 2 mm thick, respectively. The 1 mm dielectric flyer was reported to reach velocities of 7 km/s, with a load efficiency of 25%. However, when using a charge voltage of 100 kV, Osher *et al.* found that loads with a foil surface area smaller than 10 mm^2 experienced flyer disintegration on acceleration. While this disintegration could be offset by using a composite metal plate and dielectric flyer, this load design resulted in lower velocities (1.6 km/s for a 0.15 mm thick Kapton flyer bonded to a 1.0 mm thick stainless steel plate), reducing the load efficiency to 10 %. Osher *et al.* had revealed a significant stumbling block in the electric gun's development. The gun's high efficiency when converting stored electrical energy to kinetic energy in the flyer was inconsequential if the technique could not generate shock pulse lengths long enough in targets to extract meaningful measurements. The limitation in the maximum flyer thickness narrowed the electric gun's applications to projectile driven explosive initiation, which could be done with the smaller and cheaper slapper [17].

Creating an electric gun which could launch thick flyers to hypervelocity requires significant investigation and redesign of the load. However, the violent disassembly of the thick flyers made studying the destruction mechanism experimentally a highly challenging endeavour. As discussed in Section 2.3.1, the majority of diagnostics fielded to study the electric gun employed the collection of laser light reflected from the flyer's leading surface to infer measurements such as its velocity. Simply disrupting the surface could reduce the reflection; the flyer breaking up ensured it was eliminated completely. Another consequence of the loss of flyer integrity during flight was plasma breakthrough. The hot foil plasma driving the flyer was low mass and extremely bright. Thus, if the flyer broke apart, the unrestrained foil plasma could move ahead of the flyer at a higher velocity, obscuring the line of sight of diagnostics trained on the barrel or target. Whilst the distinctive, bright, foil plasma clouding the diagnostic line of sight was a strong indication that the flyer had experienced disassembly during flight, the mechanism by which the thick flyers failed was obscured [4].

Osher *et al.* stated that thick flyers failed due to high acceleration forces during launch [5]. This broad conclusion, lacking any specific failure mechanisms, is indicative of the limited tools available to the researchers. The 0D MHD model did not incorporate an EoS model in the flyer and the radiographs of the event provided only qualitative information, preventing a quantitative investigation of the states experienced by the flyer during its violent disintegration. Osher *et al.* went on to explore a number of different novel configurations of the gun, including testing a two-stage launch system, which launched thick copper slugs [5] and simulating a coaxial electric gun [59]. The former was found to disintegrate the copper slugs on launch and if experimental testing of the latter was performed, the results were never published. In fact, shortly after this in 1993, LLNL published their final paper on the topic of the electric gun entirely [58].

2.3.4 Summary of development until 1993

In this section, the development of the electric gun at LLNL, from its inception to its cessation, was discussed. In summary, whilst the electric gun demonstrated notable advantages, such as high load efficiencies and flyer velocities over 10 km/s, the technique was rendered obsolete due to limitations in the maximum flyer thickness. While this work focused on the research efforts undertaken at LLNL, similar narratives had unfolded at other facilities during the same decades. For instance, in the 1980s, the Material Research Laboratories (**MRL**), Australia, became interested in the use of electromagnetic launchers as a tool to investigate weaponry, controlled thermonuclear fusion, space launch, advanced industrial processes and EoS research [60]. In 1993, Hatt *et al.* compiled a report on the calibration and testing of a large-scale electric gun facility for obtaining Hugoniot and spall strength data [4]. Though they found some of their measurements were in agreement with published data, their electric gun had low repeatability due to plasma leakage around the edges of the flyer. Further, they found their flyers were unable to generate a shock pulse of sufficient duration in their target due to variation in the flyer density across its thickness. This resulted in Hugoniot and spall measurements with poor precision, reproducing the conclusions made by Gathers *et al.* at LLNL [3].

At the end of this period of research, a number of questions remained unanswered, including:

1. What were the failure mechanisms of flyers accelerated by the electric gun?

2. Why did a current with a faster rise-time launch thin flyers more efficiently?

3. Why did Osher *et al.* find they were able to launch thicker metal-dielectric composite flyers then they could purely dielectric flyers?
4. What physical models were necessary to accurately simulate the operation of the electric gun?

2.4 The modern electric gun

This literature review has thus far tracked the development of the electric gun in a loosely chronological order. Section 2.3 revealed the electric gun was incapable of fulfilling its intended purpose of making EoS measurements in novel pressure regimes, as it was unable to launch thick flyers to hypervelocity without damaging or destroying them. Soon after this conclusion was reached independently at both LLNL and MRL, investigation into the electromagnetic flyer plate began on the Z machine at Sandia National Laboratories. Here, researchers swiftly demonstrated the ability to accelerate flyer plates thicker than 1.0 mm to over 20 km/s [19]. It is outside of the scope of this DPhil to make comments on the political climates which typically drive scientific innovation, though it may also be of interest to reader that the Cold War officially ended in 1991. Perhaps, in the ensuing period of relative peace, one multi-megajoule electromagnetic acceleration facility was considered sufficient.

The primary use of electric gun in the modern era is to investigate the hypervelocity impact of aerospace shielding [14, 15, 61–63]. The technique is well suited to this application for a few reasons, the first being it can accelerate projectiles to velocities exceeding 10 km/s, replicating the relative velocity of debris encountered by spacecraft. Secondly, the flyers accelerated by the electric gun do not use a sabot, therefore more closely resemble the impact of a small homogenous object. Moreover, the electric gun has demonstrated the capacity to launch thin flyers across stand-off distance of up to 30 cm, facilitating the retrieval of samples post-testing for subsequent analysis. Lastly, owing to its high conversion efficiency of stored electrical energy into kinetic energy, the electric gun load permits researchers with relatively low-energy pulsed-power devices to accelerate flyers to hypervelocity. The evolution of the electric gun for ballistic impact investigations has spurred advancements in its experimental methodologies and modelling techniques, which are reviewed in this section.

2.4.1 Developments in experimental and modelling techniques

The poor repeatability of the electric gun load encountered in Section 2.3 posed an obstacle to its advancement. The variability in its performance from shot to shot was predominantly due to the challenging conditions created by the exploding foil plasma. Not only did this plasma explosion often obstruct the line of sight of velocimetry diagnostics [4], but subsequent investigations revealed the uniformity of the explosion was greatly dependent on the distribution of the current density across its surface. It was discovered that the current across the foil surface concentrated at features such as scratches, surface heterogeneities, edges and vertices, resulting in an non-uniform foil explosion [64]. This uneven explosion was found to initiate instabilities and deformations in the flyer, thereby compromising its planarity [65, 66]. The refined understanding of the foil explosion's sensitivities enabled researchers to improve its repeatability through enhanced fabrication techniques and subtle load modifications. For example, Wang *et al.* demonstrated the effect of an uneven drive could be minimised by ensuring the foil was wider than the width of the barrel, such that explosion at the edges of the foil did not interact with the flyer [14]. Another method of reducing the risk of plasma escaping around the flyer edges in the barrel involved tilting the barrel walls to minimise the deformation of the flyer edges as it accelerated [54].

In addition to refining their experimental techniques, researchers also developed more sophisticated models to predict the behaviour of the electric gun loads. Where previously Osher *et al.* had relied on a 0D model to predict the pressure states and dynamics of the exploding foil in their system, subsequent investigations recognised that the complex behaviour of the foil plasma could be better represented by a one-dimensional (**1D**) Lagrangian MHD code [62, 67]. For instance, Wang *et al.* demonstrated the effectiveness of this technique in optimising the foil thickness, width and material selection to successfully increase the flyer velocity in their load. Note, the 1D MHD codes, like the 0D model created by Osher *et al.*, did not include an EoS in the flyer, assuming the flyer to be incompressible. Consequently, while the models revealed good agreement against a range of experimentally obtained thin flyer velocimetry data, they could not accurately capture the disassembly mechanisms which continued to occur in flyers thicker than 0.5 mm.

2.4.2 Accelerating thick flyers

Despite notable improvements to the repeatability of the electric gun, the acceleration of thick flyers to hypervelocity without damage remained a challenge. Reports in modern open literature of attempts to launch flyers exceeding 0.25 mm thick are scarce, although it is unclear whether this is due to a lack of necessity or success. Thick flyers are necessary to drive a constant shock velocity in a target over the periods of time required to collect comprehensive diagnostic data to infer the material's Hugoniot and equation of state. While less critical in studies focusing on ballistic impact, the primary application of electric gun in recent years, the ability to accelerate thick flyers to hypervelocity could allow researchers to utilise the gun's high efficiency to achieve previously unattainable thermodynamic states on relatively low-energy machines.

The only modern-era paper discussing the acceleration of thick flyers, published by Song *et al.* in 2018, is of great importance to this work [15]. Within their study, the authors provide the only quantitative results from electric gun loads with flyers above 0.5 mm thick that could be found during this literature review. Notably, they report both the flyer velocimetry and target shock profile data from the acceleration of a 1.0-mm-thick flyer to hypervelocity. This velocity profile exhibited considerable noise before the signal was lost mid-flight, explained by the authors as spall and subsequent melting of its leading surface. Despite these challenges, Song *et al.* demonstrated that the 1.0-mm-thick flyer drove a shock velocity of 1.4 km/s for a duration of 270 ns in a lithium fluoride target. While the authors did not report any numerical modelling of the load, they posited their success in launching flyers above 0.5 mm was due to their pulsed power device's current rise-time (around 1.8 µs). Song *et al.* suggested this relatively long rise-time propelled the thick flyer without the forming strong shock waves inside it. This observation challenges previous notions, particularly those from early work at LLNL, which suggested that the performance of an electric gun is optimised when the current rise time matches the time for the foil to burst. However, without understanding of the thermodynamic states in the flyer, it is unclear why this long rise-time prevented the disintegration of flyer. For instance, the rise-time was longer than the flight time of the flyers, thus the peak current magnitude was not avoided. Further research is required to uncover the underlying mechanisms which result in state change and disassembly in thick flyers.

2.4.3 Summary

To summarise, recent advancements in both experimental methodologies and modelling techniques resulted in the electric gun becoming a repeatable tool for investigating hypervelocity impact of shielding. Practical enhancements to the load configuration included oversizing the foil width such that its edges did not explode under the flyer and barrel, and increasing the uniformity of the foil's explosive drive. Moreover, researchers demonstrated the ability to predict both the circuit behaviour and kinematics of thin flyers to a high degree of accuracy using 1D Lagrangian MHD codes, accelerating the load design optimisation process. The work by Song *et al.* remains a relatively recent chapter in the story of the development of the electric gun; as of yet, its intriguing conclusions regarding the effect of current rise-time on the flyer state have not been followed up on. The study underscores the importance of using both numerical and experimental results in parallel when investigating the electric gun.

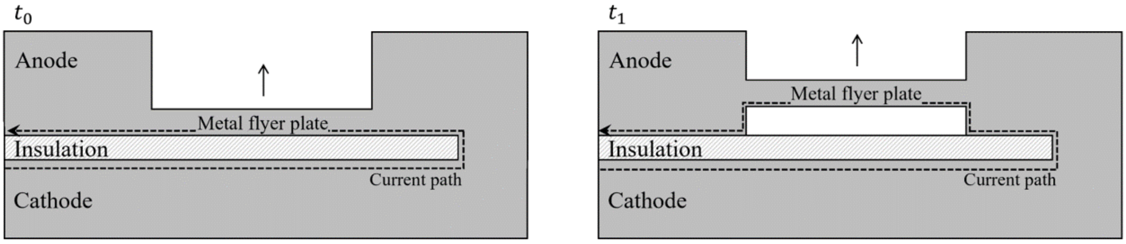

Figure 2.6: Illustration of the operating mechanism in an electromagnetic flyer plate: (t_0) the current is discharged directly through the metal flyer; (t_1) the current moves through the metal barrel walls and through flyer is it accelerates.

2.5 Electromagnetic flyer plates

Despite improvements to the electric gun, the technique remains restricted in its ability to launch thick flyers to hypervelocity. In this section, an alternative electromagnetic projectile launcher which has achieved this goal is investigated. The electromagnetic (**EM**) flyer plate has an extensive record as a tool for generating high precision EoS measurements. Through studying the history of the development of the EM flyer plate and the understanding of its mechanism, equivalent routes forward in the advancement of the electric gun are suggested.

The EM flyer plate is a pulsed-power driven projectile-driven impact technique developed at Sandia National Laboratories. While the mechanism shares some similarities with the railgun, it uses a current profile with a far shorter rise-time (around 200 ns)), resulting in the flyer reaching its maximum velocity within millimetres of launch. The technique is unique in its ability to launch thick flyer plates to velocities over 10 km/s without generating shocks in the flyer during acceleration. Violent state change in the flyer can alter its density state, causing it to drive fluctuating pressure wave profiles, or even disassemble completely. Early investigations in EM flyer plates performed by Hall *et al.* using the Z machine (**Z**), a low inductance pulsed-power generator capable (at the time) of capacitively storing 11.6 MJ, offered researchers the opportunity to access previously unattainable pressure regimes with gas gun accuracy [19].

2.5.1 EM flyer plate or electric gun with a thick foil

The EM plate flyer operating mechanism, shown in Figure 2.6, is similar to that of the electric gun. Current discharged from the capacitor bank flows around an insulating material, within which a magnetic field is propagated. This magnetic field applies a magnetic pressure (P_b) at the inner surface of the flyer plate which can be calculated using,

$$P_b(t) = \frac{B(t)^2}{2\mu_0} = \frac{J(t)^2\mu_0}{2}, \tag{2.14}$$

where B is the magnetic field strength and μ_0 is the permeability of free space. This is the same equation used by Osher *et al.* in their 0D electric gun model [57]. When discharge begins, this pressure will occur in the region of the flyer affected by the skin depth of the current. Here, skin depth refers to the penetration of alternating current (AC) into the conductor, which decreases as the frequency increases. Initially, the current flows through the foil at the skin depth, generating a magnetic field within the metal. If the magnetic field is strong enough, the electromagnetic pressure causes the metal influenced by the field to melt. On melting, the resistivity in the metal increases, allowing the magnetic field to diffuse through the foil, melting or, if the magnetic field strength is high enough, vaporising the metal it encounters. If the flyer vaporises, the resulting metallic plasma will expand outward (ablate), generating shocks in the opposite direction through the flyer as a result of conservation of momentum, contributing to this magnetic pressure. Hall *et al.* noted that this 'ablation' of the flyer plate contributed up to 15% of the final flyer velocity. This ablation is likely what researchers at LLNL would have referred to as thermal pressure. Hall *et al.* even note their attempt to launch sapphire (dielectric) flyers, a load Osher *et al.* would have referred to as a 'composite' flyer. The electric gun is simply a thin flyer plate and the EM flyer plate is a thick electric gun foil. However, unlike the pulsed-power devices used at LLNL to drive their electric gun loads, the Z machine has the advantage of shaping the current pulse it discharges. By tuning current profile shape, researcher found they were able to influence the magnetic pressure profile to control the state of the metal flyer plates. In this section, the relationship between the pulsed power device configuration and the current pulse shape is considered, and the importance of this feature in the context of launching thick flyers is discussed.

2.5.2 Pulsed-power devices

Pulsed-power devices are machines which take low-power wall plug electrical energy and store it in a bank of capacitors, compressing in time to form a high power pulse. This energy can then be discharged to drive a variety of loads, from X-pinches to EM flyer plates [42]. The machines used to drive electric gun loads at LLNL were relatively simple pulsed-power generators, known as capacitor discharge units (**CDU**s). A CDU can be represented by an RLC circuit, illustrated in Figure 2.7, thus the subsequent current profile through time produced by the machine can be determined by solving the ordinary differential equation,

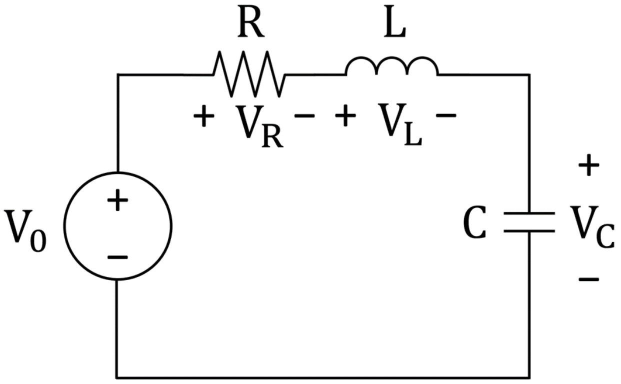

Figure 2.7: *M3* lumped circuit diagram.

$$R\frac{di}{dt} + L\frac{d^2i}{dt^2} + \frac{1}{C}I = 0, \tag{2.15a}$$

$$R = R_l + R_m, \tag{2.15b}$$

$$L = L_l + L_m, \tag{2.15c}$$

where R is the resistance and L is the inductance, while the subscript l and m refers to the load and the machine values respectively, and C is the machine capacitance. The solution to this equation is a sinusoidal current waveform. Generally, the load specific resistance and inductance are far smaller than those associated with the pulsed-power device. Consequently, the current rise-time (the time from current start to peak current) of a CDU tends to be fixed, varying little even when driving considerably different loads. As a result, a CDU is often designed to drive a specific kind of load; once built, the current rise time is fairly constant without considerable refurbishment efforts.

The circuit diagram of Machine 3 (**M3**), an example of a low impedance capacitor discharge pulsed power generator located at First Light Fusion, is shown in Figure 2.8. When charged to 200 kV, a total energy of 2.5 MJ is stored, with currents in excess of 14 MA and rise times of 2 µs are delivered to loads. M3 charges all capacitors in parallel, with half charged negatively and half positively. On triggering, the positively charged capacitors discharge in parallel through the load and into the negatively charged capacitors. With no crowbars, a switch or circuit used to short out a capacitor when it's delivering maximum current, the machine current will oscillate, and capacitors experience significant voltage reversal.

The voltage of a pulsed-power generator can be increased through the use of Marx capacitor bank modules. A Marx generator generates a high-voltage pulse by charging a large number of capacitors

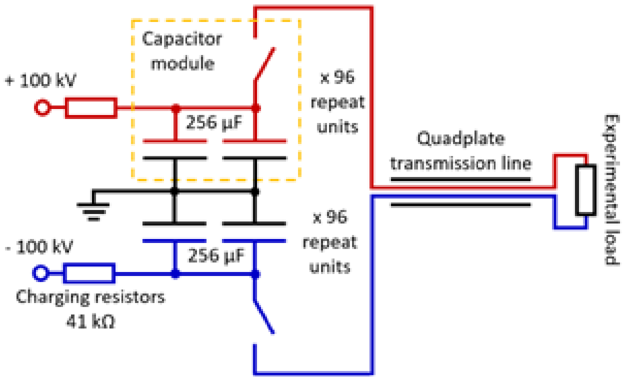

Figure 2.8: An RLC circuit diagram of M3, a 2.5 MJ CDU located at First Light Fusion [68]; relatively simple pulsed-power devices like M3 can be apprximated by RLC circuits. While more precise simulations of long transmission lines can be achieved using PSpice solvers [69], these solvers were not explored in this thesis.

in parallel, then suddenly connecting them in series. The Marx bank allows a pulsed-power device to store and discharge immense magnitudes of current, such as the 30 MA device *Atlas* [70]. In high energy configurations such as this, it is common to resistively damp the machine to limit capacitor voltage reversal and fault currents. This reduces the risk of switch damage by preventing excessive ringing of the capacitor charge through the spark gaps, extending the lifetime of the machine.

As discussed in Section 2.2, the pulsed-power machines used at LLNL were optimised to drive thin electric gun flyers by reducing the current rise-time to align with the foil 'burst'. However, this current profile was unsuitable for accelerating thick flyers, causing them to disintegrate during launch. With the machine current pulse profile largely fixed and no tools to model the states in the dielectric flyer, Osher *et al.* found their adaptations to the load were unsuccessful. With hindsight, we now know the Z machine's current pulse shaping capabilities was required to successfully accelerate the first thick flyers to over 10 km/s.

The refurbished Z machine (often referred to as simply **Z**) is one of the most powerful pulsed-power devices in the world. It is comprised of three main stages: the energy storage section, the pulse-forming section and the centre section. The energy storage section consists of a bank of capacitors in a Marx generator configuration. The pulse-forming section of Z includes 36 lines which combine to create a single current pulse shape in the central section. Each line uses a light triggered gas switch (**LTGS**), a switch triggered by a laser, which can control the discharge time by -60 ns to +650 ns by adjusting the pressure in sulfur hexafluoride gas. Decreasing this gas pressure reduces the breakdown voltage across the switch, resulting in a premature current discharge in the line. By coordinating the discharge of the 36 lines, current rise-times over a 1 μs range can be created. Other pulsed-power generators with pulse-forming sections include Thor [71], Zebra at the University of Reno [72], and MAGPIE at Imperial College London [73]. The ability to tailor the current rise-time allows these machines to efficiently drive a far wider range of loads. However, they require greater resources to build and their operation is more complex than a CDU. Ultimately, the configuration of a pulsed-power device is determined by the goals of the research platform it is built for.

2.5.3 EM flyer plates on the Z machine

Researchers investigating the acceleration of thick EM flyer plates using the Z machine had two tools available to them that scientists involved in the development of the electric gun did not: a pulsed-power generator with current pulse-forming lines and advanced multi-dimensional MHD codes. These were both utilised to design an EM flyer plate load which could be used to make precise EoS measurements over a range of thermodynamic states. This application necessitated certain conditions within the flyer. For instance, if the flyer is a known density on impact, the Rankine-Hugoniot jump conditions can be combined with continuity conditions at the surface to derive the density, pressure and internal energy in the target material. Additionally, a solid leading surface ensures a region of near-constant density across a minimum flyer thickness, resulting in the generation of quasi-equilibrated pressure states on impact. Consequently, the design objective for the EM flyer plate loads focused on reducing the state change in the plate.

The EM flyer plate is vulnerable to state change by shock formation and Joule heating during current discharge, processes which are challenging to characterise using *in-situ* measurements. Instead, the state of the flyer plate was studied using the finite element, arbitrary Lagranagian Eulerian (**ALE**), MHD code ALEGRA [74]. Initially, the results of one-dimensional simulations were compared against experimentally measured flyer velocity profiles. This analysis served to validate ALEGRA's predictions of violent events in the flyer plate, such as shock formation, Joule heating and reverberations. Lemke *et al.* reported an excellent match between numerically predicted and experimentally collected EM flyer plate flyer velocity profiles. When confident in their ability to model the system, ALEGRA was then employed to identify current pulse forms which could accelerate a flyer to generate the desired shock profile on impact, whilst maintaining a solid leading surface. By placing an emphasis on building numerical design tools and limiting experimental testing, scientists discovered methods of launching a diverse range of flyer plate thicknesses in a time and cost effective manner.

ALEGRA revealed new details about the state change mechanisms in the flyer plate, such as the progression of the melt front in the flyer in 1D. When a pulsed-power device discharges through the metal plate from the cathode to the anode, a magnetic field is created in the insulation below. Initially, this magnetic field cannot propagate beyond a few microns into the rear of the low resistivity metal flyer. However, as the strong magnetic pressure causes the metal carrying the current to heat up and melt, the resistivity in this region of the plate increases, and the magnetic field progresses a little further. This process results in the gradual diffusion of the magnetic field through the flyer plate, from back to front, melting the metal as it moves. Lemke *et al.* [1] found the velocity of this melt front (v_m) through an aluminium or copper flyer plate was directly proportional to the magnetic field strength (B), where,

$$v_m = 001276.0B + 596.0, \tag{2.16}$$

for B in Tesla and v_m in mm/µs. Equation 2.14 shows B is proportional to the magnitude of the current, thus, to ensure the front surface of the flyer plate remains solid, the current pulse length must be shorter then the time for the melt boundary to cross the flyer.

Shock formation is a non-isentropic phenomena that can cause a dramatic increase in temperature in a material as the front passes through. While Lemke *et al.* were specifically motivated to prevent shocks to avoid heating the flyer plate, shocks can be highly destructive in other ways. Shock formation in flyers can cause them to become damaged and (in extreme cases) completely disintegrate. Note, this mechanism also limits the maximum flyer thickness of other projectile launch systems, such as laser-driven flyers [75] and the modified gas gun created by Chhabildas *et al.* [44]. The precise control of the current rise-time, afforded by Z's numerous pulse-forming lines, allowed scientists to preclude shock formation by ensuring the current pulse was shaped to cause a compression in the flyer plate along the isentrope [1]. Lemke *et al.* suggested 'shock-up', the propagation of a shock front in the flyer plate, could be avoided if the flyer plate thickness was kept below the distance required for a shock to form (X_s), such that,

$$\mathrm{X}_s \leq \frac{t_r C_L(P_{min}) C_L(P_{max})}{C_L(P_{min}) - C_L(P_{max})}, \tag{2.17}$$

where t_r is the current rise-time, C_L is the material Lagrangian sound speed and P_{min} and P_{max} and the minimum and maximum pressure states in the plate flyer during launch respectively.

Another important requirement for making EoS measurements using projectile impact is ensuring the flyers are 'ballistic' (moving at at constant velocity) on impact. Again, the ability to shape the current pulse simplified the challenge, as the current magnitude could be rapidly decreased prior to impact, arresting the acceleration of the flyer.

While the current pulse shape on Z is more flexible than any alternative, it does have a minimum and maximum rise-time, which is fixed by the operating limits of the LTGS on each pulse-forming line [76]. Using the constraints that the leading flyer surface cannot melt due to Joule heating or shock up, Lemke *et al.* were able to derive the peak magnetic field which could be applied to the flyer for the longest and shortest rise-time of the machine. This analysis placed a maximum flyer plate velocity limit on Z of 72.6 km/s.

The development of the dynamic materials properties program's stripline geometry at Sandia National Laboratories is the result of extensive numerical and experimental investigations. It is feasible that a similar advancement of the electric gun could be obtained, if equivalent modelling capabilities and opportunities for experimental testing were available. Interesting questions which could be posed include:

1. What physics must a numerical model of the electric gun successfully replicate to be able to simulate the electric gun accurately?
2. What is the relationship between the dielectric flyer state and the current pulse shape?
3. What are the dominant destruction mechanisms which limit the successful acceleration of flyers on an electric gun?

2.5.4 Simplified modelling of EM flyer plates

Thus far, the EM flyer plate has been discussed only in terms of work performed on Z using ALEGRA at Sandia National Laboratory, an organisation with access to resources not available to most facilities. For example, ALEGRA is a highly sophisticated hydrocode with a comprehensive library of multi-physics, which many researchers investigating extreme states do not have access to. However, the EM flyer plate technique has another important advantage over the electric gun: it can be simulated using simplified models. One of the major limitations of simple 0D electric gun models, discussed in Section 2.3.2, was the inability to calculate the thermodynamic states of the dielectric flyer. By contrast, calculating the states in a metal flyer plate is more straightforward, as they can be calculated directly based on the magnitude of the current. Additionally, the EM flyer plate shares similar physics with other pulsed-power applications. As a result, models pioneered in these alternative fields can be adapted to describe the EM flyer plate, such as the Loughborough filamentary model [77]. The filamentary model treats the flyer plate as a number of small isolated filaments arranged in two-dimensions. Novac *et al.* found their adaptation to this model successfully simulated the 2D deformation of an EM flyer plate, without the need for a computationally expensive hydrocode [78]. It should be noted that the filamentary model cannot capture the behaviour of metals in a liquid or vapour state, thus is unsuitable for modelling high power EM flyer plates.

The reduced computational resources required to model the EM flyer plate, combined with the other positive aspects such as its repeatability and relatively low operational costs, resulted in the proliferation of EM flyer plate facilities [61, 79–82]. Consequently, a large body of modern research into the technique exists, in turn accelerating the advancement of the field. This conclusion underscores the importance of the relationship between the accessibility of a technique and its rate of advancement. Going forward in this thesis, consideration is therefore given not just on improving the electric gun load, but also the resources required to operate it.

2.5.5 Summary

It has been noted in this section that there are many similarities between the EM flyer plate and electric gun launch mechanisms. Important discoveries regarding the physics dominating the metal flyer plate are relevant to the electric gun, such as the progression of the melt surface through the foil. Furthermore, the systematic design process employed by EM flyer plate researchers to successfully extend the capabilities of the stripline geometry can be used to guide the development of the electric gun in this thesis. Considering the advantages of the EM flyer plate, two significant hurdles must be overcome to motivate the uptake of the electric gun launch mechanism:

1. The electric gun must be able to launch flyers with a near-constant density and velocity over a minimum flyer thickness to hypervelocity. Without this ability, the electric gun remains more limited in its applications than the EM plate flyer.

2. The electric gun requires a simplified model to simulate its operation. Without this, facilities without access to a sophisticated multi-physics hydrocode are unable to optimise an electric gun load for their pulsed-power generator.

2.6 Conclusions

In this literature review, the history and physics of projectile launch techniques were discussed. Projectile launch techniques generate uniform, quasi-equilibrated states, making them highly suitable tools for obtaining EoS measurements in high-energy density materials. The electric gun was created in the 1970s to access novel thermodynamic states using its high efficiencies and acceleration of flyers to over 10 km/s. However, the technique was beset by challenges. Initially, researchers did not have access to MHD numerical models, forcing them to rely on empirical trends to characterise the gun's behaviour. This experimental testing was laborious, as the gun had low repeatability in high current density configurations. However, the technique was rendered obsolete by its limitations in the maximum flyer thickness it could accelerate to hypervelocity. To accelerate flyers thicker than 0.5 mm without causing disintegration, the exploding foil width had to be significantly increased, limiting the final flyer velocity to around 4 km/s, which is significantly lower than the velocities accessible using a two-stage gas gun. Consequently, in the modern era, the electric gun is limited to use as a tool for investigating hypervelocity debris impact in the context aerospace shielding.

Subsequently, an alternative electromagnetic launch technique, the EM flyer plate, was investigated. The EM flyer plate has been extensively used at Sandia National Laboratories to investigate EoS measurements, generating quasi-equilibrated pressures that are both on the order of Mbar and yield high-precision measurements. This was achieved through sophisticated numerical modelling and current pulse shaping. Outside of Sandia National Laboratories, the EM flyer plate technique is used relatively frequently, as the technique has characteristics that make it accessible to a range of facilities. For example, accurate simplified modelling methods provide facilities with more limited computational resources the ability to design and optimise EM flyer plate loads. This thesis proposes to draw a comparison between the current state of advancement of the electric gun and the EM flyer plate, then replicate the approaches used to develop the EM flyer plate to improve the electric gun.

Chapter 3

Research goals

In the introduction (Chapter 1), four criteria were outlined which, if achieved, would propel the electric gun to a level of maturity comparable to other projectile launch techniques. The criteria were that the electric gun must:

1. Be able to be modelled and designed using accessible simulation tools.
2. Be explored numerically and experimentally to understand the dominant state change mechanisms in the flyer.
3. Be a system wherein the physics required to model the load operation are well understood.
4. Generate states in targets which can be used to investigate material properties.

Subsequently, the literature review in the previous section provided an overview of the current state of the electric gun, highlighting avenues of development that have been already investigated. Following this, the electromagnetic (**EM**) flyer plate was discussed, a projectile launch technique which shares many similarities with the electric gun. EM flyer plates are actively employed for investigating dynamic material properties [39, 43, 83], with the majority of their advancements taking place on the Z machine at Sandia National Laboratories [20, 42]. Contrasting the capabilities of the EM flyer plate with those of the electric gun, the criteria outlined above were refined into specific research objectives, which are detailed in this section.

3.1 Research goal 1: Develop simplified modelling tools

It is no coincidence that the gas gun is one of the most widespread projectile launchers: the technique is precise, requires comparatively lower resources to build and operate, and is relatively simple to model. This last feature allows researchers to design gas gun systems and simulate experiments using open source and commercially available codes, making the technique more accessible. However, the limitations in the maximum flyer velocity which can be attained with a gas gun constrain the pressure states it can access. Consequently, lasers and pulsed-power machines, such as the EM flyer plate, are required to accelerate flyers to over 10 km/s. These techniques have other drawbacks associated with them; for example, an advanced library of multi-physics models is required to accurately simulate the operating mechanism of an EM flyer plate in detail. Researchers investigating stripline geometries on the *Z* pulsed-power facility found they were able to closely replicate experimental results in simulations performed in ALEGRA by incorporating magneto-hydrodynamics (**MHD**), equations of state, and material strength effects [74]. ALEGRA is an advanced multi-material code with an extensive set of physics modelling capabilities to simulate the response of materials that are subject to large deformations and strong shocks. Its multi-physics library includes magnetics, MHD, electromechanics, and electromagnetic radiation in an arbitrary Lagrangian-Eulerian (**ALE**) reference frame [84]. A code with these capabilities is the product of decades of development; very few facilities have access to such sophisticated hydrocodes. To circumvent this challenge, researchers looking to use EM flyer plates have constructed simplified models, such as those developed by Novac *et al.* [78].

Similar simplified numerical models have been created to attempt to the model the electric gun. For instance, Osher *et al.* created a 0D model with the capability to predict the foil pressure states and flyer kinematics in electric gun loads tested at their facilities [25]. More recently, Wang *et al.* developed a 1D MHD hydrocode which incorporated improved equation of state in the exploding foil [14, 67]. However, both codes neglected the pressure state in the dielectric flyer, thus, were unable to capture the extreme state change which occurred in thick flyers [5, 15]. Without an understanding of the states in the flyer, in addition to the foil, the mechanisms for damage to thick flyers caused by these extreme state changes are poorly understood.

Complicating matters further, experimental optimisation cannot be relied upon to develop the electric gun; this route is resource intensive and has been shown to be ineffective. It was therefore made a key research goal to create a simplified model which fulfilled the following specifications:

1. The model must require low computational resources to run and be accessible to the scientific community.

2. The model must be able to predict the dynamics and state of both the foil and flyer.

3. The model must be proven through verification and validation to reliably capture trends across a wide range of the electric gun design space, i.e. for different geometries.

4. The model must be able to be used as a tool to guide the experimental design of electric gun loads in new parameter spaces.

3.2 Research goal 2: Explore the capability of the electric gun

The literature review detailed a number of projectile launch techniques. Projectile launchers are often favoured over alternative methods of generating extreme states for their ability to create uniform, quasi-equilibrated pressure states. Upon impacting a target with a flyer, a planar shock pulse is generated. If the flyer is of sufficient thickness and surface area, it can generate a constant pressure pulse for a long duration over a large volume of material. This permits the collection of diagnostic data over a relatively long duration, resulting in accurate measurements. Projectile acceleration mechanisms come with differing advantages, depending on the desired magnitude of pressure. Unlike rail guns or gas guns, the electric gun offers the opportunity to accelerate thin flyers to over 10 km/s [21]. However, the EM flyer plate, which is also driven by pulsed-power, has already been shown to be adept at this task. To motivate the uptake of the electric gun technique, this work therefore aimed to investigate its novel capabilities.

The predominant advantage of the electric gun resides in its efficiency in converting stored electrical energy to kinetic energy in the flyer (up to 25% efficient [57]). While the EM flyer plate depends primarily on the Lorentz force created by the current's return path to propel the flyer, the dielectric flyer in an electric gun load experiences considerable additional thermal pressures, exerted by the detonation of the foil. As a result, researchers have been able to use the electric gun to accelerate flyers up to 20 km/s using pulsed-power devices with relatively low energy storage capacity. However, without the ability to launch thick flyers, the benefit of these higher efficiencies cannot be made use of. The length of the pressure pulse generated in a target is proportional to the thickness of the flyer, thus the thin flyers launched by the electric gun result in low precision EoS measurements [3]. Consequently, at present, the electric gun's applications are restricted to impact testing of aerospace shielding [14, 15, 26]. If thicker flyers could be launched with the electric gun efficiencies reported in literature, the technique could offer a route to achieving novel pressure regimes on existing pulsed-power platforms.

Another novel aspect of this work was the access to M3, a 200 kV, 2 µs rise-time pulsed-power device. The majority of electric gun research conducted in the past used short rise-time pulsed-power devices with a maximum charge voltage of under 100 kV to drive the load. For a number of the years within which the electric gun was actively investigated at LLNL, researchers posited that the electric gun technique was most efficient when driven by the fastest current discharge possible. This theory was motivated by experimental observations made when launching thin flyers. At the time, researchers investigating the gun relied on optimisation through empirical observation due to a lack of access to modelling tools. However, work done by Osher *et al.* in the 1990s [5, 58] and in 2018 by Song *et al.* [15] saw a shift towards using longer rise-time machines to drive electric gun loads. In [5], while Osher *et al.* do not comment on the reasoning behind the increase in their current rise-time to 1.2 μs, they do report launching flyers up to 1.0 mm thick for the first time. Song *et al.* also used a longer rise-time device (1.8 - 2 μs) in [15], going a step further to suggest this long rise-time to be the reason behind their successful launch of a 1-mm-thick flyer to over 10 km/s. However, neither group provides a mechanism that explicitly explains the link between the machine rise-time and the flyer survival. Additionally, M3's higher energy storage offered the capability to explore new regions of the electric gun's operating space. These features of M3, combined with the simplified modelling techniques developed in Research Goal 1, provide a route to exploring the effect of the current rise-time and magnitude on the behaviour of the electric gun load.

Considering these opportunities, the following objectives were defined as part of this research goal:

1. Develop a repeatable diagnostic set-up to make measurements from an electric gun load.
2. Explore the effect of current-rise time on the behaviour of the electric gun using modelling and experimental testing.
3. Investigate the states of thick flyers accelerated by an electric gun load using modelling and experimental testing.
4. Understand the mechanism by which stored electrical energy is converted to kinetic energy in the flyer in an electric gun load and how the efficiency of this process can be improved.

3.3 Research goal 3: Investigate the impact of material strength effects on electric gun loads simulated in a hydrocode in two-dimensions

The work reviewed in Chapter 2 demonstrated that the electric gun was primarily investigated using experimental testing. The bulk of research on the launch technique predates 1990, when many of the advanced modelling tools currently available were yet to be developed. Consequently, empirical trends became the basis on which parameters such as foil thickness, flyer thickness, flight distance, and current rise time were optimised. In the modern era, the launch technique's infrequent use has resulted in limited detailed modelling of the system. A 1D MHD Lagrangian code was the most sophisticated model technique applied to the electric gun reported in open literature, wherein an equation of state was included in the foil, but not the flyer [63, 67]. While the literature review suggested this was a suitable approximation when simulating the behaviour of electric gun loads with thin flyers, thick flyers were shown to experience violent state changes during acceleration. This indicates that an equation of state in the flyer and a simulation in at least two dimensions is necessary to capture these effects in detail.

When reviewing the research into the EM flyer plate, it was stated that MHD, equations of state and material strength physics were required to replicate experimental testing of the load [74]. Given the similarities between the EM flyer plate and the electric gun load, it is reasonable to assume the same may be necessary to model the latter. Material strength is particularly relevant if it is deemed necessary in this work to attempt to accelerate solid flyers, as was specified for the EM flyer plate system by Lemke *et al.*. At the outset of this research, access to a hydrocode containing all the required multi-physics was unavailable. However, First Light Fusion's in-house hydrocode, **B2** (sometimes referred to as 'Code B' or 'B'), proved to be a close match.

B2 operates as a two-step Eulerian MHD solver, employing volume of fluid interface tracking and a second-order advection scheme. It was originally created to model the electromagnetic flyer plate as a tool for driving inertial confinement fusion reactions in First Light Fusion targets. Eulerian hydrocodes are typically used to simulate fluid flow and systems under rapid deformation, such as those subject to strong shocks, where material strength effects are often negligible [85]. Consequently, B2 lacked a material strength algorithm. This identified the need for the third research objective; implementing a robust material strength model in B2 to achieve the following objectives:

1. The strength model implemented in B2 must replicate the results of a 2D test case dominated by strength effects performed in a commercial code.
2. The strength model must be functional in two-dimensional electric gun simulations.
3. The effect of material strength on the behaviour of an electric gun load must be analysed.
4. Simulations with material strength in B2 must be used, alongside experimental results, to propose specific mechanisms by which electric gun flyers are being destroyed and methods of mitigating this damage.

3.4 Research goal 4: Understanding the electric gun load as a tool for the study of dynamic material properties

An existing tension in the requirements of all projectile launch techniques lies between achieving high flyer velocities while also maintaining flyer integrity. This challenge is particularly pronounced when using projectile impact to explore extreme states in materials, because the flyer must not only remain intact, but also maintain a region of near-constant density over a minimum thickness, leading to a sustained pressure pulse length on impact. This pulse length is crucial for extracting precise diagnostic data upon impact with a target. This requirement places strict limitations on the maximum attainable velocity of an acceleration technique. For instance, modified two-stage gas guns can destroy flyers accelerated to over around 9 km/s [44]. The rail gun melts both its rails and flyer over around 5 km/s. Laser-driven flyer acceleration grants access to higher velocities, but restricts flyer thickness to a few hundred microns at most. Pulsed-power driven electromagnetic flyer launch techniques offer a relatively low cost route to accelerating a range of flyer geometries over 50 km/s. However, achieving this while maintaining constant density and velocity in the flyer requires careful current pulse shaping and a high-energy pulsed-power device.

The literature reviewed in the previous section revealed that the electric gun could not achieve its intended purpose as a tool for investigating extreme EoS measurements [2]. Whilst issues with repeatability contributed to this outcome, the primary limitation was the gun's inability to launch flyers with near-constant density over a sufficient flyer thickness [3, 4]. At the outset of this work, overcoming this hurdle appeared to be the foremost challenge in advancing the electric gun. A comparison with stages of development of the EM flyer plate underscored the complexity of overcoming such a challenge; extensive study and design using a sophisticated multi-physics hydrocode, along with extensive experimental testing, were necessary to achieve near-constant flyer density and ballistic impact in the stripline geometry on the Z-machine [42, 74]. This thesis offers the first opportunity to apply equivalent numerical and experimental tools in parallel to the electric gun.

The final research goal of this thesis required combining the knowledge acquired from the previous three goals to develop an electric gun load for the study of dynamic material properties. The specific objectives defined within this goal are to:

1. Utilise the simplified model created as part of the research goal 1 to explore the electric gun design space.
2. Leverage the experimental techniques and understanding developed in completing research goal 2 to inform the design of the electric gun load and its diagnostic set-up.
3. Utilise the Eulerian hydrocode B2, including the material strength model derived in research goal 3, to understand the sensitivities within the load.
4. Test the electric gun load designed in this section and understand the key phenomena in the foil and flyer that prevent the generation of a continuous pressure pulse in a target on impact.

Chapter 4

Creating a simplified model of the electric gun

> All models are wrong but some are useful
>
> ---
>
> George Box

In this chapter, the development and performance of a zero-dimensional (0D) simplified model designed to achieve Research Goal 1 are detailed, including: the model's algorithm, covering aspects such as the RLC-circuit equations; the forces resulting in the foil-flyer momentum; and the pressure calculations within the exploding foil and at the foil-flyer interface. Despite its 0D nature, the model represents the foil and flyer with three distinct points, which are independently tracked and updated, enabling high-accuracy predictions of an electric gun with a thick flyer during early stages. Benchmarking against one-dimensional magnetohydrodynamic (1D MHD) simulations from the B2 hydrocode demonstrated that the 0D model closely aligns with B2's maximum flyer pressure and velocity results, while requiring significantly fewer computational resources and faster runtimes. The chapter assesses the model's success in meeting its objectives, emphasizing its low computational demands, accurate prediction capabilities, and reliability across various electric gun geometries.

4.1 Introduction

Simplified modelling techniques play a crucial role in magneto-hydrodynamic (MHD) simulations, offering notable advantages in understanding complex phenomena within plasma dynamics and electromagnetic interactions. By distilling intricate MHD systems into simplified representations, these models balance computational efficiency and accuracy, enabling researchers to explore critical parameters swiftly and effectively. Such streamlined approaches often involve approximations and reduced-order models, which capture the fundamental physics while minimizing computational resources. Despite their simplicity, these models provide valuable insights into the behavior of plasma under the influence of magnetic fields, shedding light on phenomena such as magnetic reconnection, plasma instabilities, and turbulence. Moreover, simplified MHD models serve as powerful tools for hypothesis testing, allowing researchers to explore various scenarios and assess the impact of different parameters on system behavior. While detailed MHD simulations remain essential for comprehensive analysis, simplified models serve as indispensable tools for preliminary investigations, guiding researchers more rapidly towards a deeper understanding.

This chapter contains the following paper:

- **A 0-D Electric Gun Model for the Optimization of Flyer Acceleration to Hypervelocities**

  M. D. Fitzgerald, J. D. Pecover, N. Petrinic and D. E. Eakins, "A 0-D Electric Gun Model for the Optimization of Flyer Acceleration to Hypervelocities," in IEEE Transactions on Plasma Science, vol. 51, no. 8, pp. 2347-2357, Aug. 2023, doi: 10.1109/TPS.2023.3300093

  The contributions of M. Fitzgerald include: conception of the 0D model, writing of the 0D model, 1D MHD simulation in B2, benchmarking testing, and writing and editing of the original draft. They do not include: contributions to the MHD hydrocode source code.

4.2 A 0-D Electric Gun Model for the Optimization of Flyer Acceleration to Hypervelocities

4.2.1 Abstract

The electric gun is a pulsed power projectile launcher which utilises the rapid expansion of an ohmically heated exploding foil and electromagnetic forces to accelerate thin flyers up to 20 km/s. Though the launcher has high energetic efficiencies when compared to alternative techniques, the process of launching flyers above 0.5 mm thickness in this manner often results in uncontrolled launch characteristics and premature failure of the flyer. This behavior is challenging to model numerically, limiting optimisation work to sophisticated and computationally intensive magneto-hydrodynamics (MHD) codes. This

work presents a 0D model designed to expedite the parametric optimisation process of electric gun loads to launch thick flyers to hypervelocities. The model is capable of predicting not only the foil state and flyer dynamics, but uses a novel approximation to predict the maximum pressure state in the flyer. The model is verified against 3D MHD Eulerian hydrocode 'Code 𝔹' and the validity of the approximations made in simplifying the model are discussed. With this model, the electric gun could be optimised to launch thicker flyers and achieve higher pressures and shock durations, enabling it to become a complimentary tool to existing projectile launch platforms.

4.2.2 Introduction

The conditions experienced by spacecraft, lunar habitats and fusion reactors, to name a few examples, are unlike any found naturally on the Earth's surface, reaching extreme pressures and temperatures during operation. Access to these conditions in a controlled setting enables the selection and design of resilient materials for these applications, which in turn relies upon advancement of techniques to generate ever more extreme material states. The electric gun is one such technique; a pulsed power launcher which utilises rapid discharge of a capacitor bank to accelerate a flyer to velocities up to 20 km/s. It is generally used in high pressure equation of state (EoS) research and hypervelocity ballistic testing. Much of the early activity on electric guns took place at Lawrence Livermore National Laboratory (LLNL), from 1976 to around 1990 [21, 24, 57]. More recently, the technique experienced a revival in laboratories in China [14, 15, 26].

The electric gun can be thought of as a hybrid between the exploding foil initiator (EFI), also known as a 'slapper', and the electromagnetic (EM) plate flyer launcher [16, 17]. Its projectile is driven by both a thermal explosion, as in an EFI, and the magnetic acceleration of the plate flyer. The process begins with the discharge of a high-speed capacitor bank across a thin metallic foil, resulting in a large amount of energy deposited in the foil through ohmic heating. This energy deposition drives a change in the foil state from solid to a rapidly expanding plasma. The foil plasma acts as a driver gas, accelerating an adjacent thin plate, referred to as the 'flyer'. The flyer plate is laid atop the foil in a bonded stiff assembly, such that the foil plasma 'punches out' a section of the flyer material, accelerating it typically for a few millimeters to impact a target. The plasma pressure component of the acceleration is known as the thermal drive. When large currents are discharged to vaporise the foil, considerable magnetic forces exist in the system that also act to accelerate the foil plasma. This effect is referred to as the magnetic drive.

The electric gun has demonstrated conversion from electrical capacitor bank discharge to projectile kinetic energy of up to around 15% [58]. The approach's high efficiencies emerge from its ability to convert energy from both the thermal explosion and the magnetic fields, inherent in the system, into kinetic energy in the flyer. The magnetic contribution to the acceleration allows far higher flyer velocities and impact pressures than can be achieved using an EFI, meanwhile, the addition of Joule heating to the work done accelerating the flyer gives the electric gun an energetic advantage over the EM plate flyer. Despite its higher efficiencies, the electric gun is not currently a viable alternative to the EM plate flyer due to constraints in the thickness of flyers it can successfully launch. Electric gun flyers thicker than 0.5 mm exhibit a violent change in state during launch and flight, often experiencing complete disintegration when using high energy capacitor banks [15]. The thin nature of the flyers launched induce strong but short duration shocks in targets, preventing the electric gun from investigating longer timescale phenomena and limiting its applications.

Adapting the design of the electric gun to launch thicker flyers relies upon better understanding of the mechanisms responsible for flyer breakup at larger thicknesses. *In-situ* collection of data regarding the operation of the electric gun during launch and flight prior to impact is challenging, time consuming and resource intensive. Instead, accurate modelling of the electric gun operating mechanism is a more efficient route to better understanding the interaction between the exploding foil plasma and flyer. Researchers initially struggled to numerically model the interplay between the thermal and magnetic components of acceleration in the electric gun, using simple empirical circuit models for the foil explosion [2] and the Gurney model to predict the final flyer velocity [21]. Though successful for smaller capacitor banks, these models failed to capture the behaviour of flyers launched above 10 km/s, where magnetic forces become significant. To account for this effect, Osher *et al.* adapted Lindemuth's computational model for exploding metallic switches to create a version of the 1D MHD code specific to the electric gun capable of modelling the dynamics and state of the exploding foil [57, 86]. However, the model does not consider the flyer state when calculating the flyer dynamics, making it only accurate when modelling launch of flyers under 0.5 mm thickness. Lack of consideration of the flyer state in Osher's model extends into other electric gun models, preventing simple models from being used to investigate the launch thicker of flyers [14, 67].

As simplified models for the electric gun have no means of calculating flyer state, parametric studies for numerical optimisation of the electric gun load rely upon sophisticated hydrocodes, able to model both magnetohydrodynamics and material equation of state in the foil and flyer. Not only is access to these codes limited, but the complexity of the electric gun and corresponding multiphysics requires expensive computational resource. When compared to well understood launch platforms such as gas guns, or EM launchers which can rely on established simplified modelling techniques for optimisation [78], it is understandable why the electric gun is not used more broadly. However, if a more accessible code capable of modelling the electric gun flyer state was made available, the projectile launcher could be more readily optimised to launch thick flyers on a range of pulsed power devices, enabling existing launch platforms to access the full potential of this research tool.

In this work, a model was developed for the purpose of understanding the pressure state in the flyer during launch and flight. Unlike previous 0D models used to investigate electromagnetic and thermal launch of projectiles, this model is capable of predicting states in both the foil and the flyer as well as the flyer dynamics, using a novel technique to approximate the pressure at the foil-flyer interface. This capability allows the user to perform large scale parameter scans which can consider maximum flyer pressure in minutes, as opposed to days in an MHD hydrocode with access to high performance computing. This both expedites the optimisation process of an electric gun set-up, and allows those without access to an advanced multiphysics hydrocode to design an electric gun for a specific pulsed power machine. Using the 0D model in parallel with a 3D MHD hydrocode to perform verification, this work investigates the following questions:

- Can modelling of the flyer state during electric gun operation be achieved based on prior understanding of phenomena in electromagnetic launchers?
- How does the interplay between electromagnetic, thermal and hydrodynamic behaviour influence the pressure states in the foil and flyer?
- Which effects in electric gun operation contribute most significantly to the flyer state?
- Over what range is the presented model valid, and why is this the case?

4.2.3 0D Model: Algorithm and physics

The electric gun model presented in this work represents the electric gun load as an RLC circuit to determine the current through the metal foil in the electric gun in 0-dimensions (0D). 0D simulation refers to a model where physical behavior is treated without spatial dependency but with time dependency, with the effect of reducing the computational complexity of the problem. Fig 4.1 presents the range of parameters for input geometries of the foil and flyer and machine parameters, which allow the model to calculate results for specific load designs.

The model algorithm can be broken into four sections. Firstly, the current is calculated in each timestep (Sec. 4.2.3). This is then used to find the change in the state in the foil, and update three positions in the electric gun system; the rear of the foil, the interface between the foil and flyer, the front of the flyer (Sec. 4.2.3). Next, using both the foil state and positions, a pressure gradient from the maximum pressure in the foil to the front of the flyer is established (Sec. 4.2.3). Finally, by using the position of the magnetic field along the z-axis to find the location of the maximum pressure in the foil, the pressure at the foil-flyer interface, assumed to be the maximum pressure in the flyer, is calculated (Sec. 4.2.3). This section will explore the details of the steps in the order of the algorithm, which is visualised in Fig. 4.2.

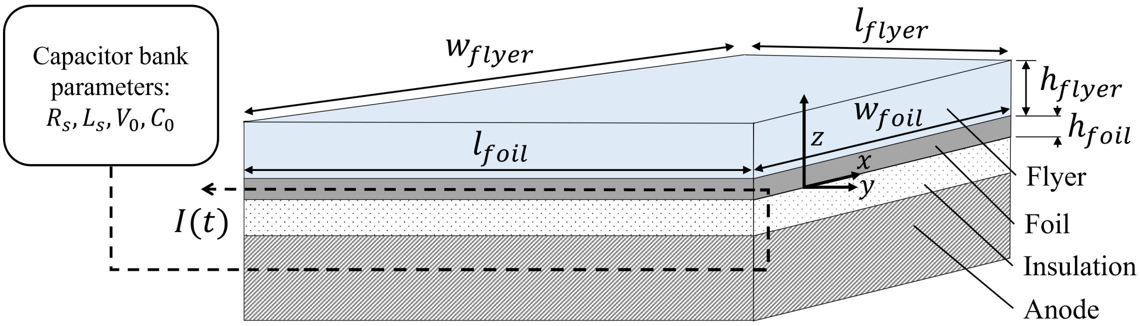

Figure 4.1: The 0D model allows the user to input detailed parameters regarding the foil, flyer and capacitor bank. These include the foil and flyer material and dimensions, and the capacitor bank parameters necessary for calculating the system current at each timestep.

Electric gun RLC circuit model

The electric gun load operates by discharging a large current produced by a pulsed power generator to a metallic foil. This circuit can be represented by the RLC circuit equations, which may be represented as,

$$\frac{dI}{dt} = \frac{1}{L(t)}\left[V(t) - I(t)\left(R(t) + \frac{dL}{dt}\right)\right] \tag{4.1a}$$

$$L = L_s + L_{foil} \tag{4.1b}$$

$$R = R_s + R_{foil} \tag{4.1c}$$

where I is the current, $V(t)$ is the voltage across the accelerator, L and R are the total system inductance and resistance, comprised of L_s and R_s, the fixed machine inductance and resistance, and L_{foil} and R_{foil}, the time dependent load inductance and resistance.

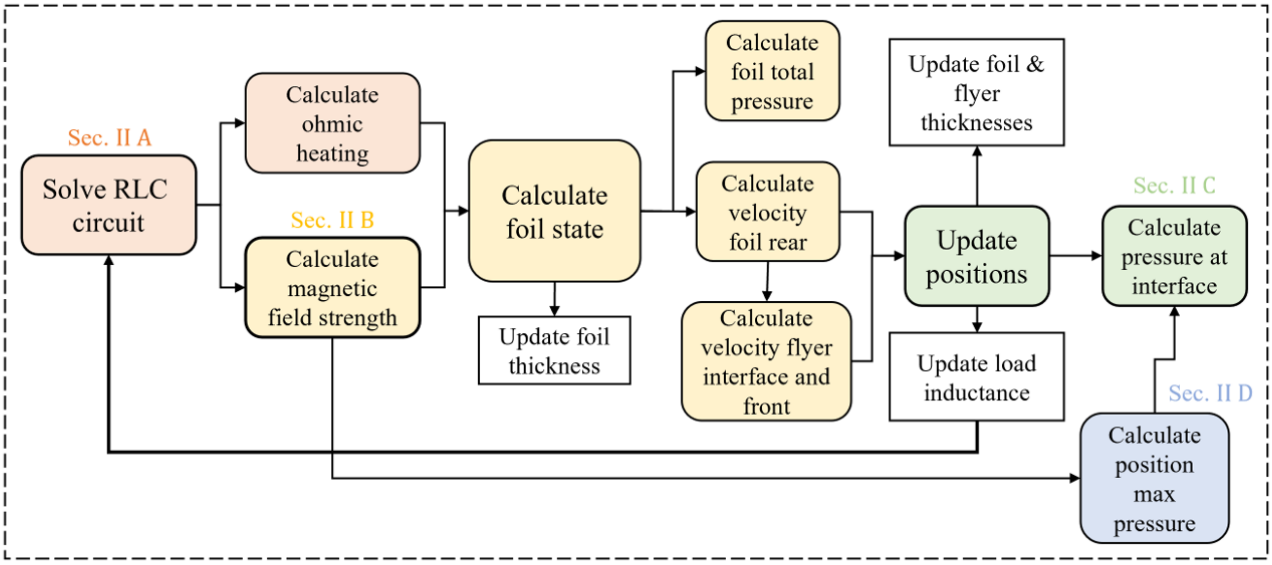

Figure 4.2: This flowchart demonstrates the model algorithm characterised as four stages *II A.* calculation of the current in the RLC circuit, *II B.* calculation of the foil state, *II C.* update positions and pressure gradient and *II D.* calculation of the pressure in the flyer. The flowchart also illustrates the dependencies of the calculated values on those upstream; clearly if the pressure in the flyer is to be calculated accurately, the foil state and projectile dynamics must be also.

The discharging circuit can be expressed as,

$$V(t) = -V_c = -\frac{Q(t)}{C(t)}, \tag{4.2}$$

where V_c is the charge voltage, $Q(t)$ is the capacitor bank charge, and $C(t)$ is the capacitance as the machine discharges. The circuit equation can be solved using the explicit Euler method by assuming a constant capacitance C_0, such that,

$$\frac{dV}{dt} = -\frac{I(t)}{C_0}. \tag{4.3}$$

The foil's inductance, and thus the current, are dependant on the conductor's flight position (z). The axes and origin for this problem is shown in Fig. 4.3. The model utilises an inductance equation developed by Novac *et al.* [78] specific to plate flyers, which states,

$$L_d(z) = \begin{cases} \frac{\mu_0 l_{foil}}{\pi} \ln\left(\frac{8x^2+w_{foil}^2}{2w_{foil}z}\right) & \text{for } z > 2w_{foil} \\ \frac{\mu_0 l_{foil}}{\frac{w_{foil}}{z}+1.21-0.11\frac{z}{w_{foil}}+\left(1-\frac{z}{2w_{foil}}\right)^6} & \text{otherwise} \end{cases} \tag{4.4}$$

where μ_0 is the vacuum permeability, l_{foil} is the foil length, w_{foil} is the foil width and z is the flight direction. The foil inductance in time is then found using the velocity, $v_z(t)$, at each timestep,

$$\frac{\partial L}{\partial t} = \frac{\partial z}{\partial t}\frac{\partial L}{\partial z} = v_z(t)\frac{\partial L}{\partial z}, \tag{4.5}$$

allowing the circuit to take both the position and velocity of the foil into account as time progresses.

The foil resistance may be approximated as,

$$R_{foil}(t) = \frac{l}{w}\eta(t), \tag{4.6}$$

where the resistivity $\eta(t)$ is calculated using the Burgess model [87], which is both temperature and state dependent. To calculate the change in temperature in the foil, the heating power Q_h can be calculated using,

$$Q_h = \int_0^t I(t)^2 R_{foil} dt, \tag{4.7}$$

with the subsequent temperature change in the foil approximated from solid state through to vapor using the change in energy in the foil,

$$E_1 = \Delta E_{heatsolid} = c_s M(T_m - T_0) \tag{4.8a}$$

$$E_2 = E_1 + \Delta E_m = E_1 + H_m M \tag{4.8b}$$

$$E_3 = E_2 + \Delta E_{heatliquid} = E_2 + c_L M(T_v - T_m) \tag{4.8c}$$

$$E_b = E_3 + \Delta E_v = E_3 + H_v M. \tag{4.8d}$$

Here, c_s refers to the solid heat capacity, M refers to the foil mass, T_m is the melting temperature of the foil, T_0 is the initial temperature of the foil, H_m is the heat of fusion, c_L is the liquid heat capacity, T_v is the boiling temperature and H_v is the heat of vaporisation.

R_{foil} is updated each timestep so the model can account for the complex change in resistivity as the foil transitions from solid to plasma.

Electromagnetic and thermal acceleration

The flyer in the electric gun is subject to forces due to both the electromagnetic field and the expanding foil plasma. The following approach to finding the accelerating force (F_z) was derived by Novac *et al.* [78]. To calculate the electromagnetic force applied to the flyer during circuit discharge, the foil is modelled as an infinitely thin plate, made from a group of straight elementary conductors all carrying the same current density $J = I/w$ across their width. The coordinate system and orientation of the foil and flyer are shown in Fig. 4.3. The magnetic field (B_x) generated at point (x_p, z_p) by an elementary conductor situated a distance x from the origin is,

$$\frac{dB_x}{dx} = \frac{d}{dx}\left(\frac{\mu_0 J}{2\pi r(x)}\right),$$

where,

$$r(x) = \sqrt{(x_p - x)^2 + z_p^2}. \tag{4.9}$$

By integrating the magnetic fields produced by all elementary conductors, the components of the total magnetic flux density produced in the foil are given by,

$$B_x(x_p, z_p) = \frac{\mu_0 I}{2\pi w_{foil}} \left[\tan^{-1}\left(\frac{x_p - w_{foil}}{z_p}\right) - \tan^{-1}\left(\frac{x_p}{z_p}\right) \right]. \tag{4.10}$$

In this model the magnetic field is approximated as being directly above the origin at all times, thus $x_p = 0$. The resulting perpendicular magnetic force F_z to B_x is then simplified to,

$$F_z = \frac{(2B_x)^2}{2\mu_0} l_{foil} w_{foil}. \tag{4.11}$$

In a typical electric gun model, the system dynamics are then calculated by adding the foil and flyer mass and determining the system momentum change. The resultant velocity of the foil and flyer are then used to update the foil's position. However, this does not account for the time for pressure information to be passed from the foil to the flyer. This approximation is valid for thin foils and flyers, as the timescales over which information propagation occurs can be assumed to be small when compared to the total flight time. However, the time necessary to communicate a change in velocity in the foil becomes significant where the foil or flyer is thick. This is particularly critical during launch, as the flyer is unable to move off until the first pressure wave has reached its leading surface.

To approximate the 1D delays in communication of pressure information in 0D, the foil and flyer are simplified in space to key locations along the z-axis. The model tracks three positions; the rear of the foil, interface between the foil and flyer and the front of the flyer, visualised in Fig. 4.3. Prior to launch, the velocity at the rear (v_{zr}) can be found using the total force driving the foil. This velocity state is then assumed to sweep through the foil in the z-direction at the relevant speed of sound, leading to an interface velocity (v_{zi}) found through,

$$v_{zi}(t) = v_{zr}\left(t - \frac{h_{foil}(t)}{c_{s,foil}}\right), \tag{4.12}$$

where $c_{s,foil}$ is the ambient speed of sound in the foil and $h_{foil}(t)$ is the updated foil thickness. As it lacks an equation of state in the flyer material, the model assumes the speed of sound in all materials to be constant, preventing the model from realising the effects of supersonic shock waves transiting through the flyer. This is an issue, as the foil typically accelerates to velocities higher than the flyer

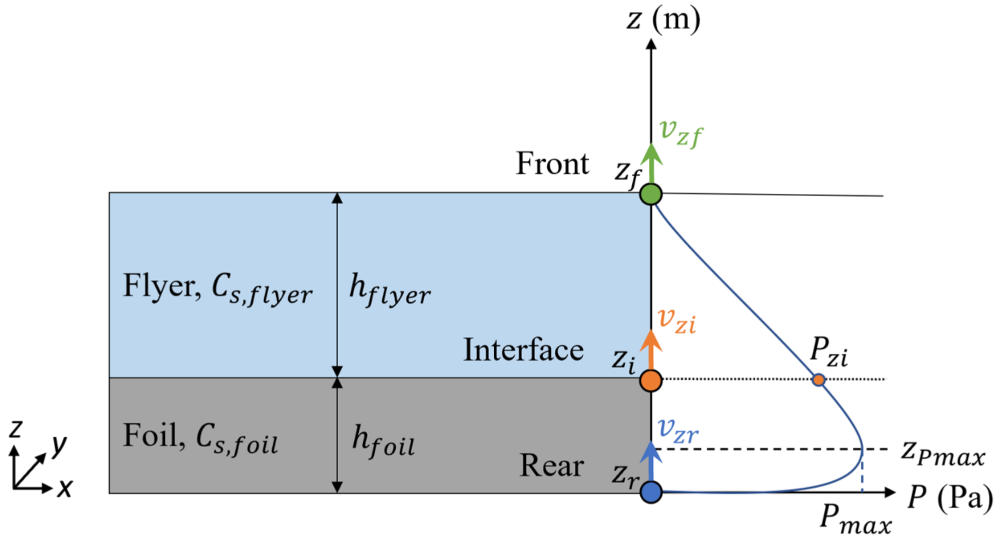

Figure 4.3: The positions of the four locations used determine the pressure at the foil-flyer interface, alongside the velocities used to approximate the foil-flyer dynamics. An example of a realistic plot of pressure in the foil and flyer is included. The model assumes the foil and flyer form a continuous interface, the pressure at the front of the flyer is zero and the pressure gradient between z_{Pmax} and z_f is linear.

sound speed within hundreds of nanoseconds, causing the interface position to overrun the flyer front in the model. To avoid this, the model updates the front velocity using either the speed of sound in the flyer or the interface velocity to approximate shock behaviour that may occur in the flyer using,

$$v_{zf}(t) = \begin{cases} v_{zr}\left(t - \left(\frac{h_{foil}(t)}{c_{s,foil}} + \frac{h_{flyer}(t)}{c_{s,flyer}}\right)\right) & v_{zi}(t) \leq c_{s,flyer} \\ v_{zr}\left(t - \left(\frac{h_{foil}(t)}{c_{s,foil}} + \frac{h_{flyer}(t)}{v_{zi}(t)}\right)\right) & v_{zi}(t) > c_{s,flyer}, \end{cases} \tag{4.13}$$

where $c_{s,flyer}$ is the speed of sound in the flyer, and $h_{flyer}(t)$ is the updated flyer thickness. The foil and flyer thicknesses are recalculated at the beginning of each timestep using the positions derived from the three location velocities at each timestep. This allows the model to capture the effect of compression and expansion in the foil and flyer on their dynamics.

Pressure calculation in the exploding foil

The maximum pressure and temperature (T) in the foil can be calculated directly using equations 4.7 and 4.11 to find the ohmic heating and the electromagnetic force when current I passes through the foil. The two most significant components of pressure in the foil will be those due to the electromagnetic force (F_z) and the thermal pressure (P_T). The electromagnetic pressure ($P_{B,max}$) is found using the maximum magnetic field strength (B, max),

$$B_{max} = \frac{\mu_0 I}{2w} \tag{4.14a}$$

$$P_{B,max} = \frac{B_{max}^2}{2\mu_0}. \tag{4.14b}$$

In this model, the temperature change (ΔT_B) in the foil due to $P_{B,max}$ is approximated using the ideal gas equation of state,

$$\Delta T_B = \frac{P_{B,max} v(t)}{N k_B}, \tag{4.15}$$

where $v(t)$ is the updated foil volume at that timestep based on $h_{foil}(t)$, N is the number of molecules and k_B is the Boltzmann constant. Previous electric gun models have found this simple equation of state to give good approximations of the foil behaviour, as the foil vaporises so early in operation [57]. The rise in temperature due to ohmic heating Q_h is then added to T_B to find the total $T(t)$. The change in total temperature ΔT in each time step is then used to find the change in the volume in the foil, with the thermal pressure P_T found using,

$$P_T = \frac{n R_0 T(t)}{V(t)}. \tag{4.16}$$

The model presented allows P_T to contribute to the system dynamics such that,

$$\frac{\partial p}{\partial t} = -\frac{P_T}{w_{flyer} l_{flyer}} + F_z, \tag{4.17}$$

where p is the combined foil and flyer momentum. Thus, when P_T is expansive it will lead to an increase in the system momentum.

Prior to launch, the foil is confined below the flyer and builds in thermal pressure, unable to expand freely whilst confined between the flyer and the insulation below, which the model assumes to act as a rigid surface. However, after the foil and flyer move away from the origin, the expansion behaviour becomes complex as compressive magnetic pressures and expansive thermal pressures influence different regions of the foil. To simplify this behaviour in the 0D model, the volume of the foil is assumed to expand until the front of the flyer moves. After this point, the foil will only expand further if the thermal pressure becomes higher than the magnetic pressure.

Pressure approximation at the flyer interface

Unlike the foil, the model has no direct method for calculating the pressure in the insulating flyer as it lacks an equation of state. To get around this, the model utilises three assumptions to estimate the pressure at the foil-flyer interface based on the maximum pressure (P_{max}) in the foil and the position of this maximum ($z_{P_{max}}$). Firstly, at early times in flight it is assumed there is a single pressure maximum in the foil, which decreases linearly to the pressure at the front of the flyer (P_{z_f}). Secondly, the pressure is assumed to be continuous across the foil-flyer interface. As a result, the gradient of the pressure can be found using,

$$\frac{dP}{dz} = \frac{P_{zf} - P_{max}}{z_i - z_{P_{max}} + h_{flyer}}. \tag{4.18}$$

Finally, when launch occurs in a vacuum, the model assumes P_f to be zero. Hence the pressure at the interface P_{z_i} is simply calculated using,

$$P_{zi} = P_{max} + \frac{dP}{dz}(z_i - z_{P_{max}}). \tag{4.19}$$

The gradient of the pressure is illustrated in Fig. 4.3. It can be understood qualitatively using this diagram that for the same P_{max} and relative z_{Pmax} in the foil, reducing the foil thickness or increasing the flyer thickness will increase the pressure at the flyer interface. These positions are recalculated for each timestep such that the pressure gradient in the model takes into account the changing foil and flyer thickness with regards to the moving position of maximum pressure in the foil, as illustrated in Fig. 4.4.

The question remains of how to predict the position of the maximum pressure $z_{P_{max}}$. At early times, the model assumes this will be the same as the position of the magnetic field maximum in the foil. This position can be deduced by understanding the thermodynamic phenomena driving state change in the foil. Initially, the current flows through the foil at the skin depth, generating a magnetic field within the metal. If the magnetic field is strong enough, the electromagnetic pressure causes the metal influenced by the field to melt. On melting, the resistivity in the metal increases, allowing the magnetic field to diffuse through the foil, melting the metal it encounters. Lemke *et al.* [1] referred to these two fronts as the magnetic diffusion front and the melt front and found the speed which this melt front will move through the metal is proportional to the magnetic field strength in the metal plate. Using an MHD hydrocode to simulate a number of experiments with input conditions from the Z accelerator, Lemke found the velocity of the melt line (v_m) in aluminium to be

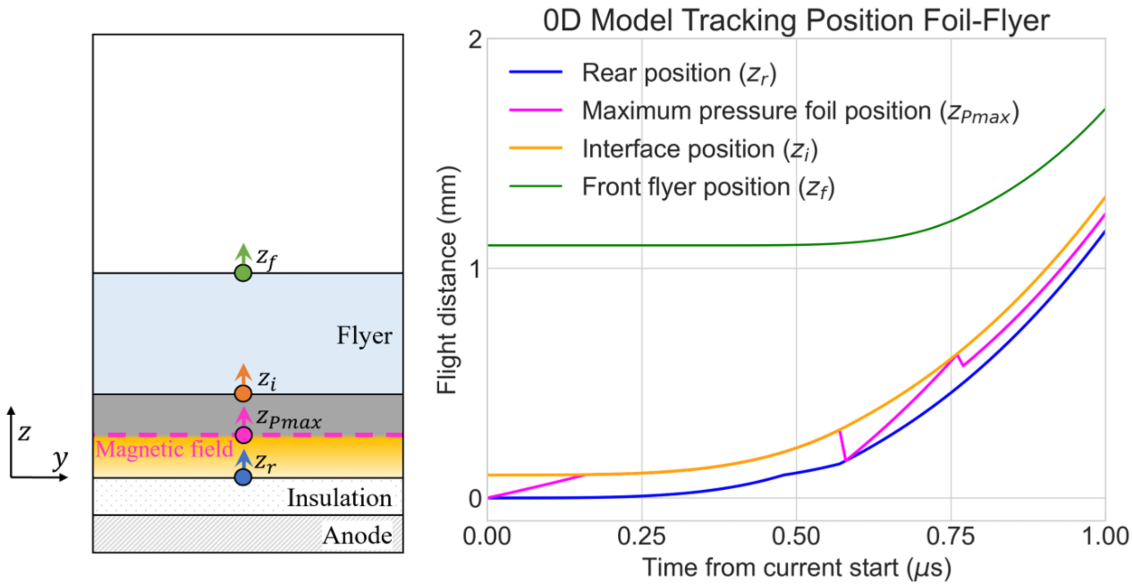

Figure 4.4: The four positions tracked by the model, alongside an example of their temporal evolution for the launch of a 0.1 mm thick foil and 1.0 mm thick flyer. The 0D model approximates the complex dynamic movement of the foil, flyer and position of maximum pressure in the foil by simplifying the system to four positions along the z-axis, allowing the model to calculate a more accurate interface pressure P_{zi} using Eq. 5.4 without need for 1D simulation.

$$v_m = 0.00127B + 0.596, \tag{4.20}$$

where B refers in this model to the maximum magnetic field strength in Tesla and $v_m$mm/μs [1]. The model therefore assumes $z_{P_{max}}$ can initially be calculated using the melt line position, illustrated in Fig. 4.4, completing the equation for the pressure gradient allowing P_i to be derived.

As the foil and flyer begin to move off, heated metal at the rear of the foil will expand to occupy the space left behind it. This forms a low density region of metallic plasma at the foil rear which is highly conductive, heating the material at the rear of the foil again and further increasing its resistance. When this occurs, the magnetic field will recede back to this region of higher resistance and cease to follow the material at the melt line. To capture this behaviour, the model uses foil temperature and foil positions to identify when the foil temperature exceeds melt and the foil has expanded above its original thickness and moved away from the origin. When this occurs, $z_{P_{max}}$ is switched from following the melt line to the rear of the foil. The location of the magnetic field maximum with regards to these hydrodynamic effects is illustrated in Fig 4.5. Once at the rear again, if the magnetic field continues to be strong enough to heat the foil, it will push forward into the metal once more.

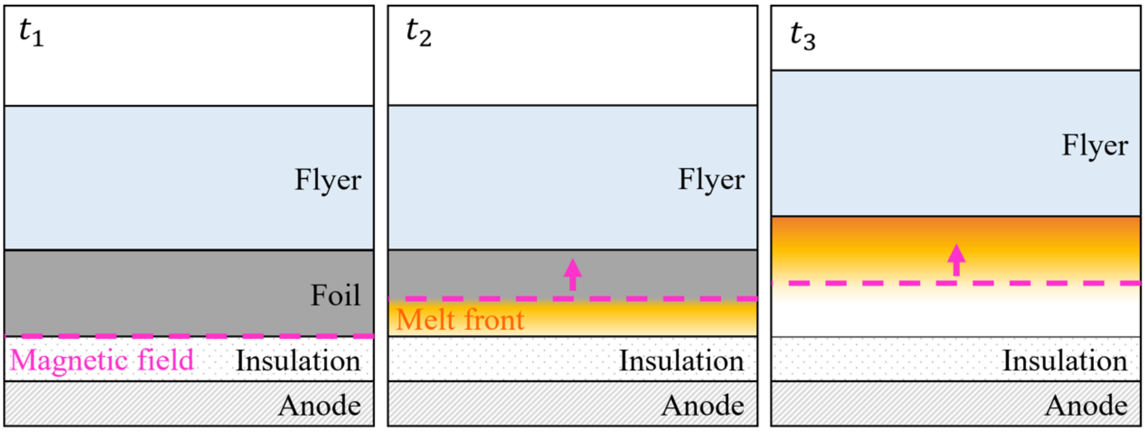

Figure 4.5: The position of the magnetic field through the foil starts at the rear of the foil when the current is first discharged (t_1). Ohmic heating and high magnetic field strengths cause the foil to melt, thus the current density accumulates in the lower resistivity region ahead of the 'melt line' (t_2). Finally, as the foil and flyer move away from the insulation, low resistivity foil plasma fills the expanding volume, and the current path returns to the rear of the foil. The high current density heats the adjacent foil material and increases its resistivity in this region, thus the magnetic field moves back to the foil rear and begin the process again (t_3).

In reality, if the foil is thin $z_{P_{max}}$ will quickly reach the front of the foil, strongly heating all the metal across the total thickness and causing a drop in density. If this is the case, the magnetic field is able to penetrate the entire foil thickness again as the heating at the rear progresses through the metal. However, in thick foils typically the melt line is still travelling through the foil when the flyer launches and the magnetic field returns to the foil rear. The material that has not interacted with the magnetic field will maintain higher density, and be more difficult for the magnetic field to penetrate on its second oscillation through the foil. To account for this, after moving $z_{P_{max}}$ to the rear, the model releases it to travel once more at v_m through the foil, but fixes the maximum position the magnetic field can reach on the second excursion to be the same as it reached on the first.

Thermal pressures will also act on the insulating flyer alongside the magnetic pressures. As this model represents the foil as a 0D object with a maximum temperature assigned to it, it has no knowledge of the temperature distribution throughout the foil. However, the maximum temperature will be the result of both P_b and Q_h, so it is assumed the thermal pressure position to be similar to P_{Bmax}. Hence, the model assumes $P_{max} = P_{Bmax} + P_T$ when calculating P_{z_i} when the foil is expanding. Otherwise, the maximum pressure is set as $P_{max} = P_{Bmax}$.

4.2.4 0D Model:Verification testing against MHD hydrocode

The 0D model presented in the previous section utilises both electromagnetic effects and hydrodynamic behaviour in the foil to calculate the flyer dynamics and state. This novel approach of calculating the pressure at the flyer interface using the position of the maximum pressure in the foil and varying foil and flyer thickness requires verification. If the model presented is to be used for design optimisation in lieu of a more complex MHD hydrocode, it must produce similar trends and results as the hydrocode in a parameter space of interest.

The hydrocode selected for this task was Code 𝔹, referred to simply as 𝔹 [88]. 𝔹 is an in-house 3D Eulerian MHD hydrocode developed by First Light Fusion, with volume of fluid interface tracking, utilising a Lagrangian-remap hydrodynamics scheme, generic plasma EoS and transport coefficients. 𝔹 uses the Frankfurt equation of state (FEOS), a semi-analytical tabulated EoS based on the well known QEOS model [89]. The FEOS was created for high energy density matter regimes. Its ability to better capture liquid–vapor two-phase region using an iterative Maxwell construction scheme makes it suitable for modelling the complex state change in the foil during electric gun launch and flight. 𝔹 has been validated for electromagnetic launch on a number of pulsed power loading platforms, and has undergone verification against similar codes such as Gorgon, the Eulerian resistive MHD code developed by Chittenden *et al.* at Imperial College London [90].

Method: Simulation configuration and capacitor bank

𝔹 has been used extensively to model EM projectile launch on pulsed power platform M3, a 2.5 MJ, 200 kV pulsed power machine at First Light Fusion's facilities [68]. M3 offers a significant research opportunity in the electric gun field, as it would be the highest energy capacitor bank used to power an electric gun in open literature, with a long rise time of around 2 μs. However, previous attempts to experimentally optimise an electric gun for M3 led to flyer failure prior to impact. The flyer failure occurred largely in the early stages of launch, prior to flyer movement. The failure was characterised by high velocity foil plasma breaking through the flyer, indicating a loss of flyer integrity. The load design for these experiments is shown in Fig 5.1. This disassembly of the flyer on launch is reflected throughout literature on electric guns [5]. The verification of the model presented focuses on electric gun loads on M3, as the machine is known to induce destructive conditions in flyers. If the model is able to accurately capture these states, it can therefore be used to design a set-up which avoids them. The details of M3 machine parameters used in this work are listed in Table 7.1.

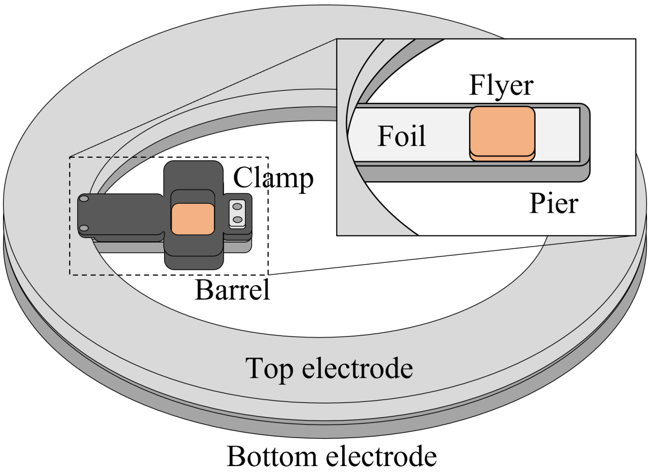

Figure 4.6: Simplified diagram showing the electric gun load set-up on M3. The close up shows the flyer atop the foil over the pier, with the barrel hidden from view. The current passes from the pier on the bottom electrode through the foil to the top electrode.

Table 4.1: Machine parameters for pulsed power capacitor bank M3.

Machine Parameters	Value	[units]
Charge voltage	140	[kV]
Capacitance	124.8	[μF]
Fixed resistance	0.1	[$\mu\Omega$]
Fixed inductance	12.5	[μH]

The verification tests presented include a detailed comparison of an individual electric gun case in the model and $\mathbb{B}$. The detailed comparison was used to evaluate how the accuracy of different variables impacted the final the flyer pressure calculation. In addition, a wide-scale parameter scan was performed in both the model and $\mathbb{B}$ to understand the extent of the model's reliability and probe the validity of the assumptions made in the algorithm. The values used in the model in these cases are included in the Appendix.

Results: Detailed testcase

The detailed testcase presented was selected to demonstrate the typical launch behaviour in an electric gun that the model simulates. It is a $24 \times 24 \times 0.2$ mm aluminium foil driving a $24 \times 24 \times 1.0$ mm PMMA flyer using M3 as the pulsed power driver. The results from the model are presented alongside those from $\mathbb{B}$ to provide a direct comparison. The pressure in the flyer is a function of the foil state and dynamics. Therefore, the model must correctly estimate the magnitude and temporal features of key variables upstream in the algorithm.

The magnetic field strength and foil temperature drive a number of key calculations and ultimately determine the change in momentum in the system. Fig. 4.7 demonstrates the magentic field strength and maximum foil temperature are comparable to results from the 1D simulation in $\mathbb{B}$, giving rise to a close match in the velocity profile of the interface position v_{zi}.

The three variables presented in Fig. 4.7 are then used to calculate the position of the maximum pressure in the foil relative to the flyer interface. The model finds good agreement with $\mathbb{B}$ on the position of maximum pressure within the foil during the first excursion though tends to be slightly delayed during the second. For the case shown in Fig. 4.8, the position of maximum pressure arrived at the foil-flyer interface around 0.2 μs later than in the 1D $\mathbb{B}$ simulation. Otherwise, the position of the interface and rear of the foil are in the model match $\mathbb{B}$ well, showing that it is able to capture compression and expansion behaviour in the foil at similar times to $\mathbb{B}$ despite being 0D.

The impact of the delay within the foil shown in Fig. 4.8 on the temporal evolution of the pressure generated in the flyer is apparent in Fig. 4.9, as the second pressure peak is delayed again by 0.2 μs, whereas the magnitude and temporal evolution of the first pressure peak produced by the model matched $\mathbb{B}$ very closely. These results suggests the model becomes less accurate at predicting the maximum pressure in the flyer at later times in flight. The error in the calculation of magnetic field strength qualitatively observed in Fig. 4.7 can be seen in the estimated pressure at the flyer interface in Fig 4.9.

These results indicate the pressure in the flyer is most strongly dependent on the position and magnitude of the maximum pressure in the foil with regards to the foil-flyer interface. In the next section the 0D model is exercised over a wide range of initial conditions to further demonstrate its ability to capture salient behaviours in the electric gun launch mechanism.

Results: Extended parameter scan

To be able to use the 0D model for wide scale investigation of the electric gun parameter space, the limits of its accuracy must be understood. To achieve this, a large sample of simulations were run in 1D in $\mathbb{B}$ and in the 0D model, across a range of aluminium foil thicknesses, PMMA flyer thicknesses and current densities. The maximum pressure was extracted for each geometry on flyer launch, which was chosen to be the moment the front of the flyer moved in either code. This was a rigorous test of the 0D model as the value of the pressure on launch relies on both the pressure

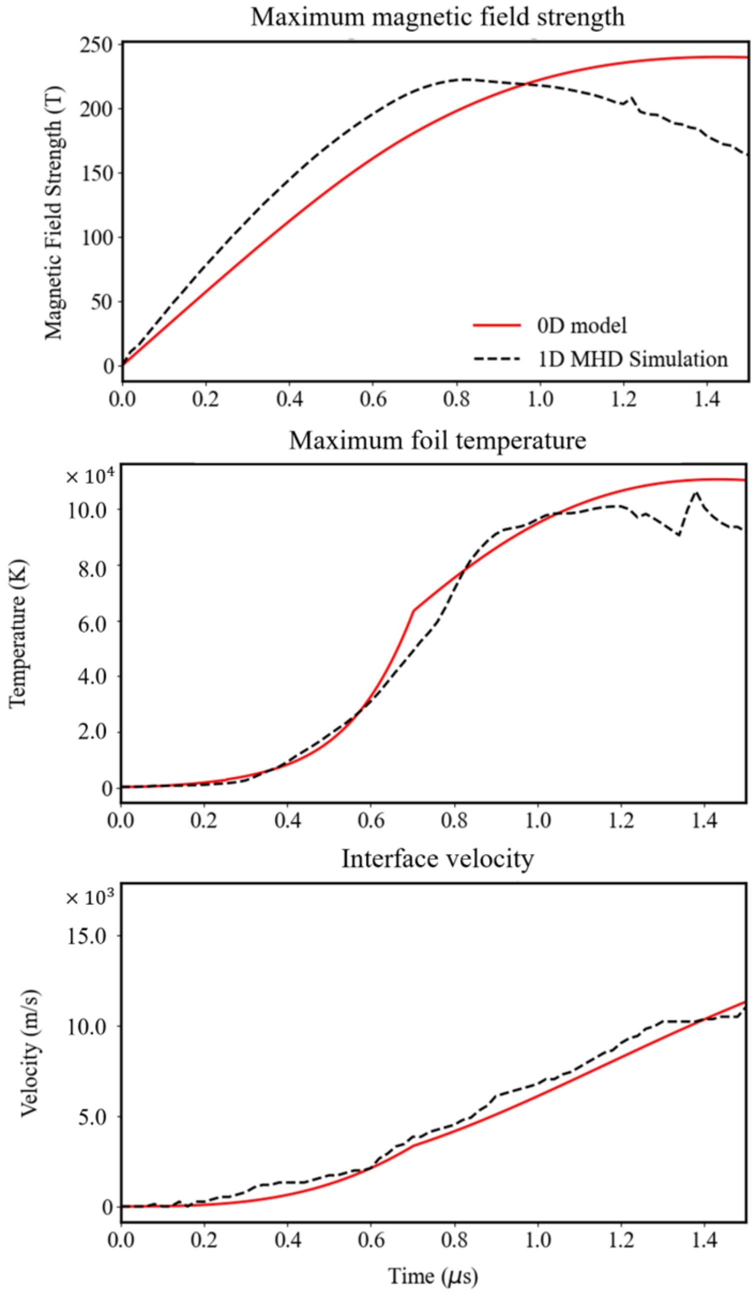

Figure 4.7: Plots showing the results from the 0D model and the 1D simulation in $\mathbb{B}$. Despite the differences in the magnetic field strength, the foil temperature and interface velocity predicted by the model are similar to those calculated by $\mathbb{B}$.

profile and launch time. The results of this parameter scan therefore assess how well the 0D model approximates EoS and spatial effects in 1D MHD simulations.

The 0D model captured overall trends in how the maximum flyer pressure on launch changed across all three parameters tested. Fig. 4.10 shows the highest flyer pressure on launch occurred in the electric gun load with the smallest surface area, thinnest foil, and thickest flyer. The pressures

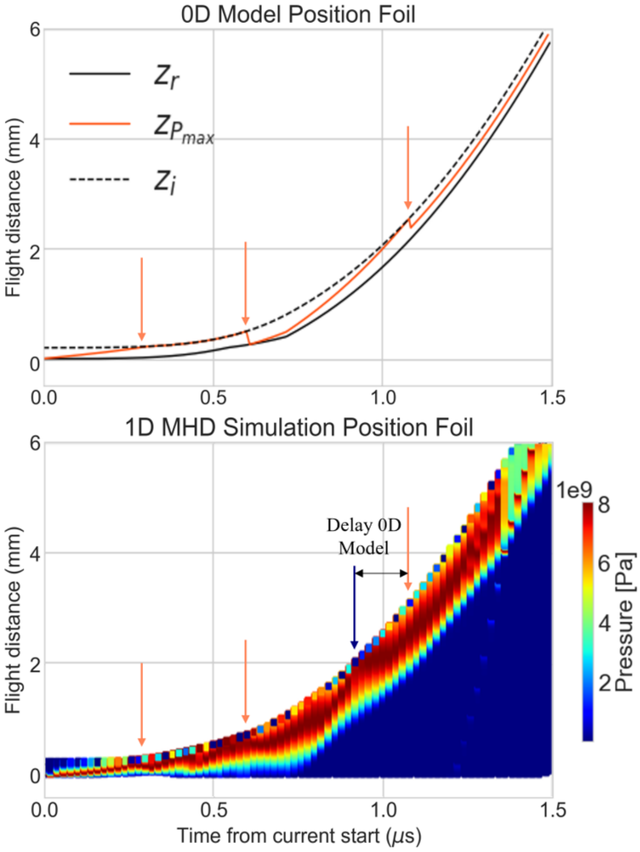

Figure 4.8: Comparison of the positions of the rear position (z_r), the interface position (z_i) and the position of maximum pressure (z_{Pmax}) in the 0D model and $\mathbb{B}$ over time. At each time step, the position of the foil is plotted, with the 1D foil material in $\mathbb{B}$ coloured by pressure to highlight the maximum pressure and rear position. z_{Pmax} reaches the interface at 0.35 μs and falls back to the rear surface at 0.6 μs in both the model and the $\mathbb{B}$ simulation, however the second excursion arrives at the interface 0.2 μs later in the 0D model (marked by the orange arrow in the 0D model and the blue arrow in $\mathbb{B}$).

in the flyers on launch reduce by roughly the same factor of increase in the surface area in both the model and $\mathbb{B}$. Secondly, both codes predicted increasing the flyer thickness led to a greater increase in the flyer pressure than decreasing the foil thickness. Thirdly, both models found the flyer pressure rapidly increased in thick flyers when the foil thickness dropped below around 0.5 mm thickness. This suggests the spike in pressure in electric gun loads with thin foils and thick flyers in this region is due to building thermal pressures in the foil before the flyer moves off. Launch is delayed using thicker flyers, as the initial pressure wave must travel further to reach the front of the flyer, causing the thermal pressure to increase in the trapped vaporised foil until its volume is able to expand as the flyer moves off. It is the 0D model's ability to track the flyer interface and front as separate points with different velocities that enables it to capture this effect.

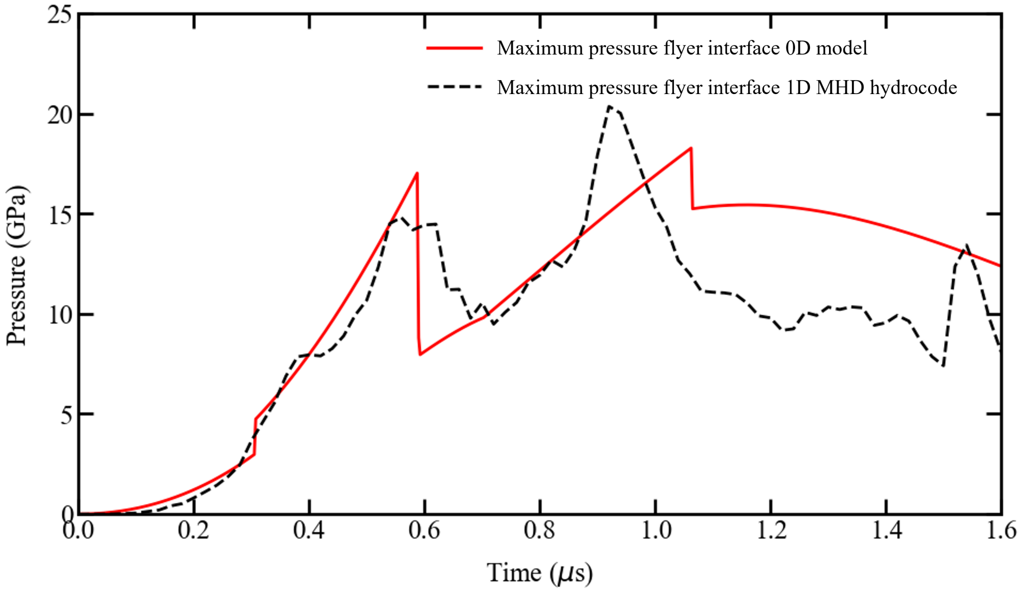

Figure 4.9: Comparison between the maximum flyer pressure in the 0D model and 𝔹. The pressures predicted by the model matches 𝔹 more closely at earlier times in flight, though remain within a factor of 1.5 of the pressures in 𝔹.

The difference in the maximum flyer pressure on launch predicted by the 0D model and B2 is compared in Fig. 4.11. The model closely replicates 𝔹 where the pressure contours overlap. Over all three current densities, the pressure estimation of the 0D model is best when the foil is thin. Across all three surface areas, flyers driven by thin foils show good agreement with 𝔹 across the range of flyer thicknesses. By analysing the pressure contours across the parameter space investigated, it can be deduced the maximum discrepancy between the codes is roughly a factor of 2.5.

Results from the parameter scan demonstrate the model correctly identifies non-linear trends in the maximum pressure on launch across a range of current densities. It is able to predict the spike in the flyer pressures prior to launch in electric gun loads with thin foil and flyers above around 3.0 mm. The model is able to replicate these more complex trends due to the novel features implemented which allow it to track the flyer positions and pressure gradient. The 0D model replicates the 1D MHD simulations best for setups with thin foils. Discrepancy with 𝔹 increases to a maximum in geometries with the highest surface area and thickest foil.

Discussion: Assessment of assumptions in the 0D model across parameter space

The results shown in the previous section present data from both 1D MHD simulations in hydrocode 𝔹 alongside those from the 0D model. The detailed testcase illustrated the accuracy of key variables

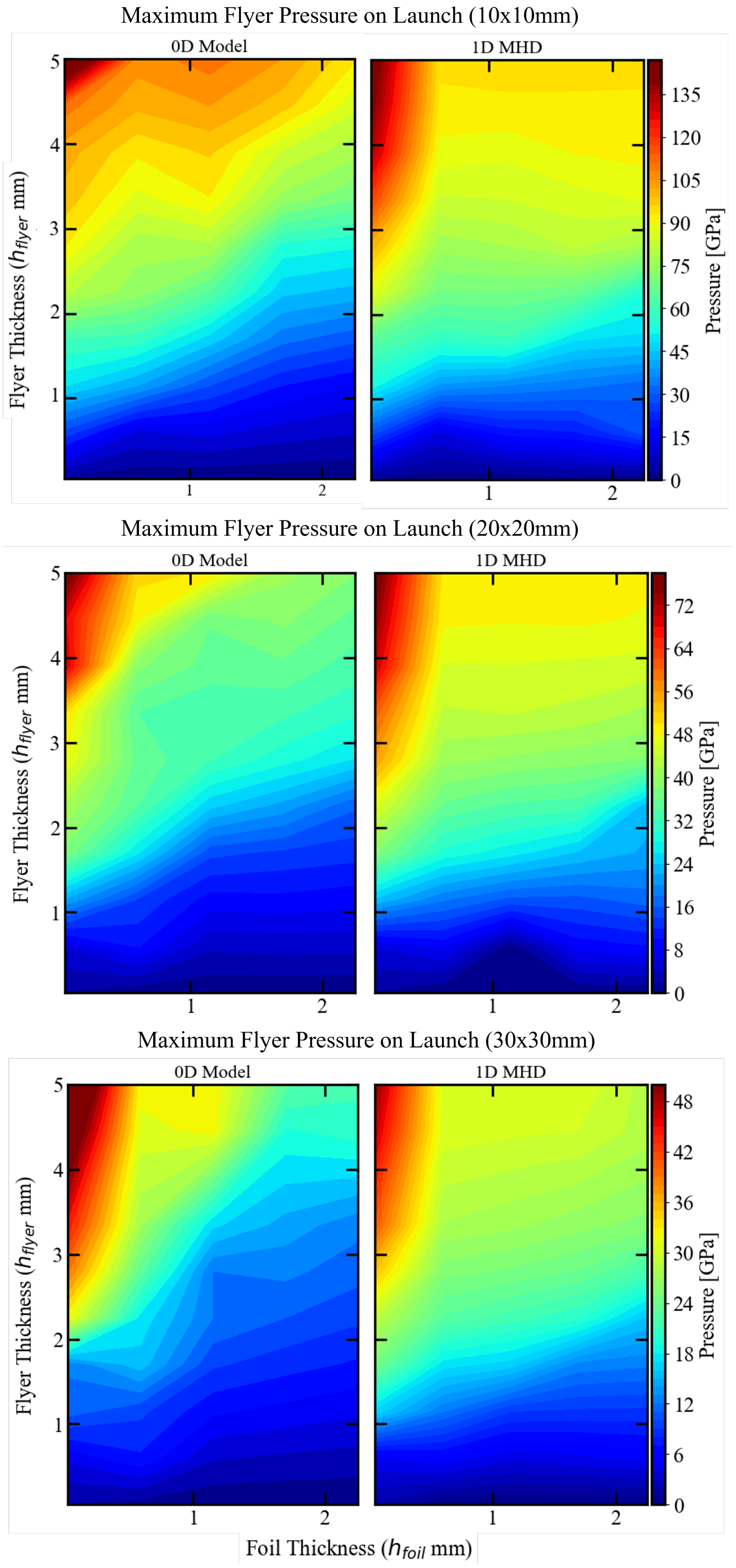

Figure 4.10: Heatmap of maximum flyer pressure on launch across a range of foil and flyer thicknesses, with varying surface area.

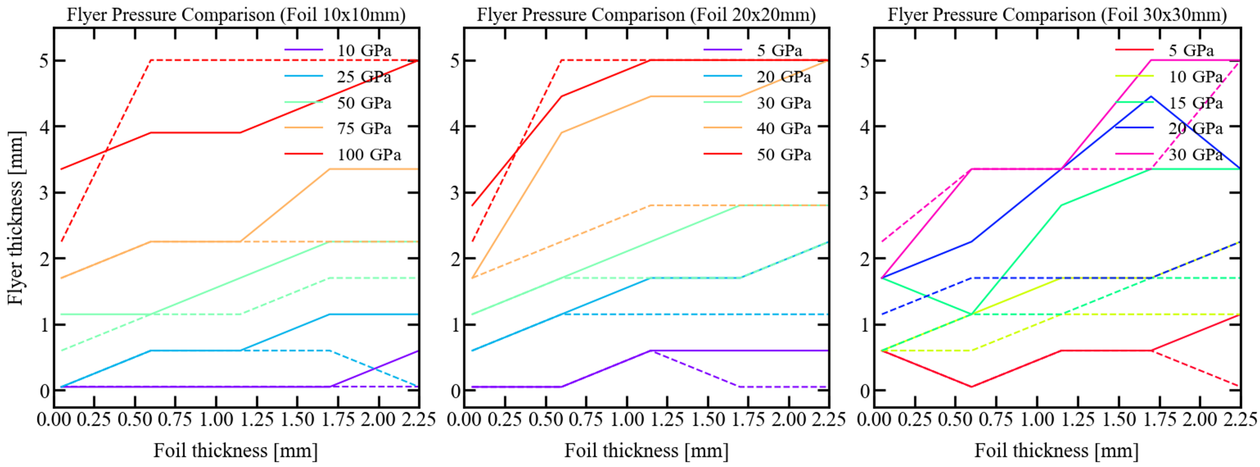

Figure 4.11: Contour plots comparing the maximum flyer pressure on launch for varying foil and flyer thicknesses for different foil surface areas in 1D MHD 𝔹 simulations **(dotted line)** and the 0D model **(solid line)**. The contours across all foil surface areas show the model underestimates the pressure in thicker flyers, with the error increasing to a factor of around 2.5 in the loads with surface area of 30×30 mm and thick foils.

in the model algorithm, whilst the parameter scan provided a broader picture of the model's ability to match the 1D MHD simulations across a range of electric gun geometries. The results also highlighted the time periods across which the 0D model most closely matched 𝔹. These are due to some of the approximations made in the algorithm to simplify the problem.

Firstly, the analysis of the detailed test case demonstrated the model is capable of capturing the temporal variations in the maximum pressure in the flyer throughout flight. Fig. 4.9 demonstrated the flyer experiences two distinct pressure maxima, which align with the movement of the position of maximum pressure within the foil shown in Fig. 4.8. This supports the 0D model's assumptions that the maximum pressure in the foil will be located in the region of lowest resistivity, which in turn moves according to the melt front and position of the foil. Additionally, the accuracy in the flyer pressure predictions suggest the treatment of the foil-flyer interface as a continuous interface, across which the pressure gradient varies linearly, is also valid. The detailed testcase illustrated both these elements of the model match 𝔹 more closely earlier in the current rise time. This is to be expected, as the equation for the melt line velocity developed by Lemke *et al.* was derived for the first current density excursion through the foil, not the second. Complex phenomena such as secondary shocks in the exploding foil plasma, which the 0D model cannot capture, also contribute to late time variation in the pressure in the flyer. However, even at these late times the 0D model continues to match 𝔹's maximum pressure within a factor of around 1.5, suggesting the most important elements of the physics are still being captured.

The parameter scan results indicated the model is able to replicate trends in flyer pressure on launch across the parameter space investigated. The model most closely predicted the magnitudes of the pressure for geometries with thin foils, across the range of flyer thicknesses tested. This supports the conclusions drawn from the detailed testcase that the model is more accurate at earlier times, as launch occurs more rapidly in cases with thin foils. The scan showed the flyer pressure is highest in cases with thin foils and thick flyers, therefore these load geometries are likely to be most at risk of flyer failure. This indicates the model matches $\mathbb{B}$ best in the most critical regions of the parameter space, making it a powerful design tool for electric gun set-ups accelerating thick flyers.

Overall, the results from the verification study suggest the 0D model is reliable over a wide region of the geometric parameter space, but importantly, is most accurate for critical time periods and load parameters. Experimental results have implied thick flyers are most likely to fail at early flight times, which is when the approximations made by the model are most valid [5]. This implies the physics chosen to be included in the algorithm is appropriate for the task of optimising an electric gun set-up for a range of flyer thicknesses and geometries.

4.2.5 Conclusion

In this work, the model presented is capable of predicting not only the dynamics of a flyer launched by an electric gun, but also the maximum pressure states in the flyer throughout flight. The results from the model were verified against 1D MHD simulations in the First Light Fusion in-house hydrocode Code $\mathbb{B}$. Comparison between the codes using both a detailed testcase and wide ranging parameter scan revealed the physics and assumptions governing the model were most accurate at early current rise times, in flyers launched by thin foils. It was concluded:

- The flyer pressure can be calculated in the model without need for an EoS, based on previous understanding of the movement of the melt line in the foil. By approximating the position of maximum current density in the foil, thereby locating the position of the maximum pressure for calculation of a pressure gradient across the foil-flyer interface, the model is able to reduce the required computational resource.

- Both the magnetic field strength and the position of the foil were found to determine the position of the maximum pressure in the foil. The thermal pressure in the foil was only found to act on the flyer when the foil was expanding, whereas the magnetic pressure in the foil contributed to the pressure gradient at all times.

- The verification parameter scan showed the pressure in the flyer on launch was most sensitive to flyer thickness in loads with thin foils. Before launch the foil volume is constrained, driving higher thermal pressures in the foil until it is able to move off as the current continues to rise. As thicker flyers delay launch, the building pressures in the foil vapor drive a rapid spike in maximum pressure at the foil-flyer interface.

- The model presented is most accurate at earlier times in flight, as this is when the approximations made in the algorithm such as constant sound speed and pressure location based on the melt line velocity are most accurate.

Validation performed comparing the model against experimental results collected from a range of electric gun loads will be presented in a forthcoming paper [15, 57, 63]. This dataset will include pulsed power devices with differing rise times and energetic capacities to understand the effect of the current profile on the model behaviour. In future work, the model will be used to redesign an electric gun load for the 2.5 MJ capacitor bank M3, based on the maximum flyer pressure states calculated for a successful electric gun shot on another smaller pulsed power machine, CEPAGE [81]. Using the states in the flyer on CEPAGE as a guide, the geometries of the foil and flyer which generate this pressure in a flyer on M3 will be determined. The design will then be experimentally tested on M3 in order to investigate the effect of long rise times on flyer state late in flight.

4.2.6 Appendix: 0D model material constants

4.3 Summary

The details and performance of the 0D simplified model created to fulfil the objectives of Research Goal 1 were presented in this chapter using the paper written as part of this thesis for the IEEE Transactions on Plasma Science. Within it, the model algorithm is explored, including: the RLC-circuit equations, the calculation of the components of force contributing the foil-flyer momentum, the calculation of pressure in the exploding foil and the calculation of pressure at foil-flyer interface. Though the model is technically 0D, the foil and flyer were represented by three separate points which the model tracked and updated independently. This formulation of the system facilitated the prediction of the behaviour of an electric gun with a thick flyer to a high accuracy at early times, when compared to 1D MHD simulation results from B2. Verification across a wide range of the electric gun geometric parameter

Table 4.2: Material specific values for aluminium and PMMA used in 0D model results [67].

Constant	PMMA	Aluminium	[Units]
Density	1170	2700	$\mathrm{kg\,m^{-3}}$
Sound speed	2757	6320	$\mathrm{m\,s^{-1}}$
Atomic weight (u)	-	26.98	
Melt temperature	-	933.3	K
Boiling temperature	-	2740	K
Specific heat	-	0.9	$\mathrm{kJ\,kg^{-1}}$
Specific heat vapor	-	0.459446	$\mathrm{kJ\,kg^{-1}}$
Enthalpy of fusion	-	396	$\mathrm{kJ\,kg^{-1}}$
Enthalpy of vaporisation	-	11370	$\mathrm{kJ\,kg^{-1}}$

space indicated the model closely matched the maximum flyer pressure and velocity calculated by B2, at a fraction of the computational resource and runtime.

The success of the 0D model was evaluated with reference the objectives set out as part of this research goal. The objectives addressed in this chapter include:

1. **The model must require low computational resources to run and be accessible to the scientific community.**

   The results from the 0D model for the paper included in this chapter were produced without high performance computing and was capable of computing hundreds of simulations within minutes using a local device. This capability is a result of the minimal information which must be conserved between explicit timesteps, the zero-dimensional nature of the problem and the analytical equation of state in the foil. The paper clearly presents the structure of the algorithm, its governing equations and the material properties utilised. This equips the reader with all the necessary information to reproduce the 0D model and tailor it to any electric gun load or pulsed-power device.

2. **The model must be able to predict the dynamics and state of both the foil and flyer.**

   The model tracked the physical position of the foil rear, the foil-flyer interface and the front of the flyer as three separate points. The velocity of the foil-flyer interface and front of the flyer were assigned by transposing the velocity of the rear based on the time necessary to communicate

Table 4.3: Material specific values for aluminium and PMMA used in 0D model results [67].

Constant	Value	[Units]
C1	-5.35×10^{-5}	[mΩ cm]
C2	0.233	
C3	1.21	
C4	0.638	
C5	1.5	
C6	0.012	
C7	3.8×10^{-3}	
C8	18.5	
C9	5.96	
C10	0.44	
C11	3.58×10^{-2}	
C12	3.05	
k	0.878	
L_f	0.107	[Mbar cm^3/mol]
T_{m0}	0.0804	[eV]
Gruneisen coefficent	2.13	

the information across the foil and flyer thickness. Additionally, it calculated the position of the maximum pressure in the foil using the relationship derived by Lemke *et al.* for the melt velocity in aluminium under a strong magnetic field. The model then assumes the pressure gradient from the position of maximum pressure in the foil to the front of the flyer decreases linearly from the maximum foil pressure to zero. The knowledge of this gradient and the positions of the maximum pressure, foil-flyer interface and flyer front permits the calculation of the pressure at the foil-flyer interface. This pressure at the interface is assumed to be the maximum pressure in the flyer.

3. **The model must be proven through verification and validation to reliably capture trends across a wide range of the electric gun design space i.e. for different geometries**.

   The verification between the 0D model and B2 demonstrated this approach to approximating the dynamics was accurate until impact over a range of geometries. The pressure states in the foil and flyer were accurate at early times in flyer flight. Later in flight, when the flyer has moved up the barrel, the 0D representation of foil plasma becomes less accurate. Consequently, the model's predictions of the pressures in the foil and flyer deviated from the solution produced in B2, though remained within a factor of 2.5. Further, the model is most accurate early in the acceleration process, which is the period of time when the most significant change in the magnitude of pressure in the flyer occurred.

The unaddressed objectives remaining, including use of the 0D model to design experimental loads, are addressed in the next chapter.

Chapter 5

Exploring the capability of the electric gun

This chapter presents an in-depth exploration of the experimental testing of an electric gun load on the pulsed-power machine M3. By leveraging the 0D model established in the previous chapter, a comparative analysis was conducted to understand the behavior of an identical electric gun load driven by CEPAGE and M3. Both devices, located at First Light Fusion, feature fixed rise-times, with CEPAGE possessing approximately half the charge voltage and rise-time of M3. While CEPAGE is similar to the typical pulsed-power devices discussed in earlier sections, M3 stands out with its longer rise-time and higher stored energy. The study aligns with findings from Song *et al.*, who successfully launched thick flyers using a machine with a similar rise-time to M3, highlighting the distinct pressure profiles that can prevent disassembly in thick flyers when driven by M3. Key observations include the significant impact of foil vaporisation and the temporal dynamics of flyer launch, both influencing flyer integrity. Furthermore, the chapter identifies a secondary destruction mechanism for thin flyers during late flight, suggesting a density-related vulnerability. This investigation meets multiple research objectives, such as guiding experimental design, developing repeatable diagnostics, exploring current-rise time effects, and improving the efficiency of electrical-to-kinetic energy conversion, with detailed results to be discussed in subsequent chapters.

5.1 Introduction

The research goal explored in this chapter centres on investigating the practical capabilities of the electric gun through a combination of experimental testing and modelling. In the previous chapter, the creation and testing of the 0D model of the electric gun resulted in a clearer understanding of the parameters the load was most sensitive to and the physical reasoning for these sensitivities, including (in order of significance):

1. **Current rise-time:** Though the dynamic resistance and inductance of the load may vary, within a pulsed power device such as a CDU the current magnitude and rise-time are approximately fixed by the charge voltage (V_0) and machine capacitance (C_0), resistance (R_c) and inductance (L_c). If the current profile cannot be shaped, then the performance of the electric gun load is largely fixed.

2. **Foil width:** The width of the foil (w) in the electric gun defines the current density within it, as $J = \frac{I}{w}$. The current density determines both the Joule heating and the magnetic field strength within the foil, which both the thermal and magnetic pressure are dependent upon. Consequently, for the same current input, the dynamic behaviour and pressure states in both the foil and flyer are predominantly dependent on the foil width.

3. **Foil and flyer thickness:** The comparison between B2 (referred to by its legacy moniker **Code** $\mathbb{B}$ in Section 4.2) and the 0D model revealed the pressure state in the flyer is affected by the thickness of the foil and flyer. In particular, when the foil is thin and the flyer is thick there is a distinct increase in the magnitude of the pressure in the flyer on launch. It was suggested this spike in pressure was due to building thermal pressures in the foil prior to launch. This idea is investigated in more detail in this chapter.

Hypervelocity projectile launch facilities require significant investment and resources to build: high power lasers and pulsed-power devices that power them are complex and often unique. As a result, these facilities are scarce and are therefore typically designed to be capable of advancing a wide range of research. For instance, while the Z machine is sometimes used to drive EM flyer plates, it is also employed to drive a range of other loads such as magnetic liner fusion targets, z-pinches and exploding wire arrays [18]. Additionally, the EM flyer plate load is flexible and can be optimised to operate successfully for a range of input current profiles, thus it is utilised at many facilities.

At the outset of this work, the electric gun was not thought to be as flexible as the EM flyer plate. Not only was it specified in the literature that a fast rise-time capacitor bank must be used, which have greater risk of electrical breakdown and shorter component life, the loads were restricted to using thin polymer films as flyers. Attempts to accelerate thicker flyers resulted in the flyers becoming damaged or disintegrating completely. This event is catastrophic in the electric gun, as any disruption across the thickness of the flyer provides an opening for the exploded foil plasma to move through. Once the foil plasma has accelerated ahead of the flyer, it can obscure the optical line of sight of the diagnostics trained on the flyer and target. Consequently, even if a portion of the flyer does survive, its impact is often entirely shrouded by the foil plasma. The electric gun is therefore difficult to operate and limited in the research it can perform.

Despite its limitations, the electric gun offers key advantages that the EM flyer plate technique cannot feasibly attain. In the electric gun the current flows through the exploding foil, which exerts thermal and magnetic forces on the dielectric flyer, whereas in the EM flyer plate, the current runs directly through the metal flyer itself. Consequently, the electric gun converts stored electrical energy to kinetic energy in the flyer with significantly greater efficiency. The dielectric flyer is also less vulnerable to state change, enabling the electric gun to drive flyers over a greater stand-off distance. The EM flyer plate is fundamentally restricted from achieving these efficiencies and stand-off distances by its operating mechanism, however, the electric gun was restricted from repeatably launching thick flyers by a lack of understanding of the mechanisms driving the flyer disassembly. This lack of understanding is addressed in this chapter in the following papers:

1. **The effect of current rise time on the acceleration of thick flyers to hypervelocities using an electric gun**

   M.D. Fitzgerald, J.D. Pecover, N. Petrinic, D.E. Eakins, The effect of current rise time on the acceleration of thick flyers to hypervelocities using an electric gun, International Journal of Impact Engineering, Volume 184, 2024, 104814, ISSN 0734-743X, https://doi.org/10.1016/j.ijimpeng.2023.104814.

   The contributions of M. Fitzgerald include: analysis using the 0D model, design of the electric gun load i.e. component material and dimensions, fabrication and assembly of the load, design of the diagnostic set-up, contributions to alignment of the diagnostics, processing of the experimental data, and writing and editing of the original draft. They do not include: design of the overall electrode (design discussed in [68]), installation of the load in M3, operation of M3, conceptualisation of the shock in block method, or creation of the diagnostic testbed i.e. VISAR set-up.

2. **Redesigning the electric gun: Launching thick flyers to hypervelocity with high efficiency**

   M.D. Fitzgerald, J.D. Pecover, N. Petrinic, D.E. Eakins, Redesigning the electric gun: Launching thick flyers to hypervelocity with high efficiency, High Energy Density Physics, Volume 52, 2024, 101119, ISSN 1574-1818, https://doi.org/10.1016/j.hedp.2024.101119.

   The contributions of M. Fitzgerald include: analysis using the 0D model, design of the electrode pier geometry, fabrication and assembly of the load, design of the diagnostic set-up, contributions to alignment of the diagnostics, processing of the experimental data, and writing and editing of the original draft. They do not include: design of the overall electrode (design discussed in [68]), installation of the load in M3, operation of M3, conceptualisation of the shock in block method, or creation of the diagnostic testbed i.e. VISAR set-up.

5.2 The effect of current rise time on the acceleration thick flyers to hypervelocities using an electric gun

5.2.1 Abstract

The electric gun is a projectile launcher which utilises both the rapid expansion of an ohmically heated exploding foil and strong electromagnetic forces to accelerate an insulating flyer up to 20 km/s. The gun's acceleration mechanism is highly efficient at converting stored electrical energy in the pulsed-power device driving the load to kinetic energy in the flyer, with values of up to 25% reported [5]. This high efficiency would allow capacitor banks to use less energy than conventional drives to generate higher pressure states in materials of interest to extreme state research. Despite its promising efficiency, the electric gun is rarely used, as the process of launching flyers above 0.5 mm thickness in this manner is highly variable, often resulting in uncontrolled launch characteristics and premature failure of the flyer. The gun is also difficult to optimise without use of a sophisticated multi-physics hydrocode, further limiting its take-up. This work presents experimental results from the successful launch of 24x24 mm flyers up to 2.0 mm thick to 10 km/s using an electric gun load on 1.2 MJ pulsed-power device: Machine 3. In combination with results from a 0D model, these findings are used to identify the mechanism for the destruction of thick flyers accelerated using electric guns, including strategies for mitigating their break-up. The results support the existing idea that flyer failure can be avoided by limiting the maximum pressure within the flyer. They also reveal a second mechanism by which the

flyer integrity can be maintained when the current rise time is longer than the flight time; high pressures in thick flyers caused their density to remain high enough to prevent the driving foil plasma from breaking through, averting their disassembly. This second mechanism provides a route to accelerate thick electric gun flyers to higher velocities with efficiencies up to around 9% whilst lengthening the shock duration on impact, broadening the gun's potential applications in extreme state research.

5.2.2 Introduction

Research into the behaviour of materials at extreme states involves an advancement of scientific knowledge relevant to many of the most consequential challenges faced by humanity today. The pressures and temperatures experienced in aerospace and nuclear fusion applications are, by their nature, found nowhere naturally on the Earth's surface. In order to design and improve hardware for these purposes, the response of materials under the conditions generated during operation must be understood, requiring access to these states in a controlled setting. The electric gun is a pulsed-power device used to access extreme pressure states, through the impact of thin flyers launched up to 20 km/s using the rapid discharge of a capacitor bank. The gun was originally developed at Lawrence Livermore National Laboratory (LLNL) in the 1970s [2, 21, 24] though it has received limited attention in recent years [14, 15, 26]. The technique has the advantage of driving highly planar shocks over a large material volume, simplifying the acquisition of diagnostics [21].

The electric gun can be thought of as a hybrid between an exploding foil initiator (EFI), also known as a 'slapper', and an electromagnetic (EM) plate flyer launcher [16, 17]. Its projectile is driven by both a thermal explosion, as in an EFI, and the magnetic acceleration of the plate flyer. The process begins with the discharge of a high-speed capacitor bank across a thin metallic foil, resulting in a large amount of energy deposited in the foil through ohmic heating. This energy deposition drives a change of state in the foil from a solid to a rapidly expanding plasma. The 'exploding' foil plasma acts as a driver gas, accelerating an adjacent thin insulating plate, referred to as the 'flyer'. The flyer plate is laid atop the foil in a bonded stiff assembly, such that the foil plasma 'punches out' a section of the flyer material, accelerating it typically for a few millimeters to impact a target. This plasma pressure component of the acceleration is known as the thermal drive. When large currents are discharged to vaporise the foil, considerable magnetic forces exist in the system that also act to accelerate the foil plasma. This effect is the origin of the magnetic drive. The approach is highly efficient, demonstrating conversion from electrical capacitor bank discharge to projectile kinetic energy of up to 25% [5]. By comparison, EM plate flyers launched on the Z machine at Sandia demonstrate efficiencies closer to 4% [20, 91].

The behaviour of the flyer in the electric gun is highly dependent on the characteristics of the capacitor bank powering it, such as current amplitude and rise time. Early investigations into the electric gun sought to optimise its performance by reducing the current rise time of the capacitor bank. This was to ensure the foil explosion occurred near peak current, thereby maximising the thermal energy extracted on launch [22]. However, researchers noted that on high energy capacitor banks the more significant contribution to the flyer acceleration came from the magnetic drive [57]. The resulting short rise time electric gun was found to be successful at launching thin flyers to hypervelocities, but researchers struggled to launch ‘thick’ flyers (over 0.5 mm) without inducing violent state change in the flyer during launch and flight. In high energy electric guns the effect is more extreme; thick flyers often experience complete disintegration shortly after launch [58]. The mechanism by which thick flyers are damaged in short rise time electric guns is not well understood, and researchers at the time lacked the numerical and experimental tools to determine the cause [5]. This stumbling block in the optimisation of electric gun performance prevented the gun from investigating longer timescale phenomena, and the technique fell into disuse due to its limited applications.

Recent developments made to the electric gun have taken advantage of improvements in numerical simulation and diagnostic techniques to begin to address the problems with thick flyer launch to hypervelocity. Wang *et al.* developed a Lagrangian hydrodynamic code with an equation of state database to more accurately model the foil burst and magnetic acceleration. This enabled them to achieve launch of flyers up to 14 km/s on a short rise time machine, though they did not launch flyers over 0.2 mm thick [14, 67] . Conversely, Song *et al.* focused their efforts on modelling the flyer impact using LS-DYNA [92] and improving their diagnostic technique, leading them to successfully launch a 1.0 mm flyer over a 14 mm flight distance. Song proposed that the flyer’s maintained integrity was a result of their capacitor bank’s long rise time (1.8-2.0 μs). However, the models used in both investigations did not include the framework to estimate the flyer state and the diagnostics fielded were only used to measure the flyer thickness and velocity. As a result, the mechanisms for both the destruction of thick flyers on the short rise time electric gun and their improved integrity on the long rise time machine remained unclear.

If the mechanisms responsible for the disintegration of thick flyers launched by the electric gun were understood, these destructive states could be anticipated and potentially avoided. This could enable the electric gun to become both an efficient and versatile projectile launcher, making it a powerful complimentary tool for existing launch platforms. In this work a numerical model, capable of simulating the electric gun dynamics and flyer pressure state, was used to investigate the difference in the evolution of the state of thick flyers on a short rise time and a long rise time capacitor bank. The results of this study were then used to inform the design of an experimental electric gun load for a 2 μs rise time, 1.2 MJ pulsed-power device. Finally, a range of diagnostic data collected from these shots, combined with results from the numerical model, was used to answer the following questions:

- What is the dependence of the maximum internal pressures in thick flyers on the machine rise time?
- How does changing the flyer thickness influence flyer state on long rise time electric guns?
- How does the pressure state in the foil and flyer influence electric gun dynamic performance?

Addressing these questions will enable the mechanism responsible for flyer break-up to be determined and importantly should lead to strategies for improving flyer survivability.

5.2.3 Numerical Modelling: The effect of rise time on flyer state

In this work, data from both a 0-dimensional (0D) model and experimental launch were acquired to build a more comprehensive understanding of the mechanism responsible for the failure of thick flyers launched by the electric gun. *In-situ* collection of data regarding the flyer state during launch and flight prior to impact is challenging, necessitating results obtained through numerical modelling to contribute to the interpretation of the diagnostic data that can be obtained experimentally.

Previous electric gun research has suggested that minimising the current rise time when launching thin flyers leads to an improved performance. However, these load configurations were unable to reliably launch flyers with thickness over 0.5 mm without incurring damage. Song et al. suggested the opposite was true for thick flyers; they found the longer rise time of their capacitor bank was advantageous in maintaining the integrity of the 1 mm thick flyers launched in their experiments. Using a 0D model recently developed by Fitzgerald *et al.*, the acceleration of a square 24.0x24.0x1.5 mm flyer powered by two different pulsed-power machines, Machine 3 (**M3**) and CEPAGE was simulated [93].

Machine 3 (**M3**) is a 2.5 MJ pulsed-power machine generally used at First Light Fusion to accelerate EM plate flyers. It is the highest energy capacitor bank used to power an electric gun in open literature, with a long rise time of around 2 μs. In order to draw comparison, the behaviour of thick flyers was examined both when launched by a long rise time capacitor bank and when accelerated by a short rise time capacitor bank more typical of electric gun launch. CEPAGE is a smaller capacitor bank which has previously been used at First Light Fusion to successfully fire electric gun flyers to over 10 km/s. Further details of both launchers are available in previous works [68, 81, 94].

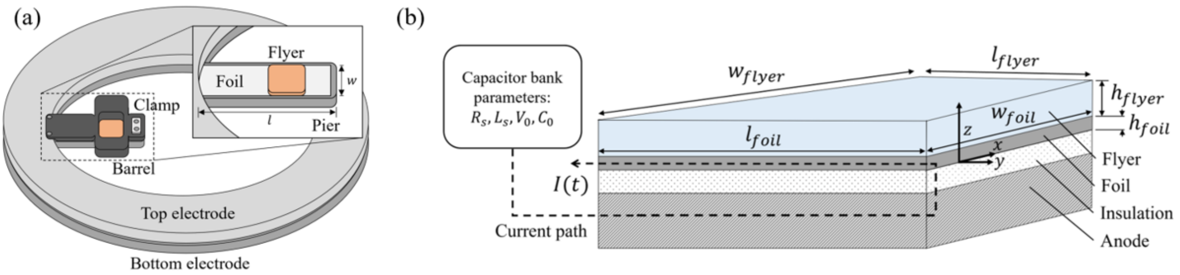

Figure 5.1: **(a)** Simplified diagram showing the electric gun load set-up, with pier foil width (w) and length (l) labelled. The close up shows the flyer atop the foil over the pier, with the barrel hidden from view. The current passes from the pier on the bottom electrode through the foil to the top electrode. **(b)** The 0D model allows the user to input detailed parameters regarding the foil, flyer and capacitor bank. These include the foil and flyer material and dimensions, and the capacitor bank parameters necessary for calculating the system current at each timestep.

Method

The electric gun model utilised in this work calculates the dynamics and pressure state of an insulating electric gun flyer in 0D. The model is flexible, with a number of input parameters, including the geometries of the foil and flyer and machine parameters which allow it to calculate results for a wide range of load designs, illustrated in Fig. 5.1b. The model's algorithm can be divided into four stages: firstly, the current is calculated at each timestep. This is then used to find state of the foil, and update three positions in the electric gun system: the rear of the foil (z_r), the interface between the foil and flyer (z_i) and the front of the flyer (z_f). Finally, it calculates the pressure at the foil-flyer interface and the maximum pressure in the flyer by using the position of the magnetic field along the z-axis ($z_{P_{max}}$) to find the location of the maximum pressure in the foil. These positions and axes are illustrated in Fig. 5.2.

In a typical electric gun model, the system dynamics are calculated by adding the foil and flyer mass and determining the system momentum change. The resultant velocities of the foil and flyer are then used to update the foil's position, which does not account for the time for pressure information to be passed from the foil to the flyer. Whilst this approximation is valid for thin foils and flyers, as the wave transit can be assumed small when compared to the total flight time, the time necessary to communicate a change in velocity in the foil becomes significant when the foil or flyer is thick. This is particularly critical during launch, as the flyer is unable to move off until the first pressure wave has reached its leading surface.

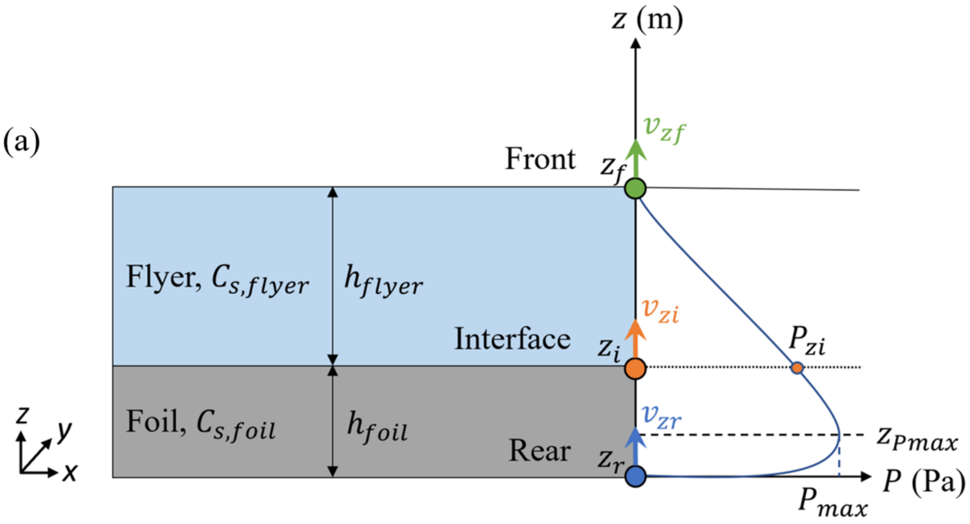

Figure 5.2: The positions of the four locations used determine the pressure at the foil-flyer interface, alongside the velocities used to approximate the foil-flyer dynamics. The model assumes the foil and flyer form a continuous interface, with pressure at the front of the flyer set to zero and the pressure a linear gradient between z_{Pmax} and z_f.

To approximate the 1D delays in communication of pressure information in 0D, the foil and flyer are simplified in space to key locations along the z-axis. The model tracks three positions; the rear of the foil, the foil-flyer interface and the front of the flyer, visualised in Fig. 5.2. Prior to launch, the velocity at the rear (v_{zr}) can be found using the total force driving the foil. This velocity state is then assumed to sweep through the foil in the z-direction at the relevant speed of sound, leading to an interface velocity (v_{zi}) found through,

$$v_{zi}(t) = v_{zr}\left(t - \frac{h_{foil}(t)}{c_{s,foil}}\right), \tag{5.1}$$

where $c_{s,foil}$ is the ambient speed of sound in the foil and $h_{foil}(t)$ is the updated foil thickness. For simplicity, the model assumes the speed of sound to be constant in all materials. As the foil typically accelerates to velocities higher than the flyer sound speed within hundreds of nanoseconds, the interface position can overrun the flyer front if left unchecked. To avoid this, the algorithm instead updates the front velocity using either the speed of sound in the flyer or the interface velocity to approximate shock behaviour that may occur in the flyer using,

$$v_{zf}(t) = \begin{cases} v_{zr}\left(t - \left(\frac{h_{foil}(t)}{c_{s,foil}} + \frac{h_{flyer}(t)}{c_{s,flyer}}\right)\right) & v_{zi}(t) \leq c_{s,flyer} \\ v_{zr}\left(t - \left(\frac{h_{foil}(t)}{c_{s,foil}} + \frac{h_{flyer}(t)}{v_{zi}(t)}\right)\right) & v_{zi}(t) > c_{s,flyer}, \end{cases} \tag{5.2}$$

where $c_{s,flyer}$ is the speed of sound in the flyer, and $h_{flyer}(t)$ is the updated flyer thickness. The foil and flyer thicknesses are recalculated at the beginning of each timestep using the positions derived from the three location velocities at each timestep. This allows the model to capture the effect of compression and expansion in the foil and flyer despite being 0D.

To reduce the computational resource required by the model, the algorithm determines the maximum pressure state in the flyer without referring to an equation of state. This is done by assuming the pressure state at foil-flyer interface is continuous throughout acceleration and the gradient between the maximum pressure in the foil (P_{max}) and the pressure at the front of the flyer (P_{zf}) is linear. As a result, the gradient of the pressure ($\frac{dP}{dz}$) can be found using,

$$\frac{dP}{dz} = \frac{P_{zf} - P_{max}}{z_i - z_{P_{max}} + h_{flyer}}. \tag{5.3}$$

When launch occurs in a vacuum, the model assumes P_f to be zero. Hence the pressure at the interface P_{z_i} is simply calculated using,

$$P_{zi} = P_{max} + \frac{dP}{dz}(z_i - z_{P_{max}}). \tag{5.4}$$

where an example of this gradient is visualised in Fig. 5.2.

The inclusion of equations 5.2 and 5.4 allow the model to capture the changing maximum pressure in the flyer due to the building of thermal pressure in the foil prior to launch and the physical proximity of the position of maximum pressure in the foil to the foil-flyer interface in 0D. The 0D model was verified against 1D simulations in MHD Eulerian hydrocode ‘Code B’, known simply as $\mathbb{B}$. Fitzgerald *et al.* found the 0D model most closely matched the 1D MHD simulations for loads with thin foils ($t < 0.5$ mm), as the approximations made to determine $z_{P_{max}}$ and P_{max} became less accurate at late flight times in thick plates [93]. The results for a load on M3 described in table 7.1, with $l = 25$ mm, from $\mathbb{B}$ and the 0D model are shown in Fig. 5.3. The model is able to closely replicate both the magnitude and temporal evolution of the maximum pressure in the flyer and the flyer velocity predicted by $\mathbb{B}$. This indicates despite the simplifications, the 0D model is able to capture the key physics dominating both the flyer pressure state and dynamics.

The 0D model makes it possible to predict the maximum pressure and flyer velocity, significantly reducing the computational resource required to investigate the electric gun. The model is used in this investigation to show how the electric gun can be optimised for a specific capacitor bank without the need for a complex multi-physics hydrocode, making the gun a more accessible tool for existing pulsed-power platforms. As the model is able to accept a range of details regarding the load design and machine parameters, the specific response of the flyer to the load design and two capacitor bank can be captured. The machine parameters utilised in this investigation are shown in Table 5.6 and the load parameters considered by the model are listed in the Table 7.1.

Table 5.1: Machine parameters for pulsed-power capacitor banks M3 and CEPAGE.

Parameters	M3	CEPAGE	[units]
Charge voltage	140	70	[kV]
Capacitance	124.8	32.0	[μF]
Fixed resistance	0.1	3.0	[$\mu\Omega$]
Fixed inductance	12.5	5.4	[nH]

Table 5.2: Electric gun load parameters used in 0D simulations.

Load Parameters	Value
Foil length	50.0 mm
Foil width	25.0 mm
Foil thickness	0.1 mm
Foil material	Aluminium
Flyer length	25.0 mm
Flyer width	25.0 mm
Flyer thickness	1.5 mm
Flyer material	PMMA

Results

The effect of current rise time on the temporal evolution of the flyer pressure was considered by using the 0D model to simulate the response of the same electric gun load powered by two different capacitor banks. Fig 5.4a shows the time-dependence of the maximum pressure in the flyer within the first 2.5 μs of current start alongside the trajectories of the foil and flyer. An initial peak in the maximum pressure in the flyer can be seen with both machines on launch. This is due to the building of thermal pressure in the exploding foil prior to the launch of the flyer. When the flyer is thin, the time taken to communicate

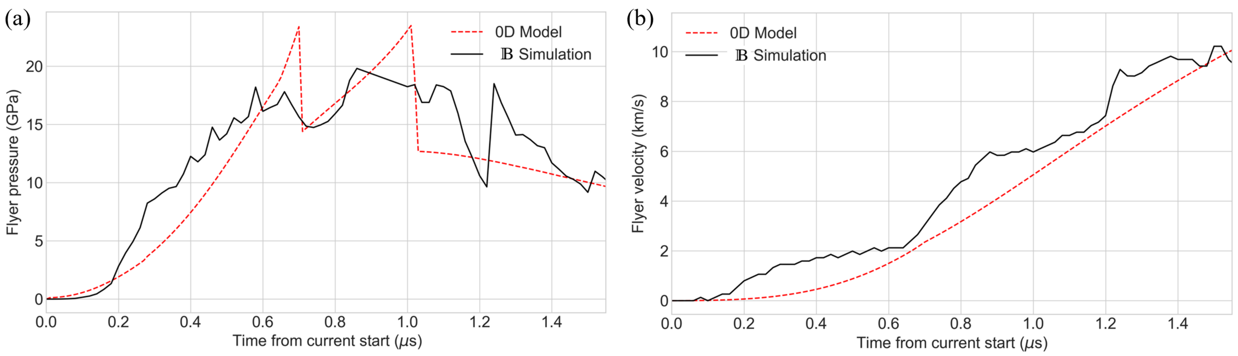

Figure 5.3: Comparison between maximum flyer pressure **(a)** and flyer velocity **(b)** calculated by the 0D model and 1D MHD simulations in 𝔹 for a 1.5 mm thick flyer used on M3.

the pressure information from the foil to the front of the flyer is negligible. However, as the flyer thickness increases, the subsequent time elapsed from current start to flyer launch, which in this work is considered to be the time the front of the flyer moves, becomes significant when compared to the current rise time. As a result, by the time the flyer launched by CEPAGE has moved off, the current begins to drop and the pressure in the foil plasma drops. In turn, the maximum flyer pressure also decreases.

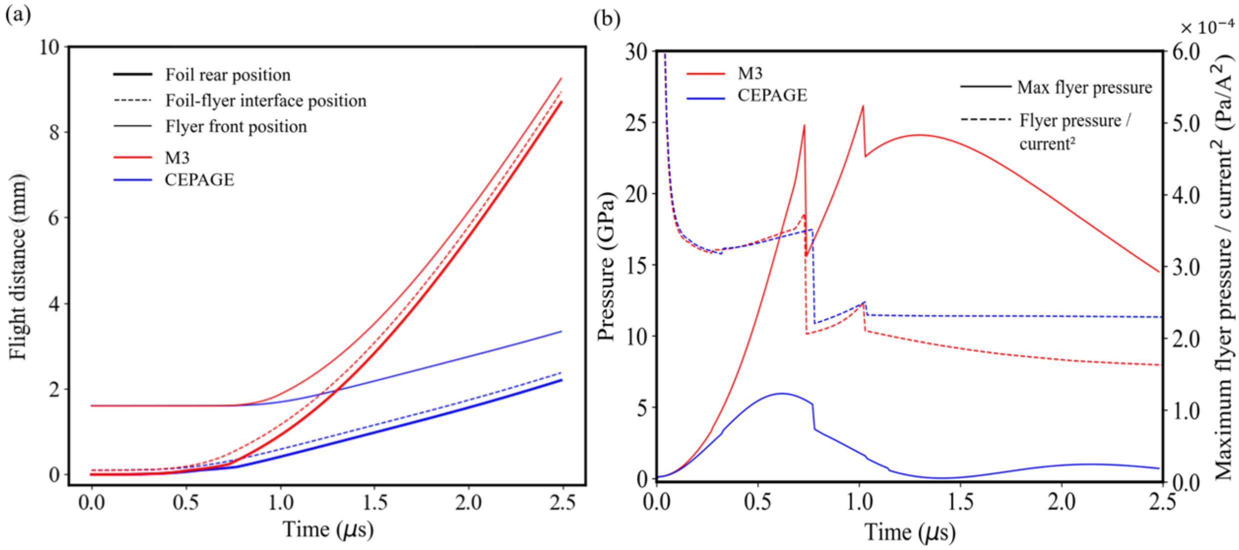

Figure 5.4: Plots tracking the temporal evolution of foil-flyer position, maximum pressure **(a)** and pressure normalised by foil current in the flyer **(b)** calculated by the 0D model throughout launch and flight. M3 has a higher energy and longer current rise time than CEPAGE, therefore the foil and flyer travel further and remain at higher pressures.

By contrast, due to its slow rise time, the maximum pressure in the flyer launched by M3 has multiple maxima. The first, as in the case of CEPAGE, is due to the building thermal pressure in the foil prior to launch. The second is related to the movement of the position of maximum foil pressure within the foil as the magnetic field diffuses through the metal plasma. Fig. 5.4a demonstrates that the flyer had already travelled 9 mm shortly after the current rise time of around 2.0 μs. M3 not only has a long rise time, but a larger amplitude of around 10 MA, thus the foil remained at an extreme pressure state due to the strong electromagnetic fields in the system until flyer impact. This high pressure in the foil subsequently maintained the pressure at the foil-flyer interface for a greater flight distance. As a result, the maximum pressure in the flyer after the current rise time is still high, with Fig. 5.4b showing it to be above 15 GPa.

Discussion

In this section, a comparison is made between the 0D modelling results of the electric gun load on the two machines to generate an understanding of how the current rise time of a machine influences the maximum flyer pressure state and the implications this has on flyer integrity. CEPAGE and M3 do not only differ in rise time: the stored energy of M3 is around twice that of CEPAGE. As a result, the magnitude of the current (I) in the exploding foil on M3 is roughly double, impacting the magnitude of the magnetic field strength (B) proportionally and the magnetic pressure (P_B) in the foil by the current squared. As shown in equation 5,

$$P_B = \frac{B^2}{2\mu_0} = \frac{(\frac{\mu_0 I}{2w})^2}{2\mu_0}, \tag{5.5}$$

where w is the foil width, l is the foil length and μ_0 is the vacuum permeability. This relationship is apparent in Fig. 5.4b, which shows the pressure normalised by the square of the current is similar for both devices. This illustrates that the pressure state in the flyer is strongly dependent on the current through the foil. As a result, the machine rise time will directly influence the evolution of the pressure state in the flyer. After around 1.0 μs, the flyer pressure over the current squared falls on M3 when compared to CEPAGE. This is because as the foil accelerates rapidly to faster than the speed of sound in the flyer, the flyer becomes compressed. When the flyer thickness decreases during flight, the pressure gradient across the foil to the front of the flyer changes relative to the foil-flyer interface. This concept is illustrated in Fig. 5.5a.

Experimental results have suggested that increasing the machine rise time led to improved flyer integrity in thick flyers [15]. As the maximum pressure state in the flyer is proportional to the square of the current through the foil, when the rise time is long, the pressure in the flyer remains high for a longer period. On the other hand, in short rise time machines the pressure will quickly rise and fall. This suggests that the maintained high pressure in the flyer material at the foil-flyer interface contributes to preventing the flyer from disintegrating during flight. It was hypothesised that if the flyer material adjacent to the foil is held at high pressure, the density of the flyer will also be maintained in this region, preventing the exploding foil from breaking through the flyer. In this scenario, it is expected that thicker flyers would be more likely to survive than thin, provided the current pulse length was longer than the flight time to the target. Fig. 5.5b shows that the 0D model predicts the maximum flyer pressure increases with the flyer thickness throughout flight. By the same logic, thick flyers could be destroyed if the current pulse length was shorter than the flight time, as the pressure in the flyer rapidly increases and falls before the flyer had time to impact a target. Fig. 5.4a shows on CEPAGE, the pressure in the flyer has dropped before the front has moved even 2 mm. If the initial pressure rise was high enough to cause the polymer to lose material strength, as the pressure drops the density could fall below solid state, allowing the foil plasma to break through. The plasma pushing through the flyer would then cause it to break up, resulting in disassembly. This narrative is consistent with the experimental observations made by Osher *et al.*, who noted that their thick flyers broke up almost immediately after moving off [5].

The 0D model lacks an equation of state or constitutive model in the flyer material, thus the flyer density and integrity cannot be simulated. Without this information, the prediction that thick flyers keep their integrity on long rise time machines due to their maintained pressure state cannot be verified. To investigate the effect of the flyer pressure on the flyer density state and dynamics discussed in this section further, experimental testing of the electric gun load on M3 was performed. The diagnostics data collected was then used in parallel with the 0D modelling results to build a more complete picture of the relationships between flyer thickness, flyer state, rise time and load efficiency.

5.2.4 Experimental Testing: parametric study of flyer thickness on a 1.2 MJ electric gun

In this section the experimental method and data from electric gun shots on M3 using the load design investigated in the 0D model are presented. The results in the previous section suggest that the disintegration of thick flyers on short rise time machines and the maintained integrity of thick flyers on long rise time machines are a result of maintained high pressures in the flyer material adjacent to the foil-flyer interface. However, owing to its simplicity, the 0D model is unable to model several

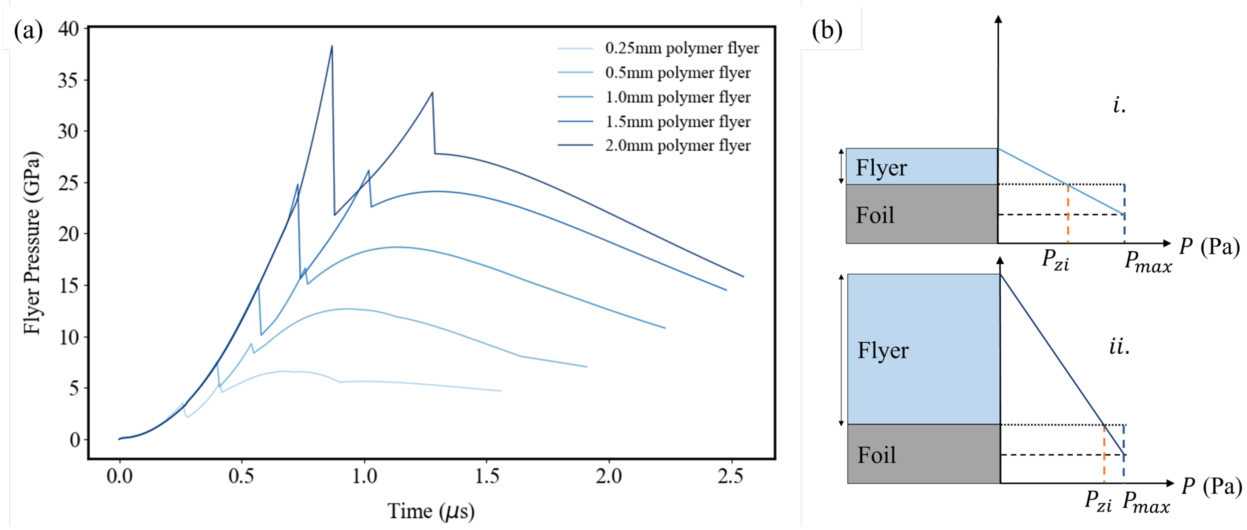

Figure 5.5: (a) Qualitative illustration of the mechanism for the higher pressures in thicker flyers later in flight. As the position of the front of the flyer is further away from maximum pressure in *ii* relative to the position of the foil-flyer interface, the maximum pressure in the flyer is greater. **(b)** Plot showing the temporal evolution of the maximum flyer pressure in flyers of different thicknesses launched by M3 over a flight distance of 9 mm. The initial spike in pressure increases with flyer thickness as the launch time occurs later. The pressure remains higher in thick flyers later due to the orientation of the pressure gradient between the pressure maximum in the foil and the flyer front, illustrated in Fig. 5.5a.

mechanisms which could contribute to the loss of the flyer's integrity. These include, but are not limited to, material strength, compressibility and circuit discharge effects.

Flyer thicknesses from 0.25 mm to 2.0 mm were launched over 9.0 mm flight distance, and a 0.5 mm flyer was launched over 20.0 mm distance. A more complete picture of the effect of flyer thickness on flyer state using long rise time electric guns was determined by evaluating the velocity of these flyers, measuring their shock velocities imparted on impact in a target and mapping their leading surface during flight.

Method

The experimental set up used in this work is shown in Fig. 5.6a, which illustrates the foil, flyer and barrel in relation to the diagnostics fielded on the shots. Measurements of the flyer state and velocity are required to characterise the operation of the gun. This necessitates acquiring the flyer's impact speed and the shock speed in a known material. The velocity profile of the flyer provides key additional data to build a more detailed picture of the processes at play. The shock speed in a target is found by projecting a 1D line of laser light through a transparent PMMA target block. As the flyer impacts the block, it induces a shockwave of a high enough pressure (over 20 GPa) to turn the PMMA opaque, thus blocking the laser light. The 1D laser is captured by a streak camera, and the position of the shock front through the block is tracked through time. 1D and 2D VISAR are fielded on the flyer, measuring the velocity of the flyer throughout flight and mapping its damage features respectively. Finally, a high speed camera images the target block in 2D to capture the shock shape and evaluate the flyer planarity and integrity on impact.

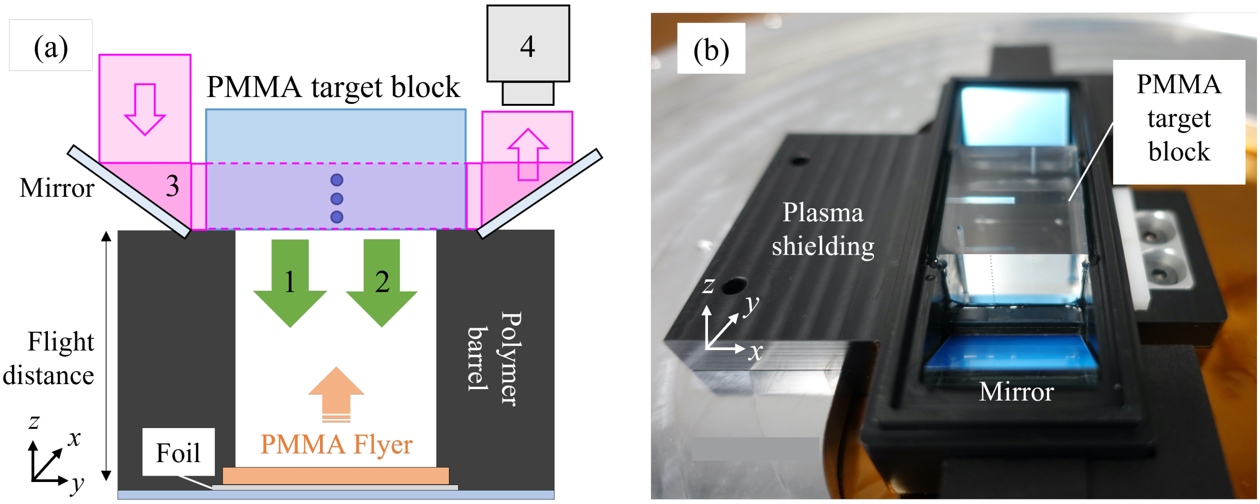

Figure 5.6: **(a)** Diagnostics fielded during the experiment include (1) 1D VISAR streak measuring projectile velocity, (2) 2D VISAR fringes mapping flyer surface damage evolution during flight, (3) 1D laser streak capturing shock velocity profile in the target block and (4) high speed imaging of the PMMA target block showing the shock front in 2D. **(b)** Image of barrel with plasma shielding, target block and mirror mount.

Attempting to collect diagnostic data from flyers launched to hypervelocity on the electric gun is challenging. This is especially true for thick flyers, as the launch process often results in the abrupt disruption of the flyer's leading surface. This can result in the reduction of surface reflectivity, preventing the collection of 1D VISAR. If the surface disruption is a result of foil plasma breaking through the flyer, the bright, high velocity plasma will overtake the flyer obscuring the 1D and 2D VISAR line of sight and causing a low speed precursor shock in the target block. Finally, large volumes of foil plasma escaping from below the top electrode fill the space around the barrel on burst. Without protective measures, this plasma can escape into the mirror mount, obscuring the flyer impact event.

Adaptations to the experimental set up to improve diagnostic acquisition are shown in Fig. 5.6b. For example the PMMA target block was tilted to eliminate ghost fringes caused by reflection of the VISAR laser at the block faces, such that laser light reflected by the flyer was more apparent. Secondly, the flyer was fixed into a recess at the bottom of the barrel to prevent foil plasma from

Table 5.3: Electric gun shot results using load seen in Fig 5.1a, 0.1x25x50 mm Al foil, 24x24 mm polyimide flyer. Shots 1 and 3 failed midflight due to plasma breakthrough.

Shot no.	Flyer thickness (mm)	Flight distance (mm)	Maximum shock speed in target (km/s)	Flyer survived until impact
1	0.25	9.0	7.0	No
2	0.5	9.0	8.0	Yes
3	0.5	20.0	8.1	No
4	1.0	9.0	9.55	Yes
5	1.5	9.0	9.8	Yes
6	2.0	10.0	10.6	Yes

escaping around the edges into the barrel on launch. Lastly, a wall of plastic was integrated into the barrel design over the join between the foil and top electrode, referred to in Fig. 5.6b as the ‘plasma shielding’, to protect the line of sight of the mirrors at the top of the barrel.

Results

The shock speeds in the PMMA target block were successfully obtained for all shots performed. The process for determining the shock speed in the block is illustrated in Fig. 5.7. The position of shock front profile was identified and a fifth order polynomial fit was applied to the position data. The fitted data was then differentiated to find the shock speed. For shots 4, 5 and 6 in Table. 5.8, images of the shock front position in the high speed camera are used instead. Again, a fifth order polynomial fit was applied to the shock position data, and the differential of the position data determined the shock velocity in the target. The second technique gave a lower time resolution, but tracked the shock front further through the block and was less sensitive to distortion due to debris in the mirror mount.

Table. 5.8 shows the highest shock speed was generated on impact by the 2.0 mm flyer. The shock speed generated on impact by 2.0 mm flyer of 10.6 km/s in the PMMA target block is equivalent to 70 GPa pressure over a 24x24 mm area [95]. The flat progression of the shock front in the target block, shown in Fig. 5.8, suggest the thickest flyers retained good planarity and a homogenous state across their width.

Converse to behaviour expected on a short rise time machine, the diagnostic data for the two thinnest flyers suggest they experienced some disassembly during flight. Fig. 5.9a shows the initial shock speed in the target is low for both the 0.25 mm flyer at 9 mm barrel length and the 0.5 mm at

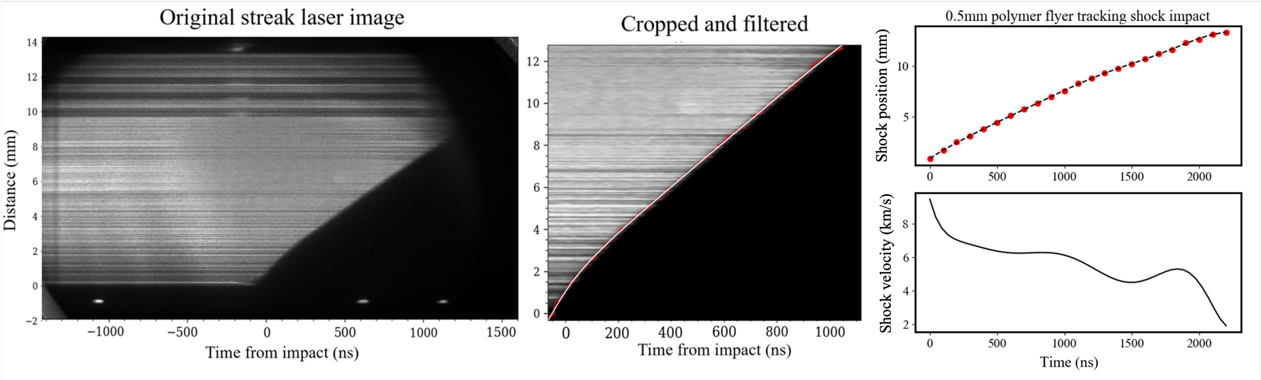

Figure 5.7: The velocity of the shock in the transparent PMMA target block is calculated by differentiating the progression of the shock front position in time. First, the position of the shock front is identified: as the shock front moves through the target its high pressure state turns the PMMA opaque, gradually blocking the laser light as it moves. The boundary between the laser light and opaque (black) region for each timestep is identified automatically by evaluating the pixel value, and the positions are extracted. A polynomial fit is then applied to the shock positions which, when differentiated, gives a less noisy shock velocity profile.

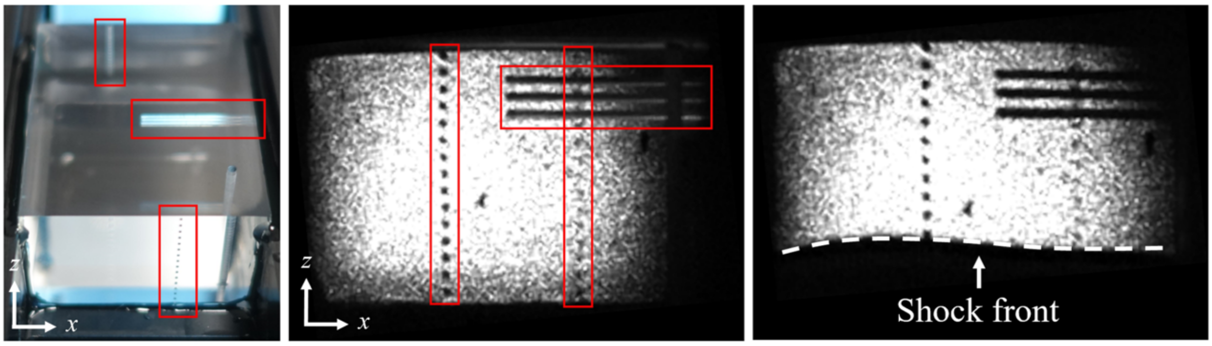

Figure 5.8: Images taken using the high speed camera focused on the target block showing an example of the shock front generated on impact using the 1 mm thick flyer (red boxes around fiducial marks relate set up to high speed camera images). The small tilt in the shock front, consistent across all shots performed, could be associated with slight asymmetries in the magnetic field strength across the bottom electrode pier [68].

20 mm barrel length due to the breakthrough of a low density plasma precursor shock at late times in flight. Fig. 5.9b shows this process occurring in the 2D VISAR imaging. The bright foil plasma can be seen breaking through the centre of the foil, as opposed to escaping around the edges.

Discussion: Measured and simulated results

The experimental results collected from the shots performed on M3 demonstrate that the electric gun load designed for this work can accelerate flyers of unprecedented thickness whilst maintaining their integrity until impact. Contrary to previous research performed on short rise time capacitor banks, it

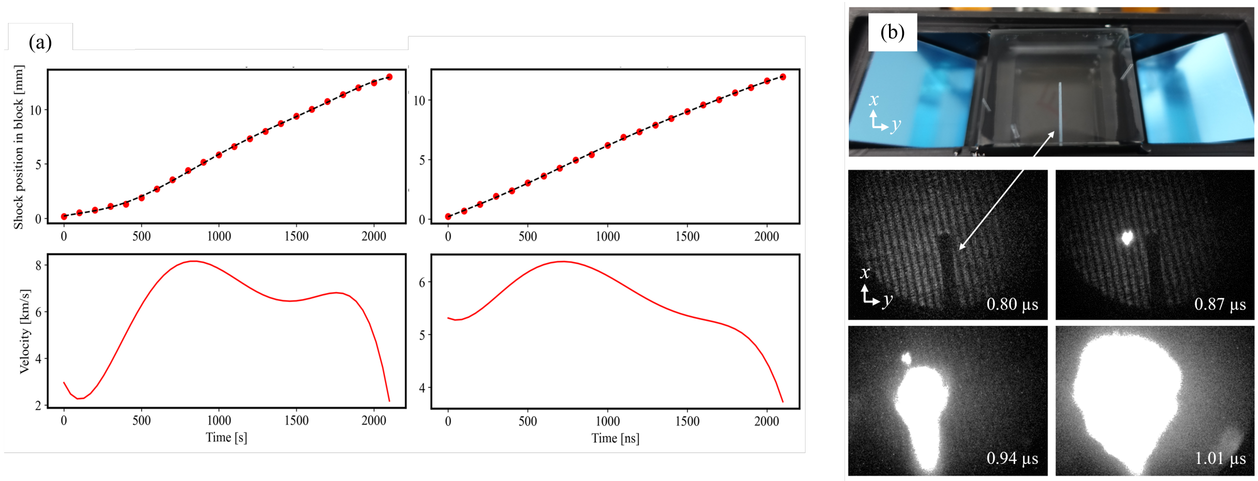

Figure 5.9: **(a)** Plots of the temporal evolution shock in block velocity profiles for the 0.25 mm thick flyer and the 0.5 mm flyer launched over 20 mm. The low initial velocity of the shock in the block in both cases is an indication that a high velocity but low density shock front arrived in the target ahead of the flyer, which on secondary impact caused the later velocity increase. This indicates that foil plasma was able to escape in front of the flyer, suggesting that the flyer experienced a loss of intergrity during flight. **(b)** Images of plasma breaking through the 0.25 mm thick flyer from the 2D VISAR fringes used to map the flyer surface. Its view was oriented down the barrel and the dark shadow of the fiducial marker in the target block can be used for reference. The plasma can be seen to first appear at 0.87 μs near the centre of the flyer, indicating the plasma forced its way through the flyer instead of escaping around the edges.

was the thinner flyers that experienced disassembly. This loss of integrity in the thin flyers occurred late in the flight time, as opposed to near launch as reported in thick flyers on short rise time electric guns. At the conclusion of the modelling performed in Sec. 5.2.3, it was suggested that the maintained pressure state in thick flyers launched using M3 could contribute to maintaining their integrity. These results support this claim, as the only two flyers which experienced plasma breakthrough had the lowest maximum pressure, demonstrated in Fig. 5.10a. The 0.25 mm flyer had low maximum flyer pressure due to the lower thermal pressures and reduced pressure gradient, whereas the 0.5 mm flyer launched over 20 mm flight distance experienced a pressure reduction late in the current rise time.

The final impact speed of the flyers at the target was not recorded due to loss of the VISAR signal from the front surface of the flyer around halfway through flight. Without the impact speed, the density of the flyer following impact cannot be estimated. However, comparison between the measured velocity profiles of the measured and simulated velocity profiles, shown in Fig. 5.10b suggest that, at early times in flight, the 0D model is able to predict the experimental velocities with reasonable accuracy. Table 7.4 shows the final impact times predicted by the 0D model approximately match the experimental results,

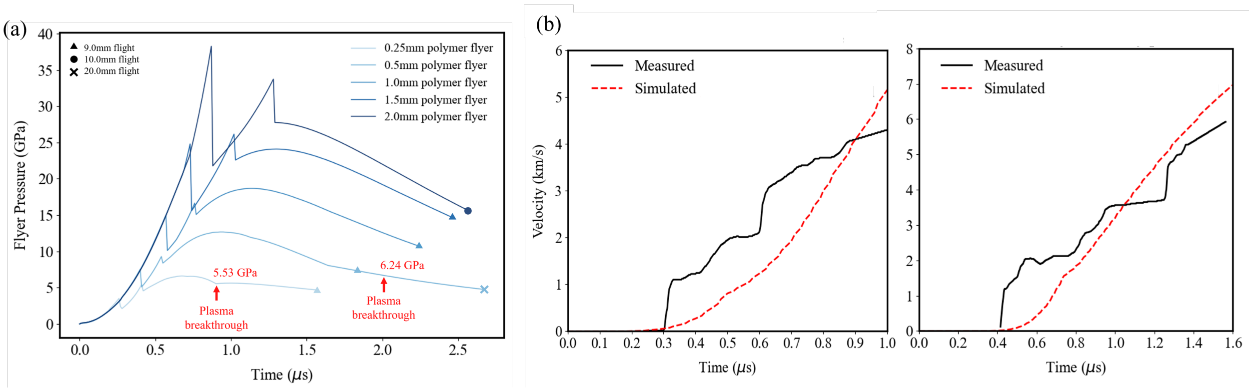

Figure 5.10: **(a)** Plot showing the maximum pressure of the flyers over time launched by M3 calculated by the 0D, for the different flyer thicknesses and barrel lengths shot experimentally on M3. The time the 0.25 mm thick flyer and 0.5 mm thick flyer shot to a flight distance of 20 mm experienced plasma breakthrough occurred when the 0D model predicted they were at similar pressures. This suggests that the foil plasma was able to force its way through the flyer when the maximum pressure in the flyer material dropped below a certain threshold. **(b)** The measured 1D VISAR velocity profiles in the early stages of launch and flight for the 0.5 mm and 1.0 mm thick flyers. The 0D model has no equation of state in the flyer, so is unable to model the release of the front surface of the flyer into vacuum. However, the simulated velocity is close to the measured profile in both cases, and is likely more indicative of the velocity of densified bulk of the flyer. The impact velocities of the flyers were not captured in this work. However, these results alongside the similar flyer impact times (Table. 5.5) indicate that the impact velocities calculated by the 0D can be used instead.

thus the numerically predicted impact speeds are used in this work to estimate the flyer density on arrival in lieu of experimentally recorded velocities. The interfacial continuity conditions state that

$$\rho_f U_f \ (V_0 - u_f) = \rho_t U_t u_t, \tag{5.6}$$

Table 5.4: Comparison between experimentally measured and modelled impact time.

Shot no.	Measured impact time (μs)	Predicted impact time (μs)
2	2.09	1.98
4	2.27	2.13
5	2.21	2.20
6	2.61	2.45

where the subscripts f and t denote the flyer and PMMA target block, ρ is density, U is the shock speed, V_0 is the flyer impact velocity and u is the particle velocity. The average density of the flyer can

Table 5.5: The values of flyer impact density calculated using the maximum shock speeds recorded in Table 5.8 and equation 5.6. Efficiency is considered to be the combined kinetic energy of the foil and flyer divided by the machine energy.

Flyer thickness (mm)	Predicted impact speed (km/s)	Flyer impact density (kg/m^3)	Efficiency %
0.5	10.5	411.0	2.59
1.0	10.05	964.8	4.10
1.5	10.1	1064	5.88
2.0	10.75	1229	8.63

be estimated by combining this equation with the LASL Hugoniot data for polyimide and PMMA [95],

$$U_f = 2.327 \text{ km/s} + 1.34 u_f \tag{5.7a}$$

$$U_t = 2.6 \text{ km/s} + 1.52 u_t. \tag{5.7b}$$

Using the data collected, the calculated flyer densities are shown in Table 5.5. The results show the density in the flyers on impact increased with their thickness. This trend persists when taking into account the maximum error in the predicted velocity, corresponding to the percentage error in the predicted arrival times shown in Table 7.4. The magnitude of the flyer density corresponds to the predicted maximum flyer pressure predicted by the 0D model. Fig. 5.10a shows the thicker the flyer, the higher the maximum flyer pressure on impact. Similarly, the experimental results find the density of the flyer on arrival increases with flyer thickness. This provides evidence for a more definitive mechanism for maintaining thick flyer integrity on long rise time machines. The thicker the flyer, the higher the maximum flyer pressure throughout flight and the higher the density of the flyer. If the flyer remains dense throughout flight, the foil plasma accelerating it cannot break through the flyer and the flyer maintains its planarity and form. It should be noted that while this method has been utilised in the past by Song *et al* to calculate the flyer density in their work [15], the Hugoniot equations provide an approximation of the density only. In the future, better estimates of the density could be made with validated simulations.

Finally, the efficiency of the electric gun was approximated by calculating the kinetic energy delivered to the target divided by the machine discharge energy, based on both the flyer and foil mass and impact speed. The maximum efficiency predicted for this electric gun load was 8.63% in the

2 mm thick flyer. This is below the 25% reported by Osher *et al.*, but remains high for a projectile launcher. For comparison, an aluminium plate flyer of the same mass and surface area as the 2 mm thick polyimide electric gun flyer would have a thickness of around 1.05 mm. For this load geometry, the 0D model predicts that the impact speed of the aluminium plate flyer would be 5.1 km/s, which is equivalent to an efficiency of only 1.8 %. This result suggests the electric gun can deliver more energy to a target than an EM plate for the same machine and load design, due to additional thermal pressures in the exploding foil accelerating the insulating flyer.

Table 5.5 shows the efficiency of the load improved as the flyer thickness increased. This result is likely to be an artifact of M3's long rise time. Thick flyers take longer to launch, thus more energy is deposited in the exploding foil due to the strong electromagnetic forces in the system. As a result, the impact velocity of the 2.0 mm thick flyer is predicted to be higher than the 0.5 mm despite its greater mass. However, the efficiency in the 1.5 mm thick flyer is higher than the 1.0 mm thick flyer, despite having an earlier measured impact time. This suggests that the expansive thermal pressure provides additional acceleration to the flyer. Analysis in Section 5.2.3 and previous work suggests the thermal pressure in the exploding foil builds prior to launch, as the electromagnetic pressure rapidly increases whilst the foil volume remains confined [93]. As the time before launch increases with flyer thickness, the thermal pressure becomes greater, contributing greater expansive acceleration forces and therefore improving the load efficiency.

5.2.5 Conclusions

In this work, the relationship between flyer integrity and the current rise time in flyers launched using an electric gun load was explored to determine the mechanism behind previously researched damage to thick flyers. Firstly, a simplified 0D numerical model was used to simulate the dynamics and maximum flyer pressure of a 1.5 mm thick flyer, launched using identical electric gun loads on two pulsed-power devices with different rise times. The temporal evolution of the maximum flyer pressure using the short rise capacitor bank CEPAGE was found to rapidly increase, before dropping significantly after the current rise time. The time taken to launch thick flyers was longer, due to its higher inertia and delays in communication of the pressure waves. As a result, the pressure in the flyer dropped shortly after launch. On the other hand, the thick flyer launched using the long rise time pulsed-power device M3 was found to maintain high pressures in the flyer until impact. After comparing the two cases, it was proposed that the maintained pressure in the thick flyers on long rise time devices was beneficial in preventing the flyer from breaking up.

To investigate the hypothesis that the extreme pressure state in flyers on long rise time devices contributed to their successful launch, a series of electric gun shots were performed on M3. The data collected from these shots, in combination with impact speeds predicted by the 0D model suggested the high pressures in the thick flyers contributed to maintaining a high density region at the foil-flyer interface. Referring to the questions initially posed in the introduction, it was concluded:

- The maximum pressure in the flyer is related to the magnitude of the current, therefore, on long rise time machines higher pressures are maintained in the flyer. The pressure in the flyer throughout flight increases with flyer thickness, due to the flyer's constant contact with the high electromagnetic pressure foil driving it.

- Experimental results from electric gun shots on M3 found that thicker flyers had higher density on impact. Thin flyers with lower pressures were found to experience plasma breakthrough and disassembly at late times.

- The dynamic performance of the electric gun was found to improve as the pressures in the foil and flyer increased. Firstly, the thicker flyers were found to have higher density on impact, which led to higher pressures in the target block. Secondly, the experimentally measured efficiencies were found to improve with flyer thickness, due to the greater thermal pressure developed in foils confined beneath thicker flyers. The maximum measured efficiency of 8.6% was over four times greater than an equivalent EM plate flyer.

Through addressing these questions, the mechanism for thick flyer break-up and strategies to improve flyer survivability were determined. Thick flyers are destroyed on the electric gun when their density drops below a certain value, allowing the high pressure foil plasma driving the flyer to break the flyer apart. If the initial pressure rise is sufficient, the flyer will lose its material strength properties. As a result, when the pressure in the flyer subsequently drops so does the flyer density. This causes the flyer's disintegration as it mixes with the accelerating exploding plasma behind it. Flyer destruction can therefore be avoided by either taking care to ensure that the flyer does not reach pressures which cause loss of strength, or conversely, by ensuring the pressures in the flyer remains sufficiently high so as to maintain the flyer density throughout flight. This generalised understanding of the flyer destruction mechanisms allows the 0D model utilised in this work to design and optimise the electric gun for an arbitrary current pulse shape.

5.3 Redesigning the electric gun: launching thick flyers to hypervelocity with high efficiency

The two papers in this chapter consider different aspects of an electric gun load on M3. The previous article addressed the effect of the current rise time on the behaviour of flyers in electric gun loads, resulting in the suggestion of two primary mechanisms by which flyers experience violent state change and disassembly. The second article in this chapter aimed to better define these flyer disassembly mechanisms and present strategies to mitigate them through geometric design.

5.3.1 Abstract

To investigate pressure states as extreme as those involved in inertial confinement fusion using projectile-driven impact, the projectile must be both moving at hypervelocity and thick enough to introduce a shock pulse sufficiently long as to be measured. The electric gun is a highly efficient pulsed-power projectile launcher: its unique drive mechanism has been reported to convert over 25% of a capacitor bank's stored electrical energy to flyer kinetic energy [5]. This high efficiency allows the gun to accelerate thin dielectric flyers to hypervelocity using relatively low energy machines [21]. However, the technique was unable to accelerate thick flyers (>0.5 mm) without causing the flyers significant damage, rendering it unsuitable for investigating extreme states of matter. In this work, previously existing results from the launch of a thin flyer on a low energy machine were analysed using a 0D electric gun model. The pressure states experienced by the flyer during this shot, performed in a well understood region of the electric gun parameter space, were used to inform the design of a new electric gun load, capable of launching thick flyers to hypervelocity. The experimental results of the testing of this load design on a 140 kV, 2.0 µs rise-time machine are presented. The load was found to successfully accelerate intact flyers up to 2.0-mm-thick, introducing shock speeds of over 10 km/s in a PMMA target block, inducing pressures of 80 GPa. This is twice as thick as those reported previously [15]. The outcomes of the study suggest the results from previous low-risk shots can be used to develop electric gun loads in new regions of the design space using simplified modelling tools.

5.3.2 Introduction

The states generated during nuclear fusion are, by necessity, some of the most extreme conditions we are capable of creating. Inertial confinement fusion (**ICF**) achieves these conditions by compressing the fuel in a target capsule to immensely high density and temperature using the inward momentum of an implosion. Our understanding of how the materials in this capsule and the surrounding chamber behave under these extreme conditions is integral to achieving a uniform implosion. Techniques such as projectile-driven impact allow researchers to investigate the behaviour of materials under these extreme pressures in a controlled setting. Electromagnetic (**EM**) projectile launchers are a powerful tool for extreme-state research: flyer plates, for example, are capable of generating planar shocks of multi-megabar pressures for microseconds over large volumes of a target material [20]. Whilst the measurements from the highest energy electromagnetic launch platform, the Z accelerator, result in higher precision measurements than can be achieved using laser drives such as NIF, the launch technique's limited efficiency prevents it from generating pressures over around 20 megabars [9].

The electric gun is an electromagnetic projectile launcher which utilises the discharge of current from a high-energy pulsed-power device to accelerate dielectric flyers to over 20 km/s [21]. The current passes through a metallic foil, which experiences extreme joule heating and rapidly changes state, from solid to plasma. The foil plasma increases in volume and 'explodes', driving an adjacent dielectric flyer as it expands, applying a thermal acceleration pressure to the flyer. Simultaneously, strong currents in the system generate Lorentz force which further accelerate the foil and consequently the flyer [94]. It is favoured for its highly planar flyer impact and long stand-off distance without use of a sabot (up to 30cm) [67]. The electric gun can be thought of as a hybrid between an electromagnetic (**EM**) flyer plate and an exploding foil initiator (**EFI**), harnessing both the electromagnetic acceleration in a flyer plate and thermal acceleration present in an EFI. As a result, the electric gun has demonstrated a higher efficiency of conversion from electrical capacitor bank stored energy to projectile kinetic energy than the flyer plate (up to 25% compared to around 4%) [5, 96]. Figure 5.11 compares further differences between the flyer plate and electric gun load. Most significantly, the current in the electric gun does not pass directly through the flyer. This feature is the origin of the electric gun's second advantage over the EM flyer plate: a greater maximum stand off distance, as the dielectric flyer does not interact with the current directly.

Whilst the electric gun had greater efficiency and stand off distance than alternative electromagnetic launchers, it was not capable of launching flyers over 1 mm thick to hypervelocity without destroying the flyer [15]. Thin flyers cannot sustain a pressure pulse in a sample long enough to obtain meaningful diagnostic data, limiting the gun's application. Modelling the electric gun requires a sophisticated hydrocode, able to capture both magneto-hydrodynamics (**MHD**) and material equation of state in the foil and flyer. Restricted access to such codes prevented researchers from investigating the mechanism behind the flyer disassembly, halting the development of the technique [57]. Recent efforts to address

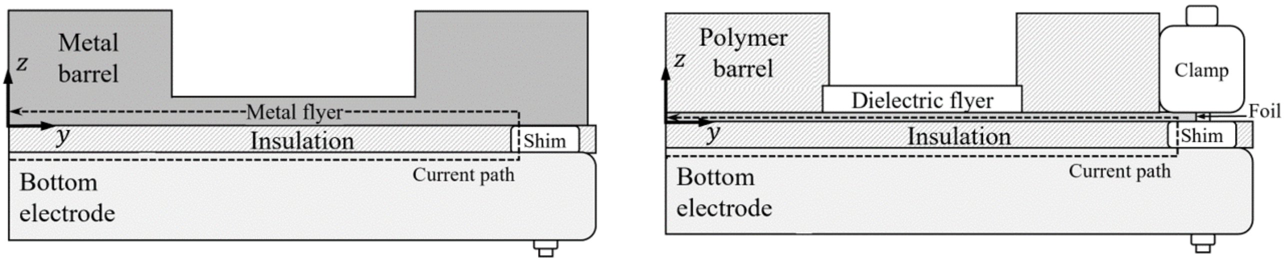

Figure 5.11: A flyer plate configuration used at First Light Fusion (left) [68] and a standard electric gun configuration (right). In an electric gun, the current passes through a thin metal foil which drives a dielectric flyer, instead of directly through a thicker metal foil in a plate flyer.

this issue led to the creation of an accessible 0D model capable of predicting the pressure states and dynamics of both the foil and flyer [93]. The model was used to design a 1.2 MJ electric gun for M3, a 140 kV pulsed power device at First Light Fusion, capable of launching thick flyers to hypervelocity [96].

5.3.3 Background: Flyer destruction mechanisms

To take advantage of the electric gun as a tool for extreme state research, it was necessary to redesign the gun to be able to launch thick flyers. Initially, researchers seeking to optimise the electric gun asserted it was beneficial to minimise the current rise-time of the capacitor bank powering the acceleration [24]. However, these set ups were unable to launch thick flyers (over 0.5 mm thick) to hypervelocity without incurring catastrophic damage to the flyer [58]. More recently, Song *et al.* succeeded in accelerating a 1-mm-thick flyer to hypervelocity. They suggested their long machine rise-time (1.8 µs) contributed to maintaining the integrity of the thicker flyer. However, in both scenarios, the researchers were unable to model or experimentally diagnose the flyer state, and thus were unable to investigate the mechanisms driving these results.

To understand these seemingly conflicting results, the 0D electric gun model created by Fitzgerald *et al.* was used to simulate the response of an identical electric gun load powered by a short rise-time machine (CEPAGE) and a long rise-time machine (M3) [96]. CEPAGE is a 70 kV, 0.5 µs rise-time machine and M3 is a 140 kV, 2.0 µs rise-time machine, both located at First Light Fusion. Specific details of both machines are given in Table 5.6. At the conclusion of this analysis, it was proposed that flyers can be destroyed during launch or flight if the flyer density becomes too low, allowing the foil plasma driving the flyer to break through the flyer, causing it to disassemble. This density decrease can occur by different mechanisms:

1. The density in the flyer can fall due to spallation at the front surface of the flyer if the pressure at the foil-flyer interface rises to an extreme magnitude then falls in quick succession. This effect occurs most significantly during the launch process. After current start, the flyer cannot move off until pressure information from the exploding foil is communicated to its front. During this time, the foil, trapped beneath the flyer, experiences a rapid increase in thermal pressure. This drives strong pressure waves from the foil-flyer interface to the flyer front. When the flyer moves off, providing free space for the foil to expand into, the thermal pressure in the foil quickly dissipates and the pressure at the foil-flyer interface drops rapidly. If the strong reflected tensile waves propagated prior to launch meet a region of lower pressure at the foil-flyer interface, the material in the region releases and the density drops. When the flyer is thicker, it takes longer to launch, therefore the thermal pressure in the foil builds to a greater magnitude, causing a more substantial density drop when the thermal component falls off after launch. It should be noted, the impact of the non-uniform explosion across the foil due to edge effects is avoided by ensuring the width of the foil is greater than the width of the flyer and barrel.

2. The density in the flyer can fall if the pressure driving the flyer at the foil-flyer interface drops too low prior to impact. This typically occurs after the current peak, as the magnetic pressure in the foil driving the flyer is proportional to the square of the current density. If the time to launch is significant compared to the rise-time of the pulsed-power device driving the load, the pressure in the flyer can fall to near zero early in flight, quickly losing density as a result. The effect of Joule heating in the dielectric flyer as a consequence of it melting was neglected in this study, however, may merit consideration in future work.

Consequently, to launch thick flyers to hypervelocity, the variation in the maximum pressure before and after launch should be limited to avoid the flyer releasing into a low-density state. Secondly, the current rise-time must be long enough to sustain the pressure in the flyer such that its density does not drop before impact. In the following sections, the 0D model is used to design an electric gun load which fulfils both these requirements.

5.3.4 Method: 0D electric gun model

The 0D model utilised in this investigation has the novel capability of calculating the pressure state in the dielectric flyer throughout launch and flight [93].It achieves this by breaking the foil and flyer into three points, the rear of the foil (z_r), the foil-flyer interface (z_i) and the flyer front (z_f), tracking

Table 5.6: Machine parameters for pulsed-power capacitor banks M3 and CEPAGE.

Parameters	M3	CEPAGE	[units]
Charge voltage	140	60	[kV]
Capacitance	124.8	32.0	[µF]
Fixed resistance	0.1	3.0	[µΩ]
Fixed inductance	12.5	5.4	[nH]

the velocity of each point individually. The model is flexible, with a number of input parameters, including the geometries of the foil and flyer (shown in Figure 5.12) and machine parameters which allow it to calculate results for a wide range of load designs. Previous verification work demonstrated the pressure state at the foil-flyer interface (P_i) can be calculated using a linear function between the maximum pressure in the foil (P_{max}) and its position relative to z_{i} and z_{f}, illustrated in Figure 5.13 [93]. A parameter scan in the same work across different foil widths, foil and flyer thicknesses demonstrated the model's prediction of the temporal evolution of P_{i} during acceleration was most significantly influenced by the foil width, flyer thickness, and input current profile.

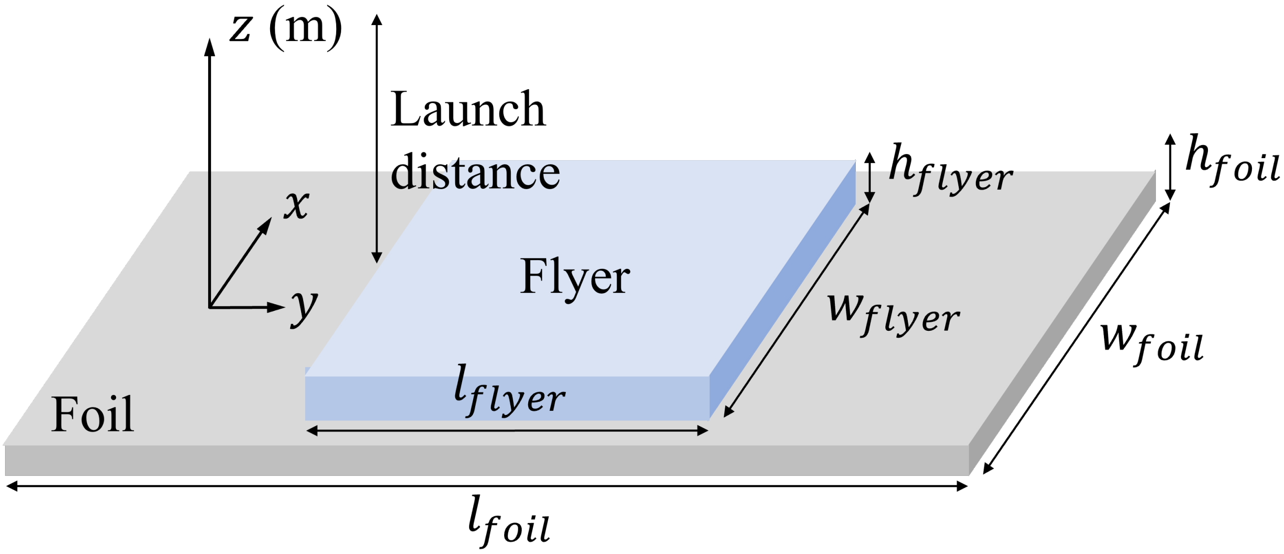

Figure 5.12: Simplified diagram showing the electric gun load set-up. The 0D model allows the user to input detailed parameters regarding the foil, flyer, and capacitor bank. These include the foil and flyer material and dimensions, and the capacitor bank parameters necessary for calculating the system current at each timestep

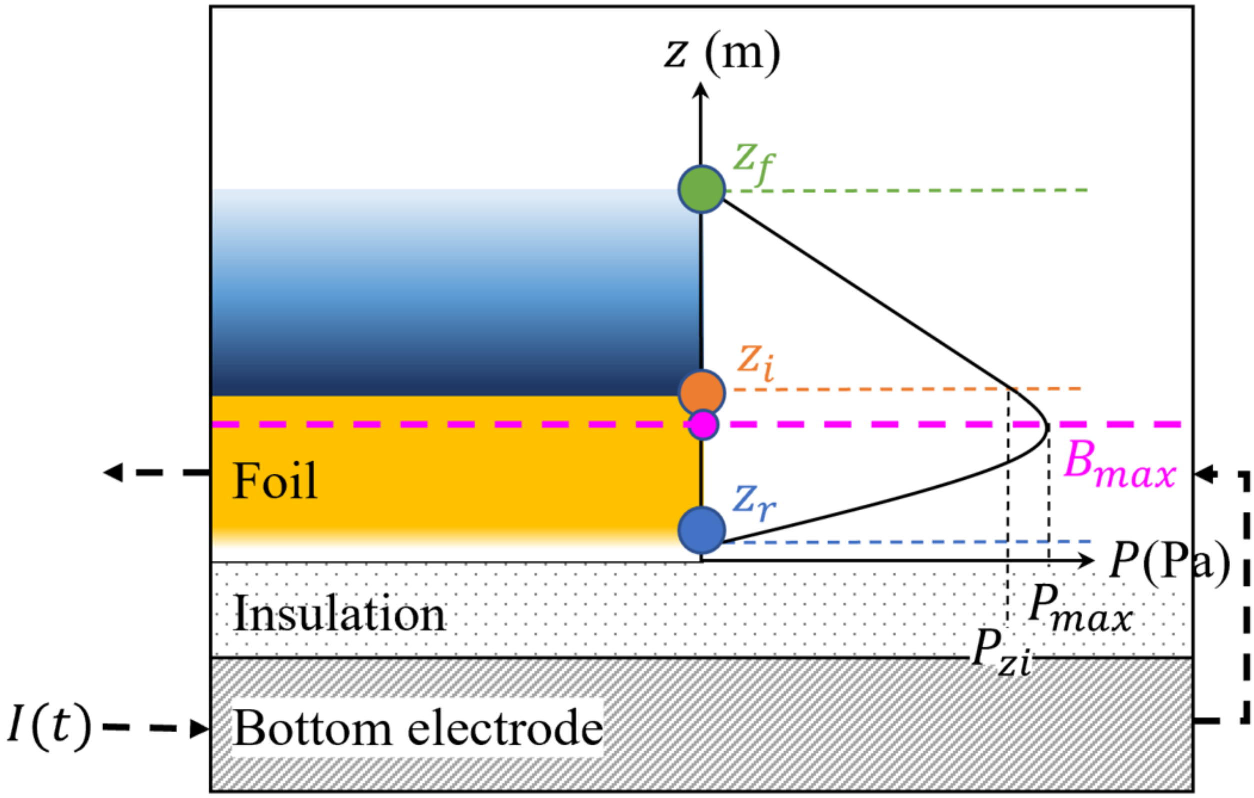

Figure 5.13: The positions of the four points used to determine the pressure at the foil-flyer interface, alongside the velocities used to approximate the foil-flyer dynamics. The model assumes the foil and flyer form a continuous interface, with pressure at the front of the flyer set to zero and a linear pressure gradient between z_{Pmax} and z_f.

5.3.5 Design: Launching thick flyers on M3

The constraints outlined in Section 5.3.3 included ensuring the flyer pressure state remained relatively steady before target impact and during launch. To ensure the pressure state did not drop too low in the thick (>1 mm) polymer flyers before impact, M3 was selected as the pulsed-power driver for its long rise-time. Preventing the flyer from experiencing disintegration during launch was a more complex requirement. The 0D model was unable to directly calculate the flyer density, hence it was unclear what magnitude of pressure drop after launch would cause plasma to break through the flyer. Instead, existing knowledge of a previous successful electric gun shot was used to guide the design of the thick flyer electric gun load for M3.

The 0D model was used to predict the pressure states experienced by a flyer in an electric gun load driven by CEPAGE. In this shot, a 0.7-mm-thick Delrin flyer, driven by a 0.1-mm-thick Al foil, was accelerated to 8.2 km/s over 6.8 mm flight distance whilst successfully maintaining flyer integrity. The geometric parameters of the load are listed in Table 7.1. The 0D model was

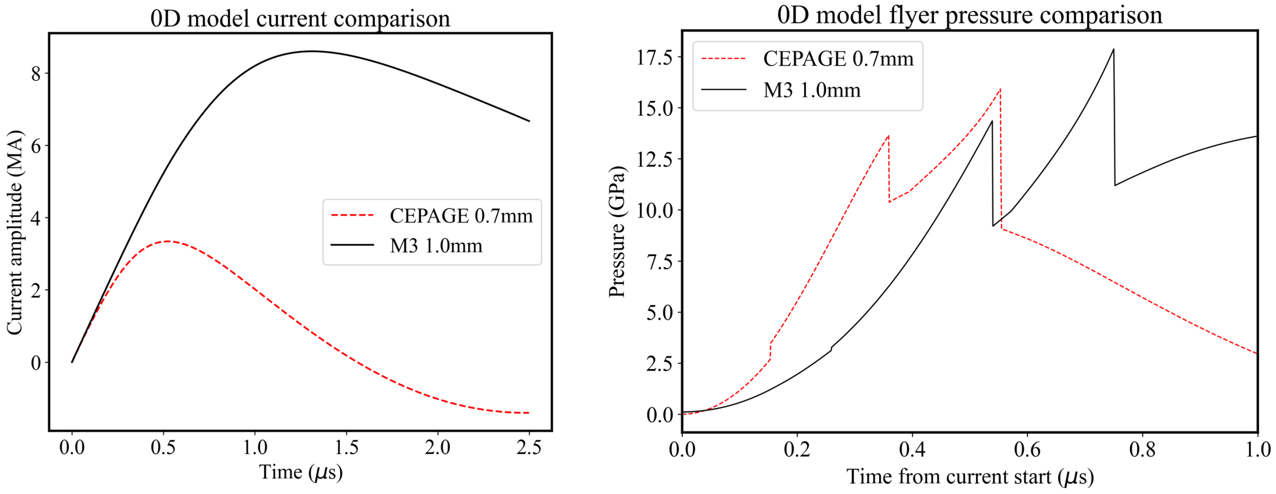

(a) **(b)**

Figure 5.14: Plot showing the current (a) and maximum flyer pressure state (b) calculated by the 0D model for the CEPAGE and M3 load specified in Table 7.1. The magnitude of the pressure peaks in the M3 load closely matches those experienced by the flyer shot on CEPAGE.

then used to design an electric gun load on M3 which produced a similar flyer pressure profile during launch in a 1.0-mm-thick polyimide flyer.

The parameters of the M3 load which can be varied to limit the maximum pressure state of the flyer are illustrated in Figure 5.12. Of these parameters, previous verification work revealed both the 0D model and the in-house MHD hydrocode **B2**, predicted that the parameter most strongly influencing the magnitude of the pressure state of a thick flyer for a fixed current input was the foil width (w_{foil}) [93]. The 0D model was used to scan across foil widths, the results of which suggested $w_{\mathrm{foil}} = 25$ mm would be optimum. The current profiles calculated by the model are contrasted in Figure 5.14a. Figure 7.7a compares the pressure in the flyer during the CEPAGE shot and a 24×24×1.0 mm thick M3 flyer driven by a 25×50×0.1 mm Al foil. The flyer was deliberately undersized to avoid asymmetries in the burst at the edges of the foil [14]. The plot demonstrates the maximum pressure peaks in the M3 flyer are similar in magnitude to those experienced by the flyer shot on CEPAGE.

5.3.6 Experimental setup

The experimental setup used to test the electric gun load designed to launch thick flyers is shown in Figure 5.15. The shock speed in a target was found by projecting a 1D line of laser light through a transparent PMMA (polymethyl-methacrylate) block. As the flyer impacts the block, it induces a shockwave of a high enough pressure (over 20 GPa) to turn the PMMA opaque, thus blocking

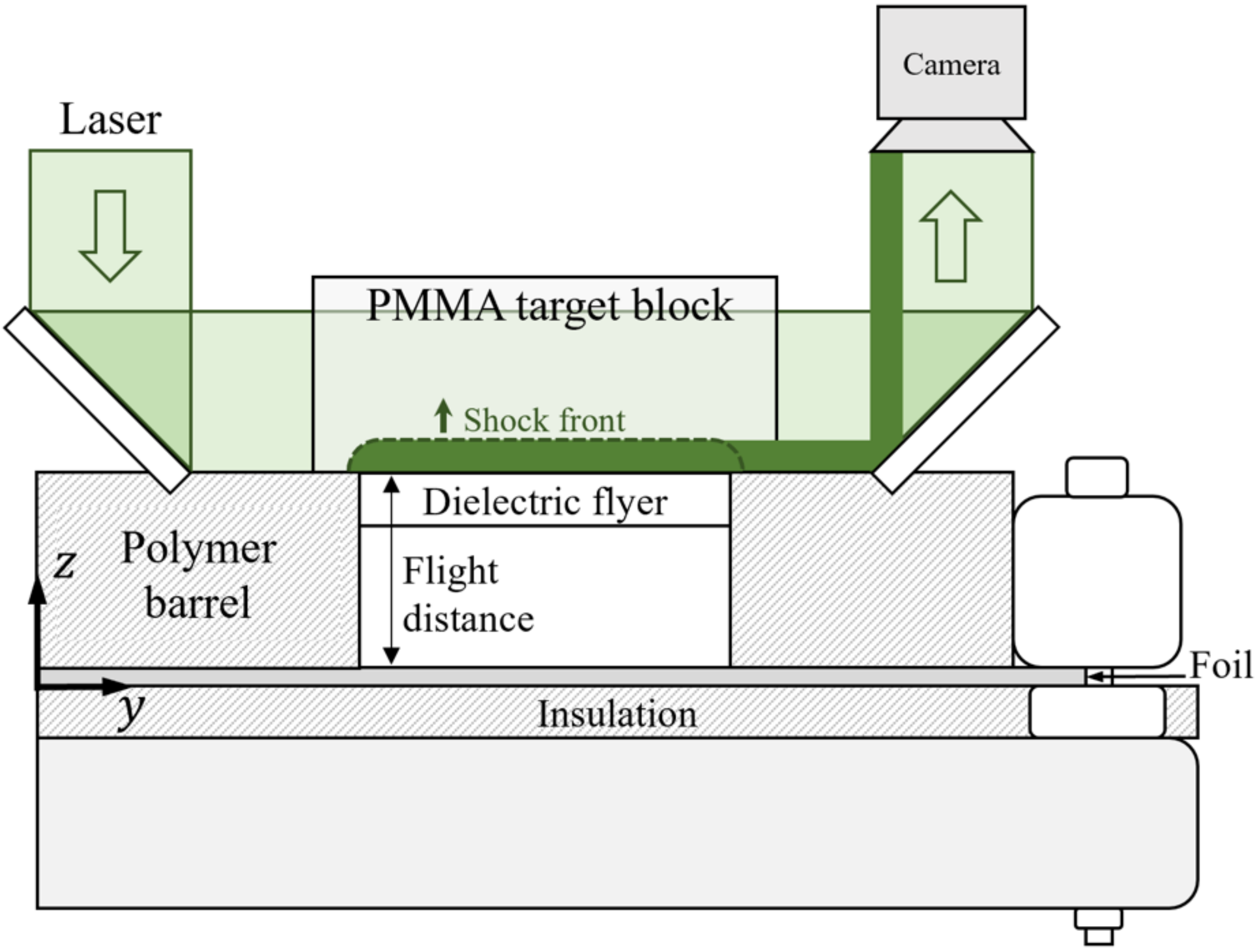

Figure 5.15: 1D laser streak capturing shock velocity profile in the target block and (4) high-speed imaging of the PMMA target block showing the shock front in 2D.

the laser light. The reflected laser was captured by a streak camera, and the position of the shock front through the block was tracked through time. This process is illustrated in Figure 5.15. The shock speed, alongside a high-speed camera imaging the target block in 2D to capture the shock shape and evaluate the flyer planarity, were used to determine whether the flyer had disassembled before impact. The aluminium foil used was 99% purity tempered annealed and the polyimide was 100% DuPont Kapton HN Polyimide film (Cirlex).

5.3.7 Results

The shock speeds in the PMMA target block were successfully measured for a 1.0-mm, 1.5-mm, and 2.0-mm-thick polyimide flyers, the values of which are shown with other parameters in Table 5.8. The high shock speeds (each over 9 km/s) in the target block indicate it was struck by a polyimide flyer, not low-density foil plasma, as would be expected if the flyer had broken up. This suggests

Table 5.7: Electric gun load parameters used in 0D simulations.

Load Parameters	CEPAGE load parameters	M3 load parameters
Foil length	12.0 mm	50.0 mm
Foil width	12.0 mm	25.0 mm
Foil thickness	0.1 mm	0.1 mm
Foil material	Aluminium	Aluminium
Flyer length	12 mm	24.0 mm
Flyer width	12 mm	24.0 mm
Flyer thickness	0.7 mm	Varying
Flyer material	Delrin	Polyimide
Current amplitude	1.2 MA	8.0 MA
Current rise-time	0.6 µs	2.0 µs

Table 5.8: Electric gun shot results using load designed in Section 7.2.4, $0.1 \times 25 \times 50$ mm Al foil, 24×24 mm polyimide flyer.

Shot no.	Flyer thickness (mm)	Flight distance (mm)	Maximum shock speed in target (km/s)	Flyer survived until impact
1	1.0	9.0	9.55	Yes
2	1.5	9.0	9.8	Yes
3	2.0	10.0	10.6	Yes

the flyers did not disassemble before impact. This result is further supported by 2D images of the shock captured by the high-speed camera. Figure 5.16 contrasts images taken from the target impact during a shot with plasma break through and a successful shot without. If a flyer disassembles, the bright, high velocity foil plasma driving the flyer escapes ahead of the main flyer body, striking the block first. This event is distinctive, as the plasma illuminates the block and the shock speed in the block is below 5 km/s. As a result, it can be asserted with high confidence the thick flyers tested on M3 were accelerated to hypervelocity whilst maintaining their integrity.

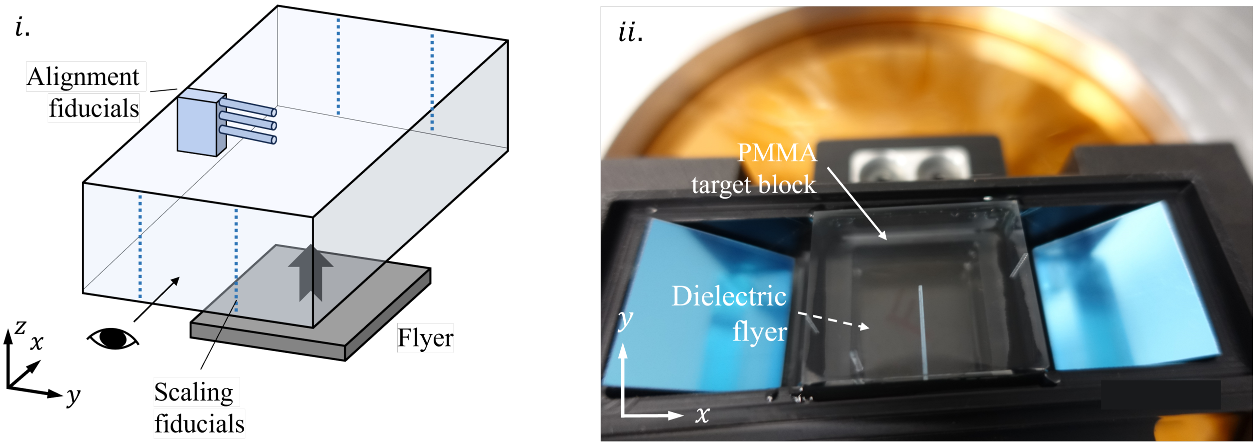

(a) Illustrations of the PMMA target block, with direction of flyer impact indicated by arrow (*i*). Image of the PMMA target block and flyer viewed from above (*ii*).

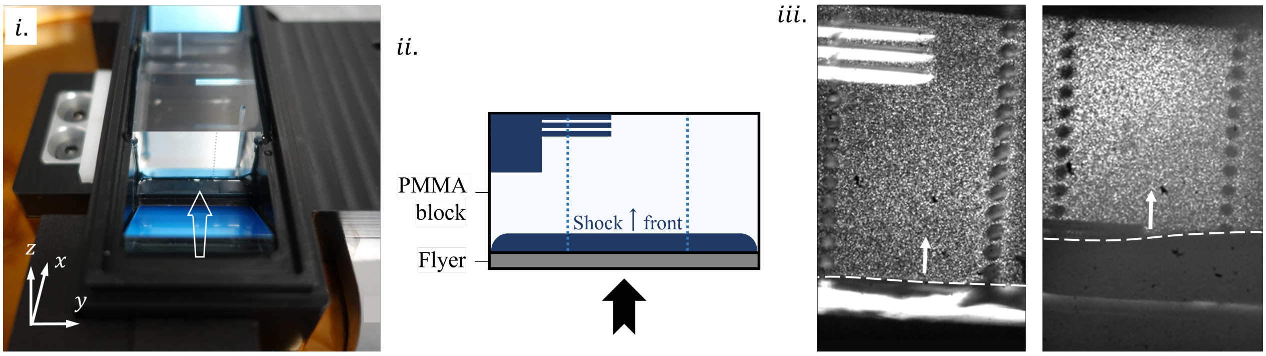

(b) Image of the PMMA target block with the shock direction labelled (*i*). The fiducial features on the PMMA block can be identified in the images taken using high-speed imaging (*ii*). The frames from the high-speed imaging show the shock front generated in the block by a disassembled 0.25 mm flyer (*iii* left) and an intact 1.0 mm flyer (*iii* right). When the flyer experiences disassembly, bright foil plasma will break through the gaps and is clearly visible on impact.

Figure 5.16: Illustrations of the PMMA target block and images of shock fronts taken by high-speed imaging.

5.3.8 Discussion: Electric gun efficiencies

The arrival of the strong shock in the PMMA block provided the impact time for each shot. These experimentally measured impact times were compared to those predicted by the 0D model. The predicted impact velocities were used to calculate the efficiencies, defined as the ratio of stored electrical energy converted into kinetic energy in the flyer, of the 1.2 MJ load on M3. Table 5.9 shows the efficiency of the load increases with flyer thickness.

It was proposed that the high efficiency of the electric gun was a result of both magnetic and thermal contributions to its acceleration [21]. The efficiency of the launch technique was found to be optimised when the 'foil burst' was synchronised with the current peak, as the amount of energy

Table 5.9: Efficiency is considered to be the combined kinetic energy of the foil and flyer divided by the electrostatic energy initially stored into the capacitor bank of the machine.

Flyer thickness (mm)	Predicted impact speed (km/s)	Efficiency %
1.0	10.05	4.10
1.5	10.1	5.88
2.0	10.75	8.63

converted to thermal pressure was maximised [24]. Whilst foil burst was defined as the time that the foil exploded, it was experimentally measured by Chau *et al.* by obtaining velocimetry measurements from the surface of dielectric flyers [22]. Burst approximately coincides with the movement of the flyer surface (referred to in this work as launch) when the flyer is thin. However, this assumption becomes invalid for thick flyers, as the time for the pressure information to pass from the foil-flyer interface to the flyer front becomes non-negligible. The results in Table 5.9 demonstrate the efficiency of the electric gun load increased with flyer thickness. This suggests the efficiency of the electric gun increases when the current rise-time is synchronised with flyer launch as opposed to foil burst. Thus, to launch thick flyers efficiently, the load should be designed to ensure the flyer launch at a similar time for a fixed machine rise-time, or the current rise-time should be adapted to match the desired flyer thickness.

5.3.9 Conclusions

In this work, an electric gun load was designed to launch thick flyers to hypervelocity. This was accomplished by firstly considering the likely mechanisms of flyer disassembly. These mechanisms were proposed by using information collated from prior studies to inform a numerical investigation using a 0D electric gun model [5, 15, 96]. This work suggested flyers can be destroyed on electric guns either by plasma breaking through the flyer later in flight, or due to flyer failure during launch. To avoid the former, a long rise-time machine, M3, was selected to drive the load. The latter informed the geometric design of the load: a 0D model was used to select a foil width which would ensure the flyers shot on M3 experienced similar pressure states to a successful, safer, shot on a lower energy machine. The experimental testing of the load demonstrated successful launch up to 2-mm flyer thickness to hypervelocity over a flight distance of 10 mm. This was twice as thick as had been achieved previously [15]. The 2-mm-thick flyer was found to be launched with the highest efficiency, due to the greater conversion of electrical energy to thermal pressure during the extended time prior to flyer launch. These results suggest:

1. The mechanisms for flyer destruction can be avoided by controlling the temporal evolution of the maximum pressure in the flyer.
2. Successful results from lower risk shots on smaller machines can be used to inform the design of more energetic electric gun loads.
3. The efficiency of the electric gun can be improved by synchronising the time of launch and the current rise-time.

With the invention of a load which can launch thick flyers, the benefits of the electric gun's high efficiency and stand-off distance can now be exploited in extreme state research. This could allow researchers to reach unexplored regions of phase space using existing pulsed-power platforms.

5.4 Summary

This chapter explored the experimental testing of an electric gun load on the pulsed-power machine M3. An investigation was performed utilising the 0D model, created in the previous chapter, to contrast the behaviour of an identical electric gun load driven by CEPAGE and M3. CEPAGE and M3 are both fixed rise-time devices located at First Light Fusion, however, CEPAGE has around half the charge voltage and rise-time. CEPAGE is analagous to the typical pulsed-power devices used in the majority of the literature examined in Sections 2.3 and 2.4. On the other hand, M3 is a long rise-time machine, with higher stored energy than any discussed in open literature. Song *et al.* reported successfully launching flyers up to 1.0 mm thick using a capacitor bank with a similar rise-time to M3. Thus, roughly, the pressure states in a thick flyer accelerated by CEPAGE would be expected to cause it to disassemble, but survive if accelerated by M3.

The study revealed two key behaviours which appear to have a significant effect on the flyer state. Firstly, when the foil is thin enough that it vaporises prior to launch, it exerts a considerable thermal pressure on the dielectric flyer. This thermal pressure builds until the flyer launches, after which point the pressure dissipates as the flyer moves up the barrel, giving the foil space to expand into. Secondly, the time taken to launch the flyer in the electric gun is dependent on the time required for the pressure information to cross the thickness of the flyer, hence thicker flyers take longer to launch. Consequently, if a rapid rise-time machine is used to accelerate a thick flyer, the flyer can end up being launched after the current peak. When the electric gun load has both a thick flyer and a short rise-time machine, this results in the pressure in the flyer rapidly rising and falling around launch. It was suggested this violent pressure peak resulted in spallation at the leading surface of the flyer, which, if significant enough, could account for the observations made in literature of thick flyers disassembling shortly after launch. When the machine rise-time is longer than the time taken to launch the flyer, the current magnitude continues to rise and thus, the reduction in pressure after launch is minimised.

The work performed in this chapter also led to the discovery of a second mechanism by which flyers can be destroyed during acceleration. Counterintuitively, the only flyers which experienced plasma breakthrough were the thinnest, at late times in flight. When considering the pressure states in the flyers predicted by the 0D model, it was observed the pressure can drop in the flyers later in flight. This resulted in the suggestion that the flyers were destroyed when their density dropped at late times. However, this explanation does not provide a specific mechanism by which the plasma breakthrough is initiated. This process of flyer disassembly at late times is explored in more detail using two-dimensional simulation in the next chapter.

A number of objectives were met in this chapter, including the following from both Research Goal 1 and 2:

- **The model must be able to be used as a tool to guide the experimental design of electric gun loads in new parameter spaces.**

  This chapter is comprised of two publications, both of which document the use of the 0D model created in the previous chapter. The details of previous successful low-risk electric gun shots (i.e. accelerating thin flyers using a pulsed-power machine with lower energy) were used to predict the pressure states experienced by flyers known to remain intact. The width of the foil and pier were then adjusted to achieve a similar pressure profile in a thick flyer on M3 at launch. This resulted in the successful launch of flyers up to 2 mm thick to over 10 km/s.

- **Develop a repeatable diagnostic set-up to make measurements from an electric gun load.**

  Practical adaptations made to the electric gun diagnostic set-up, which resulted in a demonstrably improved quality of data including ensuring the foil width was wider than the flyer, fitting the flyer into a recess in the barrel and adding plasma shielding atop the join between the foil and the top electrode. These steps reduced the chance of foil plasma entering the barrel or mirror mount, preserving a clear line of sight throughout flyer launch, flight and impact.

- **Explore the effect of current-rise time on the behaviour of the electric gun using modeling and experimental testing.**

  Literature reviewed in Chapter 2 evinced the behaviour of the electric gun load is sensitive to the current profile of the machine used to drive it. The studies in this chapter revealed the flyer state is closely linked to the magnitude of the current and the machine rise-time.

- **Investigate the states of thick flyers accelerated by an electric gun load using modeling and experimental testing.**

  Flyers from 0.25 - 2 mm thick were accelerated using the electric gun load designed for M3. It was found that thick flyers had a higher density on impact with a target than the thinner flyers. It was posited their high density was a result of the higher pressure states in the thick flyers, caused by the location of the foil-flyer interface relative to the maximum pressure in the foil and the flyer front.

- **Understand the mechanism by which stored electrical energy is converted to kinetic energy in the flyer in an electric gun load and how the efficiency of this process can be improved.**

  The studies in this chapter demonstrated the efficiency of the electric gun load on M3 improved as the flyer thickness increased. The efficiency of the 2 mm-thick-flyer-load was 8.6%, around four times greater than the efficiency predicted for a EM flyer plate of equivalent surface area and mass. The electric gun has a better efficiency than the EM flyer plate due to additional thermal pressures contributing to the kinetic energy in the flyer. Further, the thermal pressure in the foil prior to launch increases with flyer thickness. Consequently, it was suggested more electrical energy is converted to thermal energy in the foil, and thus, kinetic energy in the flyer, when the flyer is thicker.

Chapter 6

Simulation of the electric gun in an Eulerian hydrocode

In this chapter, a material strength model was integrated into the Eulerian MHD hydrocode B2 and benchmarked through cross-code comparison with Ansys AUTODYN. This model was then used in 2D simulations of the electric gun, incorporating approximations to account for complex load geometry and current loss mechanisms. A fixed current loss factor was applied to mimic parasitic currents, tuned to match experimentally measured velocity profiles. These simulations, validated by experimental data from Chapter 5, revealed new insight into the dynamics and deformation of the foil and flyer, including the formation of Rayleigh-Taylor (**RT**) instabilities at the foil-flyer interface. These instabilities, which grew significantly during acceleration, could provide a more detailed explanation for the plasma breakthrough in observed experimentally in thin flyers at late times. While material strength was a secondary consideration in the explored electric gun load designs, it may be significant in loads using dielectric flyers with higher melting temperatures. The chapter addressed the objectives of Research Goal 3, including validating the strength model against AUTODYN, ensuring its usability in electric gun simulations, analysing the effect of material strength on electric gun loads, and proposing a mechanism for flyer destruction due to RT instabilities.

6.1 Introduction

The examination of existing literature revealed that research on the electric gun launch technique has predominantly relied on experimental observations, particularly preceding the 1990s at LLNL, when access to sophisticated modeling tools was limited. As a result, parameters crucial to electric gun optimisation, such as foil and flyer thickness, flight distance, and current rise time, were primarily optimised based on experimental evidence. Furthermore, in the modern era, the electric gun's infrequent utilisation has resulted in few detailed modeling efforts. The most comprehensive modeling endeavors (in open literature) utilised a 1D MHD Lagrangian code, typically incorporating an equation of state the foil material, but not the flyer. This approach, suitable for thin flyer simulations, is incapable of predicting the violent state changes experienced by thick flyers during acceleration. To address this limitation, a more comprehensive modeling framework involving two-dimensional simulations and incorporation of an equation of state within all components of the load becomes imperative.

In the case of the EM flyer plate, a range of multi-physics was identified as necessary to accurately replicate experimental results; including MHD, equation of state, and material strength. Consequently, this work adopted a similar approach for modeling the electric gun load. At the outset of this DPhil, access to a hydrocode encompassing all required multi-physics capabilities was lacking. The closest option available was First Light Fusion's in-house hydrocode, B2, which lacked only a material strength model. This prompted the incorporation of a robust material strength model within B2 to facilitate the investigation of thermodynamic states in a range of flyer thicknesses in the electric gun load tested on M3 in Chapter 5.

In this chapter, the results from the previous chapters are reviewed to identify the questions focused on in this chapter, including uncertainties in the flyer disassembly mechanisms at late flight times. This is followed by:

1. A journal style paper describing the material strength model incorporated in B2 and its validation through a cross-code comparison with the commercial code, Ansys AUTODYN [97].

   Practical methods for the implementation of material strength into an Eulerian hydrocode

   This article is in review at the Journal of Computational Physics.

   The contributions of M. Fitzgerald include: the writing and incorporation of a strength model into B2, alongside the encoding of face-centred domain boundary and advection routines; the conceptualisation and encoding of the interface grid, scaling of the yield density factor, and shear component of the artificial viscosity; the simulation of the testcase and the benchmarking analysis and; the writing and editing of the original document. They do not include: the writing of any other modules of B2, such as the hydrocode, MHD, interface tracking methods or parallelisation routines; the simulation of the testcase in AUTODYN or; the conceptualisation of the yield density factor.

2. A section exploring 2D simulations of the electric gun load performed in B2. This portion of the chapter is not intended to be submitted as a journal article.

This chapter aims to understand the physical phenomena occurring in the electric gun load during the acceleration of flyers of varying thicknesses.

6.2 Review of previous chapters

A key challenge in the operation of the electric gun, discussed throughout this thesis, is the susceptibility of its flyers to disassembly during acceleration. The literature review investigated electric gun experiments performed by Osher *et al.* at LLNL. Osher suggested thick flyers were destroyed when accelerated by the exploding foil due to the magnitude of the force on the flyer. Their analysis relied upon results from a 0D model, capable of calculating states in the foil and radiograph images of a chunky projectile disassembling during flight. Work undertaken researching electric guns at First Light Fusion prior to this DPhil included testing electric gun loads on the pulsed-power devices CEPAGE and M3. CEPAGE (70 kV, 0.5 μs) has a similar stored energy but a shorter rise time than the pulsed-power device used by Osher *et al.* (60 kV, 1.1 μs). Researchers at First Light fusion found CEPAGE successfully accelerated 0.5 mm thick flyers to velocities over 12 km/s up to 10 cm away, however, the same load driven by the higher energy machine, M3 (140 kV, 2.0 μs), destroyed all flyers tested. This included 1.0 mm thick flyers made of polymers, alumina and sapphire. These results align with Osher's narrative: that the flyers were disassembling because they were experiencing ‘too much’ force during acceleration, but did little to illuminate the mechanism by which these flyers were being destroyed.

In Chapter 5, the response of the flyer pressure state of thick flyers driven by different pulsed-power devices was investigated. The results of modelling and experimental testing of an electric gun load designed to launch thick flyers on M3 demonstrated that thin flyers disassembled at late times. On the other hand, thick flyers (up to 2 mm) not only survived acceleration, but arrived at the target block with higher density. The work concludes that electric gun flyers, thick or thin, experience disassembly if the foil plasma breaks through the flyer. This break through process can occur if the density in the flyer drops too low during acceleration. Ultimately, the work theorised the density in the flyer can drop due to two different events:

1. The density in the flyer can fall if the pressure at the foil-flyer interface rises to an extreme magnitude then falls in quick succession. This effect occurs most significantly during the launch process. After current start, the flyer cannot move off until pressure information from the exploding foil is communicated to its front. During this time, the foil, trapped beneath the flyer, experiences a rapid increase in thermal pressure. This drives strong pressure waves from the foil-flyer interface to the flyer front. When the flyer moves off, providing free space for the foil to expand into, the thermal pressure in the foil quickly dissipates and the pressure at the foil-flyer interface drops rapidly. If the strong reflected tensile waves propagated prior to launch meet a region of lower pressure at the foil-flyer interface, the material in the region releases and the density drops. When the flyer is thicker, it takes longer to launch, therefore the thermal pressure in the foil builds to a greater magnitude, causing a more substantial density drop when the thermal component falls off after launch.

2. The density in the flyer can fall if the pressure driving the flyer at the foil-flyer interface drops too low prior to impact. This typically occurs after the current peak, as the magnetic pressure in the foil driving the flyer is proportional to the square of the current density. If the time to launch is significant compared to the rise-time of the pulsed-power device driving the load, the pressure in the flyer can fall to near zero early in flight, quickly losing density as a result.

These mechanisms serve to unify the somewhat disparate observations recorded thus far: thick flyers were destroyed if accelerated by a fast-rise time machine because the magnitude of the pressure rose and fell rapidly, thin flyers were destroyed on a long rise-time machine because their pressure (and therefore their density) dropped too low late in flight. However, these mechanisms are both qualitative, providing no quantitative measure of how much the magnitude of pressure in the flyer can vary or how low the pressure in the flyer must drop in order for plasma to break through the flyer. To determine this, detailed modelling of the problem was required.

The electric gun acceleration mechanism requires a sophisticated simulation code. It must certainly must be able to capture the magneto-hydrodynamic behaviour of the exploding foil and current path between the bottom and top electrode. It must have an equation of state which is reliable across a range of conditions, for example, from states in the solid metal foil to those in the high pressure, foil plasma. There was also a body of evidence to suggest it needed a material strength model to capture the behaviour of the dielectric flyer, particularly when considering the aims of this DPhil.

To be used as a tool in extreme state research, a projectile launcher must accelerate a flyer with a region with constant density and velocity over a minimum thickness on impact. On the inception of this work, the electric gun could do neither. At this point in the thesis, it can be claimed that an electric gun capable of delivering flyers with sufficient thickness travelling at hypervelocity has been presented. But, the flyer was not ballistic (i.e. still accelerating) on impact and its density gradient was unknown. Other launch techniques achieve a region of thickness with constant density in the flyer by ensuring this region of the flyer remains solid. A simulation code could be used to design an electric gun load which launches solid flyers, potentially necessitating the inclusion of a material strength model to predict its behaviour accurately.

The following chapter describes the implementation of a material strength model into an Eulerian hydrocode, assesses the accuracy of the model implemented before using it to model a number of electric gun loads.

6.3 Strength model

The primary objective of a numerical model is to be able to replicate measurable processes of interest as an alternative to experimental testing, in order to save time and resources. Hydrocodes simulate physical processes by applying rules derived by scientists to materials in a discretised space. How the material and space is defined can be approached in a number of ways, two common examples being either a Lagrangian or Eulerian formulation. In Lagrangian space, materials are made of points which are free to move relative to one another, whereas in Eulerian space, the materials are defined within a fixed grid, through which they are able to move. The accuracy of either formulation strongly depends on the physical processes being modelled. Any system with rapid deformation, such as one involving shock or fluid flow, can generally be represented better by an Eulerian grid. On the other hand, systems with solid parts and fixed interfaces are better captured in Lagrangian space, as each point has its own distinct location.

The accurate simulation of the electric gun requires a wide variety of physics, from material strength behaviour to vaporisation of the metal foil occurring simultaneously. This makes the choice of how to discretise the space more complex. Whilst the system is dominated by the behaviour of the exploding foil, the insulating flyer in the electric gun is initially solid. Though simulations in B2 suggest thick polymer flyers are vulnerable to state change if shocked on acceleration, other high shock impedance materials of interest, such as sapphire or ceramics, are more likely to fail before melting. Further, to increase the versatility of the electric gun beyond ballistic research, it must be able to launch flyers with a region of constant density. The simplest route to achieving this is by launching solid flyers. To be able to model the acceleration of thick solid flyers using an exploding foil, a constitutive model was implemented in B2, FLF's in-house Eulerian MHD hydrocode.

6.4 Practical methods for the implementation of material strength into an Eulerian hydrocode

The strength model implemented in B2 is similar to, but with notable improvements on, the one written for Eulerian MHD hydrocode Gorgon by Pecover *et al.* [90, 98] Like Gorgon, B2 utilises a two-step Eulerian solution scheme over a fixed rectangular mesh. The material strength effects are incorporated into the first step; a Lagrangian step in which the forces on the cells are calculated. This is followed by an Eulerian step which then maps the distorted cells back to the mesh through an advection scheme. To advance the material through the mesh in time, the change in momentum, mass and energy are found at the centre of each cell. As a result, the forces and work due to strength in the mesh must be cell centred values. This outcome is complicated by the differencing sequences involved in their calculation. The following section describes the strength model implemented in B2, the novel developments required to run an electric gun simulation with material strength and a cross code comparison of the model with AUTODYN.

6.4.1 Abstract

This study presents the framework and implementation of a material strength model within a two-step Eulerian solution scheme in the MHD hydrocode, B2. The techniques presented in this work provide the scientific community with practical solutions to problems encountered when modelling the high strain-rate behavior of solids in an Eulerian framework. Novel corrections made to the strength algorithm developed by Pecover *et al.* [98, 99] enabled the accurate reproduction of a Taylor anvil-on-rod test [100] in B2. These corrections include fully defining the logical implementation of the material strength in three-dimensions, ensuring realistic behavior in low-density mixed cells at the rod-vacuum interface, implementing slip conditions at part boundaries, and addressing oscillating numerical instabilities induced by the inclusion of strength. The Taylor test served as a rigorous validation case for the implemented strength model, suggesting its efficacy in analogous scenarios. A cross-code comparison against the results of a Lagrangian simulation in Ansys AUTODYN [97], a

well-benchmarked commercial code, of the Taylor rod deformation revealed a close match with the rod profile predicted by B2. The practical details of the routines required to implement these corrections are provided to facilitate adoption of three-dimensional material strength models in Eulerian hydrocodes.

6.4.2 Introduction

Hydrocodes simulate physical phenomena through the evaluation and evolution of forces and displacements at select points within a discretised space. The manner in which the materials and space are defined can vary, with two common approaches being the Lagrangian and Eulerian formulations. In the Lagrangian formulation, materials are represented by a grid of points that moves with the material flow, while in in the Eulerian formulation, materials are defined within a fixed domain through which they can move. The accuracy of either formulation strongly depends on the physical processes being modelled. Systems characterised by rapid deformation, such as those featuring shock or fluid flow, are typically better represented using an Eulerian grid. Lagrangian meshes become entangled when representing systems with considerable deformation and require high computational resource in three-dimensions due to the large strains typically encountered during these processes. Conversely, systems with solid components, highly-resolved interfaces and damage processes (such as crack propagation) are more accurately captured in Lagrangian space.

Incorporating a material strength model into an Eulerian hydrocode appears conceptually simple. The calculations of strain rate, stress and the subsequent addition of the behaviour of strength to the forces and work done can be accomplished using differencing schemes and established constitutive models. However, accurately capturing the dynamic behavior of materials in real-world scenarios within an Eulerian framework poses notable challenges. Material strength effects are easier to conceptualise using a Lagrangian framework, where forces between atoms (discrete points) organized into larger structures resist deformation. In an Eulerian scheme, strain rates are calculated between cells in the mesh in each direction, leading to components of the stress tensor in different locations in the cell, resulting in inaccuracies that require correction [101]. Additionally, in an Eulerian grid, the default interaction between adjacent material surfaces assumes perfect bonding, unlike the Lagrangian framework where surfaces in contact possess independent velocity fields. While a Lagrangian scheme requires a defined contact algorithm to prevent material interpenetration, an Eulerian scheme employs a single continuous velocity grid across the entire mesh, ensuring the conservation of mass, momentum, and energy while preventing non-physical material mixing. This unified velocity field effectively bonds all cells together, leading to unphysical generation of shear stress between separate solid material components [102].

Research into contact algorithms in an Eulerian framework is sparse compared to Lagrangian or arbitrary Lagrangian–Eulerian (**ALE**), as scenarios with significant contact effects are rarely considered. Benson *et al.* compared Eulerian and ALE methods of implementing slip conditions to model a Taylor anvil-on-rod test, including the behaviour at the rod-anvil and rod-vacuum interface [103]. The Eulerian formulation utilised mixture theory to adjust the stress tensor such that the shear stress was zero on the contact plane [104]. However, Benson found mixture theory to be inadequate for modelling the Taylor rod-anvil interaction, ultimately finding it necessary to represent the anvil as a rigid body with independent velocity fields [85, 105].

Research aimed at enhancing the accuracy of the simulation of solids in Eulerian hydrocodes has been relatively limited [106]. Typically, material strength effects are assumed to be negligible in processes favoring an Eulerian approach, even in systems involving solids. For instance, in scenarios with strong shock waves traversing a solid, pressures are often so high that the deviatoric stress tensor is considered insignificant [107].

However, there are cases where solids, powders and lattices undergo rapid deformation that would cause mesh entanglement in a Lagrangian grid, yet still experience material strength effects [108]. Burkett *et al.* conducted studies on dynamic tensile extrusion tests using the two-dimensional Eulerian code, MESA. In these experiments, copper and tantalum projectiles were accelerated in a gas gun to velocities ranging between 330 and 700 m/s and extruded through a high-strength steel die [109]. The interaction between the projectile and the die was achieved by defining a layer of cells along the inner surface of the die, within which the components of the stress tensor was set to zero. This enabled the projectile to pass through the computational mesh at the projectile-die interface with minimal artificial drag induced by the hydrocode's vertex-centered velocity scheme. Although effective, the requirement to manually define the projectile-die interface hindered the repeatability and rapid implementation of the model.

An alternative scenario involving a complex confluence of physical effects includes the acceleration of projectiles to high velocity for investigation of extreme pressure states. While the deviatoric stress tensor can be considered negligible in some target materials on impact, this assumption may not hold true for the projectile. For instance, electromagnetic (**EM**) plate flyer impact experiments performed at the Z machine at Sandia National Laboratories require impact using flyers of known (solid) density to collect equation of state data at 30-40 Mbar in targets of interest [20]. To achieve this, the current discharged by Z is shaped to ensure the leading surface of the flyer remains solid, thus simulations performed of the mechanism in ALEGRA require the incorporation of a material strength model [16].

Another electromagnetic launch technique, known as the electric gun, was developed at First Light Fusion (**FLF**) to accelerate dielectric flyers to velocities over 10 km/s using an exploding metal foil [93, 96, 110]. Modeling this process requires a hydrocode that can capture both the behaviour of the foil vapor and the solid dielectric flyer within the same domain, necessitating the reproduction of magneto-hydrodynamic (**MHD**), compressibility, and material strength effects. Both acceleration techniques employ complex electrode geometries, composed of multiple parts that must be able to slip past each other. Consequently, simulating these loads requires the implementation of slip conditions across detailed part interfaces in a computationally efficient and repeatable manner. The physics involved in the simulation of EM flyer acceleration favour different frameworks. However, employing a Lagrangian formulation to capture the motion of the metal plasma in more than one dimension (**1D**) would lead to mesh entanglement [111]. While an ALE code might overcome this limitation, its complex implementation led to the selection of an Eulerian hydrocode to simulate these systems.

In this work, the implementation of a material strength model in **B2**, an in-house Eulerian MHD hydrocode developed by FLF, is presented. The strength model is verified against Taylor anvil-on-rod tests generated in the commercially available code, Ansys AUTODYN [97]. As noted by Benson *et al.*, the Taylor rod-anvil interaction is a rigorous test-case: complex behaviour within the rod, at the rod-anvil, and at the rod-vacuum interfaces must be captured to calculate its deformation accurately. Using this test-case, the solutions to the following challenges are discussed:

1. What algorithm should be used to calculate the components of the stress tensor whilst ensuring the force and work due to strength are derived at the cell-centre?
2. How should the yielding of interface cells (material-vacuum) be treated to match the results of a Lagrangian formulation?
3. How should the components of the stress tensor be modified to simulate slip conditions at the rod-anvil interface?
4. What numerical instabilities exist in the system, and how can they be dealt with?

6.4.3 Mathematical model of material strength

Governing equations

When simulating a solid using an MHD hydrocode, the fundamental equations contain no assumptions about the material state. Instead, this information is accounted for within the equation of state and transport coefficients. The standard MHD equations assume the pressure tensor is isotropic. Thus, to represent shear forces, the anisotropic pressure terms in the momentum and energy equations must be re-instated, which may be written as,

$$\rho\frac{\partial v}{\partial t} + v\cdot\nabla v = -\nabla P + J\times B + \nabla\cdot\underline{\underline{s}} \tag{6.1a}$$

$$\frac{\partial U}{\partial t} + v\cdot\nabla U = -P\nabla\cdot v - \nabla\cdot q + J\cdot\underline{\underline{\eta}}\cdot J + \underline{\underline{s}} : \nabla v, \tag{6.1b}$$

where ρ is the density, v is the velocity, P is the pressure, J is the current density, B is the magnetic field strength, U is the internal energy, q is the charge, $\underline{\underline{s}}$ is the stress tensor and $\underline{\underline{\eta}}$ is the resistivity.

The stress tensor is calculated from the strain $(\underline{\underline{\varepsilon}})$, and can be expressed using Einstein's summation notation as:

$$s_{ij} = 2\eta_k(\varepsilon_{ij} - \delta_{ij}\varepsilon_{ii}), \tag{6.2}$$

where η_k is the kinematic viscosity and δ_{ij} is the Kronecker delta function. The terms in the strain rate tensor $(\underline{\underline{\dot{\varepsilon}}})$ are given by,

$$\dot{\varepsilon}_{ij} = \frac{1}{2}\left(\frac{\partial v_i}{\partial x_j} + \frac{\partial v_j}{\partial x_i}\right), \tag{6.3}$$

where x is the spatial coordinate. The strain rate tensor can be divided into a 'hydrostatic' part, which describes the change in volume without distortion, and a 'deviatoric' part, which describes distortion without a change in volume. The hydrostatic component of the strain rate tensor is already accounted for in the pressure scalar, thus only the deviatoric strain rate and stress tensor need be included.

In a solid, stresses are accumulated over time, hence the relationship between stress and strain may be represented in the Lagrangian form as,

$$\frac{\partial s_{ij}}{\partial t} = 2G(\dot{\varepsilon}_{ij} - \delta_{ij}\dot{\varepsilon}_{ii}), \tag{6.4}$$

where G is the shear modulus and $\dot{\varepsilon}_{ii}$ cancels the hydrostatic component already accounted for. In Cartesian coordinates, this term becomes,

$$\dot{\varepsilon}_{ii} = \frac{1}{3}\left(\frac{\partial v_x}{\partial x} + \frac{\partial v_y}{\partial y} + \frac{\partial v_z}{\partial z}\right). \tag{6.5}$$

The shear modulus implemented in B2 is density and temperature (T) dependent, such that,

$$G(\rho, T) = 3K(\rho, T)\frac{1-2\upsilon}{2(1+\upsilon)} \tag{6.6}$$

where K is the bulk modulus and υ is the material specific Poisson Ratio. The bulk modulus as a function of density and temperature can be derived from the equation of state,

$$K(\rho, T) = \rho\frac{\partial P(\rho, T)}{\partial \rho} = \rho c^2(\rho, T), \tag{6.7}$$

where c is the adiabatic sound speed. The shear wave velocity (c_s),

$$c_s = \sqrt{\frac{G}{\rho}} \tag{6.8}$$

is incorporated into the total material sound speed.

Yield model

When a force is applied to a solid, it will deform elastically (returns to its original shape) if the stress developed is below the yield stress (Y) of the material. When this is the case, the relationship between stress and dimensionless strain is linear. However, if the stress is considered larger than the yield stress, the material will deform plastically (the deformation is permanent). Beyond the yield stress, the relationship between stress and strain ceases to be linear and the material accumulates plastic strain (ε_p). When modelling this process, it is convenient to calculate the trial stress tensor (s^*_{ij}) using Equation 6.4, and subsequently reduce the stress based on Y, which can be calculated using a constitutive model. In this work, if the von Mises effective stress (σ^*_{eff}) [112] of the trial stress tensor,

$$\sigma^*_{\text{eff}} = \sqrt{\frac{3}{2}s^*_{ij}s^*_{ij}} \tag{6.9}$$

is less than the yield stress (Y), the material is considered to be elastic and the trial stress deviator is accepted [113]. However, if the opposite is found to be true, the new stress deviator (s_{ij}) is calculated as,

$$s_{ij} = \frac{Y}{\sigma^*_{\text{eff}}}s^*_{ij}. \tag{6.10}$$

This is essentially a uniformly scaled-down version of the trial stress deviator. The plastic strain rate $\dot{\varepsilon}_p$ accumulated on exceeding yield can then be calculated using,

$$\Delta\dot{\varepsilon}_p = \frac{\sigma^*_{\text{eff}} - Y}{3Gdt} \tag{6.11}$$

where dt is the explicit timestep. This contributes to ε_p through,

$$\varepsilon_p = \varepsilon_p + \Delta\dot{\varepsilon}_p dt. \tag{6.12}$$

To capture both the linear elastic and plastic deformation behaviour of a material, its yield stress was calculated at each cell-centre using the Johnson-Cook (**JC**) model [114], such that,

$$Y = (A + B\varepsilon_{\mathrm{p}} p^n)(1 + Cln(\varepsilon_{\mathrm{p}}^*))(1 - (T/T_{\mathrm{melt}})^m), \tag{6.13}$$

where A, B, and C are material specific coefficients, m is the softening exponent, n is an exponent, ε_{p} is the plastic strain and $\varepsilon_{\mathrm{p}}^*$ is the dimensionless plastic strain rate, and $\varepsilon_p^* = \dot{\varepsilon}_p/\dot{\varepsilon}_{p0}$ with $\dot{\varepsilon}_{p0} = 1$ s^{-1} [114].

Force and work terms

Once the stress tensor has been determined, the force and work done on the material can be calculated. The additional force, given by $\nabla \cdot \underline{\underline{s}}$, is analogous to the force created at a pressure gradient. In Cartesian geometry, the components of the force vector are given by,

$$F_x = \frac{\partial s_{xx}}{\partial x} + \frac{\partial s_{xy}}{\partial y} + \frac{\partial s_{xz}}{\partial z} \tag{6.14a}$$

$$F_y = \frac{\partial s_{xy}}{\partial x} + \frac{\partial s_{yy}}{\partial y} + \frac{\partial s_{yz}}{\partial z} \tag{6.14b}$$

$$F_z = \frac{\partial s_{xz}}{\partial x} + \frac{\partial s_{yz}}{\partial y} + \frac{\partial s_{zz}}{\partial z}. \tag{6.14c}$$

The work done due to the stress tensor, given by $\underline{\underline{s}} : \nabla v$, is analagous to the $P\nabla \cdot v$ work term. It can be expanded in Cartesian coordinates to give,

$$\underline{\underline{s}} : \nabla v = s_{xx}\frac{\partial v_x}{\partial x} + s_{xy}\frac{\partial v_x}{\partial y} + s_{xz}\frac{\partial v_x}{\partial z} + s_{xy}\frac{\partial v_y}{\partial x} + s_{yy}\frac{\partial v_y}{\partial y} + s_{yz}\frac{\partial v_y}{\partial z} + s_{xz}\frac{\partial v_z}{\partial x} + s_{yz}\frac{\partial v_z}{\partial y} + s_{zz}\frac{\partial v_z}{\partial z}. \tag{6.15}$$

6.4.4 Method: Taylor anvil-on-rod test-case

The strength model in B2 was verified using a cross-code comparison with Lagrangian simulations performed in Ansys AUTODYN-2D (AUTODYN) [97]. AUTODYN is an explicit dynamics simulation program for solving short-duration, severe-loading problems. The code has been used extensively to model scenarios such as the Taylor anvil-on-rod test [115, 116], thus its solution to the test case can be used to evaluate the accuracy of the strength model integrated into B2.

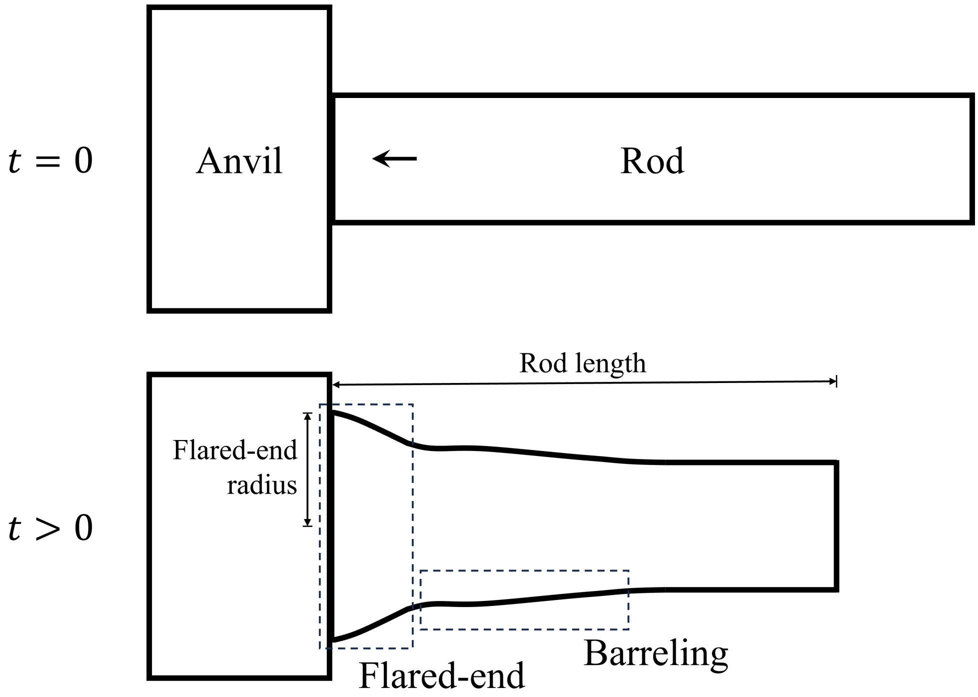

Figure 6.1: Depiction of Taylor anvil-on-rod test, including terminology used throughout this work.

The Taylor anvil-on-rod test, introduced by Taylor in 1948 [100], is a well-known method used to evaluate the characteristics of dynamic material deformation at strain-rates up to around 10^4 s^{-1}. In this test, a high-velocity rod impacts an anvil, resulting in high-strain-rates at the impact face which decrease along the length of the rod. Figure 6.1 depicts a typical Taylor anvil-on-rod test, including the regions of interest in the rod considered in this work.

At the impact-end of the rod, the rod deforms plastically, both flaring out at the impact face and 'barreling' further down the rod. Initially, researchers used the final rod length to estimate the 'dynamic yield stress' of the rod material. Later, it was found the evolution of the rod profile provided significant insight into the localised plastic flow within the rod [116]. The Taylor anvil-on-rod test provides a rigorous test-case for a material strength model, as the evolution of the rod profile is highly sensitive to the stresses, yield behaviour and plastic flow in the material.

In this work, two plates with equal and opposite velocity in a vacuum in the configuration illustrated in Figure 6.2 were used to approximate the impact of a copper plates against a perfectly rigid anvil. The simulations in both codes were two-dimensional and planar, with a mesh resolution of 0.1 mm. The plates, though both copper, were modelled as two different parts in B2 to prevent numerical welding between them. In some of the test-cases, the plate is simulated as impacting a rigid anvil instead, however, the results analysed in the cross-code comparison are in this plate-on-plate configuration.

B2 employs the Frankfurt Equation of State (**FEOS**) [89] in the copper rod, a semi-analytical tabulated equation of state based on the QEOS model [117]. The simulation in AUTODYN was constructed in the same configuration to ensure as close a comparison between the codes as possible. The simulation in AUTODYN employed a linear equation of state, where $\rho = 8.96$ g/cc, $K = 129$ GPa, $G = 46$ GPa and the specific heat capacity $c_h = 3.84\times^{-4}$ kJ/gK. The differing equations of state were unlikely to impact the results of the rod deformation, as the FEOS at low temperatures closely resembles the linear equation of state. Both B2 and AUTODYN used the same Johnson-Cook (**JC**) [114] material parameters for copper, listed in Table 6.3. Further, the interaction between the two rods was defined to be frictionless in both codes.

Table 6.1: Johnson-Cook material properties.

Material	A	B	C	n	m	Melting temp
Copper	90 MPa	292 MPa	0.025	0.31	1.09	1356 K

The Taylor anvil-on-rod test was sensitive to a number of issues which, without correction, led to significant inaccuracies in the simulated deformation of the rod. These issues are addressed in the following sections, including:

- **Determining the most accurate approach to calculating the components of force and work due to material strength.** Implementing the equations introduced in Section 6.4.3 becomes complicated in an Eulerian framework, because the location of the variables in each cell must be considered.

- **Challenges tracking the material interface in cells adjacent to a vacuum.** Numerical diffusion results in partially-filled, low-density, cells adjacent to the rod. As the JC calculation of yield is independent of density, these low-density cells are assigned erroneously high yields.

- **Slip conditions between different parts in the domain.** The Taylor rod must be free to slip over the anvil surface on impact to be able to accurately predict localised flaring (barreling) of the rod.

- **Numerical instabilities generated in regions dominated by shear force.** Without damping, these unphysical oscillations dominate the simulation.

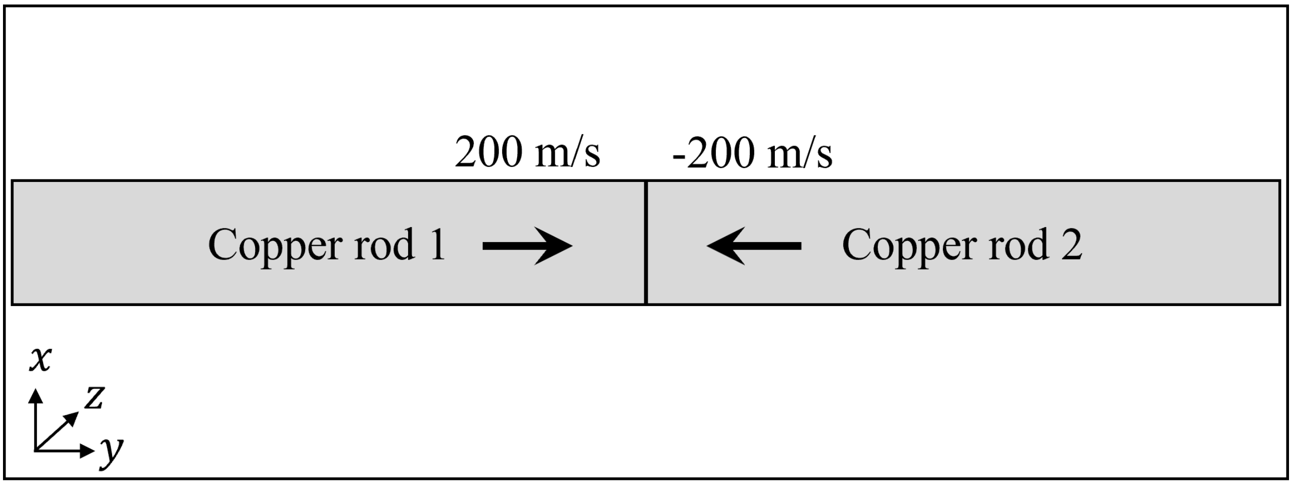

Figure 6.2: Simulation set-up of the Taylor anvil-on-rod test in B2 and AUTODYN. In some of the test-cases, the plate is simulated as impacting a rigid anvil instead, however, the results analysed in the cross-code comparison are in this plate-on-plate configuration.

6.4.5 Computational implementation of material strength

The subsequent section outlines the incorporation of a material strength model, adapted from the model devised by Pecover *et al.* [98, 99], into the MHD Eulerian hydrocode, B2. B2 operates using a two-step Eulerian solution scheme across a fixed rectangular mesh, the details of which can be found in [101]. Material strength effects were integrated into the first (Lagrangian) step, where the force and work done in each cell are computed. The second (Eulerian) step maps the distorted cells back to the mesh using a second-order MUSCL advection scheme [118]. Conserved values at the material interfaces are tracked using the volume of fluid method [119]. Interface-tracking methods are indispensable in Eulerian systems to mitigate numerical diffusion across the material boundaries; a crucial consideration when monitoring the movement of solid materials. The precise location of the part boundaries plays a pivotal role in defining their contact behavior.

The logical variable locations in the mesh are defined in Figure 6.3. Each variable is referenced in terms of the x coordinate index (i), y coordinate index (j), and z coordinate index (k). B2 derives conserved variables at the cell-centre, thus, in this work (i, j, k) refers to the cell-centred location. All cell-centered quantities are assumed to be uniform across the cell. The face-centred velocities, denoted for ease by an underscored ‘f’, are perpendicular to the cell face they are located on. In this work, the notation is simplified by thinking of the face-centred velocities as existing in a staggered mesh. For example, the velocity in the x-direction (v_{fx}) can be written as

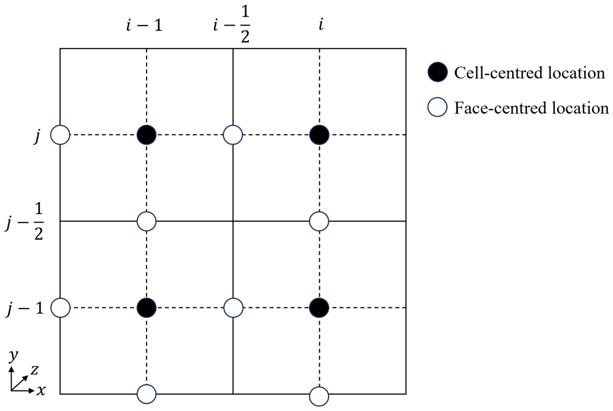

Figure 6.3: The original and staggered Eulerian mesh with the cell-centred and face-centred locations marked.

$$v_{fx}(i,j,k) = v_x(i-\frac{1}{2},j,k). \tag{6.16}$$

It is important to note the face-centred velocities are derived independently from the cell-centred velocities at the beginning of the Lagrangian step. Two-dimensional and one-dimensional meshes referenced in this section are sub-cases of the three dimensional mesh. All quantities discussed were temporally positioned at the start of the timestep.

Comparison of algorithms for calculating stress, force and work done

In B2, the conserved momenta and internal energy terms are stored at the cell-centre. Consequently, the forces and work generated by the deviatoric stress tensor must also be cell-centered values to be added to the other terms calculated during the Lagrangian step. Multiple methods of differencing and averaging can be used to achieve a cell-centred force and work term. In this work, the two algorithms trialled, referred to as Face-centred Stress and Cell-Centred Stress, are illustrated in Figure 6.4.

Face-Centred Stress In the Face-Centred Stress algorithm, a forward spatial differencing scheme was used to calculate face-centred components of the strain rate tensor for each timestep. The force and work terms were then calculated at the cell-centre using a backward spatial differencing scheme. In this scheme, Equation 6.3 for a diagonal component of the strain rate tensor (for instance, $\dot{\varepsilon_{xx}}$) becomes,

$$\dot{\varepsilon_{xx}} = \frac{\partial v_x}{\partial x} = \frac{v_x(i-1)-v_x(i)}{dx}, \tag{6.17a}$$

where v_x is the cell-centred velocity in the x-direction and dx is the distance between the cell-centres. Variables in an Eulerian mesh must be in the same location in order to be summed. Consequently,

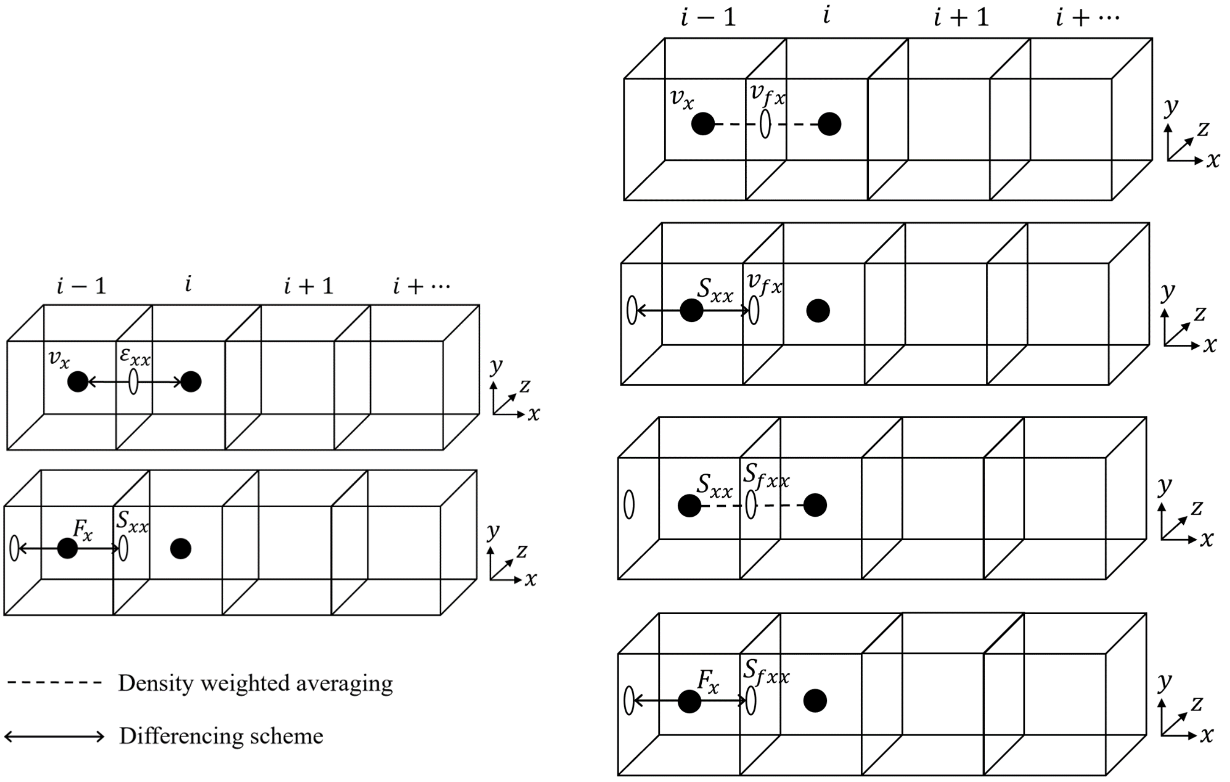

(a) Face-Centred Stress algorithm in one-dimension. **(b)** Cell-Centred Stress algorithm in one-dimension.

Figure 6.4: Illustration of two averaging and differencing schemes ordered in such a way to result in a cell-centred force and work value. The left requires fewer steps, however the stresses are located at the cell faces, which is challenging for advection in orthogonal direction and gradient calculation for the off-diagonal components of the stress tensor.

non-diagonal components of the strain rate tensor were calculated such that the gradient of the velocities involved in the summation have answers in the same location. For example, the equation for the shear strain rate component $\dot{\varepsilon_{yx}}$ becomes,

$$\dot{\varepsilon_{yx}} = \frac{1}{2}\left(\frac{\partial v_x}{\partial y} + \frac{\partial v_y}{\partial x}\right) = \frac{1}{2}\left(\frac{v_{fx}(i,j+1) - v_{fx}(i,j-1)}{2 \cdot dy} + \frac{v_y(i-1,j) - v_y(i,j)}{dx}\right), \tag{6.18a}$$

and results in $\dot{\varepsilon_{yx}}$ being located at x-face. This equation is visualised in Figure 6.5a.

Referring to the calculation of the hydrostatic component of the strain rate tensor $\dot{\varepsilon}_{ii}$ in Equation 6.5, it becomes clear $\frac{\partial v_x}{\partial x}$, $\frac{\partial v_y}{\partial y}$ and $\frac{\partial v_z}{\partial z}$ cannot be added directly, as they exist on different faces. To account for this, three face-centred components of $\dot{\varepsilon}_{ii}$ were calculated at each face. For example, at the x-face Equation 6.5 in two-dimensions $(x - y)$ becomes,

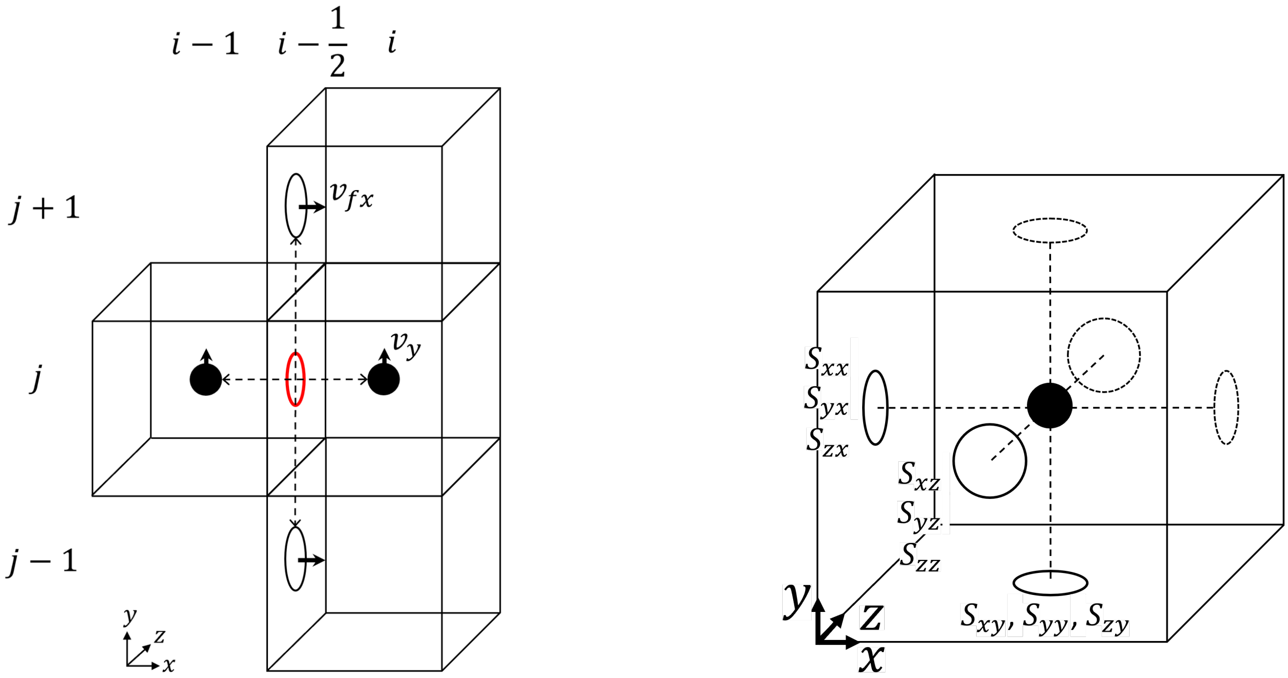

(a) An illustration of the calculation of $\dot{\varepsilon}_{yx}$ (Equation 6.18).

(b) Locations of the nine components of the stress tensor on the three cell faces.

Figure 6.5: The method for calculating the shear strain rate $\dot{\varepsilon}_{yx}$ alongside the final location of the nine components of the stress tensor.

$$\dot{\varepsilon}_{ii}(i-\frac{1}{2}, j, k) = \frac{1}{3}\Bigg[\frac{v_x(i-1,j,k) - v_x(i,j,k)}{dx} + 0.25\left(\frac{(v_y(i-1,j-1,k) - v_y(i-1,j+1,k)) + (v_y(i,j-1,k) - v_y(i,j+1,k))}{dy}\right)\Bigg]. \tag{6.19}$$

The location of the nine components of the stress tensor on three different faces of the cell also complicates the calculation of the yield behaviour of the system. Referring to Equation 6.9, it becomes clear σ^*_{eff} cannot be calculated unless all the components of the trial stress tensor are in the same cell location. Hence, following the calculation of the trial stress tensor, a single cell-centred component of σ^*_{eff} was found using,

$$\sigma^*_{\text{eff}}(i,j,k) = \sqrt{\frac{3}{2}\underline{\underline{s}}^*(i,j,k)\underline{\underline{s}}^*(i,j,k)}, \tag{6.20}$$

where $\underline{\underline{s}}^*$ is the cell-centred trial stress tensor. If the mesh size is constant, then $\underline{\underline{s}}^*(i,j,k)$ can be found for each cell using,

$$\underline{\underline{s}}^{*}(i,j,k)=\frac{1}{2}\Bigg((s_{xx}(i-\frac{1}{2},j,k)+s_{xx}(i+\frac{1}{2},j,k))+(s_{yx}(i-\frac{1}{2},j,k)+s_{yx}(i+\frac{1}{2},j,k))+(s_{zx}(i-\frac{1}{2},j,k)+s_{zx}(i+\frac{1}{2},j,k))$$
$$+(s_{xy}(i,j-\frac{1}{2},k)+s_{xy}(i,j+\frac{1}{2},k))+(s_{yy}(i,j-\frac{1}{2},k)+s_{yy}(i,j+\frac{1}{2},k))+(s_{zy}(i,j-\frac{1}{2},k)+s_{zy}(i,j+\frac{1}{2},k))$$
$$+(s_{xz}(i,j,k-\frac{1}{2})+s_{xz}(i,j,k+\frac{1}{2}))+(s_{yz}(i,j,k-\frac{1}{2})+s_{yz}(i,j,k+\frac{1}{2}))+(s_{zz}(i,j,k-\frac{1}{2})+s_{zz}(i,j,k+\frac{1}{2}))\Bigg). \tag{6.21}$$

The yield stress was then calculated using the constitutive equation at the cell-centre. This permitted the direct calculation of a single cell-centred plastic strain, using,

$$\varepsilon_p(i,j,k)=\frac{\sigma^{*}_{\text{eff}}(i,j,k)-Y(i,j,k)}{3G(i,j,k)}. \tag{6.22}$$

However, as shown in Figure 6.4a, this formulation requires the face-centred stresses to be reduced in place, such that the resulting force vector and work done are cell-centred. To achieve this, the yield at each cell face (Y_f) was calculated using a density-weighted average. For example, the face-centred yield at the lower x-face of the cell was found using,

$$Y_{fx}(i,j,k)=Y(i-\frac{1}{2},j,k)=\frac{Y(i,j,k)\rho(i-1,j,k)+Y(i-1,j,k)\rho(i,j,k)}{\rho(i-1,j,k)+\rho(i,j,k)}. \tag{6.23}$$

The face-centred value of the von Mises effective stress was then found using the density-weighted average of $\sigma^{*}_{\text{eff}}(i-1,j,k)$ and $\sigma^{*}_{\text{eff}}(i,j,k)$. The components of the trial stress tensor were then reduced using the corresponding face-centred values of the yield and von Mises effective stress.

Upon determining the accepted stress tensor, the contributions to the cell-centred force vector and work done due to material strength were calculated. The force in the x-direction (F_x) is calculated using Equation 6.14b. However, the locations of the components of stress (S_{ij}), displayed in Figure 6.5b, demonstrate the gradient of S_{yx} cannot be calculated in the y-direction in its native position on the x-face of the cell. Instead, S_{yx} must first be calculated at the y-face using simple averaging. In two-dimensions ($x-y$), F_x becomes,

$$\begin{aligned}F_x(i,j)=&\frac{(S_xx(i-\frac{1}{2},j)-S_xx(i+\frac{1}{2},j))}{dx}+\frac{(S_{xy}(i,j-\frac{1}{2})-S_{xy}(i,j+\frac{1}{2}))}{dy}\\&+0.25\left[\frac{(S_{yx}(i-\frac{1}{2},j)+S_{yx}(i+\frac{1}{2},j))-(S_{yx}(i-\frac{1}{2},j-1)+S_{yx}(i+\frac{1}{2},j-1))}{dx}\right].\end{aligned} \tag{6.24}$$

Calculating the work done also requires the components of the accepted stress tensor be recalculated at the cell-centre. For example, in two dimensions ($x-y$), Equation 6.15 becomes,

$$\begin{aligned} W_{strength}(i,j) = 0.5 \Bigg[&(S_{xx}(i-\frac{1}{2},j) + S_{xx}(i+\frac{1}{2},j))\left(\frac{v_{fx}(i,j) - v_{fx}(i+1,j)}{dx}\right) \\ &+ (S_{yx}(i-\frac{1}{2},j) + S_{yx}(i+\frac{1}{2},j))\left(\frac{v_{fx}(i,j) - v_{fx}(i+1,j)}{dx}\right) \\ &+ (S_{xy}(i,j-\frac{1}{2}) + S_{xy}(i,j+\frac{1}{2}))\left(\frac{v_{fy}(i,j) - v_{fy}(i,j+1)}{dx}\right) \\ &+ (S_{yy}(i,j-\frac{1}{2}) + S_{yy}(i,j+\frac{1}{2}))\left(\frac{v_{fy}(i,j) - v_{fy}(i,j+1)}{dx}\right)\Bigg]. \end{aligned} \tag{6.25}$$

Cell-Centred Stress The Cell-Centred Stress algorithm was derived with the intention of formulating cell-centred stresses using face-centred velocity components, which are calculated using density-weighted averaging of the cell-centred momenta. The interface tracker utilised in B2 operates using cell-centred values. It was theorised by creating cell-centred stress quantities, they might be more accurately advected from this position during the secondary Eulerian step. To calculate the strain rates, six extra face-centred components of velocity were derived using the three face-centred velocity components, v_{fx}, v_{fy} and v_{fz}. For example, v_{xy} was calculated using,

$$v_{cx}(i,j,k) = \frac{1}{4}\left(v_{fx}(i,j,k) + v_{fx}(i,j-1,k) + v_{fx}(i,j,k-1) + v_{fx}(i,j-1,k-1)\right) \tag{6.26a}$$

$$v_{xy}(i,j,k) = \frac{1}{4}\left((v_{cx}(i,j,k) + (v_{cx}(i+1,j,k) + (v_{cx}(i,j,k+1) + (v_{cx}(i+1,j,k+1)\right),, \tag{6.26b}$$

where v_{cx} is the corner-centred velocity in the x-direction. The spatial reasoning behind Eqns. 6.26 is illustrated in Figure 6.6. Unlike the Face-Centred Stress algorithm, $\dot{\varepsilon}_{ii}$ can be calculated directly as $\frac{\partial v_x}{\partial x}$, $\frac{\partial v_y}{\partial y}$ and $\frac{\partial v_z}{\partial z}$ all exist in the same location.

In this formulation, all the variables involved in calculating the plastic behaviour of the material are derived in the same location: at the cell-centre. Hence, unlike the Face-centred Stress algorithm, Equations 6.9 - 6.12 can be employed directly to (if necessary) reduce the components of the stress tensor and calculate the accumulated plastic strain.

However, unlike the Face-centred Stress algorithm, before the cell-centred forces and work done can be calculated, face-centred components of the accepted stress tensor must be derived using averaging. As indicated in Figure 6.4b, the face-centred component of S_{xx} (S_{fxx}) was calculated at the x-face using,

$$S_{fxx}(i,j) = S_{xx}(i-\frac{1}{2},j) = \frac{S_{xx}(i,j)\rho(i-1,j) + S_{xx}(i-1,j)\rho(i,j,k)}{\rho(i-1,j) + \rho(i,j)}. \tag{6.27}$$

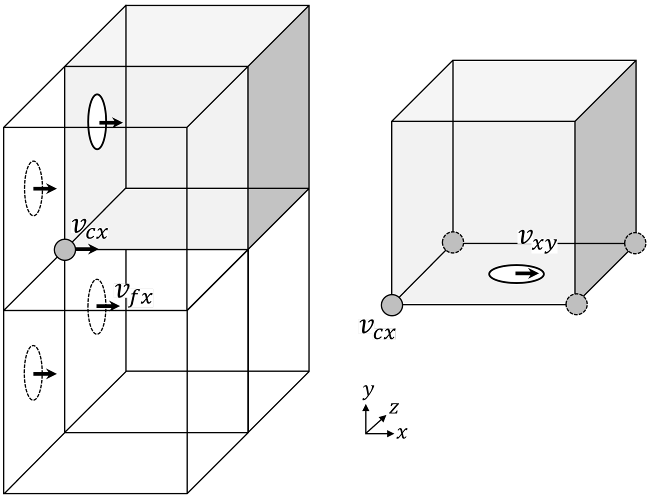

Figure 6.6: An illustration of the process for calculating v_{xy}. The left image represents Equation 6.26a and the right presents Equation 6.26b.

These face-centred components of the accepted stress tensor can then be used to calculate the force vector as required, whilst the native cell-centred components can be used to calculate the work done directly alongside the respective face-centred velocity gradients.

Comparison and Summary Both stress implementations result in the mixing of information between a cell and its neighbour in order to derive the forces and work done. In the Face-Centred Stress algorithm, this is done largely after the stresses were calculated in order to limit the stresses to the yield envelope and evaluate the plastic strain rate. On the other hand, in the Cell-Centred Stress algorithm, little averaging is done in the process of limiting the stress tensor to the yield envelope. Instead, the bulk of the averaging is performed to derive the face-centred velocities in the locations necessary to calculate the cell-centred strain rates.

Ultimately, the Cell-Centred Stress algorithm was found to be unsuitable for modelling situations involving material interfaces. As can be seen in Figure 6.6, v_{xy} is an average of values from five cells surrounding it. The extensive averaging required to find the face-centred velocity results in information mixing across material boundaries. This process was particularly distinctive at the interface between a rod and the vacuum during the simulation of the Taylor test, where the y-direction velocity gradient drops very suddenly. Face-centred velocities at the edge of the rod included contributions from low density cells with low velocity, leading to the calculation of erroneously high shear strain rates in these cells. This mechanism is illustrated in Figure 6.7a and a copper Taylor rod impact simulated in B2 with the Cell-Centred Stress algorithm is shown in Figure 6.7b. Non-physical shear forces

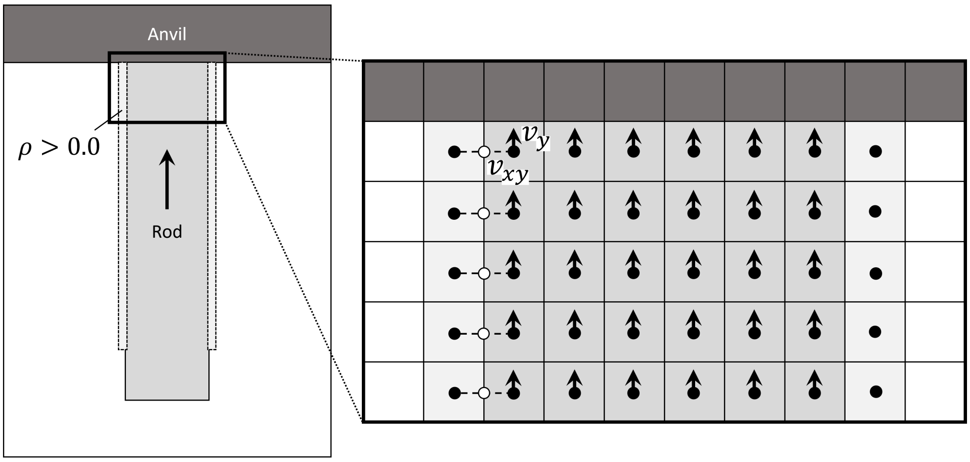

(a) A depiction of the unphysical shear forces generated at the rod-vacuum interface.

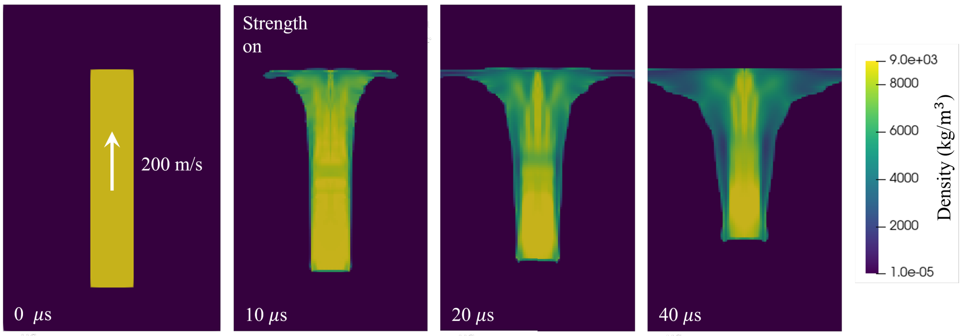

(b) An example of a simulation using the Cell-Centred Stress algorithm. The rod rapidly loses density at the rod-vacuum interface due to erroneously high shear strain rates.

Figure 6.7: The mechanism depicting the generation of high shear forces at the rod-vacuum interface and the consequences of this effect on a simulation of the Taylor anvil-on-rod test.

in the cells at the interface progressively caused the rod to experience unrealistic distortion at the material-vacuum boundary. Consequently, the Face-Centred Stress algorithm is used throughout the rest of this work. In the next section, a density-dependent yield factor is explored as a technique to improve the modelling of a material-vacuum interface.

Yield density dependence factor

Equation 6.13 demonstrates that the cell-centred yield has limited reliance on the cell density. Whilst this is appropriate in a Lagrangian framework, where each point has a known mass, it can cause unphysically high yield in partially filled Eulerian cells. The VOF interface-tracking method is fundamentally flawed, as the definition of a solid shape's interface is only as high as the grid resolution. As illustrated in Figure 6.8, a cell filled with a certain volume fraction of some solid material with

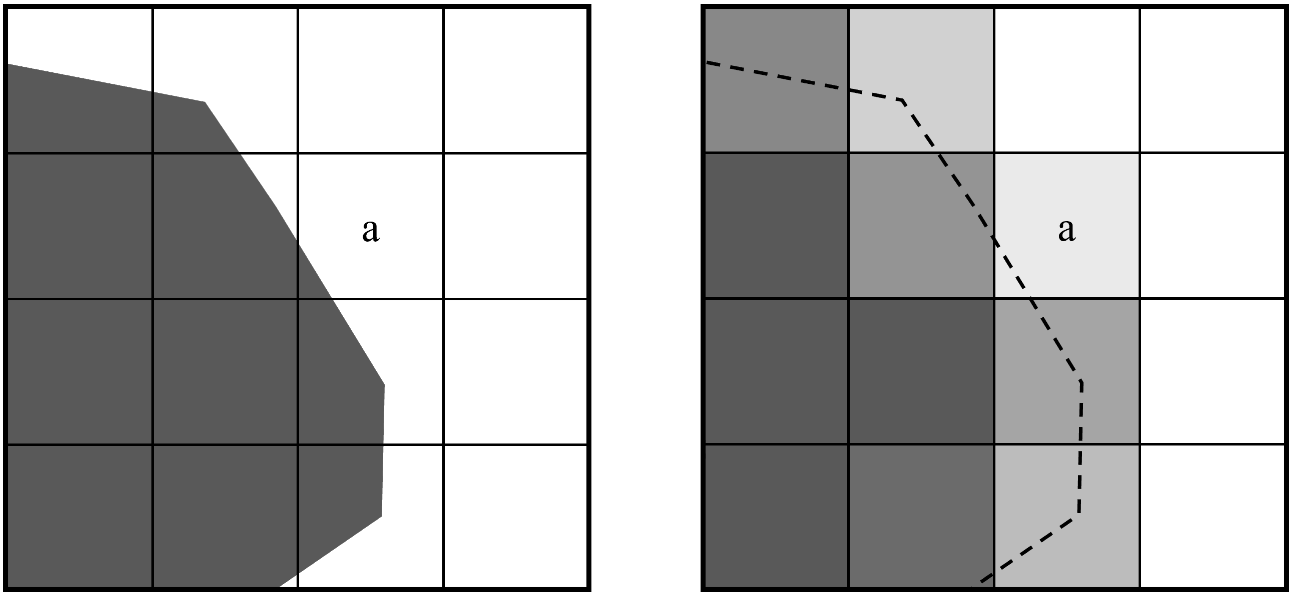

Figure 6.8: Illustration showing the representation of a solid shape in an Eulerian grid. In the uncorrected JC model, cell *a* will have the same yield as a fully occupied cell.

density (ρ_s) is interpreted in Eulerian space as a cell with a total density proportional to the volume fraction multiplied by ρ_s. As the yield is not density dependent, a cell is filled with a low volume of solid material, such as cell a in Figure 6.8, will erroneously have the same yield as a fully filled cell. This can lead to inaccuracy in the material deformation at the boundary of the solid part adjacent to vacuum. To correct this, the yield was artificially adjusted in low density cells using the density factor (Φ) proposed by Pecover *et al.* [99], whereby,

$$Y_{modified} = \Phi \cdot Y \tag{6.28a}$$

$$\Phi = e^{\frac{-(\rho - f\rho_s)}{}}. \tag{6.28b}$$

In this equation, f is the density fraction below which the yield should be reduced and is a scaling constant set to 1000 $\mathrm{m}^6/\mathrm{kg}^2$ [98]. Φ is the factor by which the yield is reduced. The exponential form of this equation was chosen by Pecover *et al.* to ensure the yield stress was unaffected above $f\rho_s$, yet decreased rapidly and smoothly to zero below $f\rho_s$. Whilst Pecover *et al.* used a value $f = 1.0$, in this work, f was found to be a parameter capable of improving the runtime and accuracy of the Taylor rod impact simulation if varied.

If f is set too low, the algorithm calculates strain rates between low-density mixed cells at the rod-vacuum interface and the main body of the rod. This results in shear forces accelerating the low density cells to unphysically high velocities. This process is depicted in Figure 6.9, where $f = 0.1$

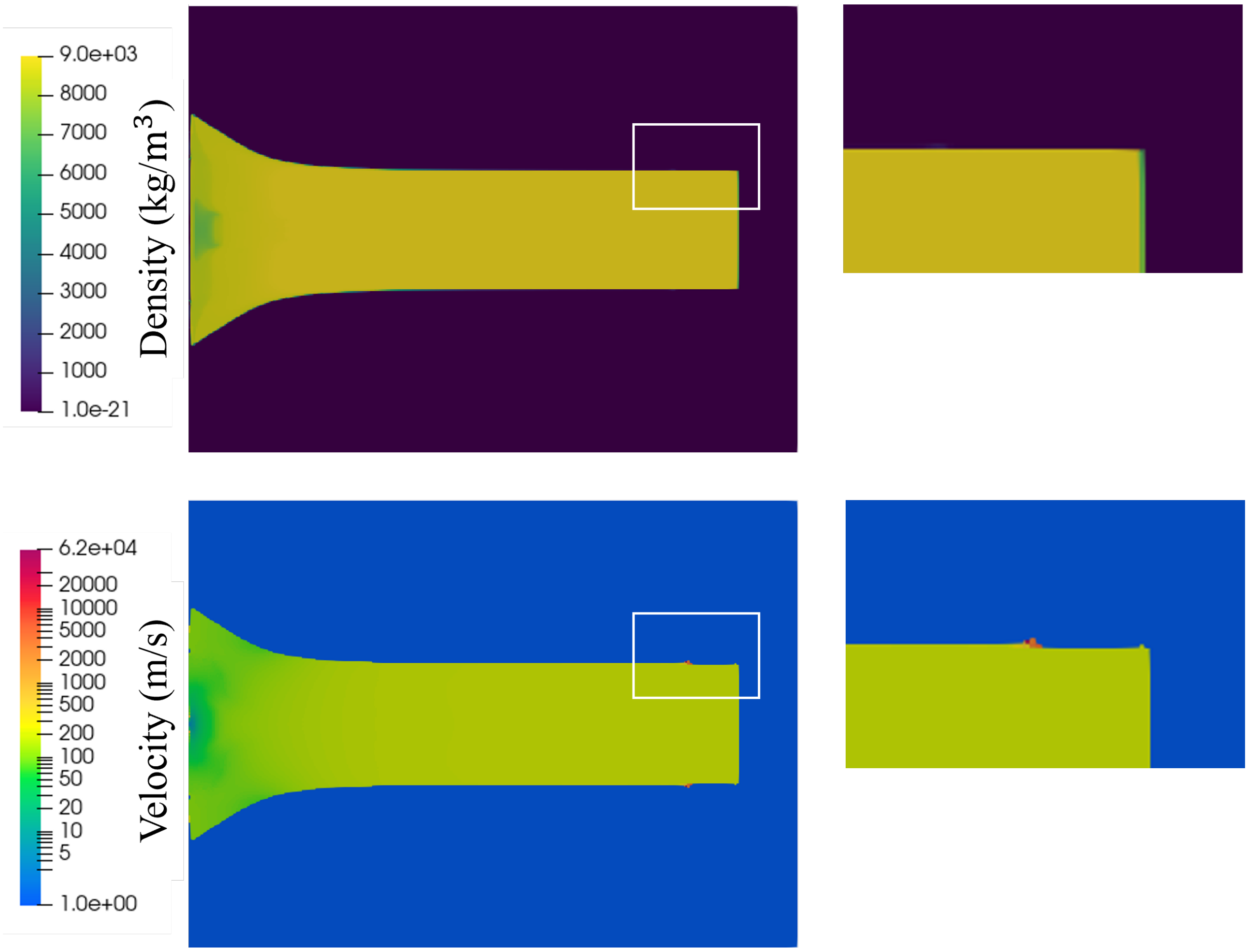

Figure 6.9: A frame in B2 from a simulation without a density-factor corrected yield. The frames highlight high-velocity low-density material at the rear of the rod, which result in excessively high simulation runtimes.

in the copper rod. High velocities in low density cells at the interface led to severe reduction in the explicit Eulerian timestep, resulting in excessively high simulation runtimes. By contrast, if f was too high the interface became prone to unrealistic deformation in material with density below the cut-off. Figure 6.10 depicts the difference between a rod with $f = 0.5$ and $f = 0.4$: Figure 6.10a demonstrates a clear loss of accuracy in the solution at the rod-vacuum interface profile.

Implementation of slip conditions

Automatically generating slip conditions between parts in an Eulerian hydrocode is challenging to practically implement in complex configurations. Slip conditions can be forced in Eulerian hydrocodes by modifying the yield condition in cells at the interface. However, typically these regions must be defined by user before launching the simulation. Further, the cells with the slip condition often must be defined as a separate material: this can require significant additional computational resources if

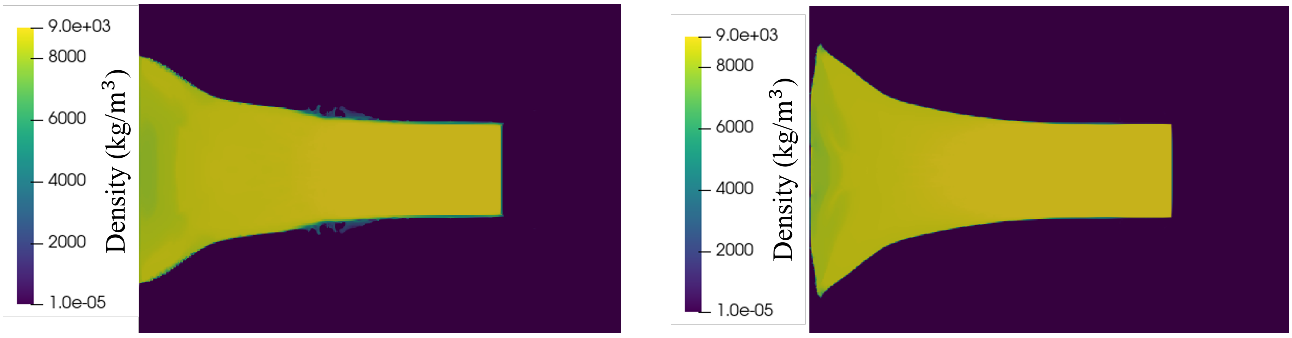

(a) B2 simulation with $f = 0.5$.

(b) B2 simulation with $f = 0.4$.

Figure 6.10: A comparison of simulations frames at 20 µs with differing f.

the parts modelled within the domain have complex boundaries [108]. Due to the complex geometries used in B2 simulation, requiring manual definition of boundaries was deeply undesirable. In this work, an automatic interface was implemented instead.

The stress formulation chosen for use in B2, as discussed in Section 6.4.5, calculates three stresses at each cell face. This is done by taking the gradient of the velocity between cell centres using a forward spatial difference scheme. To prevent the calculation of stress between two separate parts, it is common to modify the entire stress tensor in the cell at the material boundary to be zero [103]. However, in this work, only the components of the stress tensor at the cell face at the boundary between separate parts were set to zero to represent a frictionless boundary. An example of this is illustrated in Figure 6.11. The part boundary is identified in a cell in place by querying the material number in the cells surrounding it and whether these materials have a yield of greater than zero. For example, in the x-direction, if a cell at (i, j, k) and the cell behind it at $(i - 1, j, k)$ both have a yield of greater than zero and the same material number, a value of 1 was assigned in this position. If either cell has a different material number, or yield of zero, a 0 was assigned in this position in the grid instead. When repeated in each direction, this creates three face-centred structures made up of 1s and 0s, referred to in this work as the interface grid (IG). The IG was used to implement slip conditions at material-material and material-vacuum interfaces by modifying the strain rate calculation, where for example Eqn 6.17 becomes

$$\dot{\varepsilon}_{xx}(i - \frac{1}{2}, j, k) = \frac{v_x(i - 1, j, k) - v_x(i, j, k)}{dx} \cdot IG_x(i, j, k). \tag{6.29a}$$

The same approach was also used to modify the values of flux to prevent the advection of stress and plastic strain across material boundaries. The computation of the IG once in each dimension reduces resource within the material strength algorithm, as the conditional statements required to

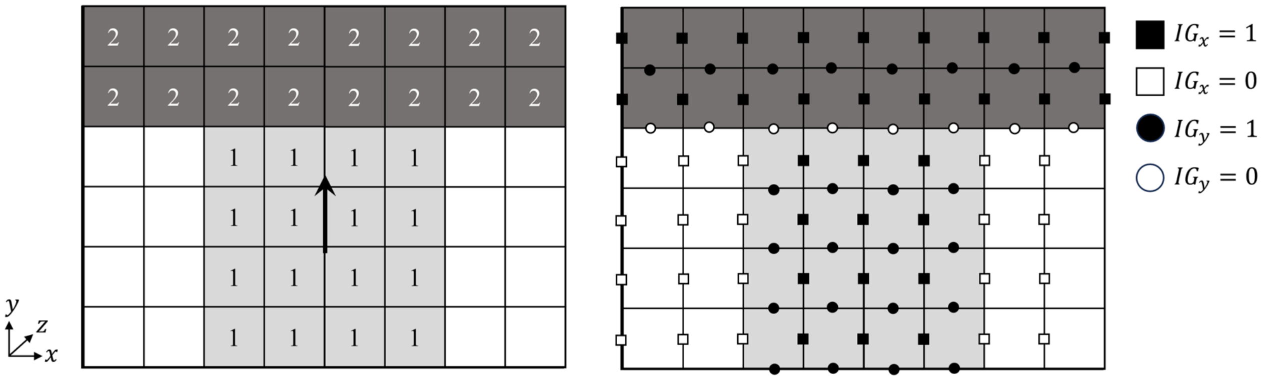

Figure 6.11: Depiction of the interface grid in two-dimensions in a domain with Material 1 and Material 2. The interface grid is set to 1 at the x face of cell (i, j, k) if $(i-1, j, k)$ if both have the same material number and $Y > 0$.

ensure the nine components of strain rate and advection fluxes are only calculated with materials with strength of the same part are replaced by a simple multiplication with either 1 or 0. Further, because the values of the ***IG*** are derived in place based on the states of cells with only their nearest-neighbours, the technique is compatible with grid-based parallelisation of the computational domain.

When combined with the yield density dependence factor, the ***IG*** becomes a powerful technique for controlling the calculation of stresses at the material-vacuum interface. Figure 6.5a demonstrates the S_{yx} in cell (i, j, k) is calculated by taking the gradient of the velocity between $v_y(i, j, k)$ and $v_y(i-1, j, k)$, and $v_{fx}(i, j-1, k)$ and $v_{fx}(i, j+1, k)$. This ensures S_{yx} is a face-centred value which exists at $(i-1/2, j, k)$. However, the gradient between $v_{fx}(i, j-1, k)$ and $v_{fx}(i, j+1, k)$, and $v_y(i, j, k)$ and $v_y(i-1, j, k)$, can introduce extreme shear forces at the rod-vacuum interface. To avoid this, Equation 6.18 was modified to become

$$\dot{\varepsilon}_{yx} = \left(\frac{1}{2}\left(\frac{v_y(i-1, j, z) - v_y(i, j, z)}{dx} + \frac{v_{fx}(i, j+1, z) - v_{fx}(i, j-1, z)}{2 \cdot dy} \cdot IG_x(i, j+1, z) \cdot IG_x(i, j-1, z)\right)\right) \cdot IG_x(i, j, z). \tag{6.30}$$

In the Taylor test, this implementation ensured velocity gradients were only taken between cells within the Taylor rod. Without this modification, material at rod-vacuum interface deformed, blurring the interface and reducing the accuracy of the solution. An example of this behaviour in the Taylor rod in B2 is shown in Figures 6.12a - 6.12b. The instabilities formed at the rod-vacuum interface were particularly prominent along the length of the rod, away from the flared-end. Note similar instabilities form in the same area in the Eulerian version of the Taylor rod simulation in AUTODYN.

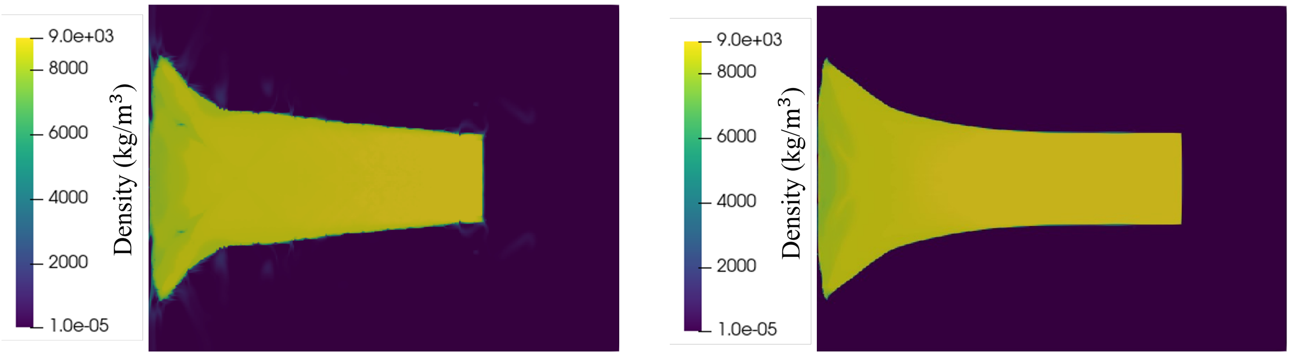

(a) B2 simulation frame 20 µs without the *IG*.

(b) B2 simulation frame 20 µs with the *IG*.

Figure 6.12: Comparison between simulations without and with the *IG*. Non-physical blurring at the rod-vacuum interface visible in Figure 6.12a are shown to have been eliminated in Figure 6.12a.

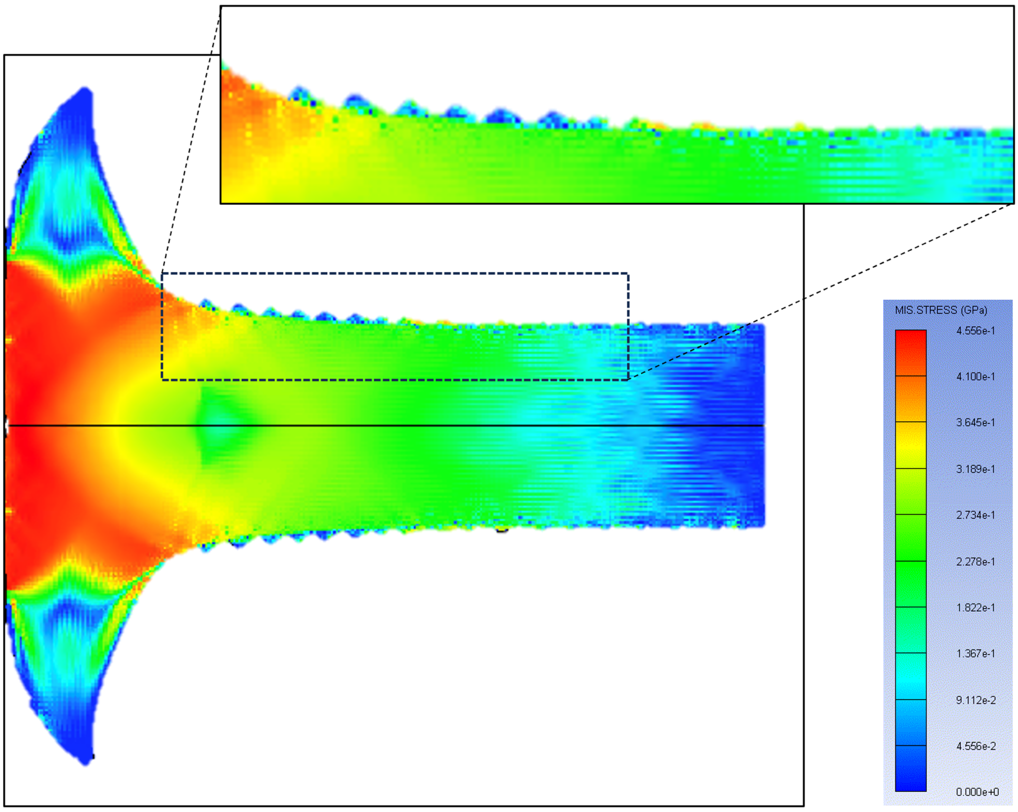

Figure 6.13: Eulerian simulation of Taylor rod in AUTODYN. The frame shows serrated edge forms at the rod-vacuum interface.

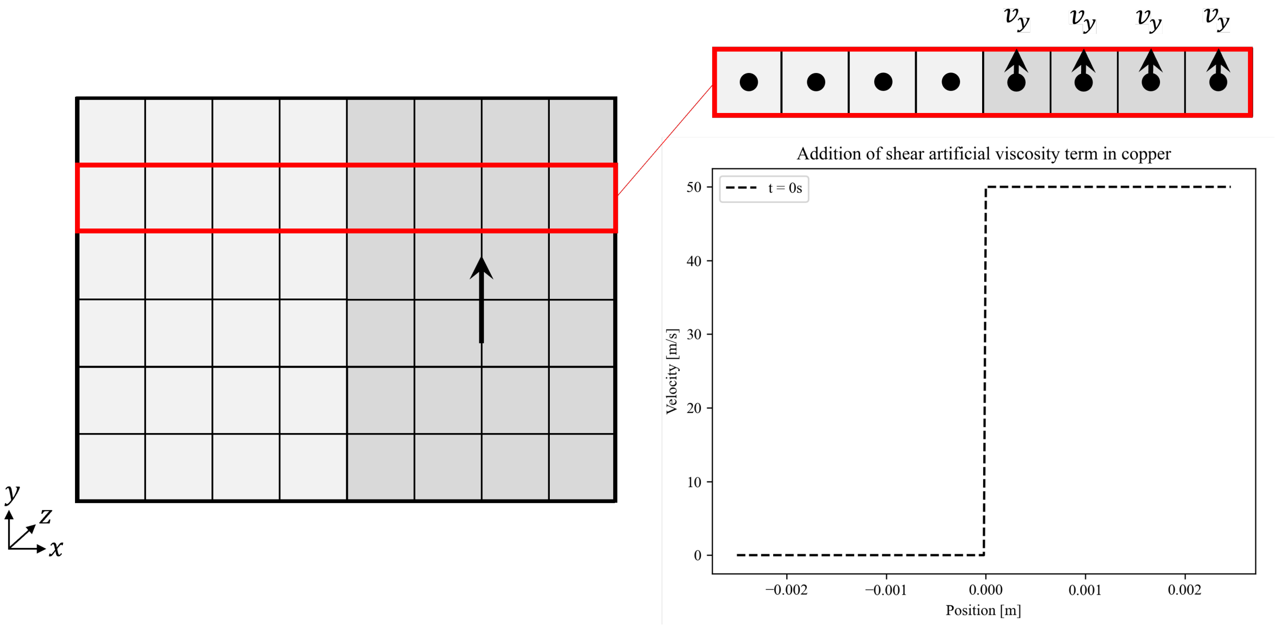

Figure 6.14: Diagram of the 1D system used to investigate shear forces.

Shear wave instabilities

In an Eulerian hydrocode with no constitutive model, changes to the momenta and internal energy in cells occur only in the direction of the motion of the flow. When a strength model is introduced, shear stresses cause change in momenta and internal energy in a direction that is orthogonal to the direction of the flow. In B2, this resulted in the propagation of significant numerical instabilities in regions dominated by shear for both stress formulations described in the previous section. These instabilities can be demonstrated in a simple 1D finite element solver.

Figure 6.14 illustrates the simplified domain simulated in the 1D solver to demonstrate the propagation of instabilities due to shear forces in the cells. In this scenario, copper filled cells oriented spatially in the x-direction experience a velocity gradient in the y-direction. In this system, S_{yx} is the only active component of stress. If the system is left to evolve in time without modification, the velocity in the cells adjacent to the gradient interface experience numerical instabilities, which propagate as the shear waves propagate. This process is demonstrated in Figure 6.15: the velocity in the cells either side of the original interface exhibits oscillatory behaviour. The largest oscillations have around 5 m/s amplitude, 10% of the original velocity in the system.

The occurrence of numerical instabilities at steep velocity gradients is a familiar concept, however, it is typically encountered at the jump discontinuities associated with shock waves. These are dealt with by the introduction of pressure-like viscosity terms, designed to smear the shock front

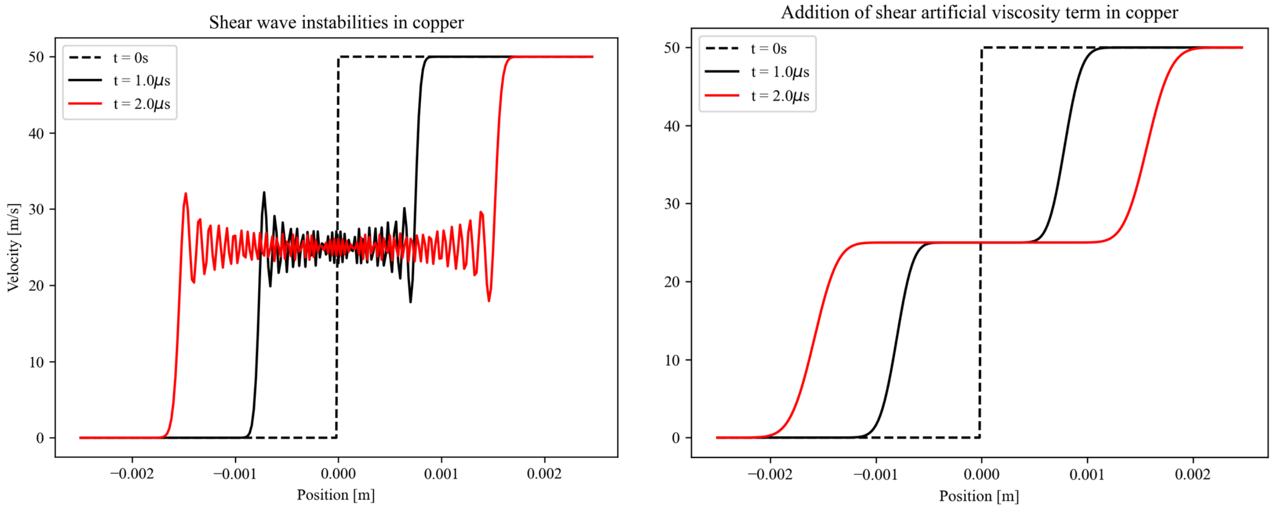

(a) (b)

Figure 6.15: Results from the 1D solver showing plots with and without the shear wave artificial viscosity modification. The simulation without artificial viscosity in B2 begins to develop complex structures, which are not present in the AUTODYN simulation.

over three to four cells [120]. A similar approach to the issue of numerical ringing in regions dominated by shear force was found to successfully dampen the instabilities. By drawing a parallel to Christensen's approximate Riemann solver [85], the shear wave artificial viscosity term (q) was calculated using the following equation,

$$q = \Delta v_{ij}\left(\frac{\rho Z^- + \rho^- Z}{\rho^- + \rho}\right) \tag{6.31a}$$

$$Z = \sqrt{\rho G}, \tag{6.31b}$$

where Δv_{ij} refers to the difference between the cell centred velocities v_i in the direction j, Z is the shear wave impedance and the - notation refers to the cell centred value to the left of the current cell being considered. This smoothly and effectively dissipates the numerical ringing created at the shear velocity gradient, as demonstrated in Figure 6.15b.

The Taylor rod deformation testcase simulated in B2 was sensitive to the the effect of the shear wave instabilities. The cumulative effects of the numerical ringing introduced by the unsuppressed instabilities in the rod are shown in the images from simulations shown in Figure 6.16. As the simulation progresses, the rod begins to develop complex structures, which are not present in the AUTODYN simulation, at the flared-end. The result at 50 µs with the shear wave artificial viscosity

(a) 10 µs **(b)** 30 µs **(c)** 50 µs

Figure 6.16: Progression of the B2 simulation of the rod without the shear wave artificial viscosity modification.

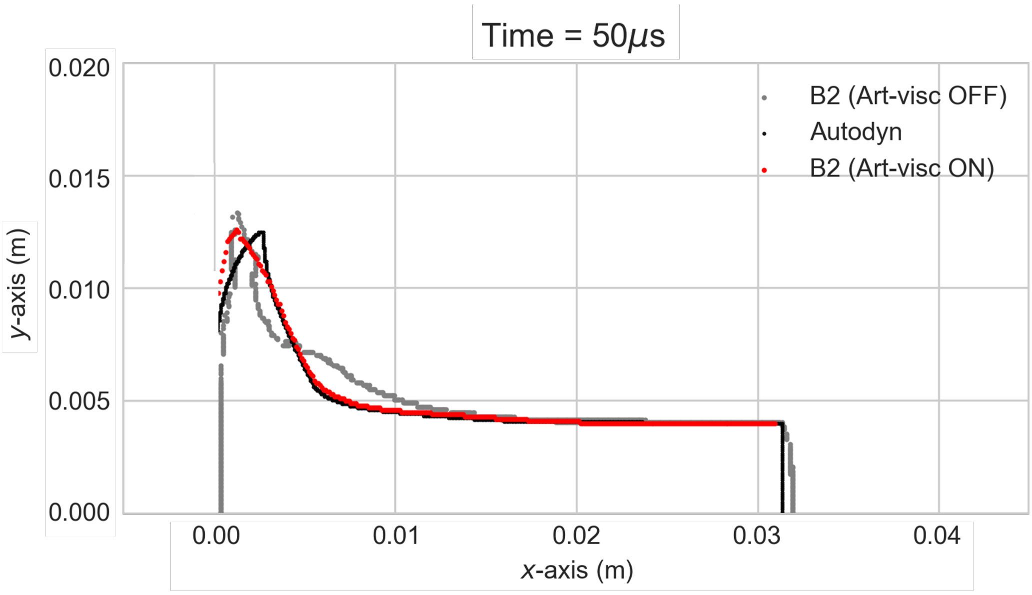

Figure 6.17: Plot of the rod profile for a 200 m/s impact in B2, B2 without shear wave artificial viscosity and AUTODYN.

term and without is plotted in Figure 6.17. The figure demonstrates this term significantly improves the match between the rod profile in B2 and AUTODYN.

6.4.6 Cross-code comparison results

The deformation of a copper Taylor rod impacting a rigid boundary condition was simulated in AUTODYN and B2 at 100, 200 and 350 m/s. The test was performed at these velocities to evaluate the algorithm in B2 across a range of strain rates. The rod deformation in AUTODYN and B2 was evaluated using both qualitative and quantitative criteria, including a visual comparison of the rod profiles and plots of the rod length and flared-end radius respectively (recall Figure 6.1). The profile of the same rod deformation without the material strength algorithm (purely hydrodynamic) is also plotted. This serves to highlight the effect of material strength on the deformation profile of the rod.

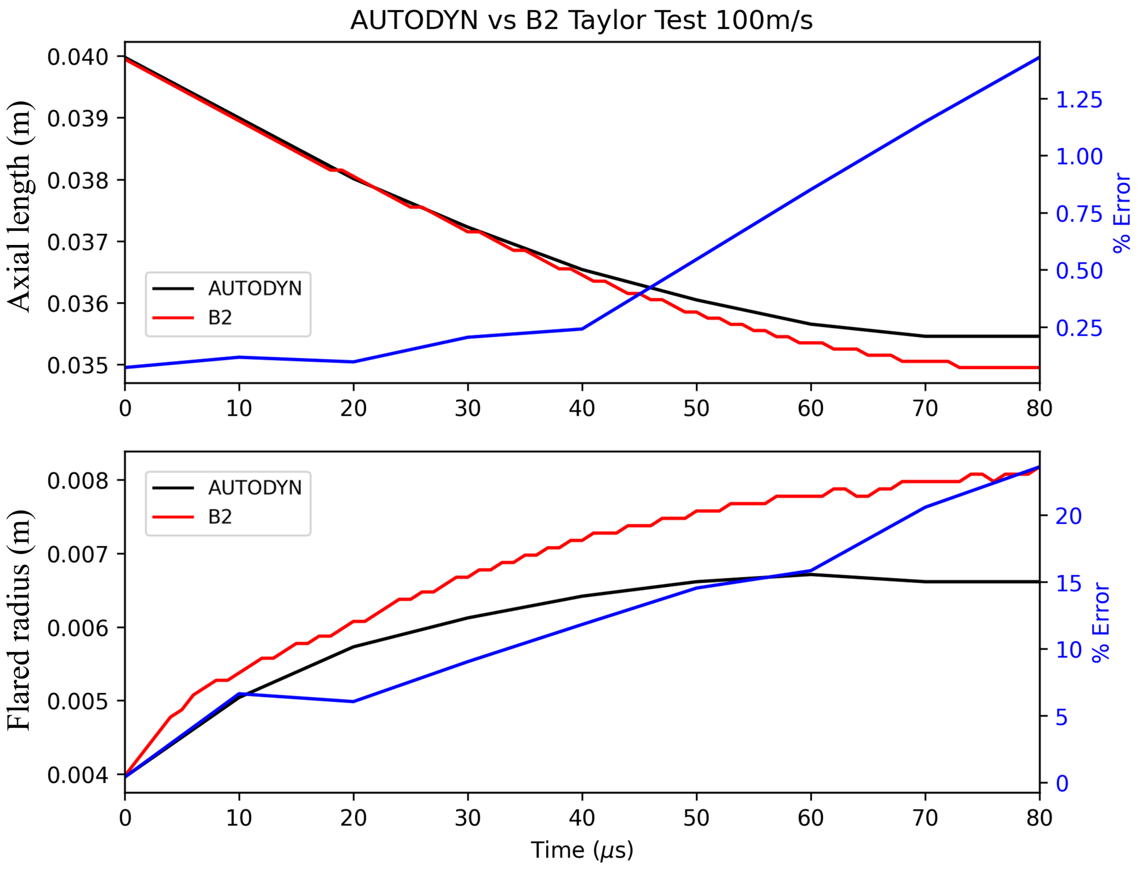

Figure 6.18: Cross-code comparison showing plots of rod length, flared-end radius and the error between B2 and AUTODYN throughout the simulation of a 100 m/s Taylor anvil-on-rod test. The rod length in the simulations match closely, however, the error in the prediction of the flared-end radius rises to over 20% at late times.

The Taylor rod at 100 m/s demonstrates a reasonable match between the codes. The plot comparing the length of the rod in Figure 6.18 reveals the difference in the instantaneous rod length is minimal, increasing to just over 0.5 % at 50 µs. The error in the flared-end radius is higher, rising to 14 % at late times. Despite this difference, the plots of the profile demonstrate the simulations with the strength model are a significant improvement over the alternative without strength, particularly regarding the predicted flared-end radius. Further, the rod profiles depicted in Figure 6.19 show the radius at the flared-end only diverges at late times. Indeed, the rod profile at 40 µs (Figure 6.19b) reveals the simulation in B2 also successfully captured the location and magnitude of the barreling in the rod adjacent to the flared-end. This suggests B2 largely captures the same behaviour as AUTODYN.

The simulation of the Taylor rod at 200 m/s in B2 compares closely to its twin in AUTODYN. Overall, the deformed rod profile plotted over 80 µs in Figure 6.21 appears visually similar: B2 successfully captured both the location and magnitude of both the barreling in the region following

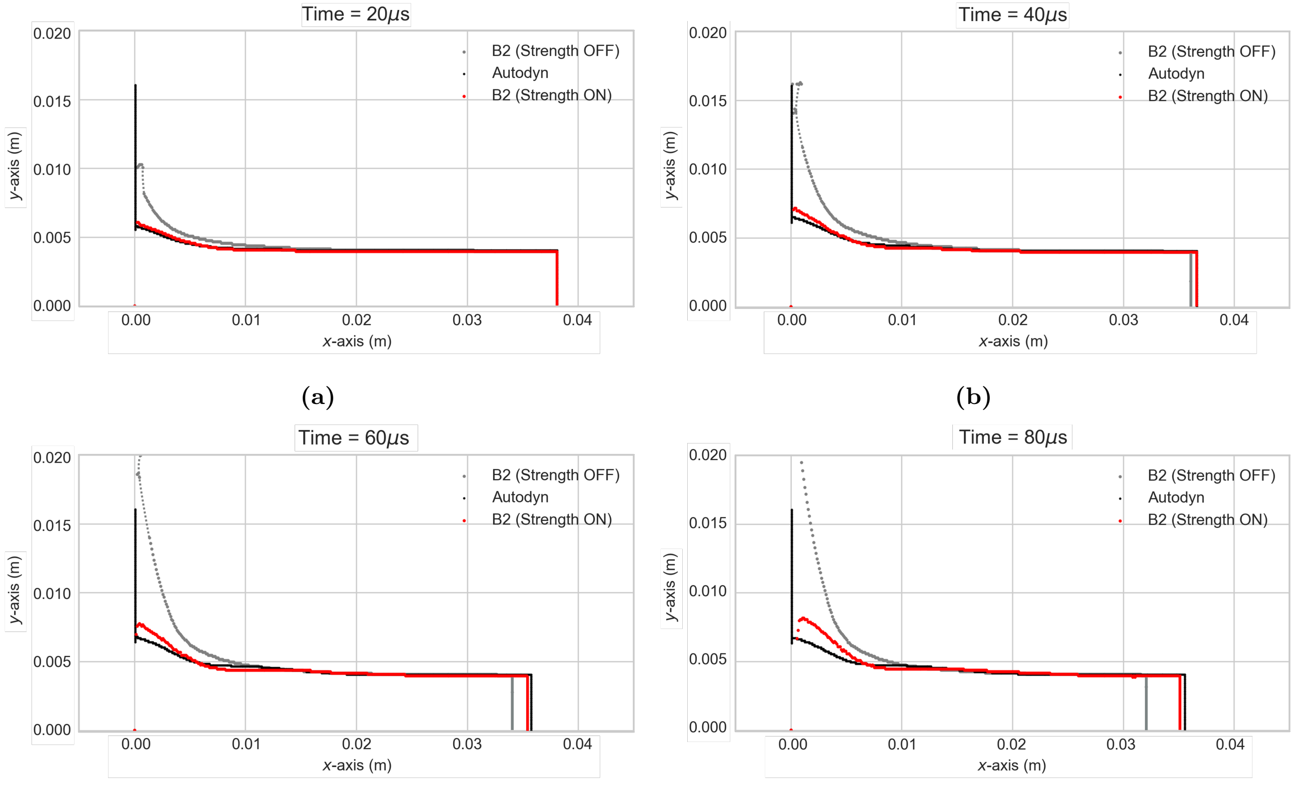

(a) (b)

(c) (d)

Figure 6.19: Cross-code comparison of Taylor anvil-on-rod test simulations profiles at 100 m/s. B2 closely replicates the profile until 40 µs, after which time it overpredicted the flared-end radius.

the flared-end and the morphology of the flared-end itself. The most significant qualitative difference between the profiles predicted by B2 and AUTODYN is the deflection of the flared-end of the rod: the edges of the rod peel back to around 5 mm at late times in AUTODYN, but only to around 2.5 mm in B2. Despite this slight deviation in the profile at the flared-end, the plots in Figure 6.20 show B2 closely matches the instantaneous crushed-end radius and rod length. The error in the axial length and radius remained below 1.5 % and 5 %, respectively, throughout the runtime.

Finally, while the simulation of the rod at 350 m/s was evaluated. The rods at 350 m/s have too high a velocity to display any distinctive barreling behaviour, the plots in Figure 6.23 demonstrate material strength remains important when predicting the rod length and flared-end radius. Figure 6.23c shows the radius of the flared-end of the rod in B2 with strength off is far greater than B2 with strength or AUTODYN. As with the rod impact at 200 m/s, the flared-end of the rod in B2 does not peel back to the same degree as it does in AUTODYN. However, the plots in Figure 6.22 show the overall error between the predicted length and flared-end radius to be 0.5% and around 6% respectively. The error in the rod length prediction is the smallest of the three test cases and the magnitude and

Figure 6.20: Cross-code comparison showing plots of rod length, flared-end radius and the error between B2 and AUTODYN throughout the simulation of a 200 m/s Taylor anvil-on-rod test. The error between the axial length and flared-end radius in the codes remained below 1.5 % and 5 %.

qualitative shape of the profile at the flared-end are similar.

6.4.7 Discussion

The Taylor anvil-on-rod test was performed at 100, 200 and 350 m/s in order to evaluate the performance of the strength model in B2 at different strain rates. The results demonstrate the error in the prediction of the final axial length was low, to within 1.25, 1.6 and 0.5% for the 100, 200 and 350 m/s impact velocities, respectively. By contrast, the final error in the flared-end radius was larger: over 20% at 100 m/s, 5% at 200 m/s, and 6% at 350 m/s. At the impact velocities of 100 and 200 m/s, the error in the axial length and flared radius increased over time. In contrast, at 350 m/s, the error in both measurements remained consistent low throughout the simulation runtime. In the past, the primary purpose of B2 has involved the investigation of extreme state, hydrodynamic scenarios, for which the volume of fluids interface tracker is effective. However, accurately tracking solid interfaces

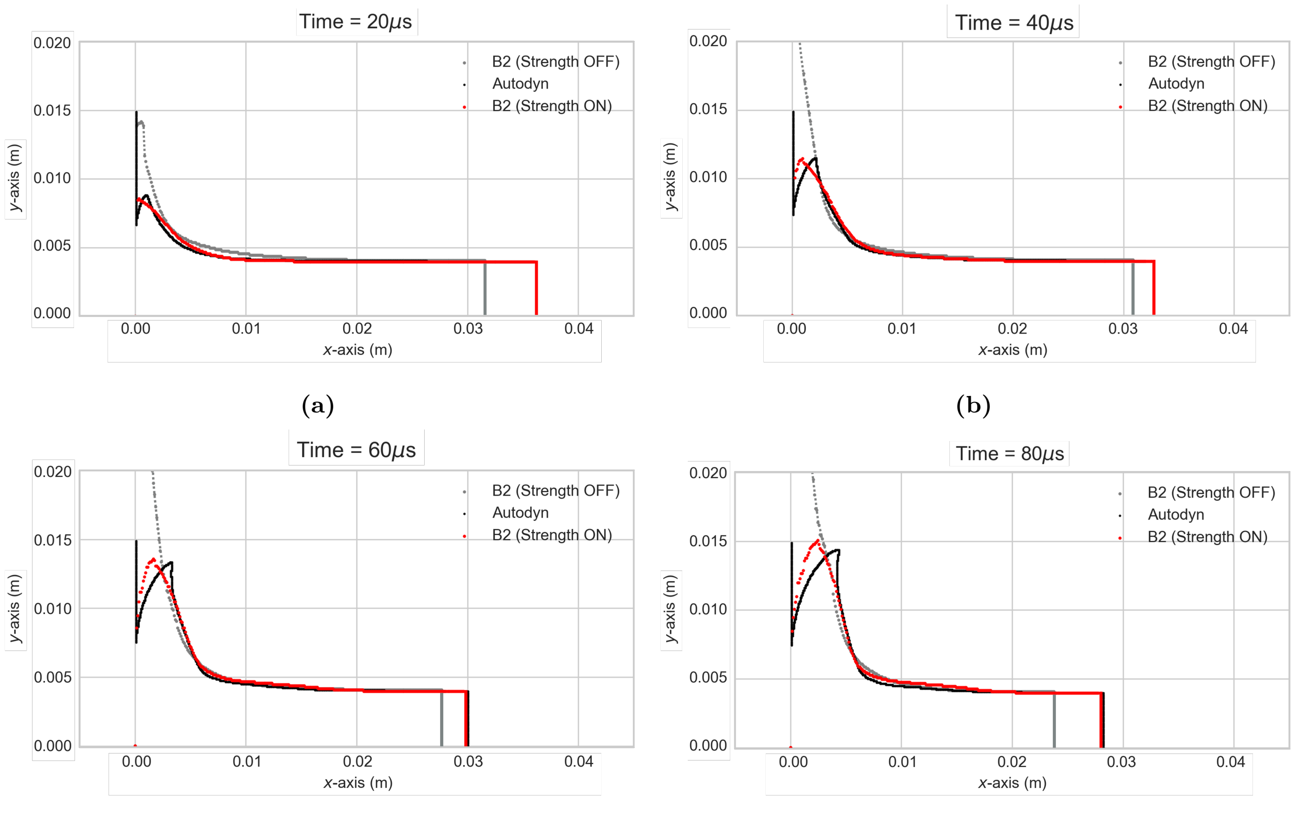

(a) **(b)**

(c) **(d)**

Figure 6.21: Cross-code comparison of Taylor anvil-on-rod test simulations profiles at 200 m/s. B2 shows good qualitative agreements with AUTODYN, although the flared-end does not rebound as much.

typically necessitates techniques which place greater emphasis on retaining the precise geometry of the interface within the cells, such as a Young's interface reconstruction algorithm [121]. Young's method, a complex to implement but highly effective interface tracking technique, is the interface tracker utilised in AUTODYN. It is proposed that to more accurately capture the evolution of solids in scenarios where material strength strongly effects the outcome, a Young's method should be incorporated into B2.

The suggestion that the differing interface tracking methods are the primary cause of the disparities between AUTODYN and B2 is supported by the differences in the magnitude of the error between the axial length and the flared radius. At each velocity tested, the flared radius had considerably higher error than the axial length. The deformation at the flared-end is a more complex process than the compaction of the rod, the former being more greatly influenced by the interface tracker. For instance, Figure 6.23a shows the rod profile adjacent to the flared-end in B2 looks similar with and without material strength, neither of which match the profile in AUTODYN. This suggests the profile in this region is not significantly influenced by material strength, thus the profile must be different to AUTODYN for another reason. Despite this, the error in the B2 simulations is still

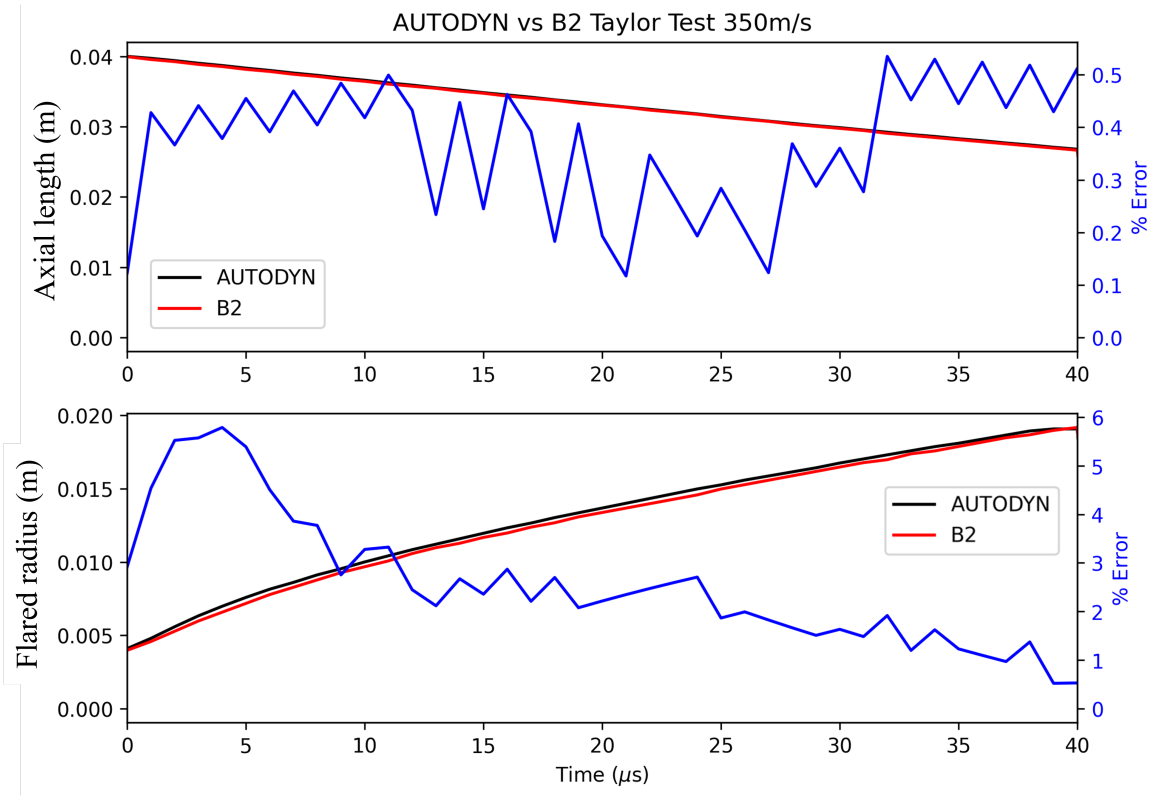

Figure 6.22: Cross-code comparison showing plots of rod length, flared-end radius and the error between B2 and AUTODYN throughout the simulation of a 350 m/s Taylor anvil-on-rod test. The error between the codes at this velocity was the lowest out of the cases considered, where the axial length and flared-end radius maximum error was 0.5% and 6% respectively.

low. Depending on the accuracy required, this work suggests the volume of fluid interface tracker, alongside the density dependence and slip conditions utilised in the work, could provide a simpler route to investigating solids in an Eulerian domain.

The overall close match between the results in B2 and AUTODYN highlights the efficacy of the methods introduced in this work to obtain an accurate profile at the rod-vacuum interface. These methods required no modification to the interface tracker and advection schemes native to B2, being contained completely within the strength algorithm incorporated into the first, Lagrangian, step of the two-step explicit solver. The yield density dependence factor and adjustment to the stress tensor using the interface grid made it possible to remove unphysical diffusion and deformation due to shear forces generated between the high velocity rod and low velocity mixed-cells. This had the additional effect of greatly improving the runtime of simulations with strength enabled. The approach to implementing slip conditions at material boundaries enabled the algorithm to recognise separate material parts and maintain the accuracy of the rod interface at the anvil and vacuum in a manner that was both

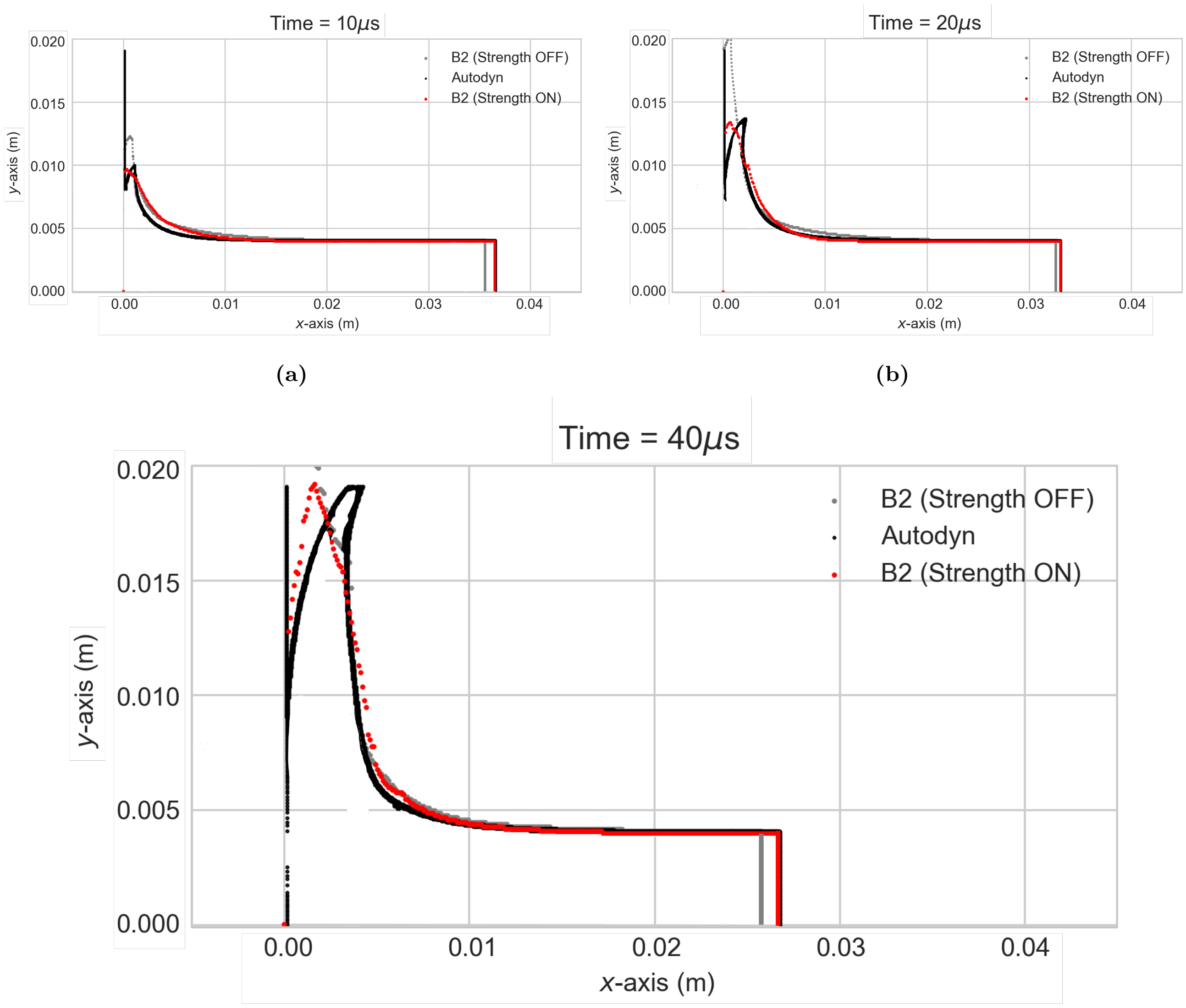

(a) **(b)**

(c)

Figure 6.23: Cross-code comparison of Taylor anvil-on-rod test simulations profiles at 350 m/s. The material strength model is clearly still important when predicting the flared-end radius, despite the high velocity of the impact.

automatic and conducive to parallel processing. Further, the additional component of artificial viscosity derived in this work successfully damped numerical instabilities introduced by shear forces, which when left unchecked resulted in a deeply unrealistic compressed Taylor rod profile.

6.4.8 Conclusions

In this work, the framework and implementation of a material strength model is demonstrated in a two-step Eulerian solution scheme in MHD hydrocode B2. This included the algorithm for the calculation in the first (Lagrangian) step. The results of Taylor test rod impact simulations in B2 were verified against those in AUTODYN. In order to be able to reproduce AUTODYN rod deformation in B2, a number of practical corrections of the stress tensor calculation were implemented. This included the following requirements and subsequent solutions:

1. The algorithm found to be most successful calculated the nine components of the stress tensor at three different cell faces from cell-centred velocities and a single cell-centred Von Mises effective stress and plastic strain.

2. To be able to model the deformation of the the Taylor rod in vacuum, mixed cells at the material-vacuum interface must have realistic yields. This was addressed by introducing a yield density factor to ensure the yield in a cell with low material density was not erroneously high, capturing realistic interface behaviour more successfully.

3. Modelling both the rod and anvil in the Taylor test required implementing slip conditions at the part boundary. This was achieved by modifying the components of the stress tensor at the cell face located at the boundary using values from an automatically generated face-centred binary array, dubbed the interface grid. This technique was found to remove instabilities formed at the rod-vacuum interface and permit frictionless interaction between separate material bodies.

4. The inclusion of strength in B2 was found to seed oscillating numerical instabilities in the velocity field in regions dominated by shear forces. This instability was also demonstrated to be present in a simplified 1D solver. An additional pressure component was derived, analogous to the artificial viscosity term used to smear shock discontinuities, based on the material shear modulus was found to completely eliminate these instabilities. The results of a simulation in B2 demonstrated without the shear wave artificial viscosity presented in this paper, the Taylor rod formed unrealistic structures at the flared-end of the rod.

The Taylor rod-anvil test was a rigorous case by which to evaluate the strength model implemented in B2, as it exacerbated known key issues when modelling solids in an Eulerian framework [103]. This included simulating slip between two separate materials and the deformation of a solid-vacuum interface over a wide range of strain rates and long time period. Verifying B2 reproduced the results of a Taylor rod deformation suggests the strength model implemented in B2 will be effective in other similar scenarios. In future work, B2 will be used to simulate experiments investigating high strain-rate behaviour in solids which cannot be done using commercially available codes, including the electromagnetic acceleration of solid flyers [96].

6.5 Modelling the electric gun with material strength

The previous section described the constitutive model integrated into the in-house hydrocode, B2. Whilst the implementation of a strength model into a hydrocode is not novel, various novel aspects of the model were developed in order to complete simulations of the electric gun with material strength in B2. For example, the density factor permitted the simulation of the development of material interfaces at a vacuum. Further, the interface slip conditions integrated into the code ensured the simulation of the frictionless interaction between different parts of materials is possible. The slip between different components in the load is required to predict the tear-out behaviour of the flyer against the barrel walls, as it is punched out of a larger sheet by the exploding foil. Moreover, the additional component of artificial viscosity prevents the accumulation of numerical instabilities in regions with shear stresses.

In the following section, simulations of the electric gun load tested in Section 5.2 with a material strength model are described. This includes the domain set-up, the results of simulations of a range of flyer thicknesses and a discussion on the impact of strength on the simulation outcomes.

6.5.1 Introduction

The electric gun is a projectile launcher capable of accelerating thin dielectric flyers to hypervelocity using relatively low-energy pulsed-power devices [21], due to its highly efficient conversion of electrical stored energy to flyer kinetic energy [57]. The electric gun operating mechanism (described in greater detail in Sections 4 and 5) is computationally challenging to simulate; the process involves a number of physical effects which are difficult to model in parallel. The electric gun utilises the discharge of a fast rise-time capacitor bank to rapidly heat a metallic foil, which changes state from solid to plasma in hundreds of nanoseconds, effectively ‘exploding’ as it increases in volume. This explosion and Lorentz force as the current from the pulsed-power devices continues to discharge accelerates a solid dielectric flyer. Consequently, the gun must model both the magnetohydrodynamic (**MHD**) effects in the foil plasma and the shocked, solid state flyer in the same domain. Further, modelling the foil and flyer at a sufficient resolution so as to achieve convergent predictions of their thermodynamic states, whilst capturing the overall behaviour of the large electrodes, oftentimes requires prohibitively expensive computational resources.

Traditionally, the electric gun has been treated primarily as a magnetohydrodynamic (MHD) problem. Hence, focus was placed on capturing the states and dynamics of the exploding foil, while modelling the flyer as simply an incompressible mass [14, 25, 67]. Traditionally, the electric gun was used to accelerate thin flyers (thickness < 0.25 mm). Research completed in this thesis has shown the change in the pressure in thin flyers is limited and the effect of sound speed in the flyer can be largely neglected. However, evidence from experiments [96] and modelling [122] has suggested thick flyers experience violent state change, spallation [110], and disassembly.

Previous chapters in this thesis focused on the development of our 0D model and performing experiments on the pulsed-power device, M3, with the goal of understanding and mitigating flyer disassembly mechanisms. At the conclusion of Chapter 5, it was apparent that a counter-intuitive effect was taking place in the electric gun load designed for M3: thin flyers exhibited plasma breakthrough late in flight. This appeared seemingly at odds with the traditional understanding that thick flyers are at greater risk of experiencing disassembly early in flight. Our 0D model, capable of predicting the pressure state in the flyer, alongside experimental results, revealed new insight into this process; the pressure, and hence the density, in thin flyers dropped late in flight. However, this does not reveal a specific mechanism by which the plasma breakthrough occurred.

To understand the behaviour of the flyers in the electric gun load designed for M3 in greater detail, two-dimensional (**2D**) simulations were performed in the MHD hydrocode, B2. A three-dimensional strength model, described in the outset of this chapter, was created for this purpose. The strength model was validated against simulations of Taylor rod-on-anvil tests performed in Ansys AUTODYN, with the goal of creating a strength algorithm which could then be used to predict the effect of material strength in the electric gun load. This included novel methods to better model the behaviour at solid-vacuum interfaces and implement slip conditions in complex load geometries. In this section, B2 is used with the strength model to answer the following questions:

1. Do the 2D simulations reveal any details about the plasma breakthrough observed during M3 experiments?
2. What physics is the electric gun operating mechanism sensitive to?

6.5.2 Background

Two-dimensional MHD simulations of the electric gun offer significant insight into the electric gun's operating mechanism that cannot be measured *in-situ* or using one-dimensional models, including the temporal evolution of the foil and flyer state and the deformation of the flyer respectively. Information regarding these details of the load can also aid the interpretation of experimentally observed behaviours, such as the flyer velocity profile and the integrity of the flyer surface.

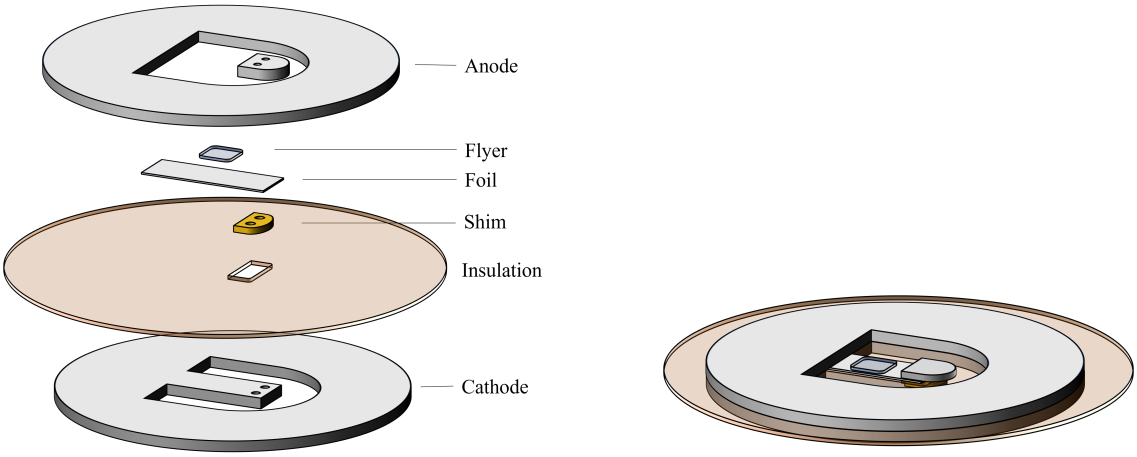

(a) Exploded view of the parts in the electric gun load (excluding the barrel).

(b) The assembled electric gun load (excluding the barrel so the foil flyer can be viewed).

Figure 6.24: Diagram of the electric gun load designed for M3 in detail.

However, representing the electric gun load in an Eulerian hydrocode is challenging for a number of reasons: modelling and analysing the electric gun load in an MHD hydrocode requires numerous approximations and assumed knowledge of the physics of electromagnetic plasma acceleration. In this section, the techniques required to simulate the electric gun load on M3, and then interpret the results of the simulation are reviewed.

Approximations and limitations

Representing the electric gun in an Eulerian domain is challenging for a number of reasons. Firstly, the load is made up of many separate parts, illustrated in Figure 6.24a, which result in frictionless contact effects which cannot be captured in B2. The current path from the cathode to the anode goes by way of the pier, through a copper shim, into the exploding foil, which is clamped in place at the end of the pier by two shoulder bolts. The copper shim, designed to pass the current through the insulation in one specific location to the foil, is represented in the Eulerian simulation as in perfect contact with both the cathode and foil. Further, heterogeneities on the surfaces prevent perfect contact. The high currents passing across these surfaces can produce plasma where contact is not perfect. This plasma can provide pathways for parasitic current loss if it reaches the outer rim of the cathode or anode (circular structure around the pier and clamp shown in Figure 6.24).

Another complication when representing the electric gun in the simulation domain is approximating electrical breakdown through the insulation between the cathode and foil. The conductivity of the

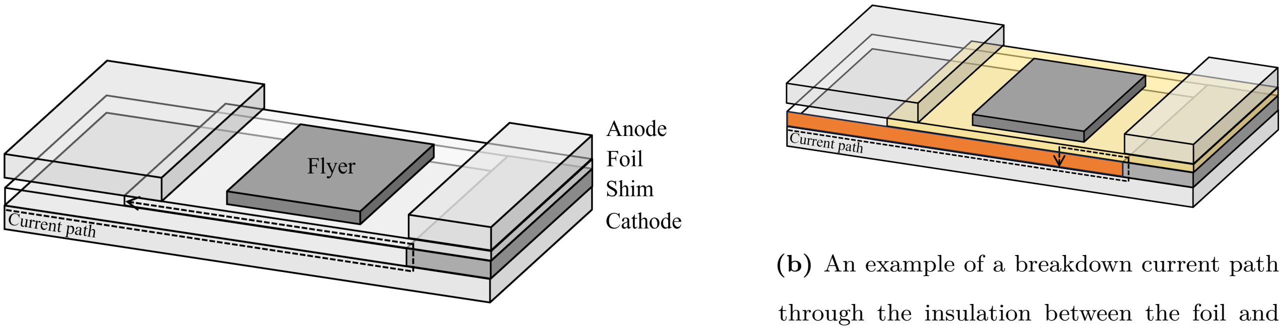

(a) The pier at the centre of the electric gun load with labelled components and the ideal current return path.

(b) An example of a breakdown current path through the insulation between the foil and cathode. In this scenario, the heated insulation became conductive on melt.

Figure 6.25: Detailed diagrams of the pier in the electric gun load designed for M3.

cathode, shim, foil and anode are calculated in B2 using the Lee-More electron conductivity model [56]. This model was created to give a consistent and complete set of transport coefficients, including electrical conductivity and thermal conductivity for dense plasmas. Furthermore, the model is adept at simulating plasmas in the presence of strong magnetic fields. However, it is expected other parts of the electric gun load will become conductive during current discharge. For instance, dielectric materials, such as the Kapton and PTFE layers used as insulation, can become conductive when melted and divert the current pathway. An example of this is illustrated in Figure 6.25b. Limited data exists to describe the conductivity of melted plastics, thus the insulating components in B2 are modelled as perfect insulators. This prevents the prediction of alternate current paths which reduce the energy available to accelerate the flyer in real-world experiments.

Electrical breakdown between the cathode and anode can also occur due to imperfections in the insulation. Texture on the surface of the insulation such as dents or scratches can cause localised regions of charge, increasing the likelihood of breakdown at these locations. Particulates such as dust trapped during assembly can induce the same effect. To minimise the probability of a breakdown path across the entire insulation thickness, a number of different layers of insulation are used. The electric gun load on M3 included a 1.0-mm-thick layer of PTFE and 40 sheets of 0.025-mm-thick Kapton. These components of the experimental load are shown in Figure 6.26. This randomises the locations of the heterogeneities in the insulation layers, reducing the statistical likelihood of a breakdown occurring. A complete breakdown path between the cathode and anode can not only cause the electric gun load to malfunction, but also cause considerable damage to the pulsed-power machine's interface platform. This is another current loss mechanism B2 cannot capture, which can result in the code overestimating the energy transfer to the foil.

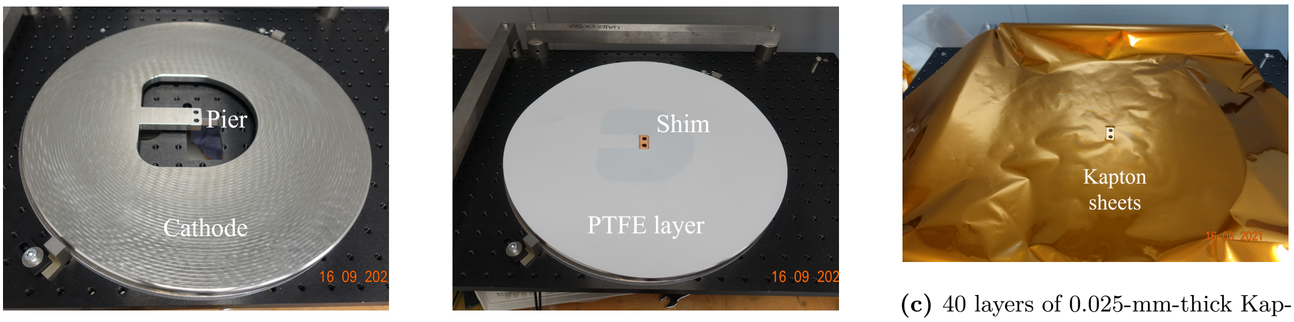

(a) The cathode used on M3, with the pier which carries the current path labelled.

(b) The layer of PTFE insulation and the copper shim which carries the current through it.

(c) 40 layers of 0.025-mm-thick Kapton sheets provide further insulation by minimising the probability of a current breakdown.

Figure 6.26: Images of the cathode and insulation layers in the electric gun load, which are difficult to model accurately.

The performance of an electric gun load is strongly dependent on the current density in the exploding foil [96]. The integral of the square of current density determines the strength of the magnetic field generated in the system, which in turn determines both the pressure state in the foil and flyer and the Lorentz force acting on the foil. To estimate the current density distribution throughout the load accurately, the electric gun load should be simulated in three dimensions and capture a number of physical features present in the physical set-up. This includes geometric details of the pier where current will accumulate, causing localised regions of increased current density, including its edges, corners and the shoulder bolt holes used to clamp the foil and shim in place. Additionally, though the pier is the region of the cathode which ideally carries the majority of the current discharged by the pulsed-power device, the cathode is in fact far larger. Figure 6.26a shows the pier juts out of a larger ring, which is used to connect the load to the pulsed-power machine's interface platform. It has been noted in 3D simulations of the EM flyer plate in B2, variations in current density across the pier caused asymmetries in the magnetic field along its length as the current passes through it. These effects are sufficiently significant as to cause flyer plates tested at First Light Fusion to tilt along the length of the pier as they accelerate, resulting in a consistent tilt on impact at the top of the barrel [68].

Work undertaken at First Light Fusion has suggested that the pier, with the shoulder bolt features and a portion of the base where it attaches to the outer ring, must be included in a 3D simulation to correctly capture the dynamic behaviour of a flyer plate load. This process could not be reproduced for the electric gun in this work as the scale of the electric gun load poses a modelling challenge not encountered when simulating a flyer plate load. Whilst the electrode, foil and flyer have lengths on the order of centimeters, the foil thickness is far smaller. Typical shots reported in this thesis have utilised aluminium foils 0.1 mm thick. This creates an uncomfortable resolution trade-off: as discussed, to be able to accurately capture the magnetic field strengths propagated in the foil, a considerable extent of the load, including precise details of the electrodes, must be simulated in 3D. At the same time, a high grid resolution is required in the foil and flyer to achieve convergent thermodynamic state predictions. B2 has a fixed mesh resolution, hence the computational resource to required to run a 3D simulation both large enough to include a significant portion of the electrodes and high enough in resolution to predict the states in the foil and flyer becomes unfeasibly large. Consequently, the simulations in this thesis were done in 2D, using the domain depicted in Figure 6.27. It should be acknowledged this simplification of the load will impact the accuracy of the modelling of the load dynamics.

Creating the MHD simulation domain

B2 uses magneto-hydrodynamic models to simulate the current in the electric gun load, the magnetic fields it generates, and the resulting Lorentz force and Joule heating in the exploding foil. Magneto-hydrodynamics in an Eulerian domain describes the motion of mixed materials in the cells using linear combinations of the mean motions of their individual components. The equation of motion can be modified to include MHD effects as follows,

$$\rho\left(\frac{\partial}{\partial t} + v \cdot \nabla\right) v = J \times B - \nabla p, \tag{6.32}$$

where ρ is the density, B is the magnetic field, p is the isotropic pressure, J is the current density and v is the velocity. Ampère's law, Faraday's law and Ohm's law are respectively,

$$\mu_0 J = \nabla \times B, \tag{6.33a}$$

$$\frac{\partial B}{\partial t} = -\nabla \times E, \tag{6.33b}$$

$$E + v \times B = \eta J, \tag{6.33c}$$

where E is the electric field and η is the electrical resistivity. Substituting Ampère's law and Faraday's law into the curl of Ohm's law yields the magnetic diffusion equation,

$$\frac{\partial B}{\partial t} = \nabla \times (v \times B) + \frac{\eta}{\mu_0} \nabla^2 B, \tag{6.34}$$

where $\frac{\eta}{\mu_0}$ is the magnetic diffusivity. Further, the Lorentz force term $J \times B$ can be expanded using Ampère's law to give,

$$J \times B = \frac{1}{\mu_0}\left((B \cdot \nabla)B - \nabla(\frac{B^2}{2})\right), \tag{6.35}$$

where the first term is magnetic tension and the second is magnetic pressure. B2 also takes into account the Hall current, the production of a potential difference transverse to the current. The Hall current is applied to the magnetic field by introducing into Ohm's law the term,

$$E + v \times B - \frac{1}{n_e e}(J \times B) = \eta J. \tag{6.36}$$

The MHD contributions to the cell-centred momentum and work terms in B2 require the magnetic field to be a face-centred value, the direction of which must be defined by the user to simulate the real-world current path. In reality, the current pathway through the electric gun is fixed by the conducting components in the load, which in turn defines the direction of the magnetic fields. In effect, B2 does the opposite: the user defines the direction in which the magnetic field strength faces in certain ghost cells (cells outside the computational domain that define the boundary conditions) and the diffusion equation advects the face-centred magnetic field through the domain at the Alfven wave speed. The magnitude of the magnetic field strength is calculated using $B = \frac{I\mu_0}{2w_{foil}}$, where w_{foil} is the user-defined foil width (which is assumed to be the same as the pier width). The magnitude and direction of the current density are then calculated in each cell based on the magnetic field strength and its direction.

B2 has two ghost cells in each dimension, which are responsible for enforcing the hydrodynamic and magnetic boundary conditions at the edge of the domain. Figure 6.28 depicts the ghost cells where the magnetic field is calculated. These ghost cell locations fix the injection point of the current such that the reduced load domain mimics the behaviour of the current path in the far larger physical electrodes. The current magnitude I is found separately using an RLC circuit of the pulsed-power machine and load. The dynamic load inductance and resistance terms were calculated using terms derived by Niasse *et al.*.

The electric gun simulations in this work were oriented in the yz plane, hence the magnetic field was assigned to the cell face in the x-direction in the ghost cells, as shown in Figure 6.28. This generates a Lorentz force in the materials which carry a magnetic field which acts in the z-direction. The figure also identifies the 'static region', a region of cells which are forced to have zero velocity throughout the simulation. This is a practical measure taken to ensure the location adjacent to the ghost cells which propagate the magnetic field remains fixed in place throughout the simulation. The static

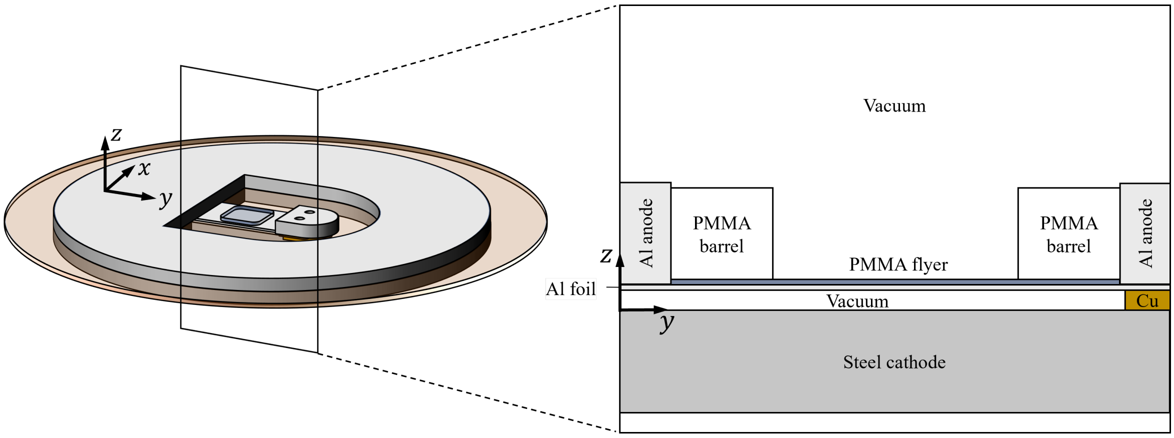

Figure 6.27: The diagram of the electric gun load (left) with regards to the two-dimensional simulation frame of the pier (right). The pressure achieved in the M3 vacuum chamber is of the order 1×10^{-6} Pa

.

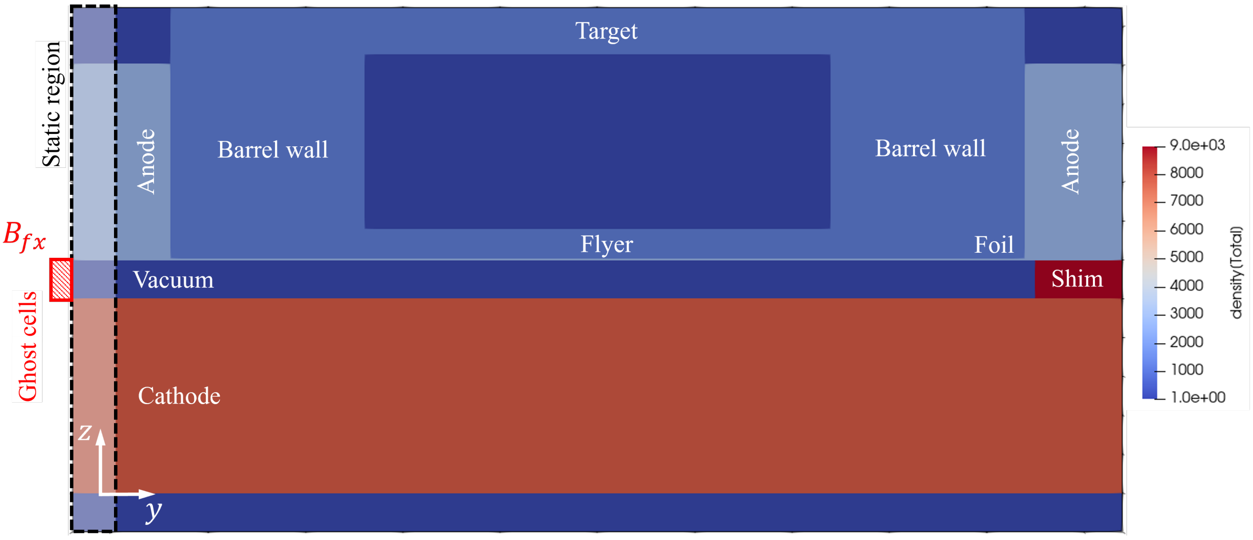

Figure 6.28: The two-dimensional electric gun load simulation domain, coloured by density, with the static region and ghost cells which define the current path illustrated and labelled.

condition employed in these simulations influences the route of the current path, occasionally resulting in non-physical distributions of current density in this region. Where this occurs, the simulation results must be rejected and the domain size increased, so as to distance the static cells from the foil and flyer.

Current loss in the load

Section 6.5.3 catalogued the various approximations and limitations associated with modelling the electric gun load in B2. It concluded that the omission of a number of current loss mechanisms can contribute to deviations between simulated and experimentally observed behaviour. When modelling the effect of material strength on the behaviour of the electric gun load, it is crucial that the flyer state is accurately estimated. The strength model implemented in B2 reduces the components of the stress tensor to zero in cells with material above melt temperature. Hence, if the current in the electric gun load is overestimated in B2, the flyer may be predicted to be above melt temperature, when in reality, the flyer is solid and subject to strength effects.

Issues with modelling the current through the load are not unique to B2. Porwitzky *et al.* [123] note challenges modelling the load current in the dynamic materials properties (**DMP**) program's stripline geometry in a high voltage pulsed shaped (asymmetric asynchronous) driving model. Their research revealed the power loss predicted by the pulsed-power codes at Sandia National Laboratories for the Z Pulsed-Power Facility was adversely affected by inaccurate modelling of plasma. The authors note that while the standard stripline geometry driven by a synchronous short pulse (100 ns rise time) current is well understood, with simulations producing accurate predictions of observed stripline velocities, the DMP stripline highlighted in this work could not be modelled by existing state-of-the-art loss models. The results presented implied the presence of a plasma source that could partially short the load, resulting in an unexpected load current loss.

Whilst M3 and the electric gun load experimentally tested in Chapter 5 are dissimilar in many ways to the Z machine and the DMP stripline, the scenario discussed in [123] bears greater similarity than usual to a typical M3 current profile, due to its extended rise-time. Clearly, accurately capturing the load current loss in such scenarios is a highly complex endeavour, stretching beyond the scope of this work. Consequently, simple approximations are employed going forward in this chapter to attempt to simulate the experimental behaviour of the electric gun.

Traditionally, the simulation of EM flyer plates which match experimentally observed velocities has been achieved at First Light Fusion [124] by applying a blanket Current-Loss Factor (C_F) to the current calculated by the RLC-circuit model (I), where in each timestep,

$$I(t) = C_F \cdot I(t). \tag{6.37}$$

When the C_F is applied to the simulation, I becomes the effective current applied to the ghost cells at the domain boundary. The Current-Loss Factor attempts to account for the energy lost in the system through the mechanisms discussed in the previous section. It is not a physical mechanism, so much as a method to reduce the total energy in the simulation to better match experimental behaviour. Typically, C_F is constant throughout the simulation. Its value is selected through comparison between the measured and simulated flyer velocity profile. It should be noted the realistic proportion of current loss in the load is likely to vary throughout operation; the Current-Loss Factor is a simplistic approximation of this process.

Instabilities in the flyer

The method of flyer acceleration in the electric gun (a low density foil plasma under the influence of an electromagnetic field accelerating into a higher density flyer) creates a system which is vulnerable to instabilities. Rayleigh-Taylor (**RT**) instabilities form when regions of materials with different densities experience a density gradient which opposes the pressure gradient. This occurs in the electric gun when the foil plasma (the low-density region) accelerates the flyer (the high-density region). The inertia of the higher-density flyer resists its acceleration, thus if penetration of the flyer occurs in any region by the foil plasma, the flyer material in this region will lag, causing the instability to grow. Physical imperfections along the surface of both the foil and the flyer, such as scratches or surface texture, will initiate interpenetration between the two and seed the RT instability. In order to understand the conditions in electric gun load which will cause the Rayleigh-Taylor instability to grow or stabilise, some of its governing equations must be considered.

The Navier-Stokes momentum equation, including viscosity and density gradients, may be linearised and described in terms of a single velocity u_z for a interface with a growing perturbation in the z direction proportional to $\exp(ik_x + ik_y + \gamma t)$ in terms of,

$$\frac{\partial}{\partial z}\left[-\rho\gamma\frac{\partial u_z}{\partial z} + \rho\nu\left(\frac{\partial^2}{\partial z^2}\right)\frac{\partial u_z}{\partial z} + \frac{\partial(\rho\nu)}{\partial z}\left(\frac{\partial^2}{\partial z^2} + k^2\right)u_z\right] = k^2\left[-\rho\gamma u_z + \rho\nu\left(\frac{\partial^2}{\partial^2} - k^2\right)u_z + \frac{\partial(\rho\nu)}{\partial z}\left(2\frac{\partial u_z}{\partial z}\right) + u_z\frac{g}{\gamma}\frac{\partial\rho}{\partial z}\right], \tag{6.38}$$

where γ is the growth rate, ν is the kinematic viscosity and μ is the shear viscosity. The case can be simplified by assuming the fluids are both inviscid and uniform, such that Eqn. 6.38 reduces to,

$$\frac{d^2u_z}{dz^2} = k^2u_z, \tag{6.39}$$

which has the solutions $u_z = u_i\exp(\pm kz)$. Eqn. 6.38 can be applied to materials either side of an interface, where u_z and $\frac{\partial u_z}{\partial z}$ are continuous across the interface, resulting in the equation,

$$u_i\frac{g}{\gamma}(\rho_0 - \rho_1) = \frac{\gamma}{k^2}(\rho_0 + \rho_1)ku_i. \tag{6.40}$$

This results in a growth rate of $\gamma = \sqrt{\alpha k g}$, where α is the Atwood number ($\alpha = \frac{(\rho_0 - \rho_1)}{(\rho_0 + \rho_1)}$). If $\alpha < 0$, the instability does not form; instead, the initial perturbation oscillates. If viscosity in the material is non-zero, the maximum growth rate becomes,

$$\gamma = \frac{3}{4}\left[\frac{(\alpha g)^{4/3}}{\nu^{2/3}}\right]^{1/2} - \frac{(\alpha g)^{2/3}}{4\nu^{1/3}}, \tag{6.41}$$

thus the effect of viscosity is to dampen the growth rate of the perturbations. This, alongside prior work [125, 126], suggests that the simulations with the strength model would decrease the growth rate of the instabilities in the simulations [127, 128].

Other than viscosity, another important mechanism that influences the growth rate of RT instabilities is the density gradient across the interface. In the case of zero viscosity, Eqn. 6.38 becomes,

$$k^2\left(\gamma\rho - \frac{g}{\gamma}\frac{\partial\rho}{\partial z}\right) = \frac{\partial}{\partial z}\left(\gamma\rho\frac{\partial u_z}{\partial z}\right). \tag{6.42}$$

Applying the boundary condition $\rho_0 = \rho_1 = \rho$, the case when the density across the interface becomes continuous, leads to a growth rate of,

$$\gamma = \sqrt{kg(\frac{4kL}{1 + 4k^2L^2})}, \tag{6.43}$$

where L is the density scale length. Consequently, in a system with an increasing density gradient, L increases and the growth rate decreases. In the context of the electric gun, this suggests if the density gradient at the foil-flyer interface decreases, the flyer will be more greatly susceptible to RT instabilities.

6.5.3 Material models and set-up

The tables presented in this section delineate the material models and parameters employed in the simulations within this section. The Frankfurt equation of state (**FEOS**) was used to capture the compressibility behaviour of the materials in the load. FEOS provides tabulated equations of state, based on the QEOS model, formulated following the methodology detailed in [89]. Additionally, the conductivity of the components were calculated in B2 using the Lee-More electron conductivity model [56].

The Johnson-Cook (**JC**) yield model was applied to capture the material strength effects in the load [114]. The loads described in Section 5.2 comprised metals and polymers, with polymer flyers. Under high strain rates and extreme pressures, polymers typically diverge from the JC model. For such conditions, other models, such as the Preston-Tonk-Wallace (**PTW**) model, may better capture the strength effects in the flyer [129]. However, recent work by Rai *et al.* [130] developed JC yield model parameters tailored for PMMA under intense shock loading, proving suitable for modeling the flyer and gun barrels in the electric gun setup. Furthermore, the JC model implemented in B2 underwent rigorous testing in a cross-code comparison against Lagrangian simulations conducted in AUTODYN (Section 6.3). A notable extension to this work could include the incorporation of a more appropriate strength model, if its effects are deemed important.

Table 6.2: A description of the parts in the electric gun load, the material models and adjusted settings.

Part	Material	EoS	Conductivity model	Strength model
Cathode	Stainless-steel	Adjusted Fe FEOS	Lee-More	Johnson-Cook
Insulation	PTFE + Kapton	PMMA	None	Johnson-Cook
Shim	Cu	Cu FEOS	Lee-More	Johnson-Cook
Foil	Al	Al FEOS	Lee-More	Johnson-Cook
Flyer	Polyimide	PMMA FEOS	None	Johnson-Cook
Barrel	PEEK	PMMA FEOS	None	Johnson-Cook
Anode	Al	Al FEOS	Lee-More	Johnson-Cook
Target block	PMMA	PMMA FEOS	None	None

Table 6.3: Johnson-Cook material properties. Polyimide is modelled using the same EoS and JC parameters as PMMA, but its melting temperature is set to 623 K.

Material	A	B	C	n	m	Melting temp
PMMA	375 MPa	90 MPa	0.077	4	0.74	433 K
Polyimide	375 MPa	90 MPa	0.077	4	0.74	623 K
PEEK	375 MPa	90 MPa	0.077	4	0.74	616 K
Copper	90 MPa	292 MPa	0.025	0.31	1.09	1356 K
Aluminium	265 MPa	426 MPa	0.015	0.34	1.0	893 K
Stainless-steel	310 MPa	1000 MPa	0.07	0.65	1.0	1673 K

Several materials listed in Tables 7.2 lacked a specific material model. Where this was the case, the most similar material model available was used. It is common practice to use the PMMA EoS to model a range of polymers. However, PMMA has a lower melting temperature than polyimide or polyether ether ketone (**PEEK**). This is accounted for by adjusting the melt temperature in the JC model parameters, listed in Table 6.3.

The current input to the simulations was calculated by solving an RLC circuit using the M3 machine parameters listed in Table 6.4. The load geometry within the domain shared identical dimensions with the load tested on M3 in Section 5.2.

Table 6.4: Machine parameters for pulsed power capacitor bank M3.

Machine Parameters	Value	[units]
Charge voltage	140	kV
Capacitance	124.8	μF
Fixed resistance	0.1	$\mu\Omega$
Fixed inductance	12.5	μH

6.5.4 Results

Two-dimensional simulations of the electric gun were performed in B2 using the techniques described in the previous section. First, an appropriate current loss mechanism was established using experimental results from Section 5.2. Subsequently, flyer thicknesses of 0.25 mm, 0.5 mm, 1.0 mm and 1.5 mm were driven using an M3 current attenuated by the current loss factor, discharged through a 0.1 mm thick Al foil. To explore the influence of material strength behavior within the load, two simulations were conducted with identical setups: one incorporating the material strength model and the other without it.

The Current Loss Factor

The velocity profile of the electric gun flyer is a useful metric of other important parameters in the load which cannot be measured *in-situ.* The flyer velocity is dependent on both the magnetic and thermal pressure in the exploding foil, which in turn governs the pressure states in the flyer. Therefore, if a simulation accurately predicts the velocity of the flyer, greater confidence can be ascribed to its predictions of the states of the foil and flyer. In the case of the 2D simulations of the electric gun, in which the flyer velocity is significantly overestimated, the states in the foil and flyer are likely to be proportionally more extreme. As a result, the experimentally measured velocities from the experiments on M3 were used to tune the Current Loss Factor.

When the electric gun is simulated in B2 without a loss mechanism, the dynamics of the flyer appear very different to the experimentally observed behaviour. The limited VISAR data collected in Section 5.2 is compared to unattenuated 2D simulations in Figure 6.29. The velocity of the flyer in the simulations was calculated by differentiating the position at the centre of the flyer's leading surface. The plots show the simulations estimate the flyer velocity to be over twice the experimentally observed value during the first microsecond. This suggests that a significant portion of the electrical energy in the experimental load is not being converted to kinetic energy in the flyer.

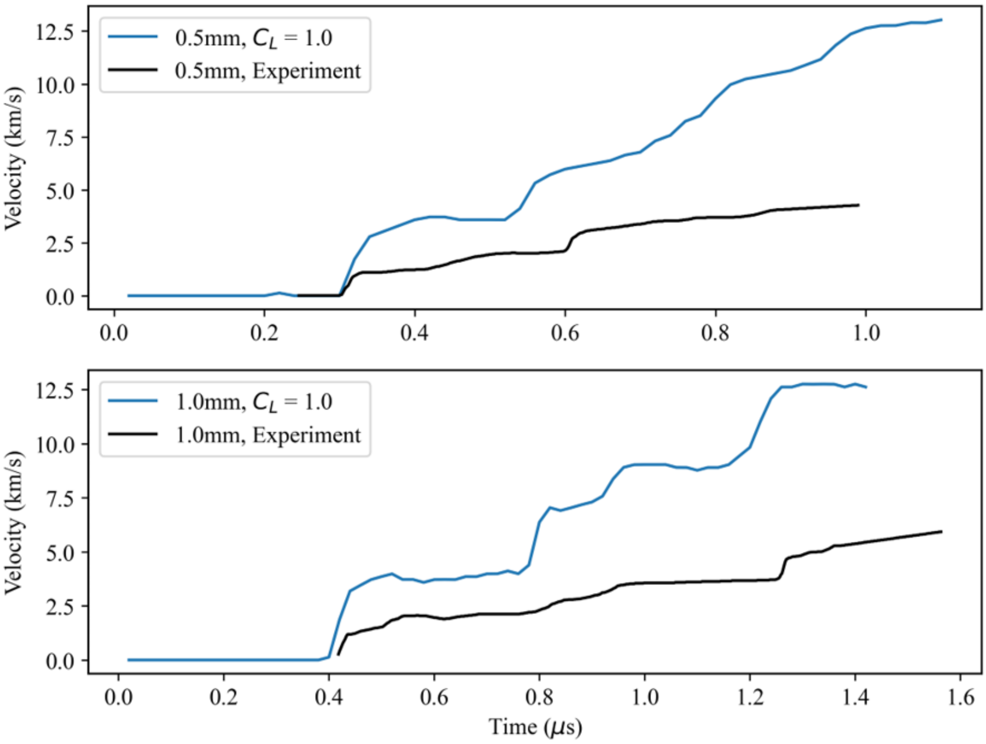

Figure 6.29: Plots of the experimentally measured velocity profiles [96] compared to 2D MHD predictions with an unattentuated current (i.e. $C_L = 1.0$)

The limited VISAR data collected in Section 5.2 was compared to 2D simulations with a range of C_F values applied to the input current. Figure 6.30 suggests simulations of the 0.5-mm and 1.0-mm-thick flyers matched the measured velocity best when $C_L = 0.45$. However, the incomplete VISAR traces make it difficult to draw reliable conclusions. To attempt to estimate the behaviour in the latter half of the flight time, the simulated and experimentally measured impact times at the target were compared. The impact times recorded in Table 6.5 also indicated the simulation impact time matches the experimentally measured impact time best when $C_L = 0.45$. In actuality, the factor of the current loss is likely to vary throughout operation. Capturing the current loss is a complex but important challenge, which merits further exploration in future work.

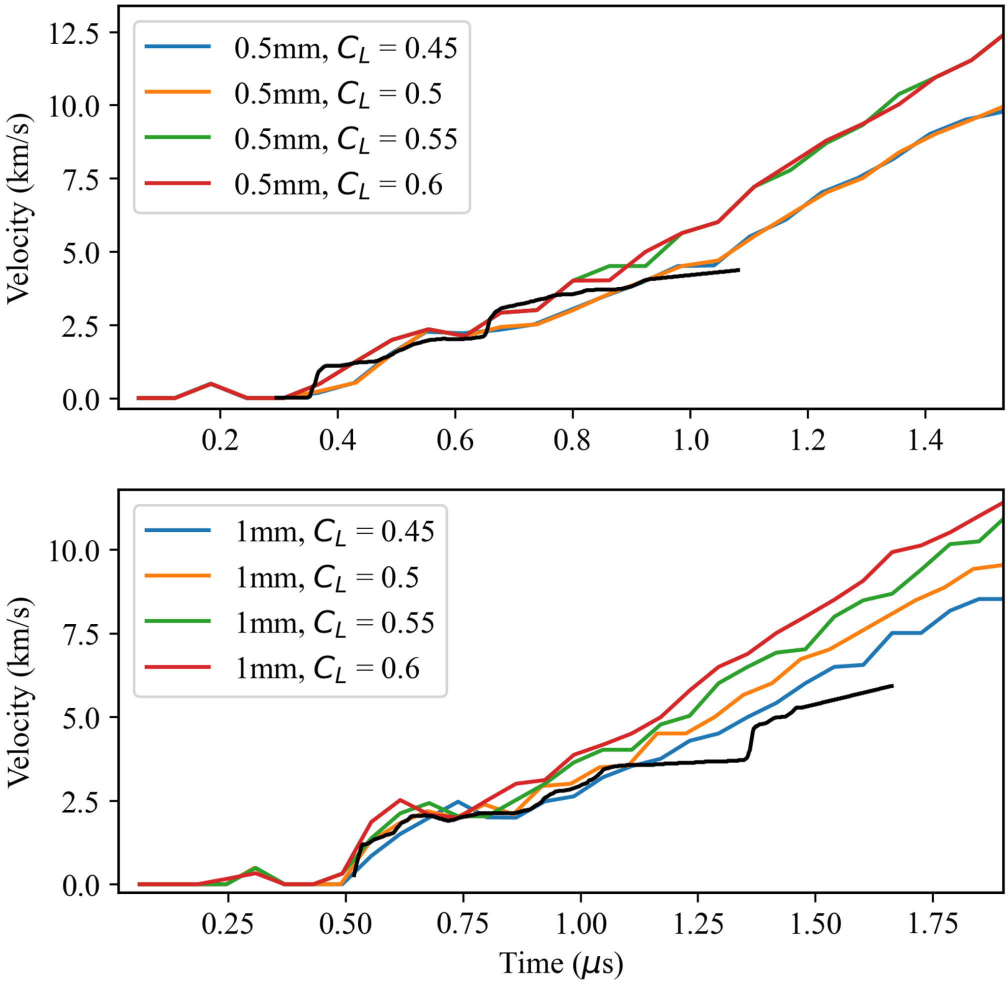

Figure 6.30: Plots comparing the experimentally measured velocity profiles (in black) [96] with 2D MHD predicitons for different load current factors. It is challenging to choose the most appropriate load current factor, as the VISAR velocimetry lost signal around halfway through flight in both cases. The application of a blanket current scaling factor is likely not representative of the real-world current loss in the load. The development of a pulsed-power load model is a promising avenue for future work to address the discrepancies between the experimental and simulated loads.

Simulations with material strength

To understand the influence of material strength in simulations of the electric gun, it must first be identified whether the effects are active. The strength model is switched off in cells containing material above the melt temperature. Therefore, if the flyer melts, strength effects will cease to influence the flyer for the remaining duration of the simulation. The melt times with respect to the overall flyer flight times are shown in Table 6.6. Note, the 1.0 and 1.5-mm-thick flyers retain a solid region for the longest duration; in fact, the 1.5-mm-thick flyer retained a solid region towards its

Table 6.5: Comparison between experimentally measured and modelled impact time for different values of C_L. The simulated impact time closest to the experimentally measured impact time have been highlighted in bold.

Flyer thickness	Measured impact time (µs)	$C_L = 0.6$	$C_L = 0.55$	$C_L = 0.5$	$C_L = 0.45$
0.25	**1.63**	1.42	1.46	1.50	**1.60**
0.5	**1.79**	1.60	1.66	1.76	**1.82**
1.0	**2.27**	1.90	1.98	2.02	**2.18**
1.5	**2.43**	2.10	2.20	**2.42**	2.46

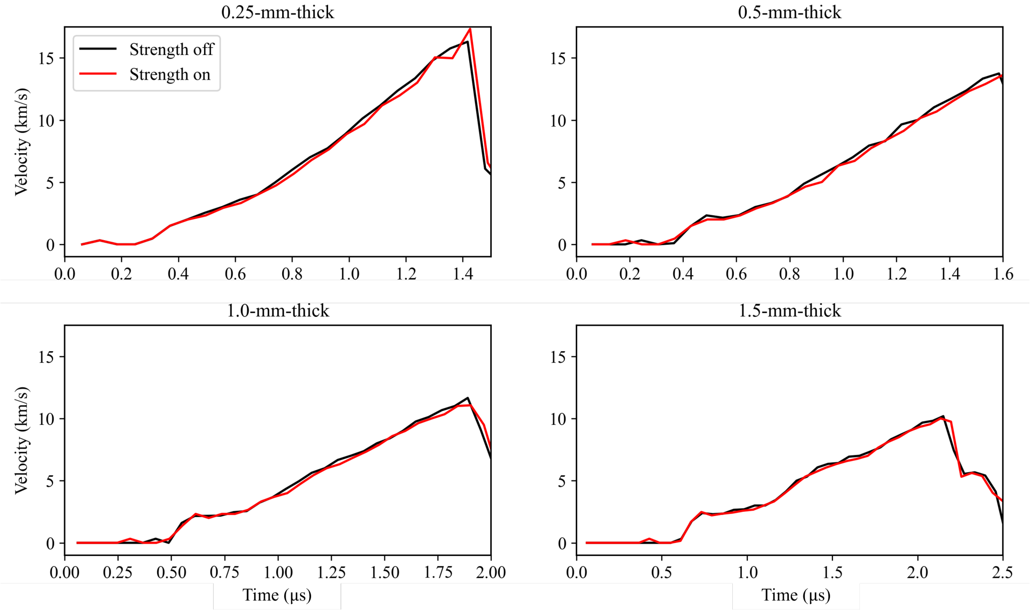

Figure 6.31: Comparison between the flyer velocity profile in 2D MHD simulations of the electric gun load with and without a material strength model. The material strength model has little impact on flyer velocity.

front surface until impact. The table demonstrates the strength model is active in all the flyers for a considerable portion of time until impact, including during launch.

Table 6.6: Flyer thickness and their melt times (time when the flyer is fully melted).

Flyer thickness (mm)	Impact time	Flyer melt time
0.25 mm	1.63 µs	0.80 µs
0.5 mm	1.79 µs	1.08 µs
1.0 mm	2.27 µs	1.54 µs
1.5 mm	2.43 µs	Does not fully melt before impact

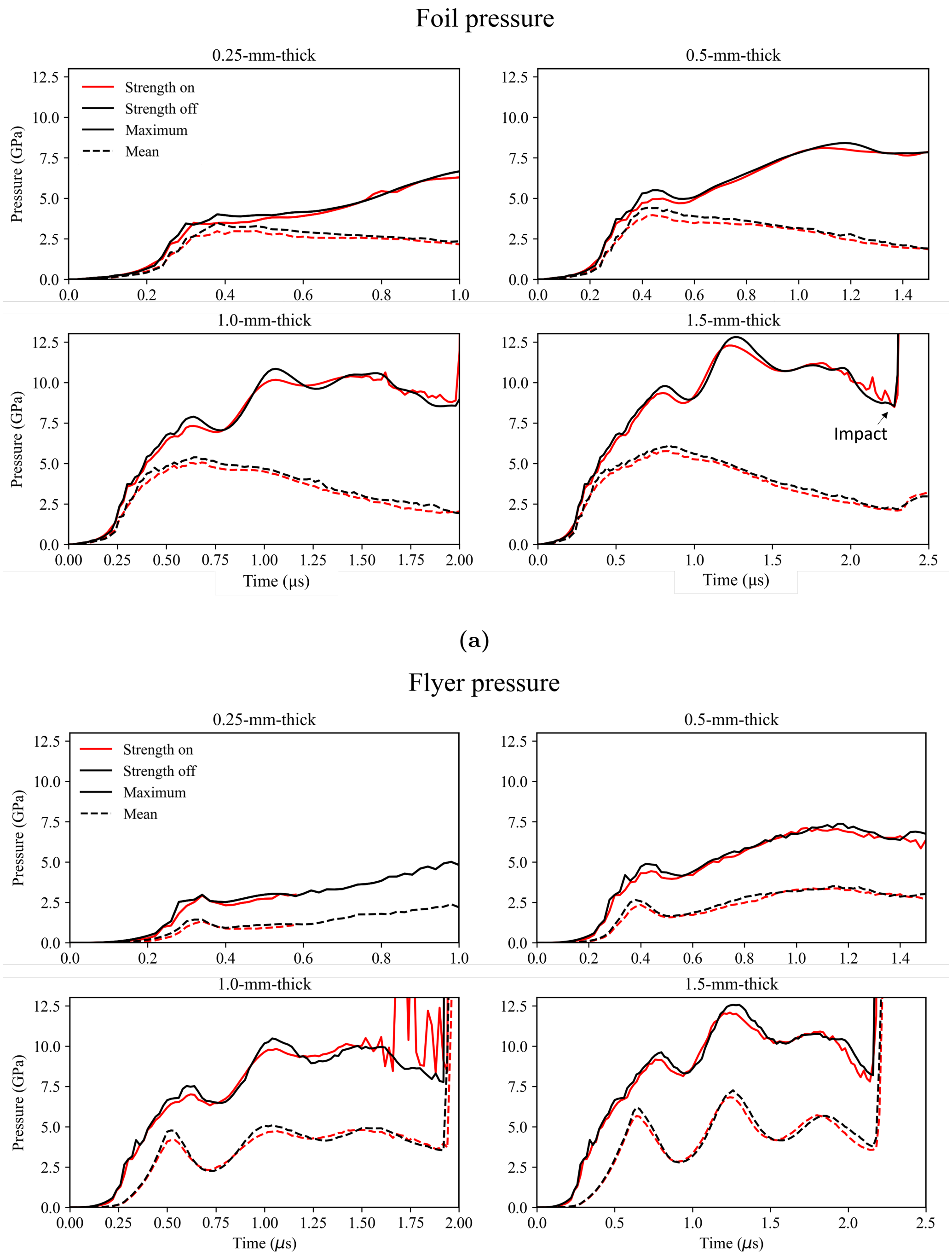

(a)

(b)

Figure 6.32: Temporal plots of the mean and maximum pressure in the foil and flyer in 2D MHD simulations with and without a material strength model. The pressure in the foil and flyer is slightly lower in simulations with material strength, though, the maximum difference between them is under 4%.

The influence of the material strength on simulations of the M3 electric gun load in B2 was investigated through qualitative and quantitative comparison of the foil and flyer dynamics, state and morphology. The dynamics of the flyer included considering the flyer velocity at the flyer surface.

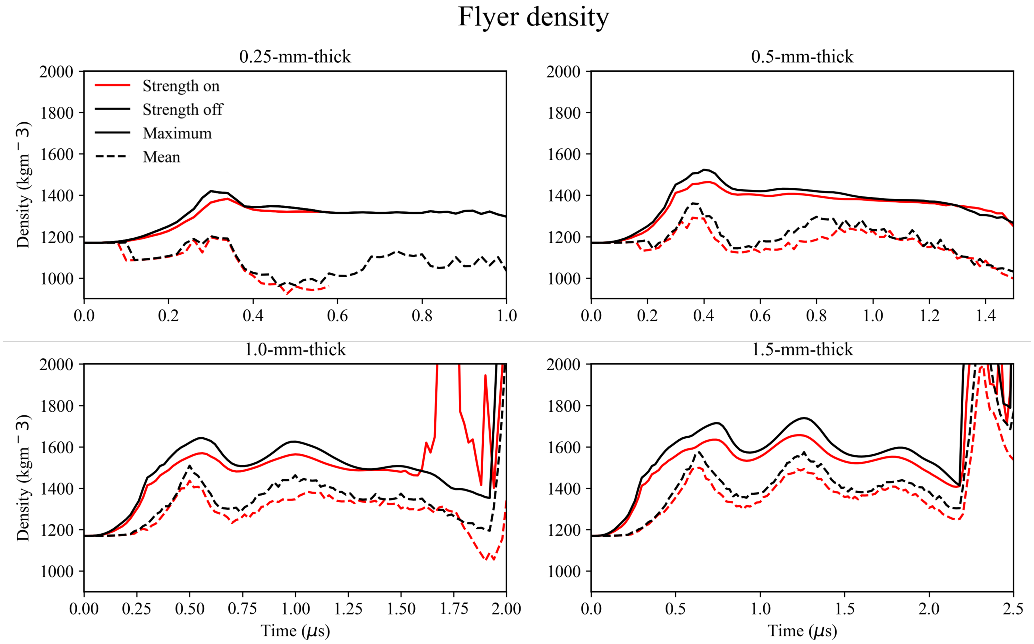

(a)

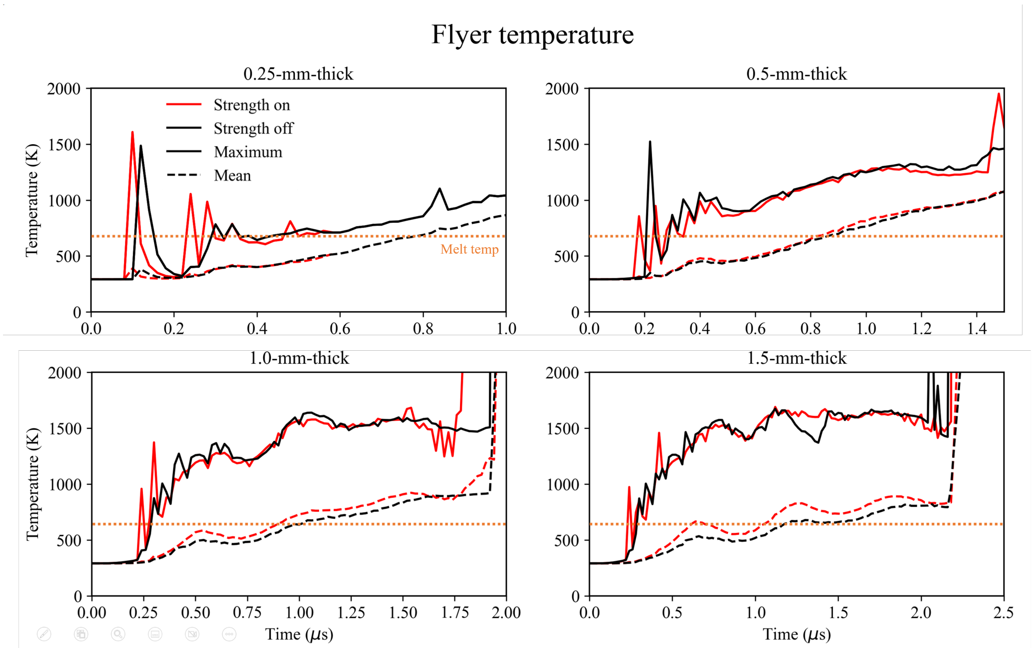

(b)

Figure 6.33: Temporal plots of the mean and maximum density and temperature flyer in 2D MHD simulations with and without a material strength model. The density in flyer is slightly lower in simulations and the mean temperature is higher in the thicker flyers with the material strength model switched on. However, the percentage difference between the values is small.

Material strength appears to have limited influence when making a quantitative comparison of the flyer dynamics. The plots shown in Figure 6.31 reveal the flyer velocity is not significantly affected

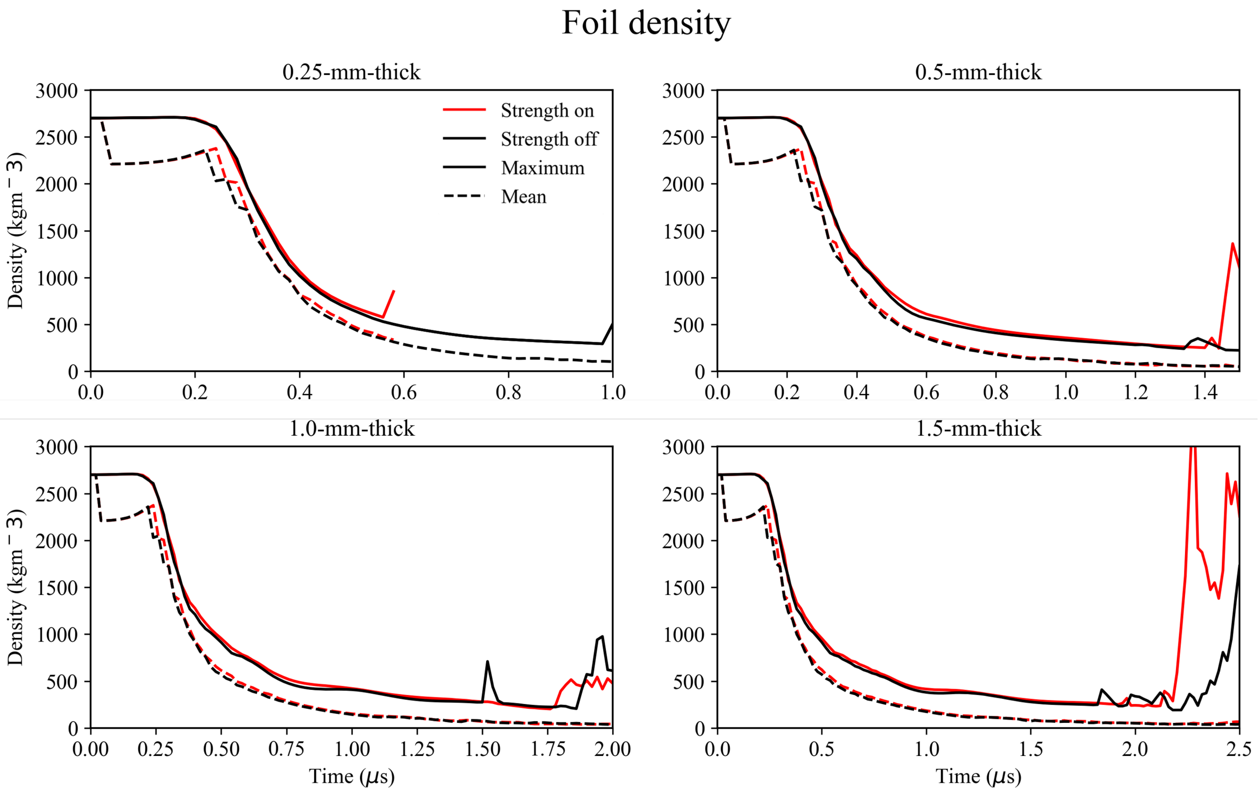

Figure 6.34: Temporal plots of the mean and maximum foil density in 2D MHD simulations with and without a material strength model. The difference in each case is negligible.

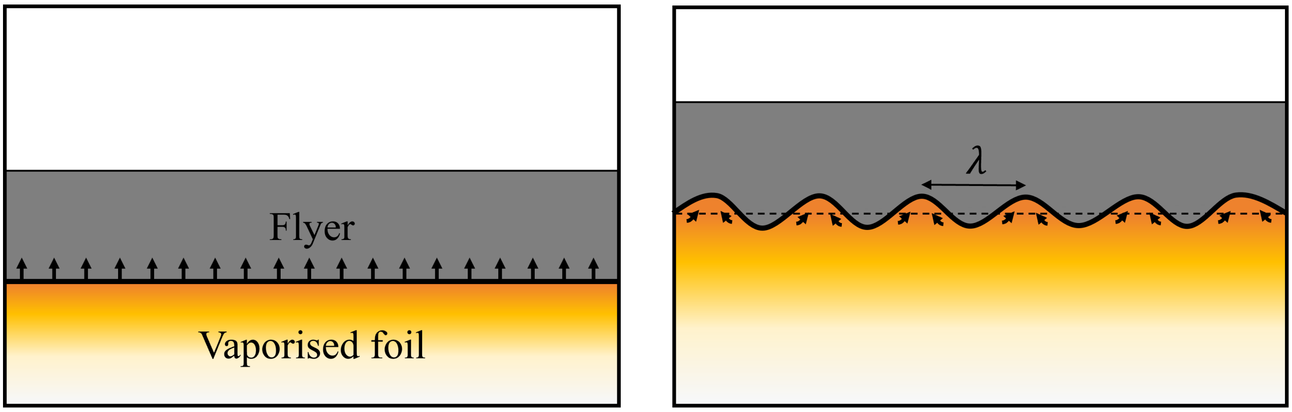

(a) Diagram showing the initially planar, uniform interface between the low-density foil driving the dielectric flyer.

(b) After some time has elapsed, heterogeneities on the foil and flyer seed RT instabilities with amplitude indicated by the dotted line and a wavelength of λ.

Figure 6.35: Diagrams illustrating the formation of the RT instabilities at the foil-flyer interface.

by the material strength model. At each thickness investigated, the impact velocity of the flyer was almost unchanged by the strength model.

While the similarities in the overall dynamics of the flyer with and without material strength, the

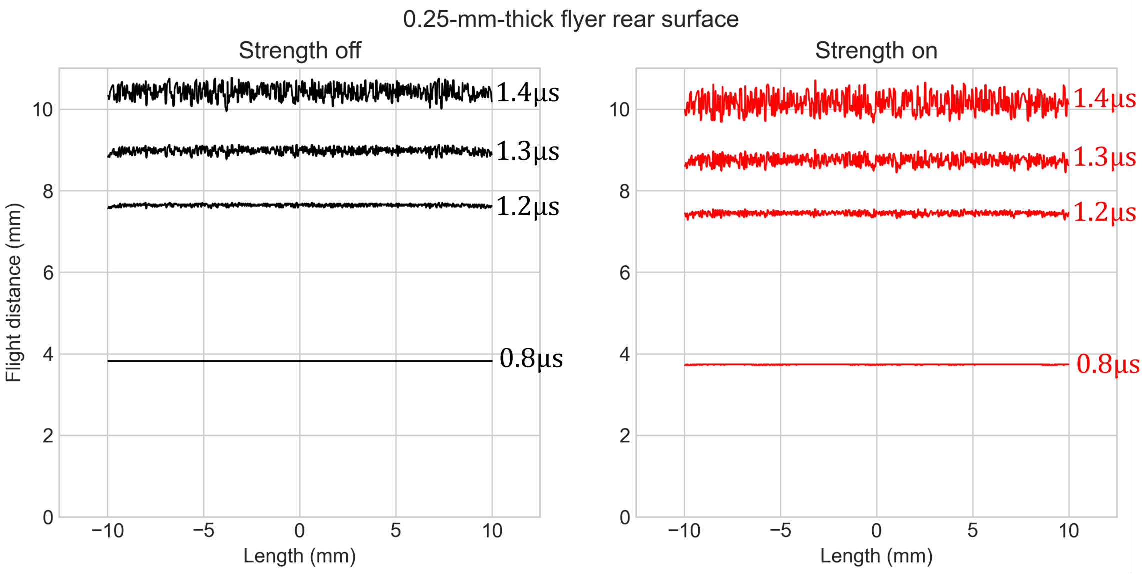

Figure 6.36: Plots showing the evolution of the foil-flyer interface in time as it progresses up the barrel in 2D MHD simulations with material strength on and off. The amplitude of the instabilities is notably larger in simulations with material strength on.

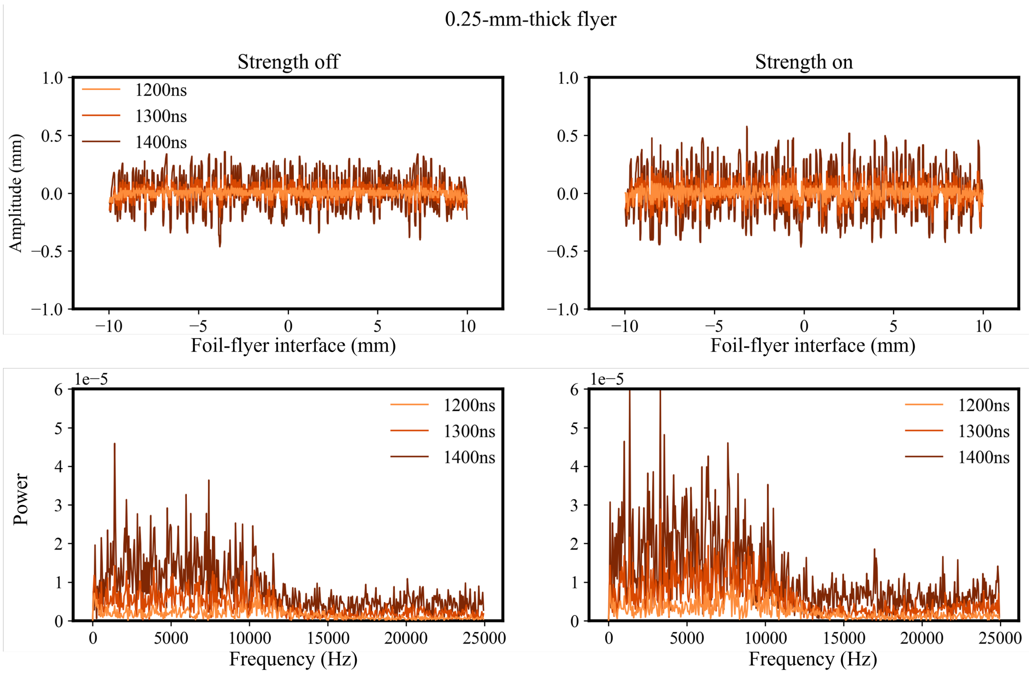

Figure 6.37: A comparison of the formation of RT instabilities at the foil-flyer over time in loads with 0.25-mm-thick flyers, including plots of their FFT signal. The amplitude of the RT perturbations is larger than the flyer thickness. The perturbations have greater range in frequencies and higher amplitude with strength on.

thermodynamic states in the foil and flyer display variation throughout operation. To avoid considering the regions of the foil and flyer trapped beneath the barrel walls at the edges, the foil and flyer states were calculated by taking the maximum and mean of cells across their thickness at the flyer centre.

The pressure, density and temperature in the flyer are dependent on the pressure in the foil, thus, the results are arranged in an order that reflect this. The maximum and mean foil and flyer pressure are plotted in Figure 6.32. While the plots reveal there was limited difference in temporal evolution of the pressure in the foil and flyer in the simulations with and without strength, the maximum pressure in the foil and flyer is slightly lower in simulations with material strength. For the 1.0 and 1.5-mm-thick flyers, the peak pressures in simulations with material strength on is around 10% lower. There were also differences in the maximum and mean density and temperature of the flyer. The plots in Figure 6.33 demonstrate the mean and maximum density in the flyer are lower in simulations with material strength, while the mean and maximum temperature are higher. The disparities in the maximum flyer density and mean flyer temperature rose to around 10% and 20% respectively in simulations with and without material strength effects.

Another key difference between the purely hydrodynamic and solid material simulations were the characteristics of the instabilities formed in the dielectric flyer. Whilst the initial density of the aluminium foil is higher than the polyimide flyer, once vaporised, the foil density decreases rapidly. Figure 6.33a demonstrates the temporal evolution foil density is largely independent of the flyer thickness. Consequently, the low-density vaporised foil accelerates into the higher-density flyer, causing RT instabilities to form at the foil-flyer interface. This process, illustrated in Figure 6.35, was observed in simulations with and without the strength model.

The profile of the instabilities at the foil-flyer interface was extracted from each simulation timestep and recorded. Figure 6.36 depicts the progression of the foil-flyer interface of the 0.25-mm-thick flyer as it moved up the barrel, with strength on and off. At 0.8 µs, disturbances in the profile with strength on are visible, which do not appear until later in the simulation with strength off. This behaviour was also true in simulations of the 0.5, 1.0 and 1.5-mm-thick flyers. In the 0.25-mm-thick flyer, the RT instabilities developed into fingers which almost spanned the thickness of the flyer. Whilst the fingers did not break through the flyer before it impacted the target, if left to accelerate further, it is highly likely the RT plumes would have penetrated across the entire flyer thickness, resulting in plasma breakthrough.

The differences in RT wavelength and amplitude are qualitatively apparent in Figure 6.36. To quantitatively compared these values, a fast fourier transformation (**FFT**) on the profile at the foil-flyer interface was performed. The results displayed in the plots in Figure 6.37 - 6.40 show in general, the amplitude and frequency of the instabilities were greater in simulations with material strength. The amplitude of the perturbations were greatest in the thinnest flyer (0.25mm,

Figure 6.37), both with and without material strength. It is important to note the wavelength of the RT perturbations was highly dependent on the mesh size, suggesting the simulations were not resolved. However, the trend of increased RT growth rates in simulations with material strength on was independent of the mesh resolution.

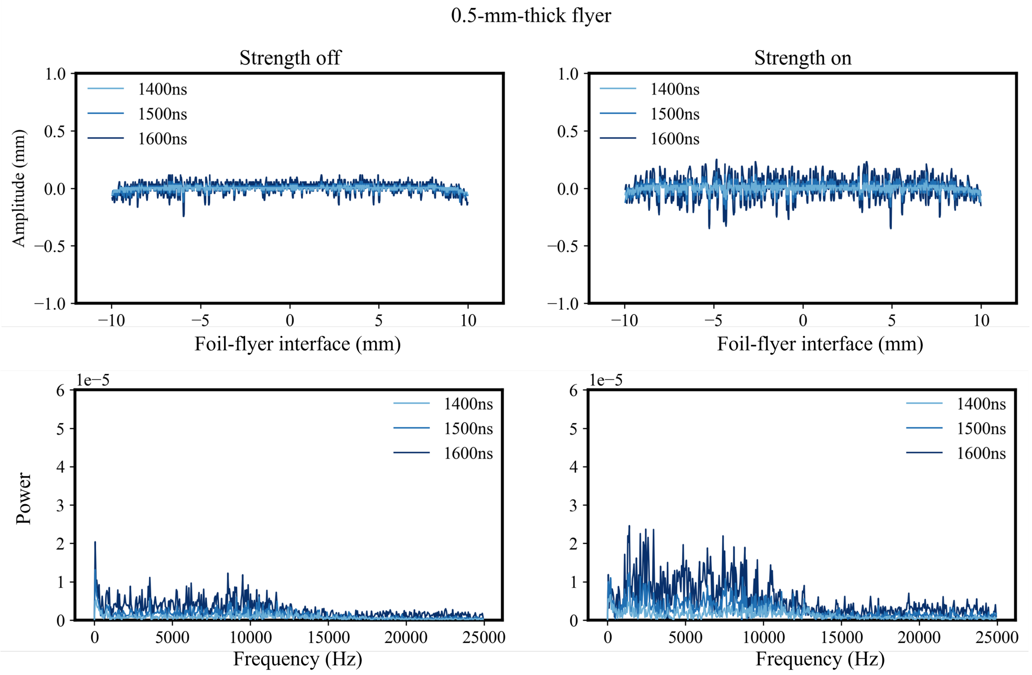

Figure 6.38: A comparison of the formation of RT instabilities at the foil-flyer over time in loads with 0.5-mm-thick flyers, including plots of their FFT signal.

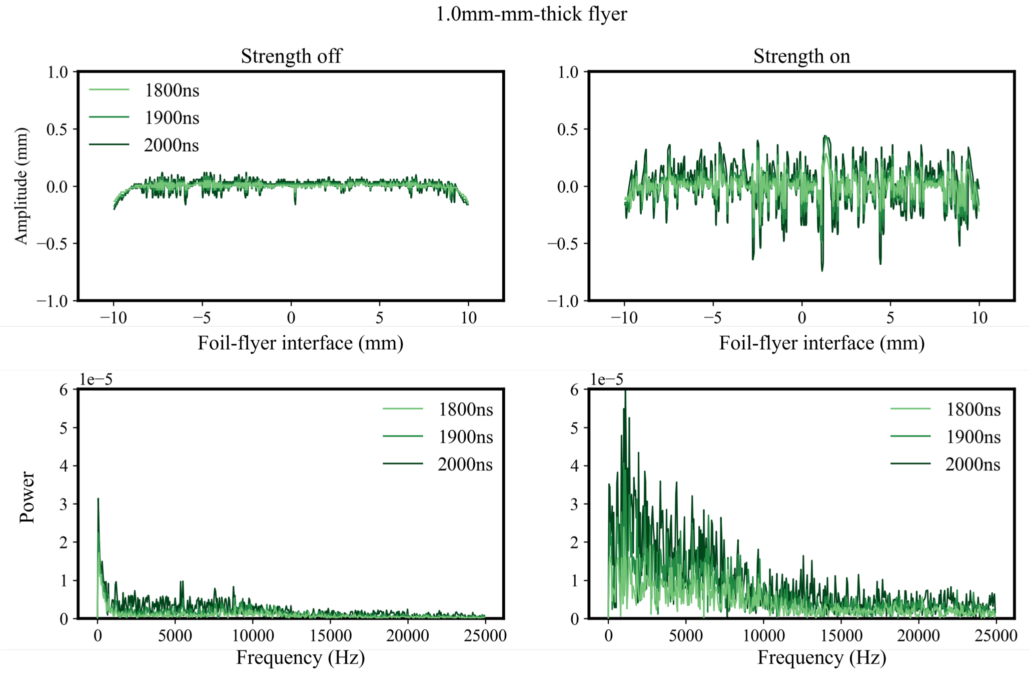

Figure 6.39: A comparison of the formation of RT instabilities at the foil-flyer over time in loads with 1.0-mm-thick flyers, including plots of their FFT signal. The perturbations have greater range in frequencies and higher amplitude with strength on, though the mechanism for this effect is unclear.

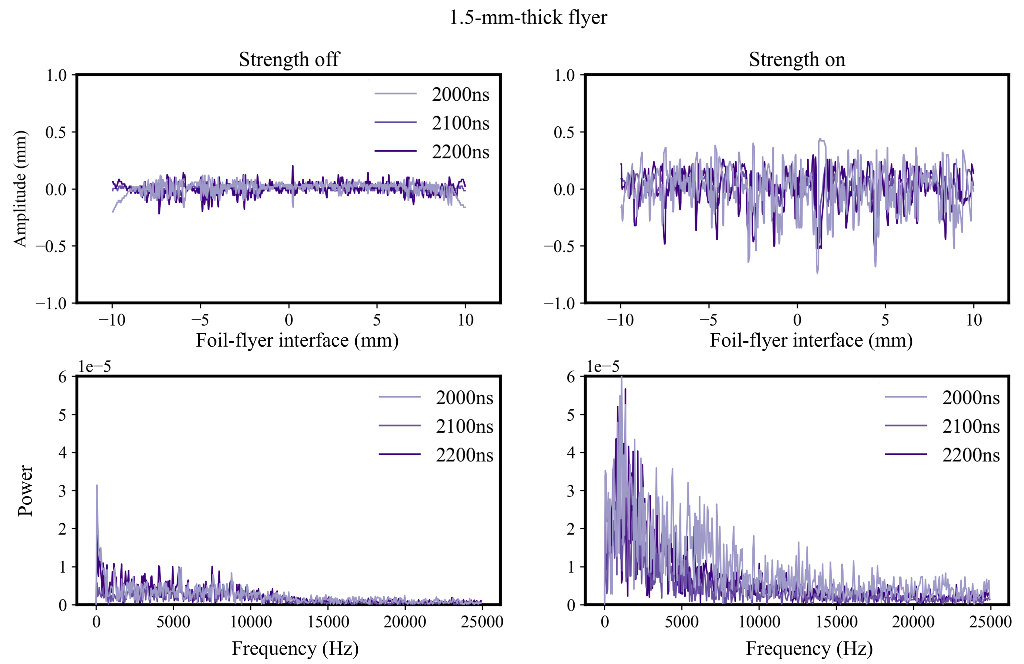

Figure 6.40: A comparison of the formation of RT instabilities at the foil-flyer over time in loads with 1.5-mm-thick flyers, including plots of their FFT signal. The perturbations have greater range in frequencies and higher amplitude with strength on, though the mechanism for this effect is unclear.

6.5.5 Discussion

Review of the results of 2D simulations

At the outset of this section of work, the 0D modelling and experiments performed in Chapter 5 had led to the development of two potential disassembly mechanisms in the electric gun flyer. The first disassembly mechanism discussed in Chapter 5 refers to the loss of integrity in thick flyers at early times due to the increase in pressure, followed by an equally rapid decrease, in-line with the decrease in thermal pressure in the foil as it expanded up the barrel as the flyer launched. This leads the flyer to experience spall at its leading surface which, if sufficiently violent, can cause the flyer to disintegrate.

The 2D simulations performed in B2 support the trends in the flyer state predicted by the 0D model and provide deeper insight into their evolution. The equation of state in the flyer in the 2D MHD simulations permit the direct calculation of the temporal evolution of the flyer density and temperature. The plots in Figure 6.33 demonstrate the maximum and minimum density and temperature states in the flyer experience a significant spike around launch. This rapid increase and decrease is less pronounced in the mean of the states for thin flyers.

The second disassembly mechanism discussed in Chapter 5 refers instead to the loss of integrity in thin flyers at times late in flight . The experiments performed in Chapter 5 revealed thin flyers (0.25 and 0.5-mm-thick over 10 mm and 20 mm flight distance, respectively) experienced plasma breakthrough at late flight times [93, 96]. The flyer density on impact was calculated using the Rankine-Hugoniot jump conditions. It was observed the density of the flyers on impact decreased with flyer thickness, due to the flyer being held at a lower pressure by the foil plasma. It was suggested this decrease in density contributed to the loss of integrity of thin flyers at late times. However, this does not isolate a specific mechanism by which the plasma breakthrough process was initiated.

Within simulations, RT instabilities occur and are numerically seeded by grid imprint whilst in reality these occur as a consequence of surface defects. Scratches or imperfections on the foil become locations of concentrated current density, disturbing the planarity of the foil explosion. Similarly, scratches and indents in the flyer offer points where foil vapor can intermix with the flyer, causing the higher inertia material to fall behind and initiate RT instability growth. Hence, whilst the simulations may not capture the source defects which initiate RT instabilities in the experimental load on M3, their predictions may still provide insight into their growth and behaviour.

The work performed in this chapter advances the understanding of the mechanisms which resulted in the plasma breakthrough observed experimentally on M3. The 2D MHD simulations demonstrate

RT instabilities were formed at the foil-flyer interface, which grow to significant amplitudes by late times. In the case of the 0.25-mm-thick flyer, the simulations plotted in Figure 6.37-6.40 demonstrate the amplitude of the RT fingers was greater than the flyer thickness. Therefore, it could be posited the plasma breakthrough recorded was a consequence of RT instabilities at the foil-flyer interface.

The RT instabilities observed in the B2 simulations and late-time plasma breakthrough in the experimental load permits the revision of the flyer disassembly mechanisms previously reviewed in Chapter 5. It instead suggests that, if disassembly due to spallation can be avoided on launch, RT instabilities cannot be permitted to grow beyond the thickness of the flyer. The growth of these perturbations pose a risk to flyers accelerated over longer stand-off distances. It is posited that to avoid this disassembly mechanism, the growth rate could be reduced by decreasing the Atwood number at the foil-flyer interface. This could potentially be achieved by limiting the minimum density of the foil accelerating the flyer by decreasing the current density.

Material strength effects in the flyer

The effect of material strength on the 2D simulations of the electric gun load designed for M3 is subtle. With regard to the flyer state, the reduced density and increased temperature in the thick flyers is the greatest difference observed in simulations with material strength. The solid flyers are less compressible, thus as the pressure rises, the compressed density is lower and as a result, the temperature state is higher. Figure 6.33a demonstrates a maximum difference of 12.5% and almost 25% in the mean density and temperature of the 1.5-mm-thick flyer over its flight. Despite this not inconsiderable difference to the flyer states, the velocity of the flyer was not significantly influenced by strength effects in the load. This is likely because the kinematics of the system are primarily dependent on the behaviour of the foil, which completely melts hundreds of nanoseconds prior to flyer launch.

The perturbations witnessed in the B2 simulations presented in this chapter are RT instabilities. To review, literature suggests material strength should have a stabilising effect on the growth of RT instabilities and the Atwood number at the foil-flyer interface is lower in simulations with material strength enabled. Despite this, the simulations with a material strength model in the load components displayed increased growth rate, resulting in higher perturbation amplitudes. This raises questions as to the source of the observed instabilities, which are challenging to answer due to issues with the grid resolution. The grid resolution studies performed demonstrated the RT instabilities observed in the electric gun simulations were dependent on the mesh size, as their wavelength reduced with the minimum cell size. However, the requirement to simulate a significant portion of the centimetre-scale load geometry hindered the completion of simulations with convergent RT instability characteristics. Moving foward, simulations with geometric perturbations should be investigated, rather than allowing the numerical artifacts to seed instabilities.

The investigation of the RT instabilities in the electric gun, including their dependence on material strength, constitutes an important avenue of further work. The work presented in this section suggests that RT instabilities could be the mechanism for late time flyer disassembly, making it of high important to capture the growth of the perturbations accurately. This could be approached using a reduced two-dimensional domain, capturing a slice of the electric gun at the centre of the foil and flyer, where its behaviour is closer to one-dimensional. It is important that this reduced domain is driven using the current profile captured from a larger simulation including more load components, so as to simulate the magnetic fields propagated in the reduced domain more accurately. This study could provide insight into the behaviour noted in this study.

Overall, the material strength appeared to be a secondary effect on the outcome of the electric gun load behaviour, when compared to the effect of the current loss. The latter was shown to significantly influence the velocity profile of the flyer, and thereby also the thermodynamic states in the foil and flyer. However, material strength affected both the flyer density and temperature state and instabilities at the foil-flyer interface. M3 is a relatively high-energy pulsed-power device and its long rise-time ensures the flyer is continuously driven to high pressures, resulting in the melting of much of the flyer. It is plausible that on lower energy pulsed-power devices, or those with shorter rise-times, material strength may have a more significant influence on the behaviour of an electric gun load.

Physical effects in the electric gun not accounted for in B2

The disparity between the predicted and experimentally measured flyer velocity profiles presented in this section strongly suggests that a significant portion of the energy contributing to the flyer's acceleration in the simulations is being lost in the experimental load. However, during this work, it was not possible to directly measure the voltage or current across the electric gun foil. Consequently, it remains unclear whether this energy is lost due to alternative current paths, poor momentum transfer to the flyer caused by compression of the insulating layers during acceleration, or some other effect that has yet to be considered. While the form of the electric gun launcher discussed thus far lacks a substantial body of research to draw upon, notable inefficiencies observed in similar systems, such as railguns, which cannot be captured in B2 simulations, are addressed in this section.

One significant phenomenon likely impacting the electric gun load used in this work is the effect of restrike across the electric gun fuse. Restrike occurs when an electrical discharge is initiated across a gap, typically in high-voltage systems where the electric field strength across the gap is sufficient to overcome the dielectric breakdown of the intervening medium, such as air, gas, or vacuum [131, 132]. The electric gun load discussed here is susceptible to restrike, as the conductivity of the aluminum plasma decreases under electric fields exceeding 10 kV/cm [133]. When restrike occurs, the current may preferentially arc across the gap instead of contributing energy to the system by passing through the foil plasma. While this effect can significantly impact the efficiency of the electric gun load, it cannot be accounted for in B2 simulations due to the stochastic nature of the breakdown process. Investigating the impact of this effect on the electric gun load in M3 would benefit from the installation of B-dot probes in the cathode to record the current profile across the foil.

Another significant physical process, briefly mentioned in Section 6.5.2, is the phase change of the Kapton material used in both the flyer and the insulation. Kapton becomes conductive upon melting and can subsequently draw current. This behavior is particularly significant for the Kapton insulation beneath the foil, which undergoes phase changes under shock loading during the foil's explosion. This process cannot be captured in B2 simulations due to the limited availability of open literature on the electrical conductivity of Kapton under the extreme pressures generated during shock loading. While it could be hypothesized that energy is lost through current diversion into the insulation, the comparison of experimentally measured and numerically predicted flyer velocities suggests this mechanism is less likely. Figure 6.29 shows that the experimental flyer velocity is lower than the simulated velocity from the moment acceleration of the leading surface begins. The 2.0 mm insulation is thicker than the flyers in both shots, meaning the shock must reach the leading surface of the flyer some time before it could potentially traverse the entire thickness of the insulation. If the efficiency of the electric gun launch were significantly impacted by phase transitions in the insulation, one would expect the velocity profiles to diverge after the shock has fully traversed the insulation. However, this possibility could be clarified through direct measurements of the current profile across the foil during discharge.

6.5.6 Conclusions

In this work, the two-dimensional simulations of the electric gun load tested on M3 in Chapter 5 were performed in MHD B2, incorporating the material strength model derived in Section 6.4. Initially, the approximations necessary to model the load behaviour and the motivations behind the domain set-up were discussed. This review underscored the challenges associated with accurately modelling the current path through the load, including the omission of mechanisms for power loss, such as breakdown and arcing. Ultimately, a simplified current loss factor was applied to uniformly reduce the current throughout the simulation. This method was applied to high-fidelity two-dimensional simulations of the electric gun load, with flyer thicknesses ranging from 0.25 - 1.5 mm thickness. The results demonstrated that material strength had some affect on the density and temperature states in the flyer and appeared to influence the formation and growth of RT instabilities at the foil-flyer interface. However, overall the effect of material strength was secondary to the significance of accurately modelling the current loss mechanisms in the load.

With regards to the questions posed at the beginning of this section (Section 6.5.1):

1. The simulations performed in this investigation revealed further evidence for the flyer disassembly mechanisms presented in Chapter 5. Firstly, the results confirmed the expected rapid increase and decrease in flyer density on launch, due to spallation when the thermal pressure drops in the foil as it expands. Secondly, the simulations appear to suggest the disassembly witnessed in thin flyers late in flight during experimental testing was a result of RT instabilities at the foil-flyer interface. The ultimate objective of the final Research Goal (discussed in the next chapter) is to use the electric gun to deliver a continuous pressure pulse. Consequently, these observations offer crucial insight into the mechanisms which must be controlled to accelerate a flyer which could achieve this goal.

2. The electric gun is highly sensitive to current loss mechanisms, which are challenging to implement realistically in B2. This was indicated by the significant difference between the experimentally measured VISAR and impact times and the velocity profiles predicted by the 2D simulations: the simulated flyer velocity was over twice that which was measured experimentally. A current loss factor of 0.45 was required to tune the current amplitude such that the flyer velocity profile better matched the simulations.

   The inclusion of material strength provided only a secondary effect on the behaviour of the load. Whilst it did not cause significant variation in the flyer velocity profile, it increased the flyer temperature and decreased the flyer density by around 10% and 20% respectively. Further, material strength appeared to increase the growth rate of RT instabilities at the foil-flyer interface. However, a mechanism for this effect could not be determined due to restrictions encountered in the minimum grid resolution.

Both the current loss mechanism and the formation of the RT instabilities constitute important topics of future work with regard to the continued development of the electric gun projectile acceleration technique.

6.6 Summary

In this chapter, a material strength model was integrated into B2 and benchmarked using a cross-code comparison with the commerical code, Ansys AUTODYN. This material strength model was then utilised in 2D simulations of the electric gun in B2. To simulate the complex load geometry in an MHD hydrocode domain, a number of approximations were made. The most significant of these approximations was the modelling of the current loss mechanisms in the load. The current loss factor, a fixed scaled reduction of the current in each timestep, was applied, attempting to mimic current lost in the foil due to alternative parasitic current paths in the load.

On determining the current loss factor, tuned to experimentally measured velocity profiles and impact times, the electric gun load designs shot in Chapter 5 were simulated in B2 with material strength. The dynamics, state and deformation of the foil and flyer were analysed, validating the trends in pressure and density suggested by the 0D model in Section 5.3. Additionally, the simulations revealed the initiation and growth of RT instabilities at the foil-flyer interface.

Whilst the RT instabilities in the simulations appeared to be seeded by grid imprint, it was proposed their growth rate could mimic the development of real-world RT instabilities. It was observed in the simulations that the RT ‘fingers’ attained an amplitude greater than the thickness of the 0.25-mm-thick flyer prior to impact. Therefore, it was posited the plasma breakthrough observed late in flight during the acceleration of the 0.25-mm-thick flyer on M3 could be due to RT instabilities at the foil-flyer interface. These instabilities could pose a significant threat to flyers accelerated over a long stand-off distance.

Overall, it appears in the region of the electric gun load design space explored on M3 that material strength is a secondary consideration. The results in this chapter instead suggest capturing the current loss in the load is of far greater consequence to the dynamics and states in the foil and flyer. Scenarios where material strength may be of importance include electric gun loads which utilise high melting temperature and impedance dielectric flyers. It is feasible on a different pulsed-power machine, material strength may play a more significant role.

The objectives defined in Research Goal 3 which were addressed in this chapter include:

1. **The strength model implemented in B2 must replicate the results of a 2D test case dominated by strength effects performed in a commercial code.**

   The strength model in B2, presented in Section 6.4, was compared to two-dimensional simulations of the Taylor rod-on-anvil test performed in Ansys AUTODYN. The strength model in B2 had novel improvements to the algorithm that significantly improved the accuracy of the results, such as a density scaling factor applied to the Johnson-Cook yield value. The results of simulations at three different rod velocities were analysed. Overall, the deformation of the Taylor rods simulated in B2 matched AUTODYN closely, with low error in the flared-end radius and length of the rod. The simulations in B2 matched AUTODYN best at the higher velocities tested (200 and 350 m/s).

2. **The strength model must be able to be utilised in electric gun simulations.**

   Customarily, slip conditions between separate parts has been achieved in Eulerian hydrocodes through manual definition of cell at boundaries where the stress tensor is set to zero [109]. This solution is impractical for the electric gun load in the simulation domain; the electric gun load is a complex geometry with many parts. In this work, a computationally cheap and automatic interface was implemented. This solution, alongside the density scaling factor which improved the accuracy of material deformation at material-vacuum interfaces, ensured 2D simulations of the electric gun with material strength effects were successfully completed.

3. **The effect of material strength on the behaviour of an electric gun load must be analysed.**

   The effect of material strength on the electric gun loads tested on M3 in Chapter 5 was explored. Whilst a range of flyer thicknesses were tested, each load utilised a thin foil of fixed width (25 mm). Consequently, the foil pressure states in each shot were of a similarly extreme magnitude, which resulted in the behaviour of the loads in the simulations being unaffected by material strength.

4. **Simulations with material strength in B2 must be used, alongside experimental results, to propose a specific mechanism by which electric gun flyers are destroyed and determine whether this can be mitigated.**

   Whilst material strength was determined not to have had a significant impact on the results of the investigation in B2, the simulations revealed the formation and development of significant RT instabilities at the foil-flyer interface. These observations suggest if the flyer survives launch, the second mechanism by which it might disassemble is due to RT instabilities at the foil-flyer interface penetrating through to the flyer surface. This would instigate plasma breakthrough late in flight, which was indeed observed during shots on M3. This secondary disassembly mechanism is of greater risk in electric gun loads with thin flyers, launched over extended stand-off distances.

It was proposed at the end of Section 6.5.5, the growth of RT instabilities at the foil-flyer interface could be inhibited by maintaining a lower Atwood number at the foil-flyer interface. This could be achieved by limiting the minimum density of the foil during acceleration. This topic is addressed in greater detail in the next chapter.

Chapter 7

Design and testing of an electric gun for equation of state research

This chapter details the development and experimental validation of an electric gun for extreme state research. The advancement of projectile launch techniques in material science research is characterised by a perpetual tension between achieving high flyer velocities and preserving flyer integrity. This challenge is particularly marked when investigating extreme material states, where maintaining flyer integrity and a region of constant density are paramount. Failure to do limits the duration over which the target pressure state is constant, in turn compromising the accuracy of the state measurement. Additionally, change to the temperature or density of the flyer invalidates the straightforward use of jump conditions, making the determination of the state much more challenging. When this is the case, the particle velocity must instead be measured in the target to make an equation of state measurement, necessitating an even longer quasi-equilibrated shock duration.

Different acceleration methods impose varying limitations on maximum achievable velocities, further complicating the endeavor. For instance, while two-stage gas guns and rail guns have their respective velocity thresholds due to flyer destruction and rail melting, laser-driven flyer acceleration enables higher velocities but constrains flyer thickness. Pulsed-power-driven electromagnetic flyer launch techniques offer promising velocity ranges but necessitate careful current pulse shaping to maintain constant density and velocity in the flyer. Despite its potential for probing extreme material states due to its high efficiency, the electric gun has predominantly been utilised for studying hypervelocity impact on ballistic shielding, due to challenges in launching flyers with constant density over sufficient thickness. This chapter seeks to overcome this challenge by leveraging modelling insights to develop an electric gun load tailored for dynamic material property studies. Simplified modeling, experimental validation, and advanced hydrocode simulations are utilised to investigate a novel electric gun load design as a tool for extreme state research.

7.1 Introduction

The experimental results presented in Chapter 5 demonstrated the novel capability of the electric gun load designed within this DPhil project to accelerate flyers up to 2 mm thick to velocities exceeding 10 km/s. This represented an improvement on existing iterations of the electric gun, which were reported in literature to be restricted to accelerating flyers below 1 mm at most. This was achieved by designing an electric gun load which avoided the density in the flyer dropping too low, whereupon the foil plasma can break through it. Initial testing in the 0D model and experimentally observed plasma breakthrough suggest this reduction in density across the thickness of the foil occurs by two primary mechanisms (discussed in greater detail in Section 5.3):

1. The density in the flyer can fall if the pressure at the foil-flyer interface rises to an extreme magnitude then falls in quick succession, resulting in a spalling effect at the front surface of the flyer. This effect occurs most significantly during the launch process. After current start, the flyer cannot move off until pressure information from the exploding foil is communicated to its front. During this time, the foil, trapped beneath the flyer, experiences a rapid increase in thermal pressure. This drives strong pressure waves from the foil-flyer interface to the flyer front. When the flyer moves off, providing free space for the foil to expand into, the thermal pressure in the foil rapidly decreases, thus the pressure at the foil-flyer interface drops. If the strong reflected tensile waves propagated prior to launch meet a region of lower pressure at the foil-flyer interface, the material in the region releases and the density drops. When the flyer is thicker, it takes longer to launch, therefore the thermal pressure in the foil builds to a greater magnitude, causing a more substantial density drop when the thermal component falls off after launch.

2. The density in the flyer can fall if the pressure driving the flyer at the foil-flyer interface drops too low prior to impact. This typically occurs after the current peak, as the magnetic pressure in the foil driving the flyer is proportional to the square of the current density. When the time to launch is significant compared to the rise-time of the pulsed-power device driving the load, the

pressure in the flyer can fall to near zero early in flight, causing the density in the flyer to drop if it has a high temperature.

These mechanisms were suggested following the investigation of pressure states in the flyer using the 0D model detailed in Chapter 4. This model was created with the goal of reducing the computational resources necessary to simulate the electric gun, thus employs intentionally simplified physics and a reduced representation of the physical domain. Subsequent work in Chapter 5 demonstrated the model was a suitable electric gun design tool in a new operating regime. However, its approximation of the system as a zero-dimensional problem becomes less accurate at the late stages of flight. Initially, the foil is trapped beneath the flyer, which tamps its expansion. But, as the flyer moves up the barrel, regions of the foil plasma continue to remain compressed against the rear surface of the flyer as it is accelerated, meanwhile, the foil's considerable thermal pressure causes the trailing plasma to expand back down the barrel. At this point, the assumption made in the model that a single position of maximum pressure exists in the foil, decreasing linearly to zero at the flyer front, breaks down. Consequently, the model's predicted maximum pressure becomes less accurate at late stages in flight. Further, the model cannot accurately predict the flyer's temperature or density; thus, it cannot be used to verify the theorised disassembly mechanisms presented above.

The veracity of the disassembly mechanisms developed in Chapter 5 were investigated using the Eulerian MHD code B2 in the previous chapter. In that chapter, the incorporation of a strength model into B2 is explored. This strength model was subsequently used to contrast the behaviour of two-dimensional simulations of the electric gun load designed for M3, with and without strength effects. Two-dimensional simulation of the electric gun load was challenging; while the electrodes span centimetres, the exploding foil thickness is 0.1 mm, creating an uncomfortable resolution trade-off. Further, the hydrocode does not account for loss of current by mechanisms such as breakdown across the insulation or parasitic current pathways. As a result, the hydrocode overestimates the current delivered to the exploding foil and hence also the velocity of the flyer. Despite these challenges using a correction factor, the simulations were deemed accurate enough to still provide some insight into the behaviour of the flyer at different stages of launch.

Firstly, the simulations in B2 captured the spallation process at the leading surface of the flyer. This spallation had been posited due to extreme jumps in the experimentally recorded flyer velocity profile. None of the flyers simulated experienced plasma breakthrough on launch, which matches the experimental behaviour of the loads on M3. Secondly, the reduction in density was observed in the flyer after the peak current. Some simulations demonstrated flyer disassembly late in time due to the formation of Rayleigh-Taylor instabilities which grew to in amplitude to span the thickness of the flyer. While the instabilities observed were dependent on the mesh-size, thus were likely seeded by grid imprints, their growth indicated the vulnerability of the flyer to Rayleigh-Taylor instabilities. Physical imperfections on the surface of the foil and flyer create regions of interpenetration at the foil-flyer interface, initiating instabilities that, if they have a similar growth rate to those simulated, could be the origin of the experimentally observed late time plasma breakthrough.

In this chapter, the understanding of the mechanisms by which electric gun flyers experience violent thermodynamic state change and disassembly is employed to design a load which maintains a near constant flyer density throughout flight. It was hypothesised this, alongside impact at a constant velocity, would allow the electric gun load to introduce a quasi-equilibrated pressure state in a target. Such an electric gun load could be an advantageous tool for equation of state measurements, particularly if it could be operated on fixed rise-time pulsed-power devices. Despite having successfully launched a 2-mm-thick flyer, for the first time in the history of the launch technique, this chapter focuses instead on the development of the electric gun as a tool for dynamic material testing. As noted during the literature review, researchers previously found the electric gun was unable to make Hugoniot measurements with suitable precision, due to the erratic shock wave profile introduced to the targets on impact [3, 4]. Hatt *et al.* specifically state this is thought to be due to an inconsistent density profile across the thickness of their flyer due its violent acceleration. Consequently, the following section serves a proof on concept, focusing on maintaining constant density through the flyer, as opposed to optimising the flyer thickness or the load's efficiency.

This chapter contains the following journal style article:

- **The design, modeling and testing of an electric gun load for the study of dynamic materials properties**

  This article is in review at the International Journal of Impact Engineering.

  The contributions of M. Fitzgerald include: analysis using the 0D model, design of the electric gun load i.e. component material and dimensions, fabrication and assembly of the load, design of the diagnostic set-up, contributions to alignment of the diagnostics, processing of the experimental data, and writing and editing of the original draft. They do not include: design of the overall electrode (design discussed in [68]), installation of the load in M3, operation of M3, conceptualisation of the shock in block method, the creation of the diagnostic testbed i.e. VISAR set-up, or the creation of the Gaussian processing scripts.

7.2 The design, modeling and testing of an electric gun load for the study of dynamic materials properties

7.2.1 Abstract

This work presents the design and testing of an electric gun load intended for characterising the properties of materials under extreme conditions. Projectile launch techniques, such as gas guns and electromagnetic (**EM**) flyer plates, are capable of creating planar, high-pressure shocks across substantial material volumes, resulting in precise equation of state measurements. However, achieving these conditions necessitates specific flyer characteristics: the flyer must maintain near-constant density and velocity across a minimum thickness, in the direction of travel, until reaching the target. This has been achieved in EM flyer plates through sophisticated current pulse shaping [1]. This work involved the adaptation of an existing electric gun design to meet these criteria while utilising a relatively simple, fixed rise-time, pulsed-power driver instead. The proposed load achieves this by accelerating a 0.5-mm-thick insulating flyer whilst minimising state change (thus maintaining near-constant density) and eliminating the forces driving the flyer prior to impact by launching it across a stand-off distance (ensuring constant velocity). A combination of our 0D model [93] and a 2D in-house hydrocode were used to determine the optimal thicknesses for its constituent parts: the driving metal foil and plastic flyer. Experimental testing was conducted using a 140 kV electric gun load to validate the model's predictions and examine the correlation between the shock pulse shape at impact and the stand-off distance from the launch site. The results reveal the optimised load successfully generated a shock pulse in a PMMA target block with a magnitude of 20 GPa for a duration of 1.0 µs, over region with 10 mm width, and at a 100 mm stand-off from the launch site. This large stand-off distance ensured the flyer reaches a steady, terminal ballistic velocity, before impacting the target and also shielded the diagnostic line of sight from plasma generated on launch, allowing for precise measurements to be made. These outcomes suggest the electric gun technique can now be used to explore dynamic properties of materials using relatively simple pulsed-power devices with a fixed current rise-time.

7.2.2 Introduction

The study of high-energy density materials requires tools capable of generating extreme states in a laboratory setting. Shock waves are commonly used to achieve the highest states possible under controlled conditions, offering precise measurements of material properties, such as its equation of state (**EoS**). This precision is due to their compatibility with high-resolution velocimetry diagnostic techniques, as the Rankine-Hugoniot relation allows for the derivation of the material state through measuring the shock and particle velocity in the target. The accuracy of these measurements improves with the duration and volume over which the shock wave acts. Consequently, the most accurate measurements are made using techniques which can generate an extended, constant pressure pulse. Projectile launchers, such as gas guns, laser-driven flyers and electromagnetic (**EM**) flyer plates, are particularly effective at producing uniform, quasi-equilibrated states. These devices accelerate a flyer into a target material, creating a shock upon impact with a pulse length proportional to the flyer thickness. Gas guns and electromagnetic flyer plates are noted for their ability to generate high accuracy EoS measurements, as both techniques are able to accelerate relatively thick flyers to terminal ballistic speeds before the target is reached [9].

The gas gun is a popular projectile launch technique, owing to its ability to accelerate thick, solid flyers, which generate a long-duration stable pressure pulse in targets on impact. However, gas guns are limited to a maximum velocity of ~8 km/s, due to sound speed limitations in the working gas [134]. In contrast, EM flyer plates can propel flyers to velocities over 70 km/s [20], but can encounter challenges in generating a continuous pressure pulse. The direct passage of current through the metal flyer in EM plate flyer loads makes it susceptible to Joule heating and the propagation of non-isentropic pressure waves induced by rapid electromagnetic acceleration [1]. Moreover, the flyer can continue to accelerate after impact if the magnitude of the current is non-negligible. These challenges have been successfully overcome through utilising current pulse shaping to control the temperature state and velocity profile of the flyer plate [16, 18, 20].

While EM flyer plates currently offer access to the highest pressures using projectile launch [39, 43, 135], the technique faces drawbacks which currently relegate their use to large research institutions. Control over the input current pulse shape necessitates sophisticated pulse forming lines in the pulsed-power driver [76]. Pulsed-power devices with these capabilities are uncommon due to their complexity and intense resource requirements. Additionally, the maximum velocity is constrained by both the overall conversion efficiency of stored electrical energy to kinetic energy in the flyer and the

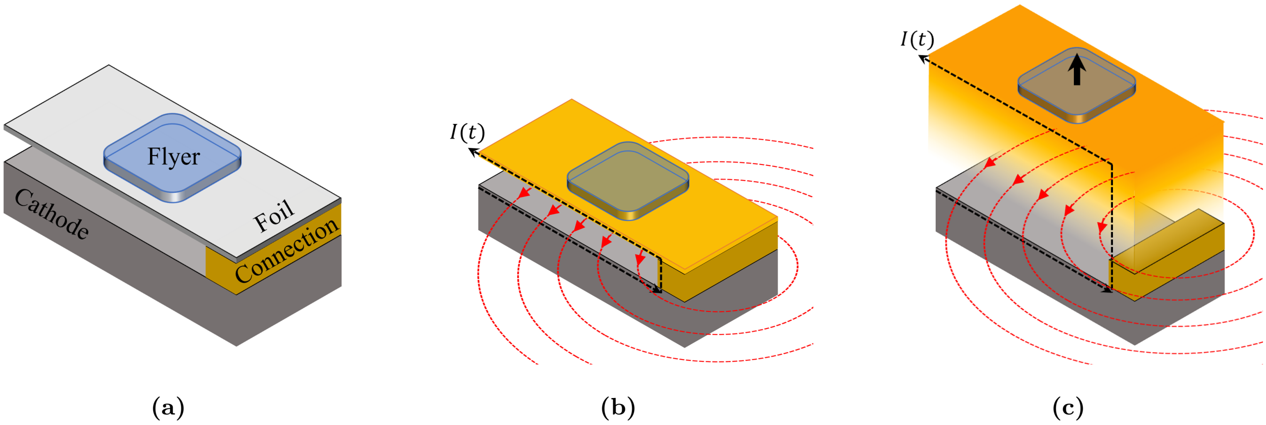

Figure 7.1: Diagrams illustrating the electric gun acceleration mechanism: the initial configuration of the foil, flyer, cathode and connection (7.1a); the foil experiences Joule heating, rapidly changing state from solid to plasma, accelerating the dielectric flyer (7.1b); continued discharge of the current causes further acceleration of the foil by Lorentz forces (7.1c).

necessity to avoid melting in the flyer [1]. Consequently, without pulse-shaping, existing pulsed-power platforms struggle to make high precision EoS measurements.

The electric gun is an alternative electromagnetic projectile launch technique that could overcome the limitations encountered by EM flyer plates. The electric gun was developed at Lawrence Livermore National Laboratory (**LLNL**) [2] and operated in a few locations until the 1990s [4]. The electric gun's operating mechanism is as follows: the current discharged by a pulsed-power device passes through a thin metal foil, rapidly heating it and causing it to transition to a plasma state through Joule heating. This plasma exerts thermal pressure on an adjacent dielectric flyer. If the current rise-time exceeds the flyer launch time (time when leading surface first moves), the foil experiences significant Lorentz force [57, 94]. In the current path configuration depicted in Figure 7.1, the magnetic force aligns with the dielectric flyer's flight direction, resulting in its acceleration by both thermal and magnetic pressures within the foil plasma. Consequently, the electric gun demonstrates enhanced efficiency compared to EM flyer plates. As the current pathway in the electric gun load move through the foil plasma rather than the dielectric flyer, the flyer is not vulnerable to state change through Joule heating. Thus, the electric gun has successfully launched flyers over centimetres stand-off distance [15].

Despite the advantages of its operating mechanism, the electric gun has faced challenges that have hindered its utilisation as a tool for investigating material responses under extreme loading conditions. The technique was found to impart damage, and in some cases complete disassembly, to thick flyers ($\geq$ 0.5 mm) during their acceleration to hypervelocity [5]. Unable to accelerate a flyer of sufficient thickness, EoS measurements made using the electric gun with fixed rise-time pulsed-power drivers had considerable error [3, 4]. The mechanism for the disassembly in thick flyers was unclear, as the thermodynamic states in the flyer during operation were not well understood, due to difficulties modelling the system [57]. These limitations prevented the electric gun from launching flyers with constant density over sufficient thickness, restricting its application to ballistic shielding tests, where its long stand-off distances, high velocity, and lack of sabot proved advantageous [14, 15].

Recent work undertaken by Fitzgerald *et al.* has begun to address these issues. The mechanisms governing the extreme state changes experienced by thick flyers during operation were found to be linked to the current rise-time of the pulsed-power device employed to drive the load [96]. A comprehensive investigation leveraging numerical modelling and experimental testing on Machine 3 (**M3**), a 200 kV, 2.0 µs pulsed-power device, revealed that the dielectric flyers experienced plasma breakthrough if their density fell below a critical threshold. This reduction in density manifested primarily in two scenarios: (1) shortly after launch due to spallation; (2) when the pressure within the flyer decreased late in flight. The former scenario was effectively managed by adjusting the width of the foil to ensure that the pressure evolution in the thick flyers within the M3 electric gun load mirrored that of thin flyers on a lower energy machine [110]. The latter scenario, thought to be potentially driven by Rayleigh-Taylor instabilities at the foil-flyer interface, resulted in the disassembly of thin flyers late in flight.

The load design developed by Fitzgerald *et al.* was found to successfully accelerate flyers up to 2.0-mm-thick over a stand-off distance of 10 mm. However, the flyers did not exhibit ballistic (constant velocity) behaviour at impact. The continued acceleration into the block post-impact is thought to be a result of the magnetic fields propagated by return current path in the foil plasma behind the flyer. Additionally, the shock pulse introduced to the target block exhibited a rapid drop-off in shock speed, suggesting that a varying density profile existed across the thickness of the flyer. If these limitations could be addressed, the electric gun could offer a technique for investigating EoS measurements on relatively simple, fixed rise-time, pulsed-power devices.

The aim of the present work was to develop an electric gun load suitable for conducting extreme state measurements on a high-energy capacitor discharge unit. To accomplish this objective, the load previously designed in [96] was modified to accelerate a dielectric flyer with a region of continuous density and velocity. This was achieved using insights from modelling in our 0D model [93] and an in-house Eulerian MHD hydrocode, **B2**. Experimental testing of the load was then performed to ascertain the stand-off distance required between the target and the launch position to ensure the flyer was no longer accelerating due to the influence of magnetic fields generated by the return current path. Through this investigation, the following questions were addressed:

- How can an electric gun load be adapted to minimise variation in the flyer state during acceleration?
- What changes to the load are required to achieve ballistic flight conditions in the flyer without the ability to shape the current profile?
- What is the capability of the electric gun as a tool for extreme state research and how can it be improved upon?

7.2.3 Background

When a flyer impacts a target, it generates a pressure wave profile that is dependent upon the conditions within the flyer. To accurately measure the material state under these conditions, the induced pressure pulse must remain relatively constant during the measurement window. This necessitates that the flyer possesses a region of uniform density and velocity across a minimum thickness. To achieve a region of uniform density, the state change in the flyer should be minimised. The predominant heating mechanism in the flyer in an electric gun stems from shock waves transferred by the foil below [93]. Consequently, numerical modelling was used to design an electric gun load which minimised the state change in the flyer throughout flight.

Previous investigations conducted using our 0D model suggested the pressure driven at the foil-flyer interface can be estimated at early times using the magnitude and position of the maximum pressure in the foil relative to the foil-flyer interface and flyer front [93]. However, the model becomes less accurate when the flyer moves up the barrel, as the foil expands into complex states which cannot be accurately represented by a 0D system. Instead, capturing the complex behavior of the foil plasma requires multi-dimensional magneto-hydrodynamic (**MHD**) simulations. The sequential stages of flyer launch and flight in the electric gun and the pressure state predictions of the 0D model and 1D hydrocode simulations are compared in Figure 7.2. These plots reveal the 0D model captures the rapid pressure increase on launch, but cannot replicate the swift drop in pressure at late times predicted by the MHD simulation. Consequently, a mixed approach was employed to design an electric gun load which could accelerate a flyer with a region of near-constant density (allowing for elastic compression effects). Initially, the 0D model was used to refine the parameter space, followed by 2D MHD simulations to investigate the thermodynamic states in the flyers with greater precision.

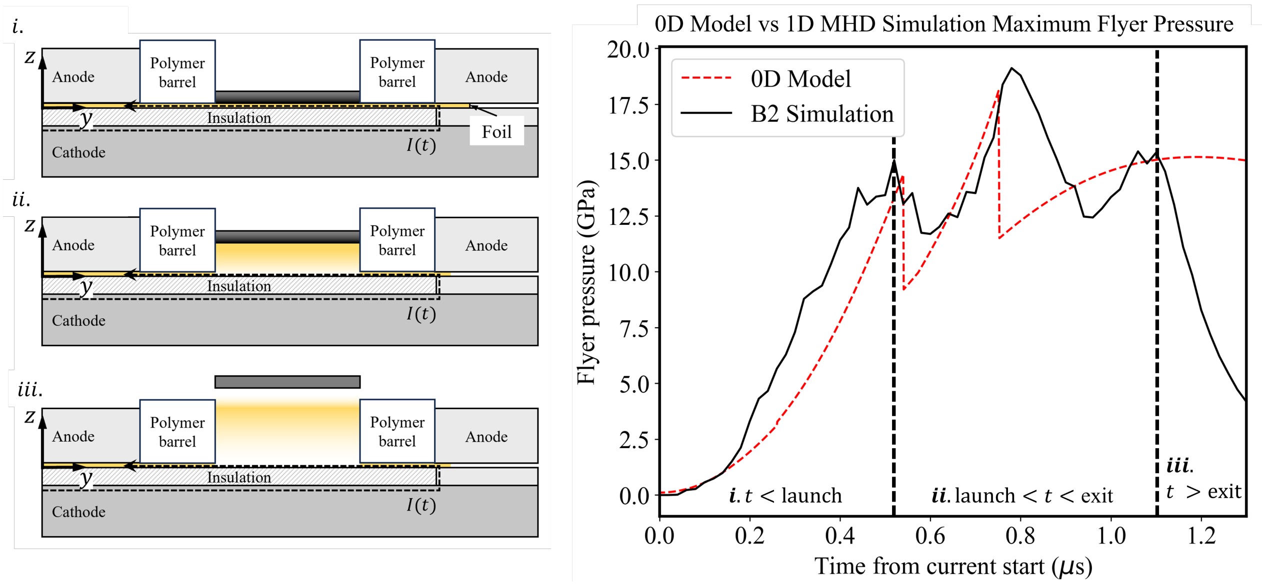

Figure 7.2: Diagrams of the flyer at three characteristic times during acceleration in an electric gun launch, alongside a typical trace of the maximum pressure in the flyer during this period. (*i*) When the current is first discharged, the foil rapidly heats and changes state from solid to a vapor, causing the pressure in the flyer to spike. (*ii*) When the flyer launches and moves up the barrel, the foil becomes free to expand and its pressure initially drops, before increasing again as the discharged current continues to increase. (*iii*) The flyer exits the barrel and the acceleration of the foil plasma abates as it expands into the free space above the barrel, resulting in a rapid drop in the pressure in the flyer.

In this work, the load is designed to generate a supported shock in the target whilst being driven by the relatively simple, fixed rise-time pulsed-power device, M3. M3 is a capacitor-discharge pulsed-power generator designed for the investigation of EM launch [68, 110] and is similar to the pulsed-power devices typically used to drive electric gun loads [15, 57]. When charged to 200 kV, M3 stores a total energy of 2.5 MJ and delivers currents in excess of 14 MA with rise-times of around 2 μs [68]. Further details of the machine, including the RLC circuit variables, are outlined in Table 7.1. It is challenging to meaningfully influence the rise-time of capacitor-discharge generators, because the fixed machine resistance and inductance are considerably greater than the dynamic load values.

Previous iterations of the electric gun load were capable of accelerating flyers up to 2.0-mm-thick using M3, however, the flyers were not thought to have constant velocity or density upon impact with the target [96]. As illustrated in Figure 7.3, the target was positioned at the top of the barrel, in close proximity to the strong magnetic fields propagated by the current return path. Consequently, upon flyer impact with the target block, the foil plasma continued to be driven by strong Lorentz forces, resulting in a varying shock speed.

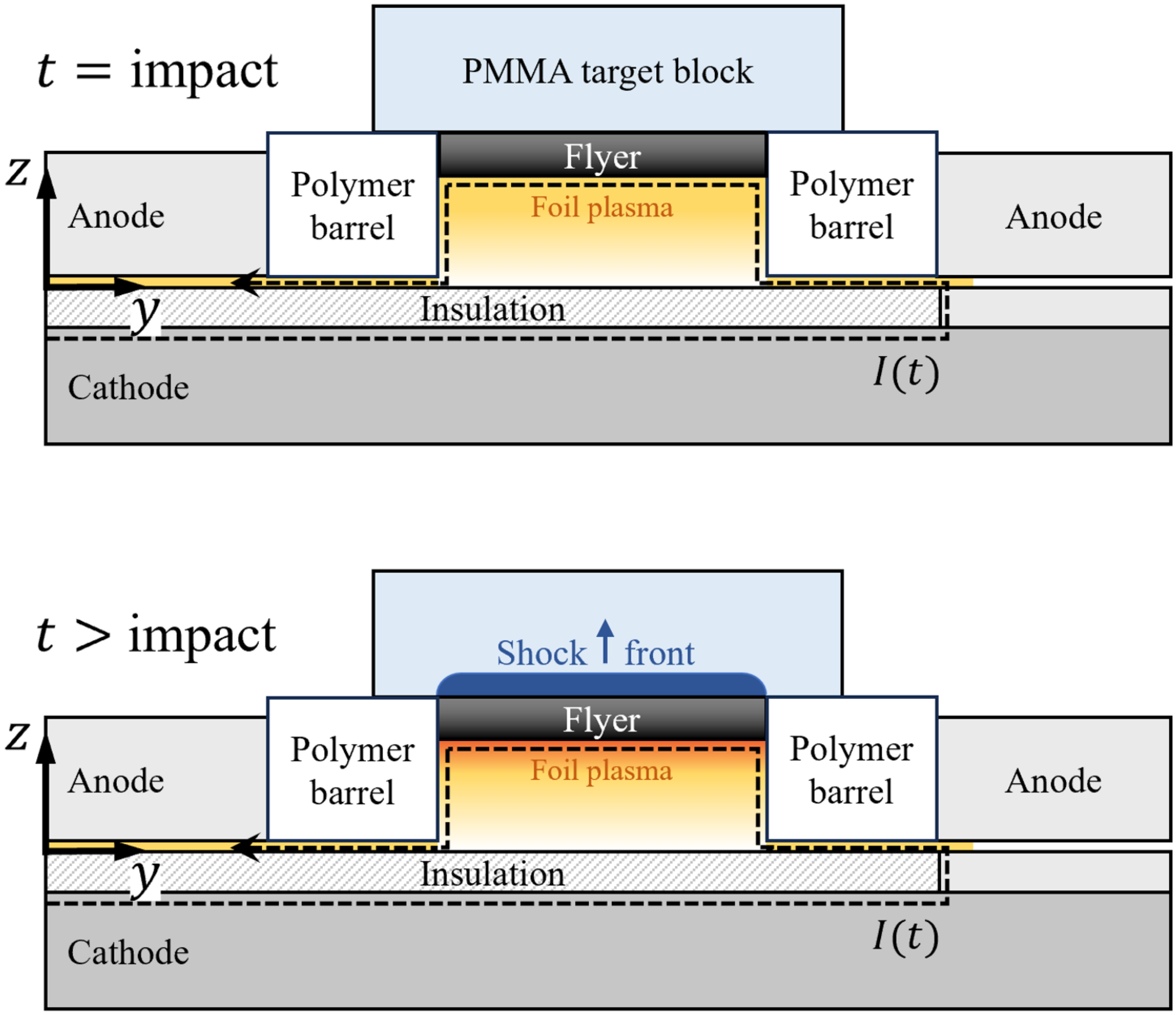

Figure 7.3: Illustrations of flyer impact in an electric gun load driven by a fixed rise-time machine. If impact occurs before the current becomes negligible (t =impact), the foil plasma will continue to drive the flyer (t >impact), causing the shock front velocity to vary.

This work took advantage of the considerable stand-off distances which can be achieved using an electric gun to impact a target placed centimetres away from the launch site. It was theorised this would ensure the impact occurred after the notable majority of the current has already been discharged and at a distance far from the current return pathway, where the magnetic fields are negligible. To achieve a supported shock in a target placed at a stand-off distance, the flyer must not deform or expand in the vacuum, thus should ideally be in a solid (or liquid) state. The numerical design of an electric gun load capable of accelerating such a flyer is discussed in the next section.

Table 7.1: Machine parameters for pulsed power capacitor bank, M3.

Machine Parameters	Value	units
Charge voltage	140	kV
Capacitance	124.8	µF
Fixed resistance	0.1	µΩ
Fixed inductance	12.5	µH

7.2.4 Modelling and design

It was determined in the previous section that to generate a quasi-equilibrated shock in a target using an electric gun, a region of constant density and velocity over a minimum thickness of the flyer must be maintained throughout flight. It was posited this could be achieved by minimising the state change in the flyer and impacting a target placed at a stand-off distance outside the influence of the magnetic fields in the system. In this section, 0D modelling is used first to reduce the electric gun load design space. Subsequently, detailed modelling is employed to determine the precise load parameters, which are depicted in Figure 7.4.

Initial parameter scan in 0D model

The findings from a previous study utilising our verified 0D model and 1D MHD B2 simulations to predict the maximum pressure in the flyer on launch indicated a decrease in flyer pressure with increasing foil thickness [93]. When the foil thickness surpasses the skin depth of the current through the metal, it melts and vaporises first at the lower surface of the foil. Subsequently, as the current continues to discharge, the magnetic field diffuses through the foil, heating it in the process. The vaporised foil exerts thermal pressure on the flyer, in addition to the magnetic pressure, when the melt boundary reaches the foil-flyer interface. The thermal pressure in the foil is highest prior to launch, as during this time, the vaporised foil is trapped between the flyer and the insulation. Consequently, if the flyer moves off before the foil vaporizes completely, the rapid increase in thermal pressure just before launch (as observed in Figure 7.2) can be circumvented. To achieve this, the foil must be sufficiently thick to prevent the melt boundary from reaching the front surface. However, a thicker foil leads to higher foil inertia, resulting in a longer launch time, thereby allowing the melt boundary to progress further before launch. Consequently, the appropriate foil and flyer thicknesses must be determined to balance these effects.

The 0D model discussed in [93] was used initially to explore the relationship between foil and flyer thickness and the progression of the melt front in the foil. It served to predict whether the position of the maximum pressure reached the front of the foil before launch, aiding in narrowing down the parameter space and reducing the number of high-fidelity simulations in B2 (which demand significantly greater computational resources). Before launch, it is assumed that the position of maximum pressure in the foil coincides with the position of the melt line. Figure 7.5 displays several traces tracking the positions of the foil, foil-flyer interface, flyer front, and position of maximum pressure in the foil. It can be observed that the position of maximum pressure reaches the foil-flyer interface, indicating complete melting of the foil prior to the flyer front, when the foil is 0.25-mm-thick for both the 0.25 mm and 0.5-mm-thick flyers. Consequently, 0.5-mm-thick aluminium foils were selected for detailed simulation in B2.

Hydrocode simulation set-up

B2 is a 3D MHD hydrocode developed by First Light Fusion, incorporating volume of fluid interface tracking and a Lagrangian-remap hydrodynamics scheme, along with a generic plasma EoS and transport coefficients. To capture the thermal and electrical conductivity in the foil, cathode, and anode, the Lee-More electron conductivity model was utilized [56]. Materials were simulated using the Frankfurt equation of state (FEOS), a semi-analytical tabulated EoS based on the QEOS model [89]. Lastly, the strength behaviour in the polymer flyer was captured using a Johnson-Cook (**JC**) constitutive model [114] developed for PMMA under strong shock loading, shown in Table 7.2 [130, 136].

Table 7.2: Johnson-Cook material properties. Polyimide is modelled using the same EoS and JC parameters as PMMA, but its melting temperature is set to 623 K.

Material	A	B	C	n	m	Melting temp
PMMA	375 MPa	90 MPa	0.077	4	0.74	433 K
Polyimide	375 MPa	90 MPa	0.077	4	0.74	623 K
Copper	90 MPa	292 MPa	0.025	0.31	1.09	1356 K
Aluminium	265 MPa	426 MPa	0.015	0.34	1.0	893 K
Stainless-steel	310 MPa	1000 MPa	0.07	0.65	1.0	1673 K

In addition to the complex multi-physics required to simulate the behaviour of the foil and flyer during current discharge, the physical scale of the electric gun load poses a modelling challenge. While the electrode, foil and flyer have dimensions on the order of centimeters, the foil and flyer

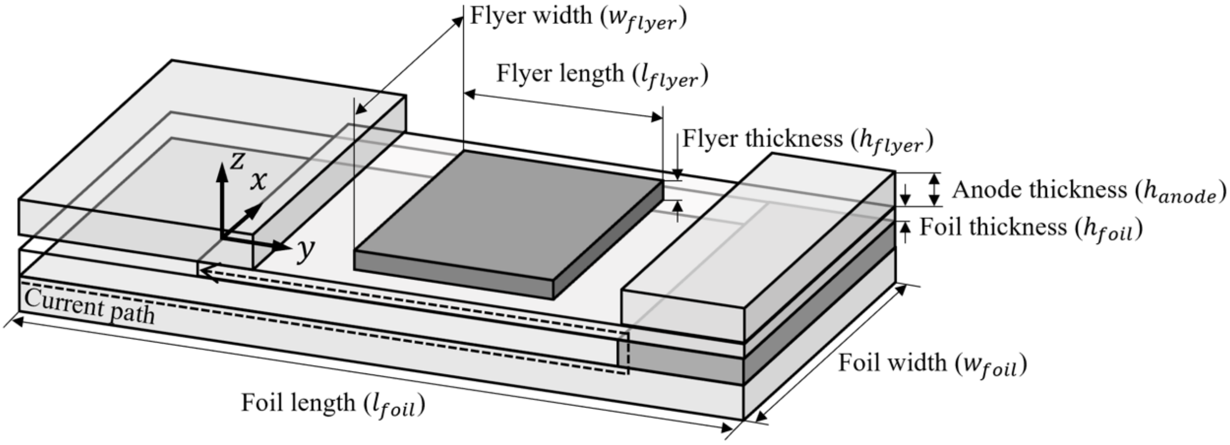

Figure 7.4: An illustration of the key geometric parameters which can be varied to control the states and dynamics of the flyer.

thicknesses are of the order 0.1-2.0 mm. This introduces a resolution compromise: to accurately capture the current magnitude through the foil, a significant portion of the load, including precise details of the electrodes, must be simulated in 3D. Simultaneously, high resolution is necessary in the foil and flyer to achieve convergent thermodynamic state predictions. However, B2 has a fixed mesh resolution, making it computationally impractical to run a 3D simulation large enough to encompass a significant portion of the electrodes while also maintaining sufficient resolution to predict the states in the foil and flyer. Consequently, the simulations were done in 2D with the acknowledgment that this may lead to the overestimation of the magnitude of the current in the load. Similar research exploring modelling of EM stripline geometry, employed for studying dynamic materials properties on the Z machine, indicates the complexity of correctly predicting the current load [76]. To address this discrepancy in B2, a reduction factor of 0.5 was applied to the current to mimic the current loss effects experienced by a typical load on M3.

The simulation set-up in B2 is illustrated in Figure 7.6, depicting the domain and boundary conditions. It was crucial to maintain the position of the material adjacent to the boundary, where the face-centered magnetic field was propagated, as static (zero velocity), as this ensured the point of current injection remained fixed. To model the tear-out behavior of the dielectric flyer accurately, the barrel walls and flyer were treated as separate parts. This approach prevented the material strength algorithm from inducing non-physical stresses between the components. In recognition of the higher melting point of the polyimide flyer, a melt temperature of 623 K was assigned to the flyer, while the barrel was modeled with a melt temperature of 433 K. Above these temperatures,

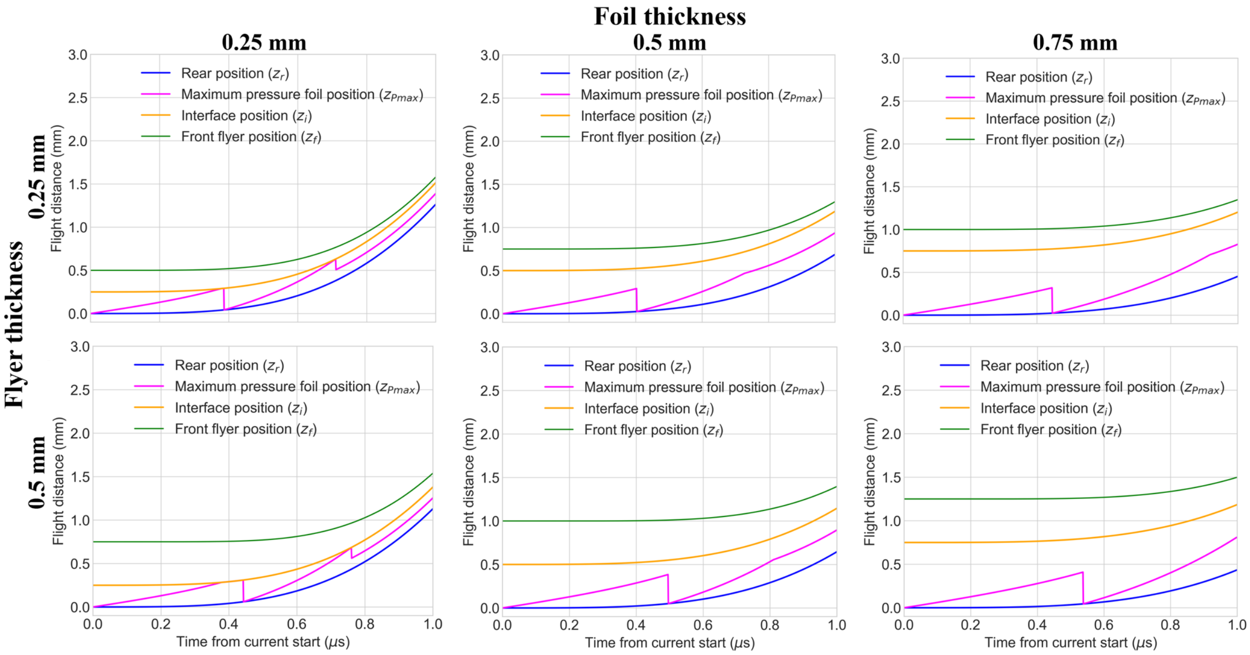

Figure 7.5: A matrix of traces of the positions of the foil rear, foil-flyer interface, flyer front, and melt-line predicted by the 0D model, for a range of foil and flyer thicknesses. These traces were used determine a combination of foil and flyer thickness which would avoid the melt-line reaching the foil-flyer interface, thus limiting the maximum pressure in the flyer.

the components of the stress tensor were set to zero, effectively disabling material strength effects (neglecting the phenomenon of melt temperature variation with pressure).

2D simulation results

The impact of increasing the foil thickness on the density, pressure, and temperature state of the insulating flyer were explored using 2D B2 simulations. A comparison was made between the behavior of a $25 \times 50 \times 0.5$ mm aluminium foil with a $24 \times 24 \times 0.5$ mm polyimide flyer and a previously tested electric gun load on M3, featuring a $25 \times 50 \times 0.1$ mm mm Al foil and a $24 \times 24 \times 0.5$ mm flyer, shot over a 20 mm stand-off distance [96]. The previously tested flyer exhibited disassembly before reaching the target, which was indicated by plasma breakthrough. Results depicted in Figure 7.7a reveal that the initial rapid pressure increase upon launch, attributed to thermal pressure built up in the trapped vaporized flyer, was absent when the foil thickness increased to 0.5 mm. This is consistent with the predictions made by the 0D model. Correspondingly, Figure 7.7b illustrates a lower mean temperature increase in the flyer during this period. The temperature within the dielectric flyer driven by the 0.5-mm-thick foil increased steadily throughout flight whereas a fluctuating pattern

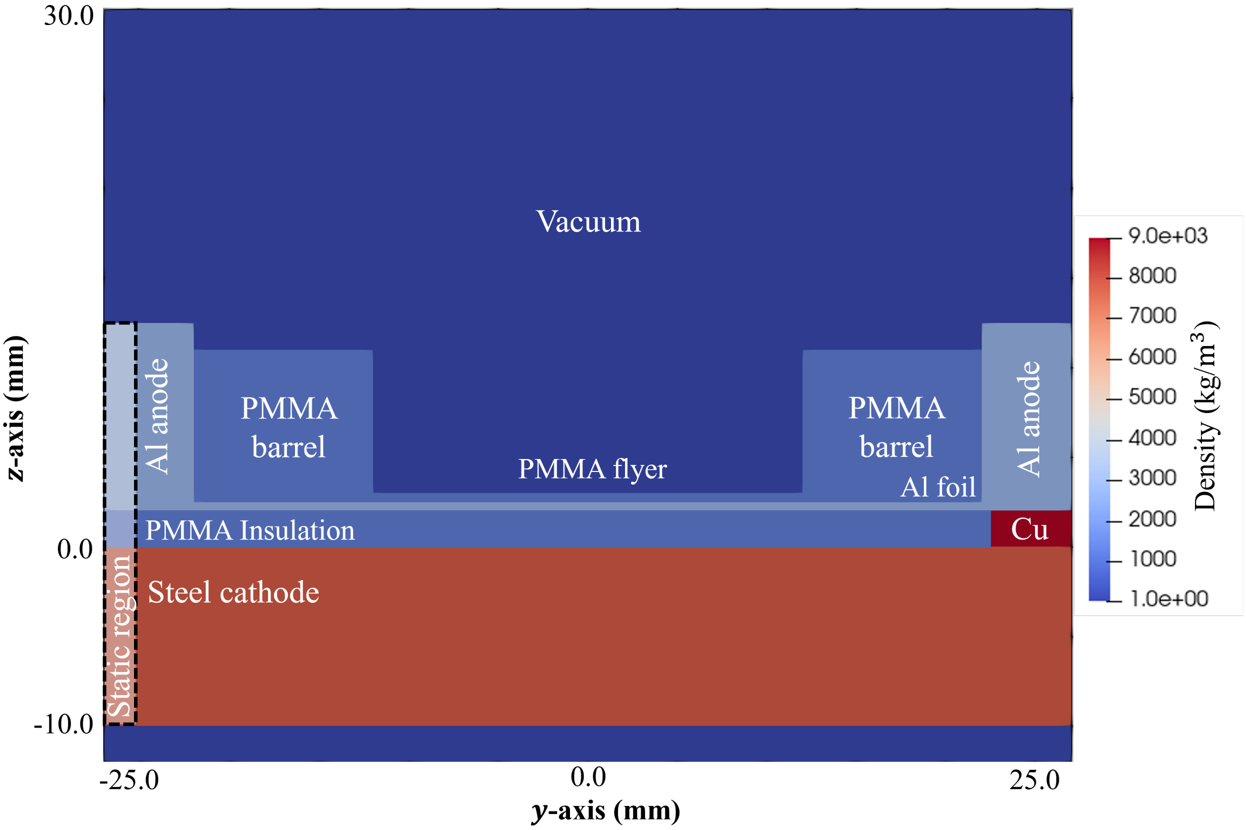

Figure 7.6: Illustrations of the simulation set-up (coloured by density), including the region kept static (zero velocity) to fix the point of current injection.

can be observed in the flyer driven by the 0.1-mm-thick foil. The resulting effect on the density profile across the flyer thickness is shown in Figure 7.7c, indicating that the density in the flyer driven by the 0.5-mm-thick foil remained at the solid density of PMMA (1170 kg/m^3), whereas the flyer driven by the 0.1-mm-thick foil dropped below this threshold.

Typically, in the electric gun, the flyer is ‘punched out’ of a larger sheet by the expanding foil below it moving up the barrel. This method was demonstrated to prevent plasma from escaping around the edges of the flyer during operation [94]. However, the interaction of the flyer edges and the barrel can decrease the usable surface area of the flyer [54] . Figure 7.8 displays four visualisations of the simulation domain. For a barrel of width 24 mm, the planar region of the flyer on exiting the barrel is 16 mm. This indicates the usable surface area of the flyer was reduced by 44%. The tear-out behaviour of the flyer, the flyer dynamics and the flyer states were similar in simulations with material strength switched on or off, suggesting it had a negligible effect on this load design.

The increased foil thickness had the additional benefit of reducing the growth rate of Rayleigh-Taylor (**RT**) instabilities at late times in simulations. Within simulations, RT instabilities occur and are

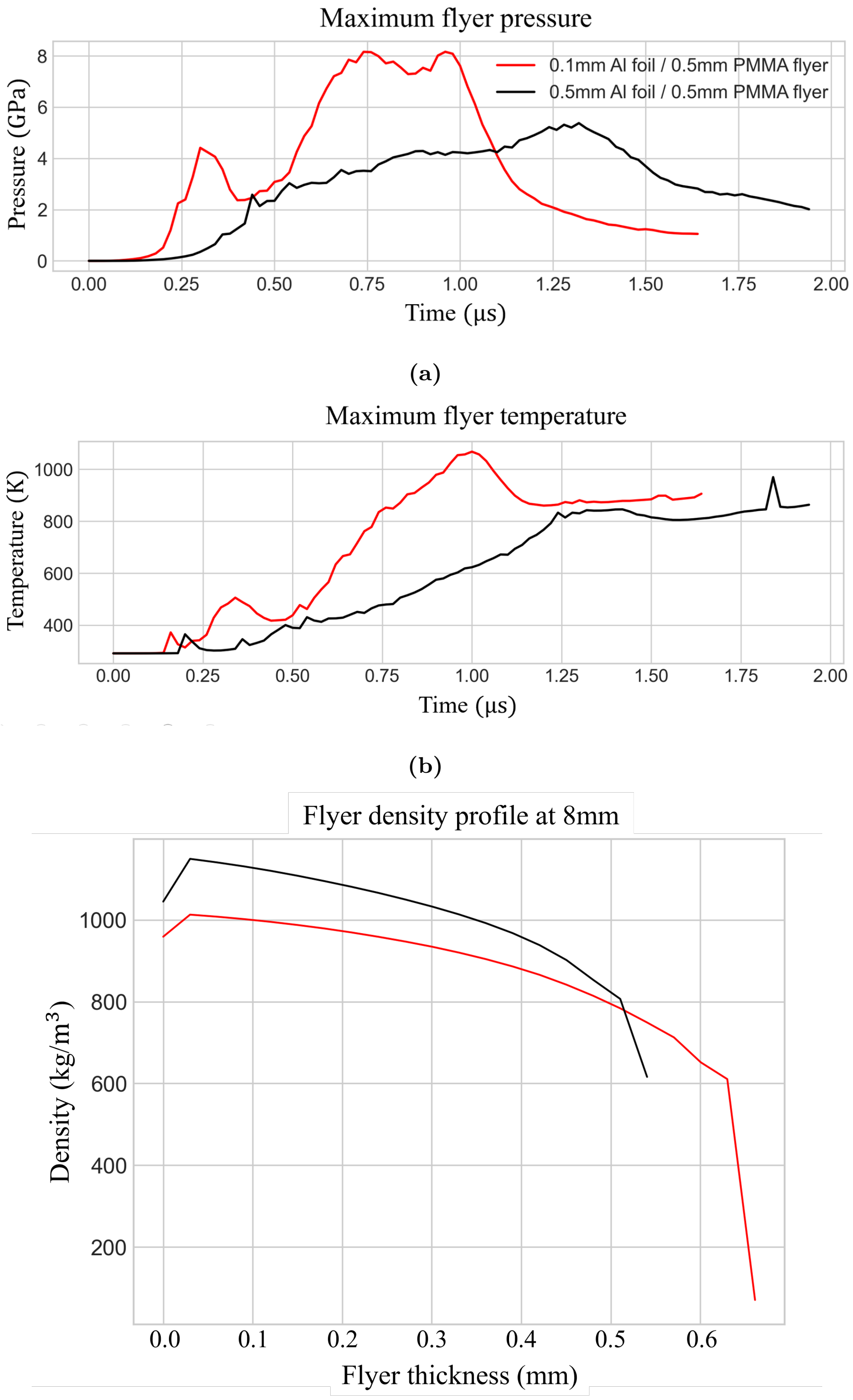

(a)

(b)

(c)

Figure 7.7: Plots contrasting the simulated flyer pressure, temperature, and density states in an electric gun flyer driven by an 0.5-mm-thick and a 0.1-mm-thick foil. The 0.5-mm-thick foil shields the flyer from extreme fluctuations in pressure, resulting in it remaining near solid density late in flight.

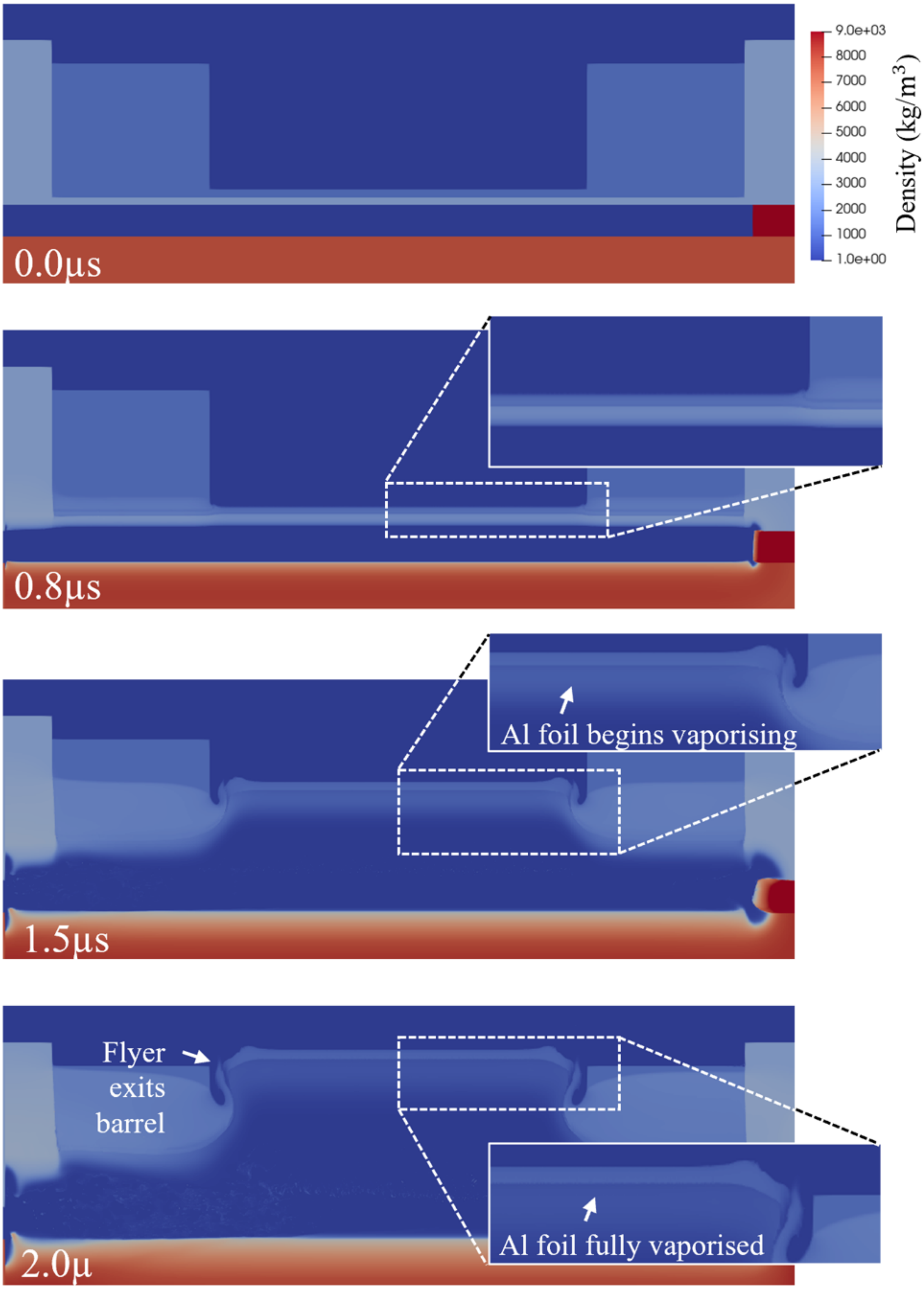

Figure 7.8: B2 simulation domain density profiles for 4 characteristic times during flyer launch. The foil vaporises at late times, exhibiting a significant drop in density by 2.0 μs.

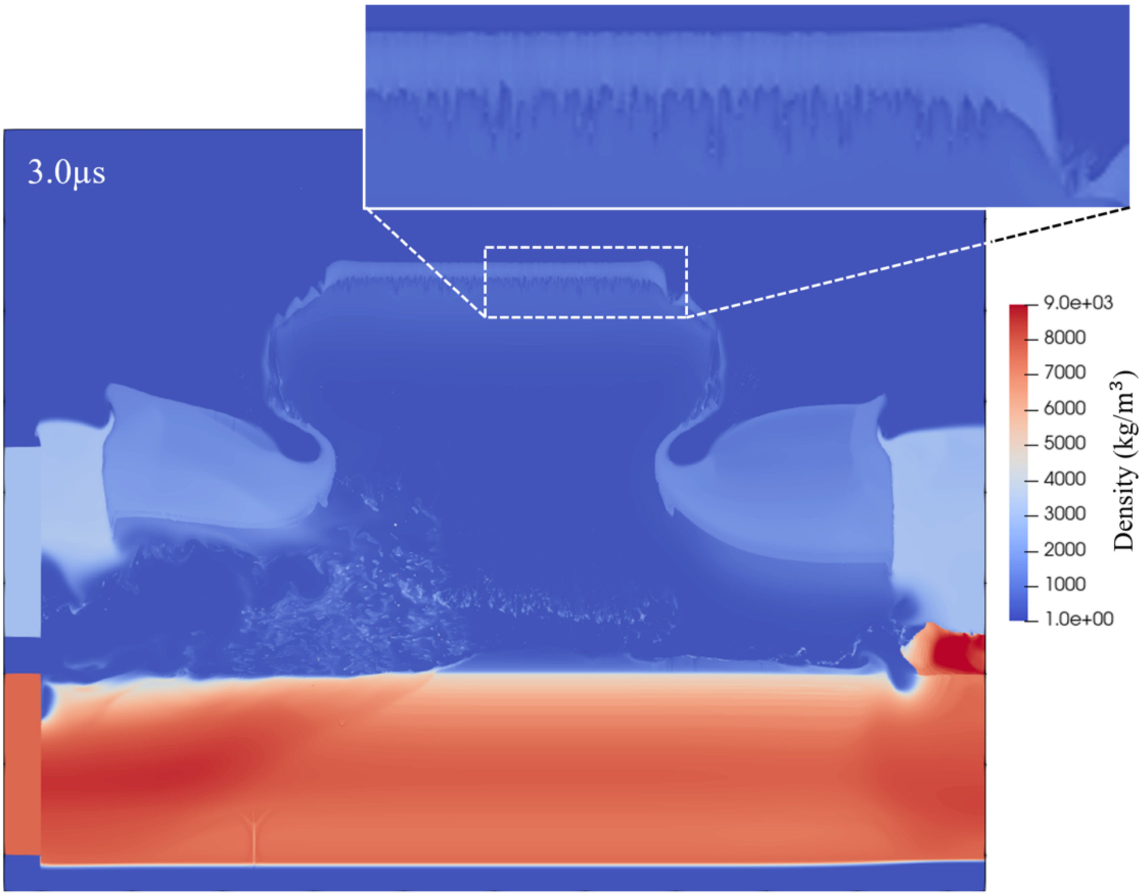

Figure 7.9: B2 simulation domain (coloured by density) instabilities at the foil-flyer interface late in flight. Increasing the foil thickness reduced the growth rate of the RT instabilities compared to electric gun simulations with thinner foils.

numerically seeded by the grid imprint, whilst in reality, these occur as a consequence of surface defects. Scratches or imperfections on the foil initiate locations of concentrated current density, disturbing the planarity of the foil explosion. Similarly, scratches and indents in the flyer offer points where foil vapour can intermix with the flyer, causing the higher inertia material to fall behind and initiate RT instability growth. In a typical electric gun, when the foil vaporises its density decreases rapidly, increasing the Atwood number at the foil-flyer interface and resulting in a system where the low-density foil vapour accelerates the now higher density flyer. However, when the foil is thicker, it maintains a higher density at the foil-flyer interface until later in flight, as shown in Figure 7.8. The simulations reveal some RT instabilities at the foil-flyer interface after the flyer exits the barrel, however, their amplitude is considerably less than the flyer thickness, as shown in Figure 7.9. It was proposed the thicker foil could suppress the growth of RT instabilities to destructive amplitudes within the experimental load.

Discussion

The results in the previous section presented simulations of an electric gun load with a 25×50×0.5 mm aluminium foil and 24×24×0.5 mm polyimide (PMMA EoS with polyimide JC melting point) flyer. B2 simulations predicted the max temperature of the dielectric flyer was raised above the melting point at standard atmospheric temperature, however still maintained a region of thickness at solid density. Determining the exact state (i.e. solid or liquid) of the flyer is a complex matter due to the high pressures it experiences during acceleration by the foil plasma. Whilst simulations in B2 can calculate the temperature state of the flyer, they overlook several significant factors that could impact the real-world behavior of the flyer: for instance, research suggests that polymers, amongst other materials, melt at higher temperatures under extreme pressures [**seeger2004melting**].

The simulations were also unable to capture the dynamic behaviour of the flyer beyond approximately 2 cm stand-off from the exit of the barrel. To achieve convergence in the flyer states in the simulation, the grid resolution was set to 20 µm. However, this high-resolution prevented the completion of simulations of the flyer over longer flight distances. Consequently, the numerical prediction of how far the flyer must travel from the return current path before reaching constant velocity remained uncertain. Consequently, experimental evidence was required to overcome the limitations of these simulation techniques and further investigate both the evolution of the flyer state and dynamics over long stand-off distances. The final design specifications of the electric gun load tested are outlined in Table 7.3.

Table 7.3: Electric gun load parameters determined using numerical modelling.

Load Parameters	Value
Foil length	50.0 mm
Foil width	25.0 mm
Foil thickness	0.50 mm
Foil material	99% purity anealed Aluminium
Flyer length	25.0 mm
Flyer width	25.0 mm
Flyer thickness	0.50 mm
Flyer material	Kapton Polyimide

7.2.5 Experimental validation

Method and set-up

The objective of the experiment detailed in this work was to accelerate a polymer flyer, with a region constant density and velocity, across varying stand-off distances. The experimental set-up is depicted in Figure 7.10. PMMA target blocks were placed at stand-off distances of 8 mm, 50 mm or 100 mm, with the velocity of the shock generated upon flyer impact measured using a high-speed camera. PMMA becomes opaque when subjected to pressures high pressure, facilitating the tracking of shock front positions through block thickness over time. The position-time data can then be used to calculate the shock front velocity in the block. The 50 mm and 100 mm blocks were intentionally oversized to capture the two-dimensional profile of the shock in the PMMA target block, as illustrated in Figure 7.11. This 2D shock profile enables the inference of the flyer surface area upon impact, its planarity, and uniformity. Additionally, the velocity of the flyer during launch was recorded using one-dimensional Velocity Interferometer System for Any Reflector (**VISAR**). This velocity profile provides meaningful validation data; the flyer dynamics rely on the electromagnetic and thermal states within the flyer. If there is good agreement between the experimentally observed flyer kinematics and the earlier predictions from B2 simulations, it suggests that the state predictions made using the MHD code are also accurate.

The primary challenge in collecting diagnostics during the operation of an electric gun was excluding the large volume of bright plasma produced when the foil vaporised from the diagnostic line of sight. The shroud structure, visualised in Figure 7.10, was designed to prevent stray foil plasma from blocking the high-speed camera (the magenta-coloured observation path trace). The plasma shielding surrounding the anode, employed in [96], continued to be an effective way of containing a majority of the foil plasma produced outside the barrel until after impact had been captured.

Results

The results of four shots are presented in this section, each utilising the same load configuration, driven by M3 at 140 kV. The VISAR velocity profile was captured for the first 1.5 µs of acceleration. Figure 7.12 shows the plots of the simulated and experimentally measured velocity. There is good agreement between the B2 simulation prediction and measured VISAR velocity traces. Whilst VISAR data was lost after the first 1.5 µs, which could be an indication of the flyer surface melting, there is excellent agreement between the measured impact time (found using light emission on impact captured in the 1D VISAR streaks) and that predicted by the simulation. The impact times at

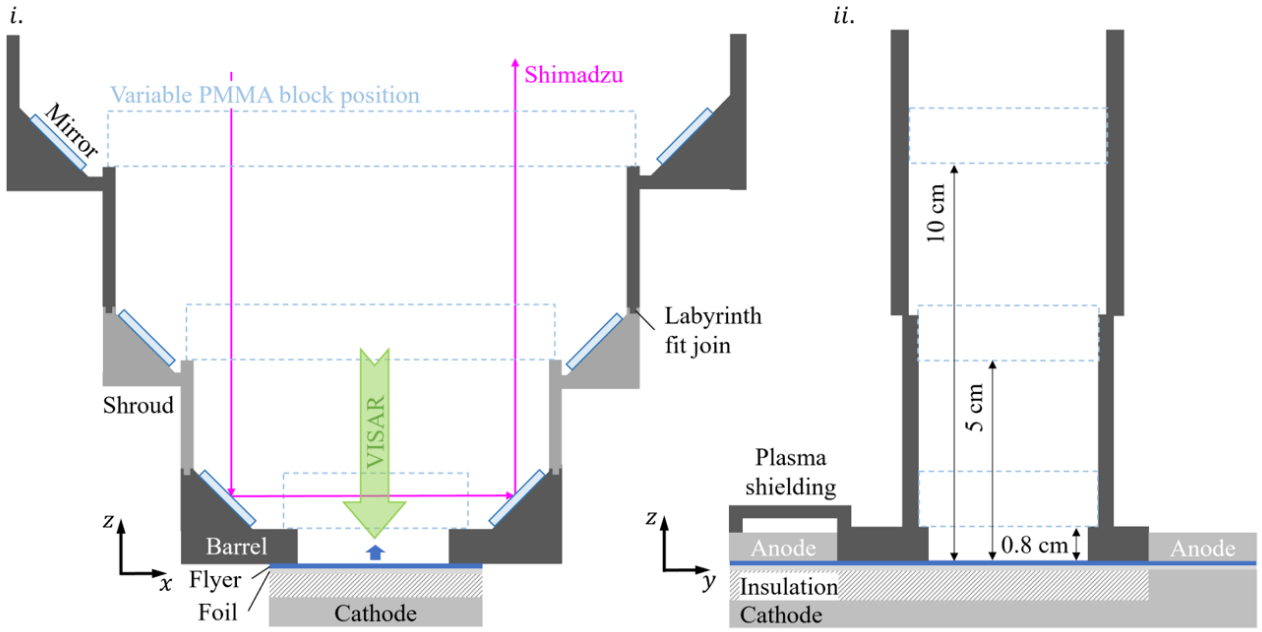

Figure 7.10: Illustrations of the experimental set-up in the *xz* (*i*) and *yz* (*ii*) plane, including the plasma shroud designed to protect the diagnostic line of sight, plasma shielding to suppress foil plasma emitted at the join between the foil and anode, and variable block positions. The velocity of the flyer is measured using 1D VISAR trained on its surface and the velocity of the shock in the PMMA block is captured by a high-speed camera.

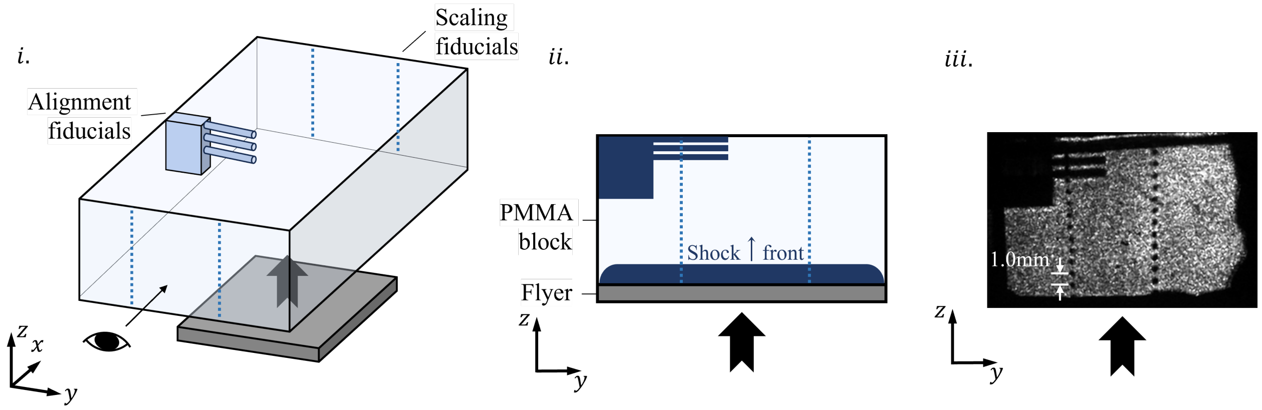

Figure 7.11: Diagrams demonstrating the layout of the side-on images of the block captured by the high-speed camera including: a diagram of the PMMA target block and flyer with the shock direction labelled (*i*); a diagram of the block from the perspective of the high-speed camera (*ii*); and an example of a high-speed camera frame (*iii*).

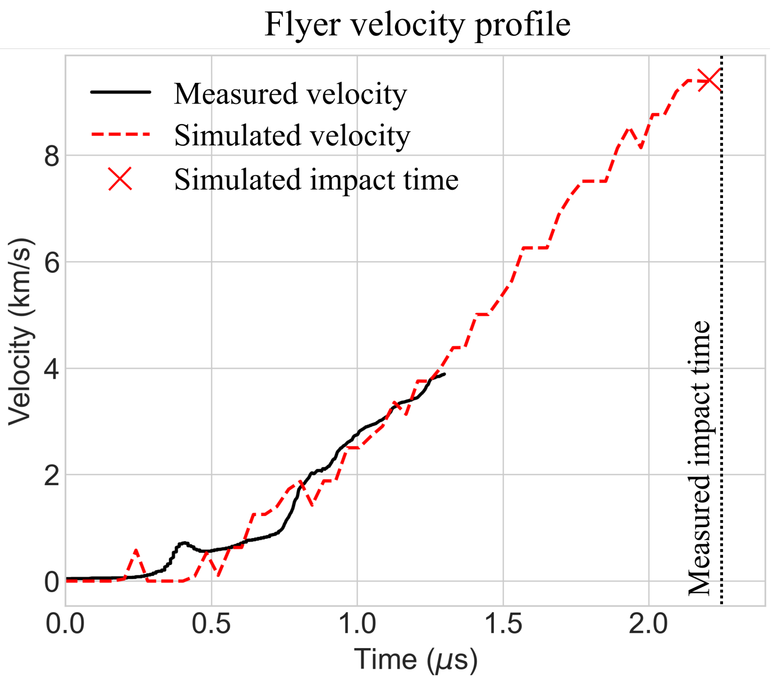

Figure 7.12: Plot of the measured experimental velocity over time and the velocity predicted by the 2D MHD hydrocode simulations for an 8 mm stand-off. The simulated impact velocity is used in analysis going forward as the VISAR signal was lost at around 1.5 µs. This could be an indication of the flyer surface melting.

50 mm and 100 mm stand-off distance, measured using the high-speed imaging of the target block, were also recorded and are included in Table 7.4.

Table 7.4: Measured impact times and predicted velocity. Simulations could not be completed for the 50 mm and 100 mm cases.

Stand-off distance	Measured impact time	B2 predicted impact velocity
8 mm	2.28 µs	8.47 km/s
50 mm	6.07 µs	-
100 mm	8.68 µs	-

The 2D images taken by the high-speed camera were analysed to assess the planarity and lateral extent of the flyer on impact. While the flyer and the PMMA block at 8 mm stand-off shared the same width, the blocks at 50 mm and 100 mm were intentionally oversized to capture the shape of the shock front at the flyer edges, as illustrated in Figure 7.10. In Figure 7.13b, the shock front generated by the flyer at 8 mm appears largely planar, progressing at an angle of 6.3°, which is consistent with previous observations attributed to magnetic field asymmetry across the foil [96]. At 50 mm,

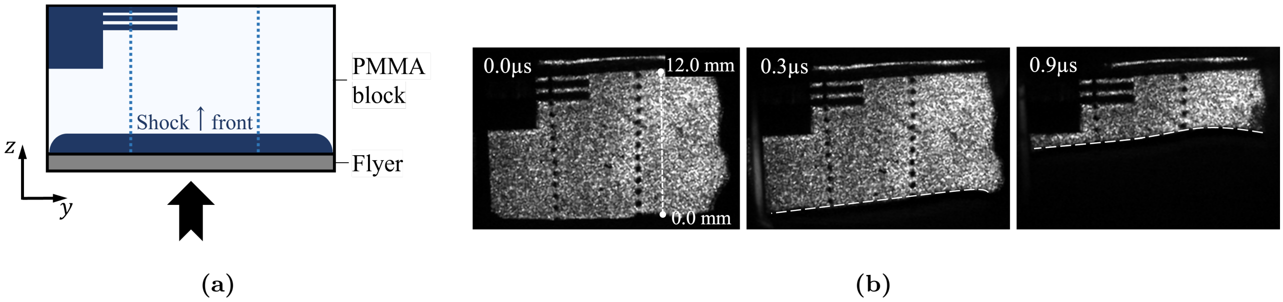

(a) (b)

Figure 7.13: A diagram showing the ratio of the flyer-to-block width at 8 mm stand-off (a) and 2D images of the shock front taken using high-speed imaging (b). The shock front appears planar and continuous throughout the block.

Figure 7.14b shows slow precursor shock fronts are generated at the edges of the block. The precursor shocks were only visible in the *yz* plane. This was thought to be due to debris at the edge of the flyer collecting at the walls of the protective shroud, which is narrower in the *yz* plane than the *xz* plane. Thus, in the *xz* plane, material at the edges of the flyer had space to expand and decelerate on leaving the barrel, however, in the *yz* plane the material instead hit the shroud walls and was compressed upwards by the accelerating flyer. This effect is also apparent at a 100 mm stand-off in Figure 7.15b, though the more noticeable precursor shocks in the PMMA block appear to be caused by the expansion of material forced into the evacuation tube prior to impact.

The length of the planar region of the shock on impact was used to infer the lateral extent of the flyer in the *yz* plane. At 50 mm, the planar region of the shock was 11.5 mm and at 100 mm it was 10 mm. This was smaller than the prediction made by the simulation in B2, however, the simulation did not account for the behaviour of the entrained material at the wall of the shroud. Additionally, the width of the flyer varied little between 50 mm and 100 mm, suggesting the flyer did not experience further significant deformation between these two points.

This work intends to utilise the behaviour of the shock velocity profile in the target block to infer information about the flyer density profile and acceleration. However, the sparse temporal resolution of the positional data necessitates fitting a function to the shock front positions, which can then be differentiated. The selection of a line using standard methods, such as fitting a polynomial, requires predisposed notions as to what the positional relationship is expected to look like to prevent over or under-fitting to the data. This risks introducing a paradoxical effect, in that the expected shock velocity profile necessarily influences the calculation of the profile. To minimise the influence of human bias in the fitting of a function to the positional data, Gaussian Process (**GP**) regression was applied

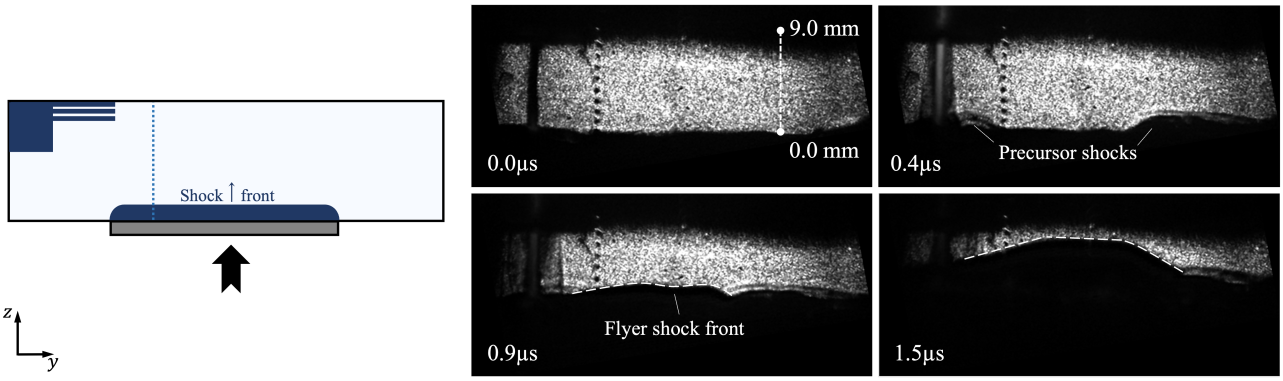

(a) **(b)**

Figure 7.14: A diagram showing the ratio of the flyer-to-block width at 50 mm stand-off (a) and 2D images of the shock front taken using high-speed imaging (b). The block was deliberately oversized to capture the shock profile at the edge of the flyer. Figure 7.14b shows slow, asymmetric precursor shocks arrive at the edges of the block before the flyer. The flyer shock front appears to be planar and continuous across the block thickness.

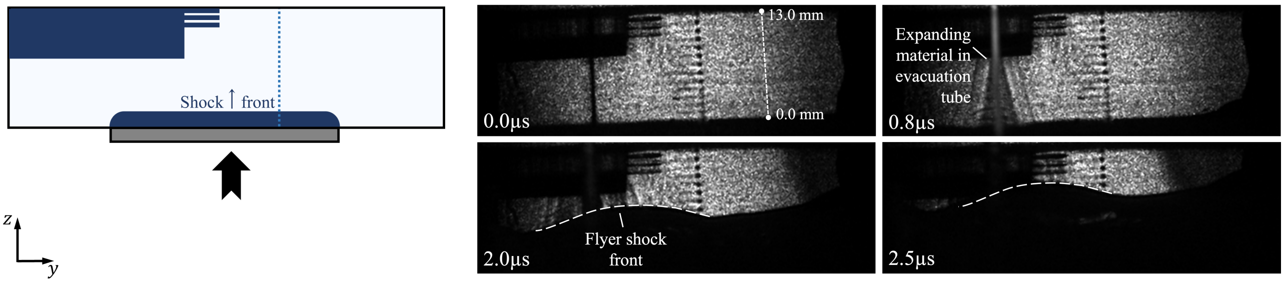

(a) **(b)**

Figure 7.15: A diagram showing the ratio of the flyer-to-block width at 50 mm stand-off (a) and 2D images of the shock front taken using high-speed imaging (b). The block was deliberately oversized to capture the shock profile at the edge of the flyer. Figure 7.15b shows slow, asymmetric precursor shocks arrive at the edges of the block before the flyer. The flyer shock front appears to be planar and continuous across the block thickness.

to the shock front positions instead to derive a posterior mean and covariance (uncertainty) based on the positional dataset. As differentiation is a linear operator, the mean of the distribution of derivatives is the derivative of the posterior mean. Consequently, the mean and the covariance of the derivative of the posterior function distribution can be calculated directly using the equations derived in [137]. An additional benefit to GP regression is that it can be applied to a positional data set which includes all the pixel locations where the shock front could be, thus the uncertainties in the shock front position are directly incorporated into the derivation of the GP model.

Figure 7.16 illustrates the raw shock front positions in the PMMA target blocks over time, alongside the GP model mean ± two standard deviations and the resulting shock profile velocity. Analysis of the profiles indicated that the shock velocity varies within the block at stand-off distances of 8 mm and 50 mm, while it remained relatively constant at 100 mm. These shock front velocity profiles are compared in Figure 7.17. At 8 mm, the shock front velocity continually increased after impact. While the 50 mm the shock front velocity also increased initially, this acceleration arrests later in the measurement window. The peak shock velocity in the target at 100 mm stand-off is lower than at 8 mm or 50 mm. However, unlike the impact recorded at targets closer to the launch position, the shock velocity profile at 100 mm is relatively constant for the duration of the measurement window.

Discussion

The experimental results from the shots performed on M3 demonstrate that this electric gun load successfully accelerated 0.5-mm-thick polyimide flyers over stand-off distances of up to 100 mm. It was hypothesised that to achieve this, the flyer must retain a region of constant density as it travelled across the vacuum. The load designed in this work achieved this by increasing the foil thickness, thereby minimising the state change in the flyer during acceleration. The close match between the experimentally measured and simulated flyer velocity profiles suggests the flyer states predicted by the 2D MHD simulations in Section 7.2.4 were accurate. If this is the case, the flyer was likely heated to temperatures at the border between solid and liquid state late in flight.

The shock velocity profile in the target blocks varied with stand-off distance. At 8 mm stand-off, the shock velocity briefly increases from around 5.0 km/s to 10.0 km/s at the end of the measurement window. This later increase is thought to be a result of the continued acceleration of the foil plasma, due to the target's close proximity to the return current path. At 50 mm, the shock velocity on impact is lower (~ 2 km/s), before increasing to a peak of ~10 km/s at 0.75 µs. The velocity profile subsequently decreases again towards the end of the measurement window. Again, this could indicate the flyer is still within the influence of the accelerating magnetic field, though to a lesser extent than the target at 8mm. The low initial shock velocity at 8 mm and 50 mm was most likely caused by the impact of low-density material, though some caution should be given to reading deeply in to the velocity profile at the beginning and end of the time window, as this is where the differential of fitted functions tend to be least accurate. Finally, at 100 mm stand-off distance, an approximately constant shock front speed of 6.0 km/s was recorded over 1750 ns. This is equivalent to a shock pressure of 20 GPa in the PMMA block [95]. This suggests the flyer had the desired region of constant density and velocity, as it was capable of generating a shock with considerable duration in the target.

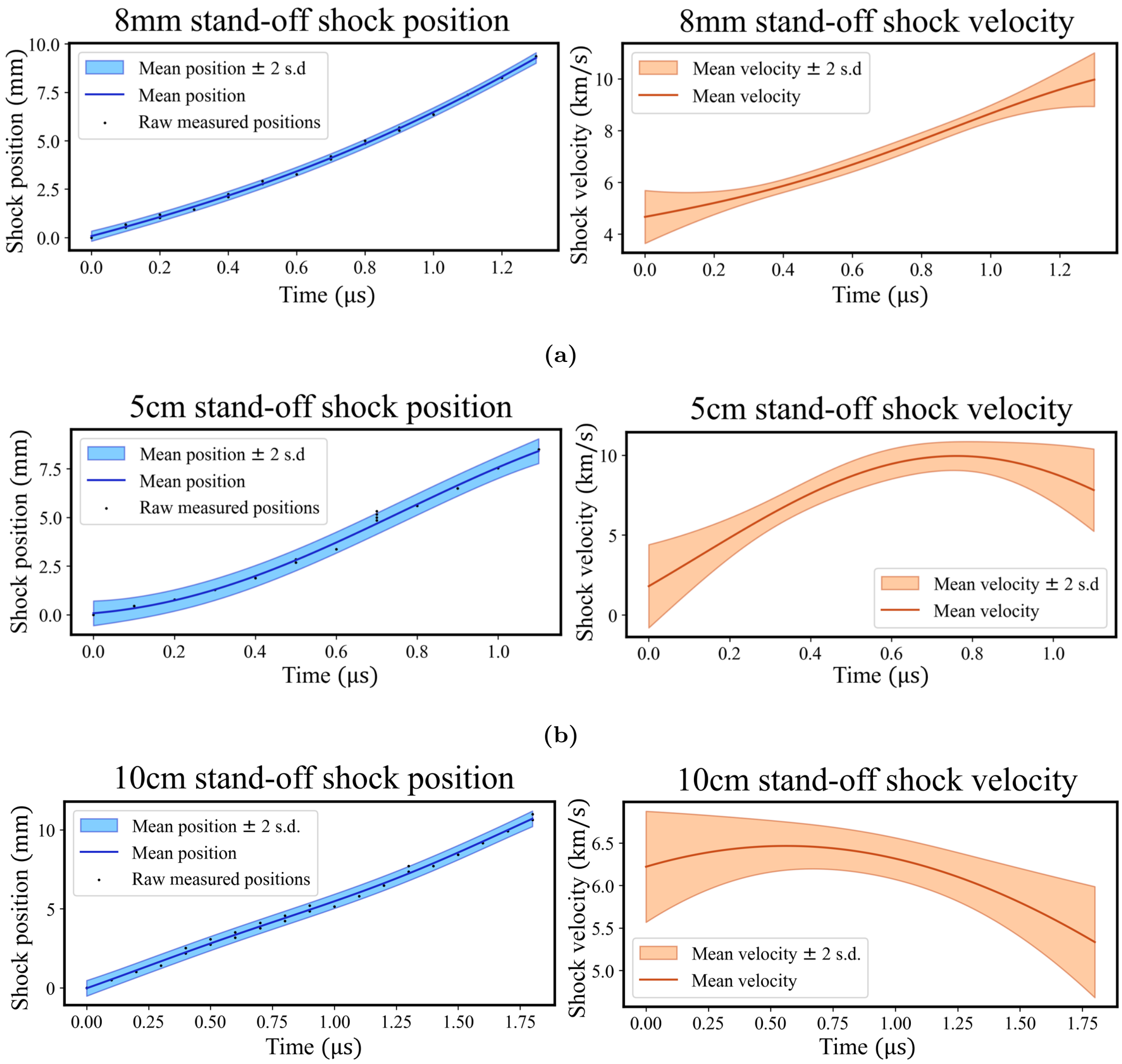

(a)

(b)

(c)

Figure 7.16: Plots showing the measured shock front position over time at stand-off distances of 8 mm, 50 mm, and 100 mm. Plots on the left show the position-time data in black, with the GP model mean ± 2 standard deviations in blue. The plots on the right show the GP model predicted mean ± 2 standard deviations in orange. Note, the uncertainty in the velocity profiles is highest at the beginning and end of the measurement window.

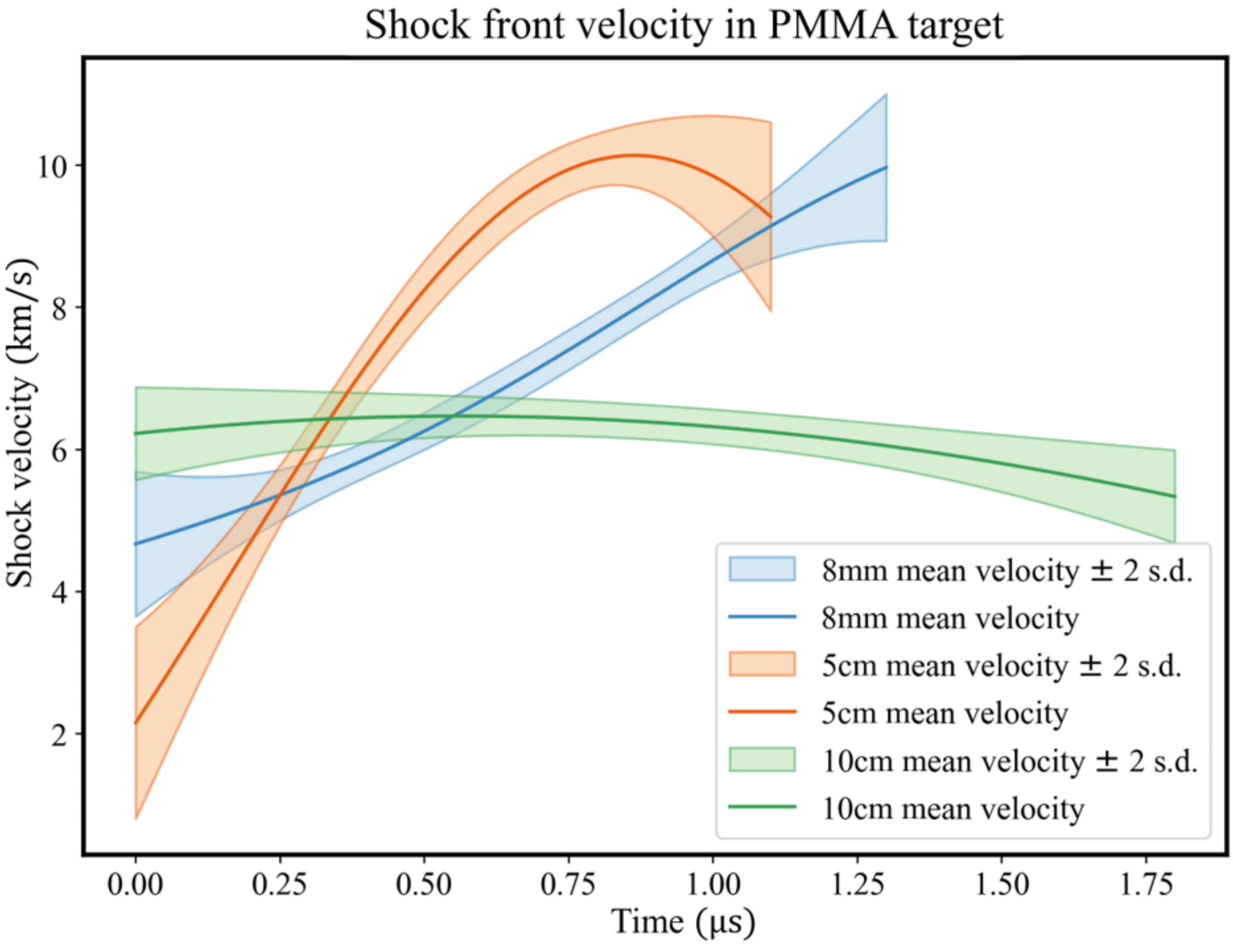

Figure 7.17: Plots of the shock velocities measured at different stand-off distances side-by-side. The shock velocity at 100 mm is lower than at 50 mm or 8 mm, however, the velocity of ~6 km/s is constant for a duration of 1.0 µs.

It might be suggested that the impact times at 50 mm and 100 mm could potentially allow for the estimation of the flyer's velocity at these stand-off distances. However, Figures 7.14b-7.15b imply that the flyer experienced significant interaction with the barrel wall, which could have exerted a decelerating drag force. Additionally, the entrained barrel material at the flyer edges could increase the flyer's mass, thereby reducing its velocity. These mechanisms could account for the lower-than-expected shock front velocity in the block at 100 mm. To mitigate this effect in the future, widening the shroud in the *yz* direction could prevent the collection and acceleration of debris in the flight path.

7.2.6 Conclusions

In this work, an electric gun load suitable for exploring extreme states of materials and its experimental validation was presented. Projectile launch techniques offer the advantage of generating high-pressure, planar shocks across large material volumes, ensuring precise measurements. However, achieving these conditions requires specific flyer characteristics: it must maintain near-constant density and velocity over a minimum thickness upon reaching the target. This work involved adapting an existing electric gun design to meet these criteria. It was proposed the load could achieve this by accelerating an insulating flyer without significant state change (constant density) and eliminating the forces driving the flyer prior to impact by placing it at a considerable stand-off distance (constant velocity). First, 0D modelling was used to narrow the parametric design space. Subsequently, high-fidelity 2D simulations were conducted using the in-house hydrocode B2 to determine the optimal foil and flyer thickness. Finally, experimental testing was carried out to validate the model's predictions and examine how the shock pulse shape at impact correlates with the stand-off distance from the launch site.

The results demonstrated that increasing the foil thickness successfully minimised the significant increase in the flyer pressure on launch that is typical of electric guns [96]. Further, it prevented the disassembly of the flyer late in flight, witnessed in electric gun loads on M3 in previous experiments [110]. This is thought to be due to the reduced growth rate of RT instabilities at the foil-flyer interface. The results underscore the effectiveness of the numerical modelling approach utilised in designing the novel load.

Referring to the questions initially posed in the introduction, it was concluded:

- The electric gun load can be adapted to minimise variation in the flyer state by increasing the thickness of the foil. In this work, the foil thickness was increased from 0.1 mm to 0.5 mm. The 0.1-mm-thick foil was found to cause plasma breakthrough in a 0.5-mm-thick flyer shot over 20 mm in previous work [96, 110]. The new load design with increased foil thickness accelerated a 0.5-mm-thick polyimide flyer over 100 mm stand-off, generating a shock velocity of 6.0 km/s over a 10×10 mm area for a duration of 1750 ns in a PMMA target block. This, alongside modelling, suggest the flyer temperature and density state were successfully controlled to prevent vaporisation and disassembly.

- M3, the pulsed-power device used to drive the electric gun load in this work, has a fixed current rise-time of around 2.0 µs. Fixed rise-time pulsed-power devices are more common as they are simpler to design and build. If the current profile cannot be shaped, the flyer must instead escape the influence of the magnetic fields propagated by the return current path to impact the target at a constant velocity. In this work, a constant pressure pulse over 1.0 µs was achieved by launching a flyer over 100 mm stand-off distance. The shock velocity in targets at 8 mm and 50 mm was also measured, demonstrating variation in the velocity profile over the 1.0 µs recorded.

These results highlight the importance of the stand-off distance in ensuring ballistic impact at the target.

- The electric gun in this work accelerated a 0.5-mm-thick flyer over a 100 mm stand-off distance, generating 20 GPa in a PMMA target block over 1.75 µs. This suggests the electric gun could be utilised to make EoS measurements on existing pulsed-power platforms with a fixed rise-time by adjusting the stand-off distance of the target. Beyond ensuring ballistic flight of the flyer, the 100 mm stand-off holds other advantages: the increased space between the launch site and the target protects the diagnostics from plasma and debris generated during launch. In previous work, at a 10 mm stand-off, the diagnostic view was often obstructed by the excess of foil plasma [94]. However, at 100 mm the view of the camera remained unobstructed for over the entire measurement window. The load designed in this work could be improved by simply widening the shroud surrounding the exit of the barrel, preventing the entrainment of material at the edges of the flyer and improving the planarity of the impact shock in the block.

Possible extensions to this work include attempting to image dielectric flyers in free flight using x-ray radiography using an external X-pinch driver [138]. This additional information could provide valuable insight into the state and morphology of the flyer on exiting the barrel.

7.3 Summary

The final chapter of this thesis explored the theory, design and experimental testing of a potential electric gun for extreme state research. It utilised learning from each of the previous chapters to inform the study presented and obtain a successful result. The electric gun has a number of unique characteristics which set it apart from other hypervelocity projectile launchers. Its operating mechanism involves passing the current from a high energy pulsed-power machine through a thin foil, which in turn drives a dielectric flyer atop it. This operating mechanism offers the opportunity to accelerate dielectric flyers over relatively long stand-off distances and is highly efficient at converting stored electrical energy to kinetic energy in the flyer. Both these attributes are highly desirable in a projectile launcher: firstly, a stand-off distance between the launch and impact location permits recovery of the target and improves repeatability and time required to reload. A higher load efficiency enables research platforms to access extreme states with existing pulsed-power devices that might otherwise be restricted. Despite these advantages, on the inception of this thesis the electric gun could not be used as a tool to make extreme state measurements. It was incapable of accelerating a flyer with a constant density over a thickness sufficient to drive shocked states for an extended duration. Previous literature remarked the gun was limited to launching thin films of Kapton, which created ephemeral shocked states, resulting in low precision equation of state measurements.

Chapter 5 discussed the successful acceleration of flyers up to 2 mm thick until impact. However, experimental testing of an electric gun load revealed the flyers produced shocks with a fluctuating velocity profile in the PMMA target block. This suggests either that the density profile varied across the flyer thickness, the velocity of the flyer was not constant on impact, or both. Consequently, the shock velocity profiles presented in this chapter would not have been suitable for extracting extreme state measurements. To achieve this result on M3, a CDU with a rise-time largely fixed by the machine parameters, a load was designed which could launch an intact flyer over a stand-off distance to a target, such that it escaped the influence of the magnetic field surrounding the current path. This goal required the flyer to be in either a liquid or solid state, as a vaporised flyer would neither have a region of near-constant density, nor be capable of travelling across the vacuum without experiencing significant deformation.

The design of the electric gun load in this chapter utilised both the 0D model (described in Chapter 4) and 2D simulations with material strength effects in B2 (described in Chapter 6). The 0D model was used to identify promising regions of the parametric space, before exploring these regions with greater accuracy using simulations in B2. Ultimately, a 25×50×0.5 mm Al foil and 24×24×0.5 mm Kapton Polyimide flyer were selected for the load. The thicker foil served dual purposes: it both reduced the temperature in the flyer and reduced the growth rate of Rayleigh-Taylor instabilities at the foil-flyer interface. Whilst simulations in B2 were able to identify a load design which seemed to maintain a region of constant density in a liquid state, the hydrocode was unable to simulate flight beyond around 3 cm of the barrel exit. Consequently, an identical load design was used to launch a flyer across three different stand-off distances. The shock profile generated on impact with a PMMA target block was measured and analysed to infer details regarding the flyer state and acceleration.

The shock velocity in the PMMA target block at stand-off distances of 8 mm, 50 mm and 100 mm was successfully recorded. The flyer density predicted by B2 at the barrel exit was close to solid density for PMMA. Further, the shock front at 100 mm was only around 1 mm wider than at 50 mm, providing evidence the flyer likely did not deform significantly between these two points. The shock velocity profiles in the target blocks at 8 mm and 50 mm fluctuated, whilst a continuous shock velocity of 6.5 km/s over a duration of 1000 ns was recorded at 100 mm. The flyer velocity and density on impact at 100 mm could not be accurately estimated, thus it could not be directly verified that this shock velocity was a result of the flyer having a region of constant density and velocity. However, the significant duration of the continuous shock velocity provides strong evidence that this was the case. Having successfully proven this concept, the load designed in the final chapter can now be improved upon in order to maximise the pressure generated by the flyer on impact. While the flyer could be accelerated to higher velocities by reducing the thickness of the foil, the results in this chapter suggest the fundamental aspects of the load need not be altered to achieve higher pressures. The flyer at 50 mm stand-off generated a shock with a maximum velocity of over 10 km/s in the PMMA target, equivalent to around 70 GPa. The experimental evidence indicated the flyer slowed between 50 mm and 100 mm stand-off due to interaction between the flyer and the narrow *yz* dimension of the shroud. This suggests the current electric gun load could generate constant pressures of 70 GPa at 100 mm stand-off simply by redesigning the shroud.

The continuous shock velocity at 10 mm demonstrates the achievement of the goals that this DPhil ultimately set out to accomplish. The modelling tools, experimental methods and, perhaps most crucially, the overall understanding of the electric gun mechanism developed in the previous chapters were utilised to design an electric gun load which could be used to measure extreme states. The improved quality and control of the shock velocity profile in a target extends the potential applications of the projectile launcher beyond ballistic impact studies. The objectives generated as part of Research Goal 4 were assessed:

1. **Utilise the simplified model created as part of the Research Goal 1 to narrow down the electric gun design space.**

   When writing the simplified 0D model, it was discovered the maximum pressure in the flyer spiked when the melt line, behind which the foil was vaporised, reached the foil-flyer interface before launch. It was determined this event should be avoided in order to limit the state change in the flyer. Simulations across a wide range of foil and flyer thicknesses were performed using the 0D model to select a combination of the two wherein the flyer launched before the melt line reached the foil-flyer interface. This approach significantly reduced the time and computational resources that would have been required to perform the same study in B2.

2. **Leverage the experimental techniques and understanding developed in completing Research Goal 2 to inform the design of the electric gun load and its diagnostic set-up.**

A significant obstacle when developing the electric gun resides in the high cost of each experimental shot on a pulsed-power machine like M3. Varying the foil and flyer thickness had the considerable benefit of allowing key elements of the load, such as the anode and cathode, to remain the same as those shown to work successfully in Chapter 5. Beyond this, the practical experience obtained during these prior shots informed the design of the mirror mount and shroud to shield the line of sight of the diagnostics from the excess of bright foil plasma surrounding the set up. Ultimately, the experimental techniques and understanding developed in completing Research Goal 2 ensured diagnostic data was captured in every shot.

3. **Utilise the Eulerian hydrocode B2, including the material strength model derived in research goal 3, to select specific dimensions within the load.**

   The thickness of the foil and flyer in this study were selected following the analysis of simulations in B2. The tear-out behaviour of the thicker foil and flyer were of concern, however, results from B2 revealed material strength effects had little impact on the flyer dynamics or morphology. If the flyer were made of a dielectric material with a higher melting temperature, such as a ceramic, material strength would be expected to have far greater impact on the flyer behaviour.

4. **Test the electric gun load designed in this section and understand the key phenomena in the foil and flyer that prevent the generation of a continuous pressure pulse in a target on impact**

   The electric gun load designed in this chapter was tested on M3 and found to successfully generate a shock velocity of 6.5 km/s in PMMA over a duration of 1000 ns in a PMMA target block, positioned at a stand-off distance of 100 mm. The increased foil thickness was thought to have suppressed RT instability growth at the foil-flyer interface, preventing plasma breakthrough whilst the flyer is in the barrel. Further, despite M3's fixed long rise-time, the 100 mm stand-off distance appears to have sufficiently removed the flyer from the influence of the magnetic field generated by the return current in the load, both spatially and temporally, such that it had a constant velocity. The 100 mm stand-off also had the additional benefit of distancing the impact location from the foil explosion, shielding the line of sight of the streak lasers from bright plasma and improving the reliability of the launch technique.

Chapter 8

Conclusions and Future Work

8.1 Summary of the thesis

On the inception of this thesis, the electric gun was a pulsed-power projectile launcher with unrealised potential. Its promising advantages, including its extensive stand-off distance and its highly efficient conversion of stored electrical energy to kinetic energy in the flyer, could not be made use of; the launch mechanism often damaged the flyer during flight, rendering it incapable of driving a high pressure, planar shock with sufficient duration to make accurate state measurements [3, 4]. However, the compromise of the surface of the flyer carried greater risks to the outcome of the shot than not creating the desired shock pulse shape in the target. If the damage to the flyer was sufficiently great to allow the exploding foil plasma driving the flyer to seep through, the bright, high-velocity, plasma obscured the diagnostic view of the flyer and the target, preventing the further acquisition of any meaningful measurements. That is, the plasma shrouded not only the impact, but also the nature of the flyer damage mechanism.

In this work, four research goals were defined with the intention of developing the electric gun to a state of maturity which is in-line with other projectile launch techniques, such as the electromagnetic flyer plate [1, 16, 19, 20]. The criteria, listed below, were reevaluated:

1. **The electric gun must be able to be modelled and designed using accessible simulation tools.**

   The electric gun was modelled using both a 0D model developed in this work and 2D MHD simulations. The 0D model was verified against 1D simulations in the 3D MHD code, B2. The 0D model was found to accurately capture the dynamics of the foil and flyer, alongside the pressure states in the foil and flyer early in flight. It was used to design an electric gun load for the 140 kV pulsed-power device, M3. The load was used to successfully accelerate 24×24 mm polyimide flyers up to 2-mm-thick to velocities over 10 km/s, for the first time in the electric gun history.

2. **Offer advantages over existing projectile launch techniques.**

   The unique launch mechanism of the electric gun is highly efficient at converting stored electrical energy to kinetic energy in a flyer. This is because it is capable of accelerating the flyer using both thermal and magnetic components of acceleration from an ohmically exploded foil, under the infleunce of strong electromagnetic fields. The $24 \times 24 \times 2.0$ mm electric gun load designed for M3 was found to be four times more efficient than an EM flyer plate with an equivalent surface area and mass. This high efficiency gives the electric gun the potential to explore extreme pressure regimes on pulsed-power devices with fixed rise-times.

   Additionally, the electric gun was reported in previous work to be capable of launching flyers over a long stand-off distance. A greater stand-off distance is favourable, as it permits the potential recovery of the target post-shot and distances the target from the current return path, shielding the diagnostic line of sight from obstructive plasma and debris. This is unfeasible in high-energy EM flyer plates, as the metal plate carries the current directly, causing it to vaporise in flight. An electric gun load was designed in this work for M3, a high-energy machine, to launch a substantially large flyer to velocities in excess of 10 km/s over an extended stand-off distance. It successfully delivered shock in a target block 10 cm away from the launch site.

3. **Be a system wherein the physics required to model the load operation are well understood.**

   The electric gun and the physical models required to model the load were explored when developing the 0D model and reviewing 2D MHD hydrocode simulations of the load. In the 0D model, the flyer dynamics and state were captured more accurately by incorporating an approximation of the effect of sound speed on the communication of acceleration information from the foil to the flyer front. This was shown to be essential to modelling the increase in thermal pressure in the foil prior to launch, a process that plays a significant role in determining both the pressure states in the flyer and the flyer acceleration profile.

   2D simulations in B2 revealed that at the extreme energy densities delivered on M3, material strength need not be considered, as it did not significantly affect the dynamics or thermodynamic states in the foil and flyer. Instead, capturing the current loss mechanisms in the load and pulsed-power device was found to affect the performance of the load far more significantly. Improved modelling of this process is highly recommended in future work.

4. **Generate states in targets which can be used to investigate material properties.**

   Ultimately, this goal was achieved in the final chapter through leveraging learning generated in each chapter prior. The 0D model, described and benchmarked in Chapter 4, was utilised to probe a broad parameter space, reducing the required number of high-fidelity simulations in B2. The experimental load developed and the flyer disassembly mechanisms derived in Chapter 5 were used as a basis for the load design which could launch flyers over an extended stand-off distance and measure their impact. Finally, the 2D simulations in B2 with material strength were used to demonstrate that the greatest disassembly risk in flyers launched over a stand-off distance was due to RT instabilities at the foil-flyer interface. This threat was avoided by increasing the foil thickness such that it vaporised later in flight, thus maintaining a lower Atwood number at the interface for longer.

   The cumulative product of each chapter of work in this thesis resulted in the acceleration of a $24 \times 24 \times 0.5$ mm flyer over a 10 cm stand-off distance (previously a $24 \times 24 \times 0.5$ mm flyer experienced plasma breakthrough at 2 cm in Chapter 5), delivering a constant pressure pulse of 20 GPa over a duration of 1000 ns in a PMMA target block. This is an order of magnitude higher than can be achieved using long-pulse lasers, which have a duration closer to 10 ns. Notably, this result was achieved using a relatively simple fixed rise-time pulsed-power device. This suggests the electric gun could grant a greater range of pulsed-power platforms the ability to make equation of state measurements using projectile launch.

8.2 Future work

Scientific investigations appear to have the side-effect of generating more questions than were present at the start. Whether these questions will eventually all be answered, or whether scientists will be left with exponentially more questions *ad infinitum*, is not yet apparent. Certainly, during this thesis, a number of lines of inquiry have been raised, including: attempting to image the electric gun flyer using x-ray radiography; creating a better model for power loss in the electric gun load; investigating the upper limits of the velocities that can be achieved using the electric gun; exploring the performance of the load on a pulsed-power device with current shaping; and investigating the use of different foil and flyer materials.

8.2.1 X-ray radiography of the electric gun flyer

Two-dimensional simulations of the electric gun revealed features which significantly influenced the integrity and planarity of the flyer during acceleration, such as RT instabilities at the foil-flyer interface. Further, experimental testing of the load over 5 and 10 cm stand-off distance indicated significant precursor shocks at the edges of the target block, suggesting barrel material was swept up by the edges of the flyer. Both of these effects are difficult to investigate indirectly, but would be revealed using x-ray radiography.

Investigating the electric gun using x-ray radiography is challenging, due to the logistics of producing and measuring a sufficient amount of high-energy x-rays close enough to the load, whilst simultaneously discharging a pulsed-power device. However, recent advancements in X-Pinch technology permitted the imaging of an EM plate flyer on the 70 kV pulsed-power device, CEPAGE [138]. This experimental set-up could provide powerful information such as the flyer deformation throughout flight, potentially giving insight into its strength behaviour and state.

8.2.2 Power loss models

The primary challenge faced during this work when modelling the electric gun in a hydrocode is the difficulty representing the pulsed-power device and load. The simulation of the foil and flyer at a sufficient resolution so as to predict convergent thermodynamics states across their thickness, while also capturing the behaviour of the large electrodes, is realistically unfeasible, as the computational resource is too high.

Additionally, the initiation of breakdown paths at various locations in the load, such as through the insulation between the anode and cathode and from the pier to the outer rim of the electrode, is a stochastic process. They are often seeded by random imperfections in the load, such as trapped dust in the insulation layers or scratches.

Finally, the excess of foil plasma produced on its explosion can create pathways through which current can arc. This process is particularly challenging to model, as often the models used to describe the resistivity and state of the plasma in the phase space are incomplete [139]. As a result, capturing the real-world magneto-hydrodynamic behaviour of the plasma, and to what extent it draws current away, is captured inaccurately in hydrocodes.

Recent work undertaken at First Light Fusion has demonstrated a path to predicting flyer dynamics in B2 which more accurately match experimentally measured flyer velocity profiles without using adjustable parameters. First, the entire load is simulated at low-resolutions in three-dimensions using an accurate experimentally measured current profile (no such current profiles were successfully measured for the electric gun loads on M3 during the load testing). The magnetic field strength profile in the metal flyer is recorded, and a higher resolution simulation of a reduced portion of the load in two-dimensions is driven using the magnetic field produced in the 3D simulation. This method could potentially work well for the electric gun, if an accurate current profile could be measured during an experiment.

A limitation faced during this work was the inability to measure a voltage or current across the electric gun foil. While a B-dot probe, a sensor which measures the rate of change over time in magnetic fields, was installed in the cathode, it was unable to measure the current across the fuse due to damage inflicted during the discharge of the capacitor bank. Either of these measurements would be invaluable in benchmarking the code and could provide clarity on the mechanisms of energy loss in the system. For instance, if the measured current and simulated current align well, then it could be assumed the issue with the modelling was routed in the MHD routines in B2. However, if the experimentally measured current across the fuse was lower than the numerically predicted current, it is likely the disparity in the representation of the systems lies in the modelling of M3 and aspects of the load such as the insulation and electrode design. In either case, obtaining these diagnostics is vital to ensuring efforts are directed to improving the parts of the model where it is most necessary.

Alternatively, the MHD simulation could be driven by a more comprehensive pulsed-power model. Currently, the simulations solved an RLC-circuit model to calculate the current through the load. The work performed in Chapter 6 demonstrates the power loss in the system, the exact mechanism for which is still unclear, has a significant effect on the current density in the foil and thus the dynamics of the flyer. The introduction of an integrated model could allow the user to more accurately capture the power loss in the system for a specific pulsed-power device and load it is driving. This is essential for correctly predicting the thermodynamic states of flyers in future load designs, for instance, in loads where the foil width has been reduced to increase the flyer velocity.

8.2.3 Electric gun physics at higher energies

The phenomena encountered in the electric gun load are highly dependent on the integral of current density squared in the exploding foil, which in turn is fixed by the pulsed-power unit's energy storage potential and the foil width. Prior research clearly noted the behaviour of the electric gun loads capable of accelerating flyers over around 10 km/s is distinctly different from lower energy configurations, as the the magnetic field strength profoundly impacts the Lorentz force and thermodynamic states of the foil. To draw a comparison with the EM flyer plate, the models necessary to accurately capture the behavior of the metal flyer in smaller devices, such as those used by Novac *et al.* [78], differ significantly from those required for higher energy devices, such as the electromagnetic stripline geometry on the Z machine [76]. This is because the thermodynamic states experienced within the load are much more extreme on the Z machine, introducing different physical processes, such as vaporization of the load and operation in less well-understood regions of equations of state [139].

The pulsed-power device, M3, utilised throughout this work is the highest energy machine (2.5 MJ) used to power an electric gun in open literature. By contrast, the Z machine has a maximum energy storage of 20 MJ. The foil and flyer dynamics on a machine the size of *Z* are likely to exhibit significant differences compared to those on M3, similar to how M3 revealed new behavior when compared to Weingart's original 40 kJ capacitor bank at LLNL in 1979 [21]. Investigating the electric gun at higher energies likely offers valuable opportunities to explore novel behavior and physical phenomena within the load. This investigation is also essential if the electric gun is to be used to accelerate flyers to velocities above 20 km/s.

Exploring the behaviour of the electric gun load at higher current densities can be performed on medium energy storage pulsed-power devices, such as M3, by reducing the foil width. The electric gun loads explored in this thesis used a foil width of 25 mm, which is relatively wide for an electromagnetic projectile launcher [14, 15, 20]. Consequently, the foil width could likely be reduced significantly without compromising the collection of diagnostics from the flyer surface. Continuing exploration of the electric gun using a modified load on M3 is a lower risk route forward than attempting to launch an electric gun on a new, higher energy pulsed-power device.

8.2.4 The effect of shaping the electric gun current profile

A considerable advancement in the capabilities of the EM flyer plate was achieved on the Z machine by utilising sophisticated current tuning methods to 'shape' the machine's rise-time. This feature of *Z* allows researchers to precisely control the acceleration and state of the metal flyer, such that the same pulsed-power device can be used for equation of state studies at ultra-high pressure in a range of materials [42].

The electric gun would also benefit from control of the current profile: instead of adapting the load geometry to control the acceleration of the flyer and tune the pressure profile generated in a target on impact, the rise-time could be manipulated to the same effect. For instance, the experimental shots performed on M3 were dependent on not causing the flyer to disassemble on launch. To achieve this, the foil and flyer width were increased, reducing the maximum velocity attainable. Current pulse shaping could subvert this constraint, allowing the electric gun to make better use of its intrinsically high efficiencies and accelerate flyers to considerably higher velocities. This could be effectively investigated through simulations in an MHD code, such as B2, provided an appropriate power loss model is incorporated into the code. Without a benchmarked power loss model, the load is unlikely to behave as numerically predicted.

8.2.5 Electric gun loads with alternate materials

The fundamental questions surrounding the electric gun operating mechanism precluded the opportunity to make significant changes between load designs. Consequently, the same foil and flyer materials were used throughout this thesis (99% purity aluminium and 100% DuPont Kapton HN Polyimide film). A significant benefit of the electric gun load design is the considerable range of potential dielectric materials for the flyer: ranging from polymers to high-impedance ceramics. Future studies could purposefully select a flyer material to achieve specific impact conditions or optimise the load behaviour on a machine. The exploration of high-impedance flyers necessitates the implementation and benchmarking of a damage model in B2, as the Johnson-Cook model currently implemented would be inappropriate for this purpose. The incorporation of a Johnson-Holmquist damage model [140] in B2 for this purpose was completed using the procedure set out in [141], however, the benchmarking remains incomplete, hence it is not discussed in this thesis.

Additionally, the foil material, widely unchanged in the majority of the literature reviewed, offers a potentially valuable route to controlling the behaviour in the gun. For instance, the RT instabilities noted in Section 6.5 could be inhibited by a higher density foil material. Alternatively, more general research into the optimisation of high-speed gun suggests the propellant should have the greatest temperature possible with the least molecular mass. Consequently, the propellant thermal energy is used to accelerating the flyer, rather than the propellant itself. In connection with this, lighter metals as the foil that have a lower atomic mass than aluminum could be used to obtain greater velocities [142], or by doping the foil [143]. Adaptations to the foil material, using alternatives such as gold, silver, and copper, could be evaluated at low cost using MHD codes.

Chapter 9

Appendix

A number of details of the electric gun fabrication and experimental procedure were not included in the main body of the thesis. This was largely due to the integrated format, wherein the content in the chapters was written either as, or in the style, of journal articles. Consequently, practical aspects of these processes the author considers integral to a successful electric gun shot have been compiled in these appendices. It is hoped they may be of use to others looking to experimentally investigate the launch technique.

9.1 Fabrication procedures

9.1.1 Exploding Foil Layer

The exploding foil fabricated for each shot during this project was made by the method laid out in Figure 9.1 in order to establish a repeatable workflow. For each shot, three foil-Kapton layers were created and the best chosen for the actual assembly. This ensured a high quality foil was used each time. Fastidious inspection of the foil beneath barrel and flyer is included in the electric gun quality checklist created for this project.

9.1.2 Flyer fit in barrel recess

Precursor plasma waves obscure both the 1D VISAR and the shock in block shadowgraphy, making it impossible to assess the flyer state. To address this issue, in addition to using a thinner flyer, a recess was introduced at the base of the barrel, as shown in Figure 9.2. The flyer clips into this recess and, upon launch, is torn out as it interacts with the walls above it in the barrel. This tear-out process

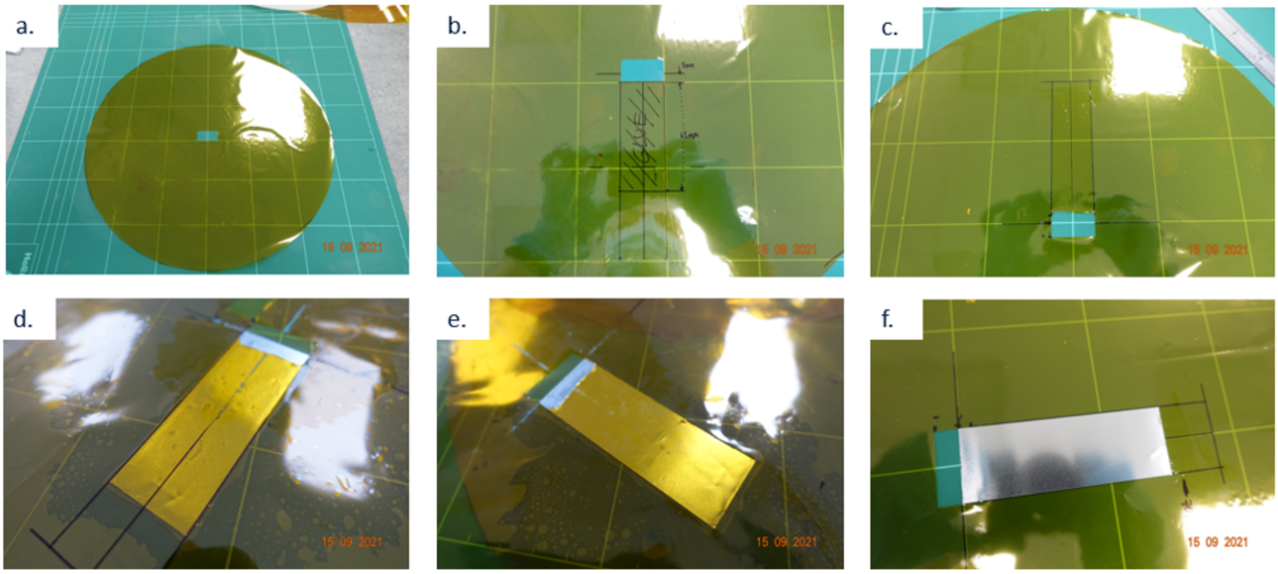

Figure 9.1: Foil-Kapton fabrication workflow. First, a circular layer of Kapton with diameter 150 mm is cut out (a). Then the position of the foil and glue is marked up (b). Using a microbrush, degassed epoxy resin is applied to the Kapton (c). The previously cut foil is carefully laid atop the glue (d). The foil and Kapton is turned over, and the trapped air bubbles are pushed out (e). The foil is inspected for damage and rejected if surface damage exists on either side (f).

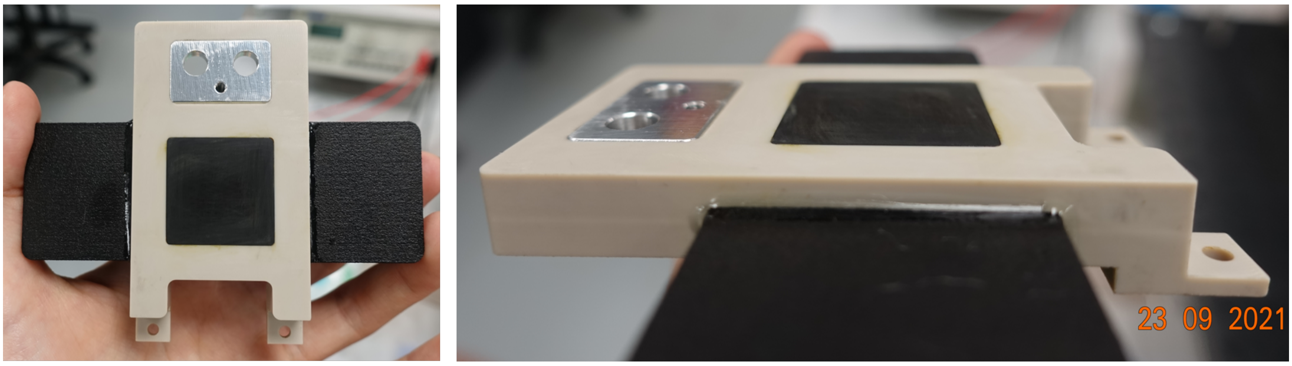

Figure 9.2: The 26.2 x 26.2 mm flyer fits into the 1.6 mm recess, such that the flyer torn out into the barrel is 23 x 23 mm. This recess holds the flyer in place whilst loading and suppress plasma breakthrough.

ensures that the flyer remains above the exploding plasma and prevents it from escaping around the flyer edges. Figure 9.3 highlights the difference between a poorly shaped flyer (shot 0198) and a well-fitted one (shot 0199), along with the corresponding streak camera diagnostics for the setup discussed in Chapter 5. The improved flyer in shot 0199 was fabricated by deliberately cutting it oversized with a scalpel and then sanding it down by hand to fit precisely into the barrel recess.

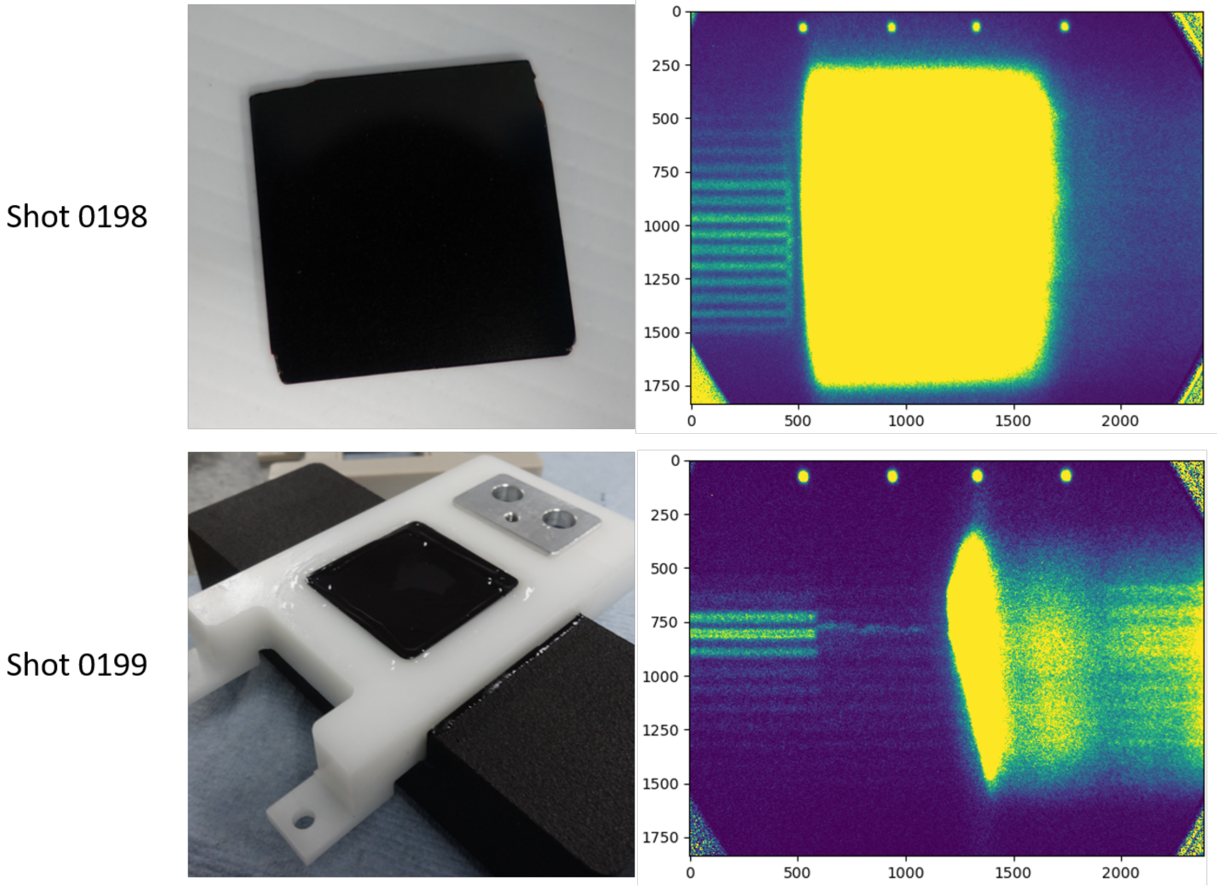

Figure 9.3: Comparison between the a poorly fitted flyer (shot 0198) and a flyer with an improved fit (shot 0199). The 1D VISAR from the poorly fitting flyer shows bright light dominating the frames from the first timing dot, thought to be light from plasma escaping in front of the flyer. In contrast, loses VISAR loses the reflective surface at a similar time, but no plasma breakthrough occurs.

9.1.3 Adaptations to the barrel and mirror mount

Initial electric gun shots on M3 revealed the propensity of aluminium plasma generated during the foil explosion to enter the diagnostic line of sight positioned at the top of the barrel. A wide field of view camera, trained on the join between the foil, barrel and upper electrode during a shot revealed the excessive amounts of bright, low-mass plasma filling the vacuum around the barrel and shielding. Over a couple of shots it became clear the plasma was entering the streak camera line of sight through the join between the barrel and mirror mount, as opposed to from within the barrel itself. At this point, the author redesigned First Light Fusion's barrel and mirror mount to be a single, 3D printed part and added plasma shielding (discussed in Chapter 5). Further, the join between the mirror mount and shroud were changed to be a labyrinth fit. These adaptations were found to successfully exclude the plasma from the diagnostic line of sight for long enough to make the measurements presented in this thesis.

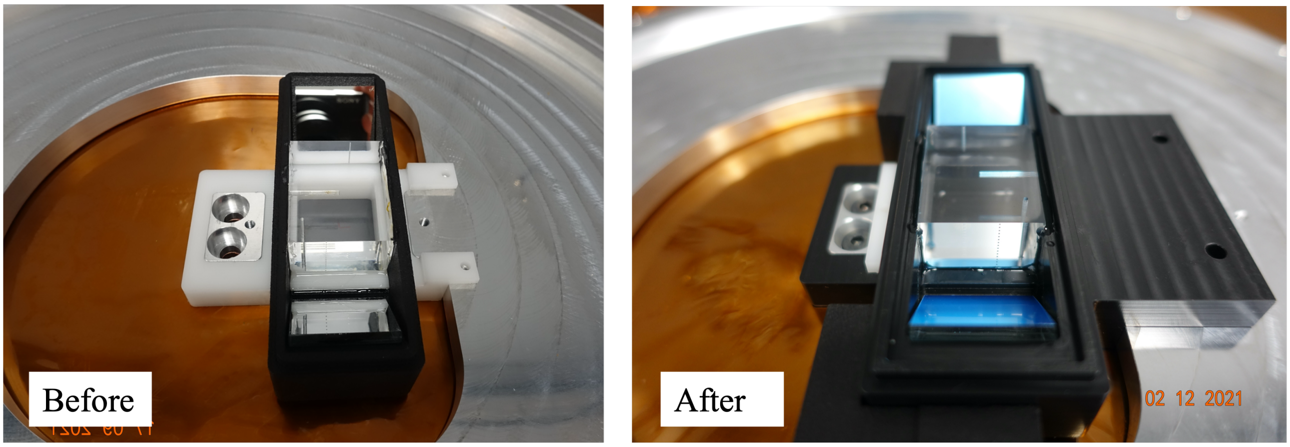

Figure 9.4: Comparison between the barrel and mirror mount designs, before and after improvements made by the author. The original barrel and mirror mount were designed in the past at First Light Fusion.

9.2 Experimental procedures

9.2.1 Vacuum levels and rate of rise

The vacuum chamber in M3 is large and must be evacuated to very low pressure (on the order of $<1 \times 10^{-6} Pa$) to avoid electrical breakdown during capacitor discharge. The vacuum level must be this low, because 30 seconds before M3 is discharged, all electronic systems surrounding it must be switched off to avoid damage to their circuitry during the shot, including M3's cryogenic pumping system [68]. Consequently, First Light Fusion's internal procedure states that M3's rate of rise must tested prior to shooting to ensure the vacuum levels hold to below around $25 \times 10^{-6} Pa$.

9.2.2 Assembly of the electric gun load

In order to create the electric gun, the load was assembled on a large breadboard, specifically designed by First Light Fusion. This breadboard was designed to mimic the load interface in M3, allowing the lower electrode to be fixed in place on the board with screws. The breadboard also included rails with brackets, which could be adjusted to fix the position of the upper electrode. With the top and bottom electrodes fixed in place at reference points, the electric gun load components could be repeatably assembled and moved from the target fabrication rooms to M3 without the load twisting or shifting. This procedure was found to be highly successful and is recommended over the alternative option of assembling the electric gun directly at the load interface.

References

[1] Raymond W Lemke et al. “On the scaling of the magnetically accelerated flyer plate technique to currents greater than 20 MA”. In: *Journal of Physics: Conference Series*. Vol. 500. 15. IOP Publishing. 2014, p. 152009.

[2] RC Weingart et al. *Acceleration of Thin Flyers by Exploding Metal Foils: Application to Initiation studies.[PETN, TATB, PBX-7404, NM]*. Tech. rep. California Univ., Livermore (USA). Lawrence Livermore Lab., 1976.

[3] GR Gathers et al. *Hugoniot measurements with the LLNL electric gun facility*. Tech. rep. Lawrence Livermore National Lab.(LLNL), Livermore, CA (United States), 1989.

[4] David J Hatt and Philip FX Ryan. *Calibration and testing of a large-scale electric gun for shock Hugoniot measurements*. Department of Defence, DSTO Materials Research Laboratory, 1993.

[5] J Osher et al. “Hypervelocity Acceleration and Impact Experiments with the LLNL Electric Guns”. In: *International Journal of Impact Engineering* 10.1-4 (1990), pp. 439–452.

[6] Alessandra Benuzzi et al. “Indirect and direct laser driven shock waves and applications to copper equation of state measurements in the 10–40 Mbar pressure range”. In: *Physical Review E* 54.2 (1996), p. 2162.

[7] TJ Nash et al. “Comparison of a copper foil to a copper wire-array Z pinch at 18 MA”. In: *Physics of plasmas* 11.10 (2004), pp. L65–L68.

[8] NB Meezan et al. “Indirect drive ignition at the National Ignition Facility”. In: *Plasma Physics and Controlled Fusion* 59.1 (2016), p. 014021.

[9] MC Marshall et al. “Developing quartz and molybdenum as impedance-matching standards in the 100-Mbar regime”. In: *Physical Review B* 99.17 (2019), p. 174101.

[10] Hallock F Swift. “Light-gas gun technology: a historical perspective”. In: *High-pressure shock compression of solids VIII: the science and technology of high-velocity impact*. Springer, 2005, pp. 1–35.

[11] TF Thornhill et al. “Particle launch to 19 km/s for micro-meteoroid simulation using enhanced three-stage light gas gun hypervelocity launcher techniques”. In: *International journal of impact engineering* 33.1-12 (2006), pp. 799–811.

[12] Kathryn E Brown et al. “Simplified laser-driven flyer plates for shock compression science”. In: *Review of Scientific Instruments* 83.10 (2012), p. 103901.

[13] Max Karasik et al. “Acceleration to high velocities and heating by impact using Nike KrF laser”. In: *Physics of Plasmas* 17.5 (2010).

[14] Guiji Wang et al. “The Techniques of Metallic Foil Electrically Exploding Driving Hypervelocity Flyers to More Than 10 km/s for Shock Wave Physics Experiments”. In: *Review of Scientific Instruments* 82.9 (2011), p. 095105.

[15] Zhenfei Song et al. “Study on Launching Technique of a 98 kJ Electric Gun for Hypervelocity Impact Experiments”. In: *International Journal of Impact Engineering* 122 (2018), pp. 419–430.

[16] RW Lemke et al. “Characterization of magnetically accelerated flyer plates”. In: *Physics of Plasmas* 10.4 (2003), pp. 1092–1099.

[17] Ron Varesh. “Electric detonators: EBW and EFI”. In: *Propellants, Explosives, Pyrotechnics* 21.3 (1996), pp. 150–154.

[18] Marcus D Knudson. “Megaamps, megagauss, and megabars: Using the Sandia Z Machine to perform extreme material dynamics experiments”. In: *AIP Conference Proceedings*. Vol. 1426. 1. American Institute of Physics. 2012, pp. 35–42.

[19] CLINT A Hall et al. “High velocity flyer plate launch capability on the Sandia Z accelerator”. In: *International journal of impact engineering* 26.1-10 (2001), pp. 275–287.

[20] Raymond W Lemke, Marcus D Knudson, and J-P Davis. “Magnetically driven hyper-velocity launch capability at the Sandia Z accelerator”. In: *International Journal of Impact Engineering* 38.6 (2011), pp. 480–485.

[21] RC Weingart et al. *Electric gun: a New Tool for Ultrahigh-Pressure Research*. Tech. rep. California Univ., Livermore (USA). Lawrence Livermore Lab., 1979.

[22] HH Chau et al. “Electric gun: a Versatile Tool for High-Pressure Shock-Wave Research”. In: *Review of Scientific Instruments* 51.12 (1980), pp. 1676–1681.

[23] H Chau et al. “Performance of a 100 kV, 78 kJ electric gun system”. In: *AIP Conference Proceedings*. Vol. 78. 1. American Institute of Physics. 1982, pp. 691–695.

[24] JE Osher et al. “Application of a 100-kV Electric Gun for Hypervelocity Impact Studies”. In: *International Journal of Impact Engineering* 5.1-4 (1987), pp. 501–507.

[25] JE Osher et al. *Capabilities and some applications of the LLNL 100-kV electric gun*. Tech. rep. Lawrence Livermore National Lab.(LLNL), Livermore, CA (United States), 1989.

[26] Wang Guiji et al. “Speed Test of Small Size Flyer of Explosive Foil Detonator”. PhD thesis. Explosion and shock, 2008.

[27] Percy Williams Bridgman. “The electrical resistance of metals under pressure”. In: *Proceedings of the American Academy of Arts and Sciences*. Vol. 52. 9. JSTOR. 1917, pp. 573–646.

[28] Percy Williams Bridgman. “The effect of pressure on the thermal conductivity of metals”. In: *Papers 32-58*. Harvard University Press, 1964, pp. 1471–1522.

[29] Percy Williams Bridgman. “Polymorphic changes under pressure of the univalent nitrates”. In: *Papers 12-31*. Harvard University Press, 1964, pp. 877–922.

[30] Percy Williams Bridgman. “The viscosity of mercury under pressure”. In: *Papers 59-93*. Harvard University Press, 1964, pp. 2155–2174.

[31] GJ Sizoo and H Kamerlingh Onnes. “Further experiments with liquid helium. cb. influence of elastic deformation on the supraconductivity of tin and indium”. In: *Commun. Phys. Lab. Univ. Leiden* 180 (1925).

[32] Daniel H Dolan. “Foundations of VISAR analysis.” In: (2006).

[33] DH Dolan. “Extreme measurements with photonic Doppler velocimetry (PDV)”. In: *Review of Scientific Instruments* 91.5 (2020).

[34] DG Hicks et al. “High-precision measurements of the diamond Hugoniot in and above the melt region”. In: *Physical Review B* 78.17 (2008), p. 174102.

[35] DG Hicks et al. “Dissociation of liquid silica at high pressures and temperatures”. In: *Physical Review Letters* 97.2 (2006), p. 025502.

[36] EI Moses et al. “The National Ignition Facility: Ushering in a new age for high energy density science”. In: *Physics of Plasmas* 16.4 (2009).

[37] EB Royce. *GRAY, A THREE-PHASE EQUATION OF STATE FOR METALS.* Tech. rep. California Univ., Livermore. Lawrence Livermore Lab., 1971.

[38] Travis Sjostrom and Scott Crockett. “Orbital-free extension to Kohn-Sham density functional theory equation of state calculations: Application to silicon dioxide”. In: *Physical Review B* 92.11 (2015), p. 115104.

[39] MP Desjarlais, MD Knudson, and KR Cochrane. “Extension of the Hugoniot and analytical release model of α-quartz to 0.2–3 TPa”. In: *Journal of Applied Physics* 122.3 (2017).

[40] AB Zylstra et al. “Record energetics for an inertial fusion implosion at NIF”. In: *Physical review letters* 126.2 (2021), p. 025001.

[41] SW Haan et al. “Design and simulations of indirect drive ignition targets for NIF”. In: *Nuclear fusion* 44.12 (2004), S171.

[42] Marcus D Knudson et al. “Advances in pulsed power and MHD technology to enable high pressure material dynamics studies”. In: *2004 International Conference on High-Power Particle Beams (BEAMS 2004)*. IEEE. 2004, pp. 730–733.

[43] MD Knudson and MP Desjarlais. “Shock compression of quartz to 1.6 TPa: Redefining a pressure standard”. In: *Physical Review Letters* 103.22 (2009), p. 225501.

[44] LC Chhabildas et al. “An impact technique to accelerate flier plates to velocities over 12 km/s”. In: *International Journal of Impact Engineering* 14.1-4 (1993), pp. 121–132.

[45] RA Muller, RL Garwin, and B Richter. “Impact fusion with a segmented rail gun”. In: *Proc. LASL Impact Fusion Work* (1979).

[46] DV Keller and JR Penning. “Exploding foils—the production of plane shock waves and the acceleration of thin plates”. In: *Exploding Wires: Volume 2 Proceedings of the Second Conference on the Exploding Wire Phenomenon, Held at Boston, November 13–15, 1961, under the Sponsorship of the Geophysics Research Directorate, Air Force Cambridge Research Laboratories, Office of Aerospace Research, with the Cooperation of the Lowell Technological Institute Research Foundation.* Springer. 1962, pp. 263–277.

[47] LC Chhabildas et al. “Enhanced hypervelocity launcher-capabilities to 16 km/s”. In: *International Journal of Impact Engineering* 17.1-3 (1995), pp. 183–194.

[48] Mike Hinton and Steve Gilbert. “UK electric gun national overview”. In: *2004 12th Symposium on Electromagnetic Launch Technology*. IEEE. 2004, pp. 9–14.

[49] AH Guenther, DC Wunsch, and TD Soapes. “Acceleration of thin plates by exploding foil techniques”. In: *Exploding Wires: Volume 2 Proceedings of the Second Conference on the Exploding Wire Phenomenon, Held at Boston, November 13–15, 1961, under the Sponsorship of the Geophysics Research Directorate, Air Force Cambridge Research Laboratories, Office of Aerospace Research, with the Cooperation of the Lowell Technological Institute Research Foundation*. Springer. 1962, pp. 279–298.

[50] Paul W Dueweke. “A technique for launching intermediate velocity thin plastic sheets”. In: *Review of Scientific Instruments* 41.4 (1970), pp. 539–541.

[51] Ronald W Gurney. *The initial velocities of fragments from bombs, shell and grenades*. Tech. rep. Army Ballistic Research Lab Aberdeen Proving Ground Md, 1943.

[52] TJ Tucker. “Behavior of exploding gold wires”. In: *Journal of Applied Physics* 32.10 (1961), pp. 1894–1900.

[53] JW Kury et al. “Metal acceleration by chemical explosives”. In: *fourth symposium (International) on Detonation*. US Government Printing Office Washington, DC. 1965, pp. 3–13.

[54] KE Froeschner et al. “Shock Hugoniot experiments using an electric gun”. In: *AIP Conference Proceedings*. Vol. 78. 1. American Institute of Physics. 1982, pp. 174–178.

[55] RONALD S Lee. *Simple models for electric gun operating characteristics*. Tech. rep. Lawrence Livermore National Lab.(LLNL), Livermore, CA (United States), 1988.

[56] Yim T Lee and RM More. “An electron conductivity model for dense plasmas”. In: *The Physics of fluids* 27.5 (1984), pp. 1273–1286.

[57] John E Osher et al. “Operating Characteristics and Modeling of the LLNL 100-kV Electric Gun”. In: *IEEE Transactions on Plasma Science* 17.3 (1989), pp. 392–402.

[58] RS Lee et al. “1 MJ Electric Gun Facility at LLNL”. In: *IEEE transactions on magnetics* 29.1 (1993), pp. 457–460.

[59] JE Osher et al. “Electric-gun Studies of Conductors in High Magnetic Fields and Experiments in Dynamic Flux Compression”. In: *Megagauss fields and pulsed power systems*. Taylor & Francis, 1990.

[60] Yong-Chia Thio and MATERIALS RESEARCH LABS ASCOT VALE (AUSTRALIA). *Electromagnetic launchers: background and the MRL program*. Materials Research Laboratories, 1982.

[61] Guiji Wang et al. “The compact capacitor bank CQ-1.5 employed in magnetically driven isentropic compression and high velocity flyer plate experiments”. In: *Review of Scientific Instruments* 79.5 (2008).

[62] Bin-Qiang Luo et al. “Unified numerical simulation of metallic foil electrical explosion and its applications”. In: *IEEE Transactions on Plasma Science* 41.1 (2012), pp. 49–57.

[63] Binqiang Luo et al. “A 200 kJ electrical gun for hypervelocity launch”. In: *Review of Scientific Instruments* 92.12 (2021).

[64] William Neal and Christopher Garasi. “High fidelity studies of exploding foil initiator bridges, Part 3: ALEGRA MHD simulations”. In: *AIP conference Proceedings*. Vol. 1793. 1. AIP Publishing. 2017.

[65] TM Willey et al. “X-ray imaging and 3D reconstruction of in-flight exploding foil initiator flyers”. In: *Journal of Applied Physics* 119.23 (2016).

[66] NJ Sanchez et al. “Dynamic exploding foil initiator imaging at the advanced photon source”. In: *AIP Conference Proceedings*. Vol. 1979. 1. AIP Publishing. 2018.

[67] Guiji Wang et al. *Magnetohydrodynamics of metallic foil electrical explosion and magnetically driven quasi-isentropic compression*. InTech, 2011.

[68] Paul Holligan et al. “An overview of the diagnostic developments for M3, a 2.5 MJ low inductance capacitor discharge machine”. In: *APS Division of Plasma Physics Meeting Abstracts*. Vol. 2018. 2018, GP11–088.

[69] Angelo Raciti et al. “Electrothermal PSpice modeling and simulation of power modules”. In: *IEEE Transactions on Industrial Electronics* 62.10 (2015), pp. 6260–6271.

[70] WM Parsons et al. “An overview of the Atlas pulsed-power systems”. In: *Digest of Technical Papers. 12th IEEE International Pulsed Power Conference.(Cat. No. 99CH36358)*. Vol. 2. IEEE. 1999, pp. 976–979.

[71] David Reisman et al. *Thor: a modern pulsed power accelerator for material science applications.* Tech. rep. Sandia National Lab.(SNL-NM), Albuquerque, NM (United States); Sandia ..., 2016.

[72] Stephan Fuelling et al. “A Zebra experiment to study plasma formation by megagauss fields”. In: *IEEE transactions on plasma science* 36.1 (2008), pp. 62–69.

[73] IH Mitchell et al. “The MAGPIE generator”. In: *AIP Conference Proceedings*. Vol. 299. 1. American Institute of Physics. 1994, pp. 486–494.

[74] RW Lemke et al. “Self-consistent, two-dimensional, magnetohydrodynamic simulations of magnetically driven flyer plates”. In: *Physics of Plasmas* 10.5 (2003), pp. 1867–1874.

[75] Kazuo A Tanaka et al. “Multi-layered flyer accelerated by laser induced shock waves”. In: *Physics of Plasmas* 7.2 (2000), pp. 676–680.

[76] Andrew J Porwitzky, Christopher T Seagle, and Brian J Jensen. “Zero to 1,600 m/s in 40 microns: Sensitive pulse shaping for materials characterization on Z”. In: *Procedia engineering* 204 (2017), pp. 337–343.

[77] AY Wu and KS Sun. “Formulation and implementation of the current filament method for the analysis of current diffusion and heating in conductors in railguns and homopolar generators”. In: *IEEE Transactions on Magnetics* 25.1 (1989), pp. 610–615.

[78] Bucur M Novac et al. “Numerical modelling of a flyer plate electromagnetic accelerator”. In: *IEEE Transactions on Plasma Science* 40.10 (2012), pp. 2300–2311.

[79] Tommy Ao et al. “A compact strip-line pulsed power generator for isentropic compression experiments”. In: *Review of Scientific Instruments* 79.1 (2008).

[80] David B Seidel et al. “An optimization study of stripline loads for isentropic compression experiments”. In: *2009 IEEE Pulsed Power Conference*. IEEE. 2009, pp. 1165–1170.

[81] Alexandre Lefrancois et al. “High-velocity flyer-plate developments on two high-pulsed-power generators based on a strip-line design (GEPI and CEPAGE)”. In: *IEEE Transactions on plasma science* 39.1 (2010), pp. 288–293.

[82] K Omar et al. “Foil-flyer electro-magnetic accelerator initial results from a new AWE pulsed power generator”. In: *2011 IEEE Pulsed Power Conference*. IEEE. 2011, pp. 636–642.

[83] Jeffrey H Nguyen and Neil C Holmes. “Melting of iron at the physical conditions of the Earth’s core”. In: *Nature* 427.6972 (2004), pp. 339–342.

[84] David A Crawford and Otto Eric Strack. *CTH and ALEGRA: Sandia Shock Physics Software*. Tech. rep. Sandia National Lab.(SNL-NM), Albuquerque, NM (United States), 2009.

[85] David J Benson. “Computational methods in Lagrangian and Eulerian hydrocodes”. In: *Computer methods in Applied mechanics and Engineering* 99.2-3 (1992), pp. 235–394.

[86] Irvin R Lindemuth et al. “A computational model of exploding metallic fuses for multimegajoule switching”. In: *Journal of applied physics* 57.9 (1985), pp. 4447–4460.

[87] Thomas J Burgess. *Electrical resistivity model of metals*. Tech. rep. Sandia National Labs., Albuquerque, NM (USA). Pulsed Power Theory Div., 1986.

[88] J D Pecover. *Demonstration of Numerical Capability at First Light Fusion*. 2019. URL: `https://firstlightfusion.com/science-hub/demonstration-of-numerical-capability-at-first-light-fusion`.

[89] Steffen Faik, Anna Tauschwitz, and Igor Iosilevskiy. “The equation of state package FEOS for high energy density matter”. In: *Computer Physics Communications* 227 (2018), pp. 117–125.

[90] JP Chittenden et al. “X-ray generation mechanisms in three-dimensional simulations of wire array Z-pinches”. In: *Plasma Physics and Controlled Fusion* 46.12B (2004), B457.

[91] DB Sinars et al. “Review of pulsed power-driven high energy density physics research on Z at Sandia”. In: *Physics of Plasmas* 27.7 (2020).

[92] John O Hallquist. “LS-DYNA theoretical manual-nonlinear dynamic analysis of structures”. In: *Livermore, California: Livermore Software Technology Corporation, Livermore, California* (1998).

[93] Mila D Fitzgerald et al. “A 0-D Electric Gun Model for the Optimization of Flyer Acceleration to Hypervelocities”. In: *IEEE Transactions on Plasma Science* (2023).

[94] Mila Fitzgerald, Daniel Eakins, and James Pecover. “The design and testing of a novel electric gun: A pulsed power hypervelocity flyer launcher”. In: *AIP Conference Proceedings*. Vol. 2844. 1. AIP Publishing. 2023.

[95] Stanley P Marsh. *LASL shock Hugoniot data*. Vol. 5. Univ of California Press, 1980.

[96] MD Fitzgerald et al. “The effect of current rise time on the acceleration of thick flyers to hypervelocities using an electric gun”. In: *International Journal of Impact Engineering* 184 (2024), p. 104814.

[97] ANSYS Autodyn. “Theory manual revision 4.3”. In: *Century Dynamics, Concord, CA* (2005).

[98] JD Pecover and JP Chittenden. “Instability growth for magnetized liner inertial fusion seeded by electro-thermal, electro-choric, and material strength effects”. In: *Physics of Plasmas* 22.10 (2015), p. 102701.

[99] J. D. Pecover. “Instability growth for magnetised liner inertial fusion seeded by electro-thermal, electro-choric and material strength effects”. Available at `https://spiral.imperial.ac.uk/handle/10044/1/26586`. PhD thesis. Imperial College London, Sept. 2015.

[100] Geoffrey Ingram Taylor. “The use of flat-ended projectiles for determining dynamic yield stress I. Theoretical considerations”. In: *Proceedings of the Royal Society of London. Series A. Mathematical and Physical Sciences* 194.1038 (1948), pp. 289–299.

[101] J Michael McGlaun, SL Thompson, and MG Elrick. “CTH: A three-dimensional shock wave physics code”. In: *International Journal of Impact Engineering* 10.1-4 (1990), pp. 351–360.

[102] Charles E Anderson Jr. “An overview of the theory of hydrocodes”. In: *International journal of impact engineering* 5.1-4 (1987), pp. 33–59.

[103] David J Benson and Shigenobu Okazawa. “Contact in a multi-material Eulerian finite element formulation”. In: *Computer methods in applied mechanics and engineering* 193.39-41 (2004), pp. 4277–4298.

[104] James D Walker and Charles E Anderson Jr. “Multi-material velocities for mixed cells”. In: *AIP Conference Proceedings*. Vol. 309. 1. American Institute of Physics. 1994, pp. 1773–1776.

[105] David J Benson. “A mixture theory for contact in multi-material Eulerian formulations”. In: *Computer methods in applied mechanics and engineering* 140.1-2 (1997), pp. 59–86.

[106] DA Mandell, KS Holian, and R Henninger. “MESA: A 3-D Eulerian hydrocode for penetration mechanics studies”. In: *Shock Compression of Condensed Matter–1991*. Elsevier, 1992, pp. 931–934.

[107] Gareth S Collins. “An introduction to hydrocode modeling”. In: *Applied Modelling and Computation Group, Imperial College London* (2002), pp. 2–11.

[108] Michael W Burkett et al. “Modeling anisotropic plasticity: 3D Eulerian hydrocode simulations of high strain rate deformation processes”. In: *AIP Conference Proceedings*. Vol. 620. 1. American Institute of Physics. 2002, pp. 279–282.

[109] Michael W Burkett. “Eulerian hydrocode modeling of a dynamic tensile extrusion experiment”. In: *Hypervelocity Impact Symposium*. Vol. 883556. American Society of Mechanical Engineers. 2019, V001T09A011.

[110] MD Fitzgerald et al. “Redesigning the electric gun: Launching thick flyers to hypervelocity with high efficiency”. In: *High Energy Density Physics* (2024), p. 101119.

[111] Harry Schulz, André Simoes, and Raquel Lobosco. *Hydrodynamics: Advanced Topics*. BoD–Books on Demand, 2011.

[112] R v Mises. “Mechanik der festen Körper im plastisch-deformablen Zustand”. In: *Nachrichten von der Gesellschaft der Wissenschaften zu Göttingen, Mathematisch-Physikalische Klasse* 1913 (1913), pp. 582–592.

[113] Lars Westerling. *An implicit method for a strain rate dependent constitutive model implemented in Autodyn as a user subroutine*. Tech. rep. FOI-R–O3, 2002.

[114] Gordon R Johnson and William H Cook. “Fracture characteristics of three metals subjected to various strains, strain rates, temperatures and pressures”. In: *Engineering fracture mechanics* 21.1 (1985), pp. 31–48.

[115] Grigori Volkov, Elijah Borodin, and Vladimir Bratov. “Numerical simulations of Taylor anvil-on-rod impact tests using classical and new approaches”. In: *Procedia Structural Integrity* 6 (2017), pp. 330–335.

[116] DE Eakins and NN Thadhani. “Instrumented Taylor anvil-on-rod impact tests for validating applicability of standard strength models to transient deformation states”. In: *Journal of applied physics* 100.7 (2006), p. 073503.

[117] AJ Kemp and J Meyer-ter-Vehn. “An equation of state code for hot dense matter, based on the QEOS description”. In: *Nuclear Instruments and Methods in Physics Research Section A: Accelerators, Spectrometers, Detectors and Associated Equipment* 415.3 (1998), pp. 674–676.

[118] Bram Van Leer. “Towards the ultimate conservative difference scheme. IV. A new approach to numerical convection”. In: *Journal of computational physics* 23.3 (1977), pp. 276–299.

[119] David J Benson. “Volume of fluid interface reconstruction methods for multi-material problems”. In: *Appl. Mech. Rev.* 55.2 (2002), pp. 151–165.

[120] John VonNeumann and Robert D Richtmyer. “A method for the numerical calculation of hydrodynamic shocks”. In: *Journal of applied physics* 21.3 (1950), pp. 232–237.

[121] David L Youngs. “Time-dependent multi-material flow with large fluid distortion”. In: *Numerical methods for fluid dynamics* (1982).

[122] M Fitzgerald. *Shockwave-Driven Cavity Collapse in the Context of Nuclear Fusion.* 2020.

[123] Andrew Porwitzky et al. “Large time-varying inductance load for studying power flow on the Z machine”. In: *Physical Review Accelerators and Beams* 22.9 (2019), p. 090401.

[124] Nicolas Niasse. June 6, 2023.

[125] AR Piriz et al. “Rayleigh-Taylor instability in elastic solids”. In: *Physical Review E* 72.5 (2005), p. 056313.

[126] AR Piriz, JJ Cela, and NA Tahir. “Rayleigh–Taylor instability in elastic-plastic solids”. In: *Journal of Applied Physics* 105.11 (2009).

[127] Hye-Sook Park et al. “Strong stabilization of the Rayleigh–Taylor instability by material strength at megabar pressures”. In: *Physics of Plasmas* 17.5 (2010).

[128] Bruce A Remington et al. “Rayleigh–Taylor instabilities in high-energy density settings on the National Ignition Facility”. In: *Proceedings of the National Academy of Sciences* 116.37 (2019), pp. 18233–18238.

[129] Dean L Preston, Davis L Tonks, and Duane C Wallace. “Model of plastic deformation for extreme loading conditions”. In: *Journal of applied physics* 93.1 (2003), pp. 211–220.

[130] Nirmal Kumar Rai et al. “Mechanics of shock induced pore collapse in poly (methyl methacrylate)(PMMA): Comparison of simulations and experiments”. In: *Journal of the Mechanics and Physics of Solids* 143 (2020), p. 104075.

[131] Jerald V Parker. “Why plasma armature railguns don’t work (and what can be done about it)”. In: *IEEE Transactions on Magnetics* 25.1 (1989), pp. 418–424.

[132] Ian R McNab. "Progress on hypervelocity railgun research for launch to space". In: *2008 14th Symposium on Electromagnetic Launch Technology*. IEEE. 2008, pp. 1–8.

[133] Bucur Novac. Dec. 4, 2024.

[134] AJ Piekutowski and KL Poormon. "Development of a three-stage, light-gas gun at the University of Dayton Research Institute". In: *International journal of impact engineering* 33.1-12 (2006), pp. 615–624.

[135] MD Knudson and MP Desjarlais. "Adiabatic release measurements in α-quartz between 300 and 1200 GPa: Characterization of α-quartz as a shock standard in the multimegabar regime". In: *Physical Review B* 88.18 (2013), p. 184107.

[136] Mila Fitzgerald et al. "Practical Methods for the Implementation of Material Strength into an Eulerian Hydrocode". In: *Available at SSRN 4948242* (2024).

[137] A. McHutchon. "Nonlinear Modelling and Control using Gaussian Processes". Available at `https://mlg.eng.cam.ac.uk/pub/pdf/Mch14.pdf`. PhD thesis. University of Cambridge, Aug. 2014.

[138] J Read et al. "Point projection radiography of electromagnetically accelerated flyer plates with an external X-pinch driver". In: *Review of Scientific Instruments* 95.2 (2024).

[139] MP Desjarlais, JD Kress, and LA Collins. "Electrical conductivity for warm, dense aluminum plasmas and liquids". In: *Physical Review E* 66.2 (2002), p. 025401.

[140] GR Johnson and TJ Holmquist. "A computational constitutive model for brittle materials subjected to large strains, high strain rates, and high pressures". In: *Shock wave and high-strain-rate phenomena in materials*. CRC Press, 1992, pp. 1075–1082.

[141] Duane S Cronin et al. "Implementation and validation of the Johnson-Holmquist ceramic material model in LS-Dyna". In: *Proc. 4th Eur. LS-DYNA Users Conf.* Vol. 1. 2003, pp. 47–60.

[142] Arnold E Seigel. *The theory of high speed guns*. North Atlantic Treaty Organization, Advisory Group for Aerospace Research ..., 1965.

[143] John E Osher. *Hydrogen loaded metal for bridge-foils for enhanced electric gun/slapper detonator operation*. Tech. rep. Lawrence Livermore National Lab.(LLNL), Livermore, CA (United States), 1992.